CHEMICAL REVIEWS

pubs.acs.org/CR

Review

Design of Single-Atom Catalysts and Tracking Their Fate Using *Operando* and Advanced X-ray Spectroscopic Tools

Bidyut Bikash Sarma,* Florian Maurer, Dmitry E. Doronkin, and Jan-Dierk Grunwaldt*

Cite This: *Chem. Rev.* 2023, 123, 379−444

Read Online

ACCESS | Metrics & More | Article Recommendations

ABSTRACT: The potential of *operando* X-ray techniques for following the structure, fate, and active site of single-atom catalysts (SACs) is highlighted with emphasis on a synergetic approach of both topics. X-ray absorption spectroscopy (XAS) and related X-ray techniques have become fascinating tools to characterize solids and they can be applied to almost all the transition metals deriving information about the symmetry, oxidation state, local coordination, and many more structural and electronic properties. SACs, a newly coined concept, recently gained much attention in the field of heterogeneous catalysis. In this way, one can achieve a minimum use of the metal, theoretically highest efficiency, and the design of only one active site-so-called single site catalysts. While single sites are not easy to characterize especially under operating conditions, XAS as local probe together with complementary methods (infrared spectroscopy, electron microscopy) is ideal in this research area to prove the structure of these sites and the dynamic changes during reaction. In this review, starting from their fundamentals, various techniques related to conventional XAS and X-ray photon in/out techniques applied to single sites are discussed with detailed mechanistic and *in situ*/*operando* studies. We systematically summarize the design strategies of SACs and outline their exploration with XAS supported by density functional theory (DFT) calculations and recent machine learning tools.

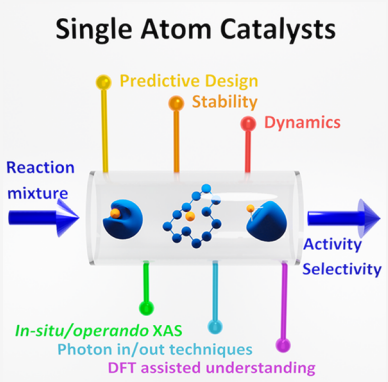

CONTENTS

1. Introduction 380
 1.1. Single-Atom Catalysts (SACs)/Atomically Dispersed Catalysts 380
 1.2. Dynamic Behavior of Solid Catalysts 381
 1.3. X-ray Absorption Spectroscopy (XAS) for Characterizing SACs 384
 1.4. Hard X-ray Probes as Emerging Technique: Advanced Photon in/out Techniques and New Analysis Tools 384
  1.4.1. Basics of X-ray Absorption Spectroscopy 384
  1.4.2. EXAFS Fitting 387
  1.4.3. Wavelet Transform (WT) Analysis of EXAFS 387
  1.4.4. Application of XAS on Solids 388
2. Single-Atom Catalysts (SACs): Strategies toward Synthesis and Their Reactivity over Different Supports 389
 2.1. SACs Incorporated over Oxide Supports 389
  2.1.1. SACs Dispersed on Metal Oxides Surfaces 389
  2.1.2. SACs Incorporated on Polyoxometalates (POMs) Framework 392
  2.1.3. SACs Confined in Zeolites 395
 2.2. SACs as Composite Materials 397
  2.2.1. SACs as Single Atom Alloy (SAA) and Intermetallic Structure (IMS) 397
 2.3. SACs Supported in Soft Matrices 402
  2.3.1. SACs Incorporated on 2D Boron, Carbon Host 402
  2.3.2. SACs Incorporated in Metal−Organic Frameworks (MOFs)/Covalent Organic Frameworks (COFs) 404
  2.3.3. SACs Inside Porous Organic Polymers (POPs) as Host 406
 2.4. SACs over Other Supports 406
  2.4.1. SACs Supported in Metal Carbides/Sulfides/Nitrides/Phosphides 406
  2.4.2. SACs in Perovskites as Host Structure 410
 2.5. Summary of SACs over Various Supports 412
3. *In Situ*/*Operando* XAS Studies on SACs: Tracking the Fate of Single Atom Catalysts 412
 3.1. *In Situ*/*Operando* Studies at Synchrotron Radiation Sources 412

Received: July 12, 2022
Published: November 23, 2022

3.2. Concept of Designing Cells: Finding the Best Compromise 413
3.2.1. Cells for Gas-Phase Reactions 413
3.2.2. Cells for Liquid-Phase and Electrochemical Reactions 416
3.3. Tracking the Active Sites of SACs for Gas–Solid Reactions 416
3.3.1. Stable Single Atom Catalysts under Reaction Conditions 416
3.3.2. Agglomeration of Single Atoms to Clusters and Nanoparticles 418
3.4. Tracking the Active Sites of SACs for Liquid–Solid Reactions 421
3.5. SACs for Electrochemical Reactions: A Liquid–Solid Interface 422
3.5.1. Oxygen Reduction Reaction (ORR) 422
3.5.2. CO_2 Reduction Reaction (CO_2 RR) 423
3.5.3. Hydrogen Evolution Reaction (HER) 425
4. DFT-Assisted XAS Studies on SACs 425
4.1. Supported over Bulk Metal Oxides 425
4.2. Confined in Zeolite Framework 426
4.3. Inside Carbon-like Host Materials 428
5. Machine Learning Approach toward SACs 428
6. Conclusion and Outlook 430
Author Information 431
Corresponding Authors 431
Authors 431
Author Contributions 431
Notes 431
Biographies 431
Acknowledgments 432
Abbreviations 432
References 432

1. INTRODUCTION

1.1. Single-Atom Catalysts (SACs)/Atomically Dispersed Catalysts

Atomically dispersed catalysts are currently a flourishing area in heterogeneous catalysis and in such materials atoms are anchored on the solid surface via different routes such as attaching a molecular complex over the support, ion-exchange, stabilizing in the confinement, thermal trapping and alloying, etc.[1−5] We divide this broad category, atomically dispersed catalysts into two subcategories (a) single site heterogeneous catalysts (SSHCs)[6] and (b) single-atom catalysts (SACs) as clarified in Scheme 1. On SSHCs, each and every site is uniform and usually surrounded by the ligands of the precursors. In contrast, on SACs, the active sites are nonuniformly distributed and ligand-free (from precursors), as outlined e.g. by Zhang and co-workers.[7] With SSHCs, there can be more than one type of metal present which have a similar coordinating environment. With SACs, there is only one type of metal anchored over the support where the metal can have different coordinating environments. Molecular complexes supported on high surface area solids such as silica or alumina,[8] magnesia,[9] zeolite,[10] and other porous structures are classified under SSHCs. This field of research was tremendously developed by Basset, Copéret, and their co-workers as Surface Organometallic Chemistry (SOMC).[11,12] A comprehensive topic that has been reviewed by Flytzani-Stephanopoulos and Gates in this area of research is atomically dispersed supported metal catalysts.[13,14] Flytzani-Stephanopoulos,[15,16] Iwasawa,[17] and their co-workers claimed the importance of isolated catalytically active sites a long time ago but, due to lack of sufficiently high-resolved electron microscopy and universal spectroscopic techniques, this field did only partially come to the center of attention. Now, both the synthesis and the characterization strategies have been significantly improved. Between SSHCs and SACs, there are numerous examples that overlay with each other due to the method applied for anchoring of the atoms on the support and the consecutive treatment procedures. In this review we will address mainly SACs, i.e. those that do not have additional ligands bonded to the metal center after treatment and are truly bonded to support via covalent interactions.

SACs, very similar to atomically dispersed where atoms are anchored directly on the surface, have only recently raised strong attention.[19] The term *single-atom catalyst* was first coined by Zhang and his co-workers,[20] where single platinum atoms were directly anchored on iron oxide without any stabilizing agent or ligand. In the past decade, numerous reports claimed higher activity per mass of metal of SACs over the analogous cluster or nanoparticle. Since then, this field of research has been guiding the way for new catalysts design and their various applicability. Figure 1 shows the number of publications in literature with the word "Single Atom Catalysts/Catalysis" in the title of articles since 2011.

Since then, SACs have been proven to be an elegant set of materials where the coordinatively unsaturated metal centers resemble a molecular complex and hence they hold the potential to bridge the gap between homogeneous and heterogeneous catalysis.[7,21−25] Theoretically, SACs provide maximum catalyst efficiency with a tunable charge property of the metal.[19,22,26] They are also treated as nanozymes, a material that can give information about the role of enzymes in biocatalysis.[27] The isolated metal atoms are usually covalently bonded to the support, meaning that there is a strong interaction between the metal and support and hence, unusual for heterogeneous/supported catalysts, SACs are claimed to show high stability under harsh reaction conditions.[28,29] The higher stability and sinter-resistant behavior of SACs make it possible for applications toward energy transformations.[30] Single atoms, when anchored on a solid surface, can stabilize themselves in various coordinating environments such as on the terrace, step-edges, or even in the subsurface regions, as shown in Figure 2. Single atoms can be stabilized/relocated depending on the preparation method and even under operating conditions. Hence, uniform structural elucidation of SACs, comparisons of activity with clusters/nanoparticles, and finding the active species is necessary, as pointed out by Christopher and co-workers.[31,32]

In the past decade, SACs has been shown to be very effective for various applications with large scale synthesis possibilities. We would like to point out the advantages and disadvantages of SACs in the Table 1.

Until now, most efforts have been dedicated to the preparation of SACs and less have been devoted to studying them under reaction conditions. There are only a few techniques that are well studied, among them X-ray absorption spectroscopy (XAS) and related techniques. XAS[35] is a rapidly advancing technique that allows identifying the structure of atoms on a molecular level. In fact, SACs are especially suitable to be studied by bulk averaging techniques such as XAS. Beyond the *ex situ* characterization, more important is to understand the dynamic behavior of SACs with XAS under operating conditions, as

https://doi.org/10.1021/acs.chemrev.2c00495
Chem. Rev. 2023, 123, 379−444

Scheme 1. General Scheme Describing Two Major Categories of the Atomically Dispersed Metal Catalysts and Conventional Supports with Some Prominent Examples[7,18] (In SACs, the Active Site Is Not Coordinated to Additional Ligands from the Metal Precursor and Directly Bonded to Support through Heteroatoms Like O, N, or S)

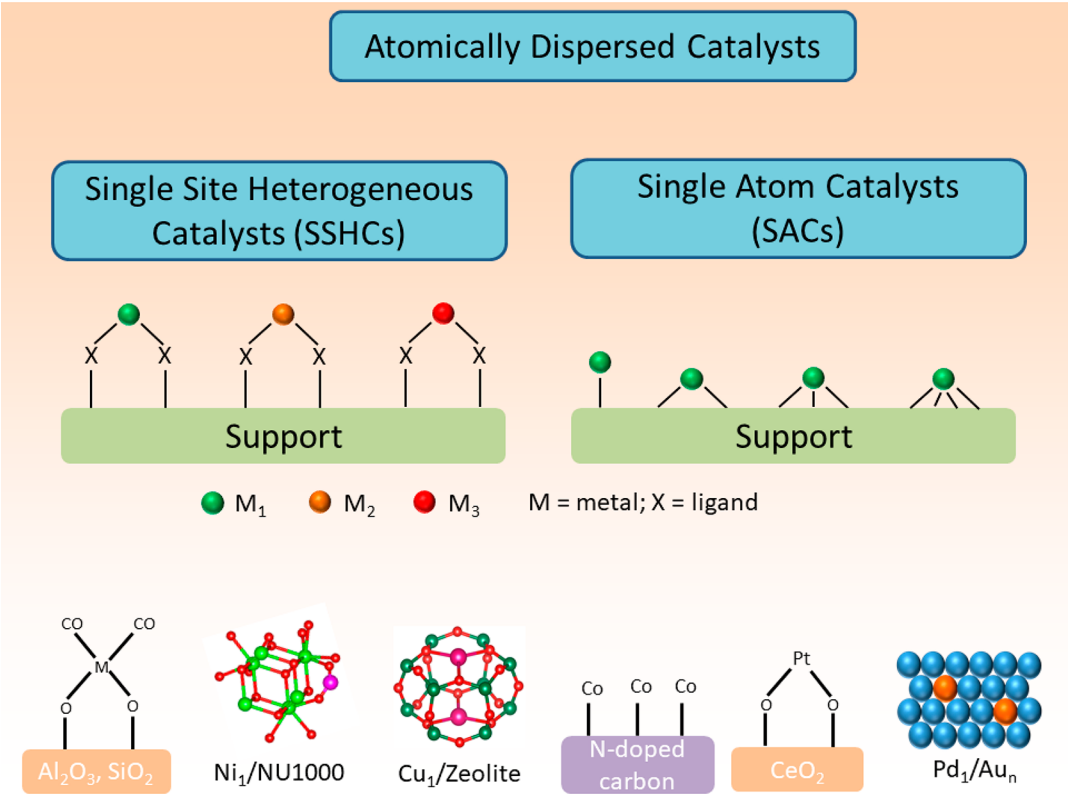

pointed out by various research groups.[36−41] As X-rays can penetrate easily through solid materials in either crystalline or amorphous phase, XAS can account for reversible or irreversible transformation in catalysts sintering/agglomeration from atom to nanoparticle under oxidizing[42] or reducing atmosphere[43] as shown in Figure 3.

One major challenge while conducting *in situ*/*operando* XAS is to design a proper cell for universal application. To emphasize this, we will briefly review the design strategies of various types of cells used for *in situ*/*operando* XAS studies in the gas and liquid phase. Finally, we will discuss the importance of DFT-assisted XAS analysis to identify the active site structure in SACs and the rise in machine learning tools for rapid analysis of larger data sets.

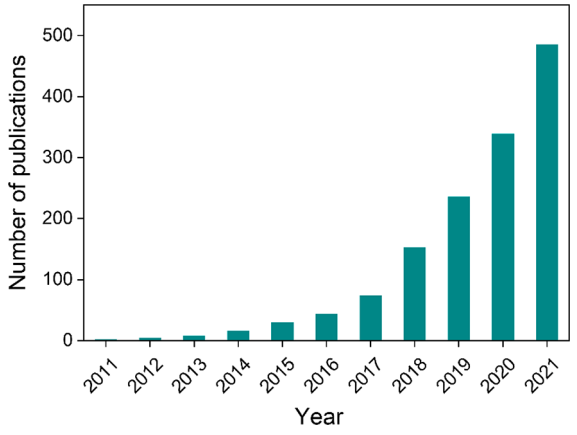

Figure 1. Number of publications where "Single Atom Catalysts/Catalysis" is in the title since 2011. Source: Web of Science.

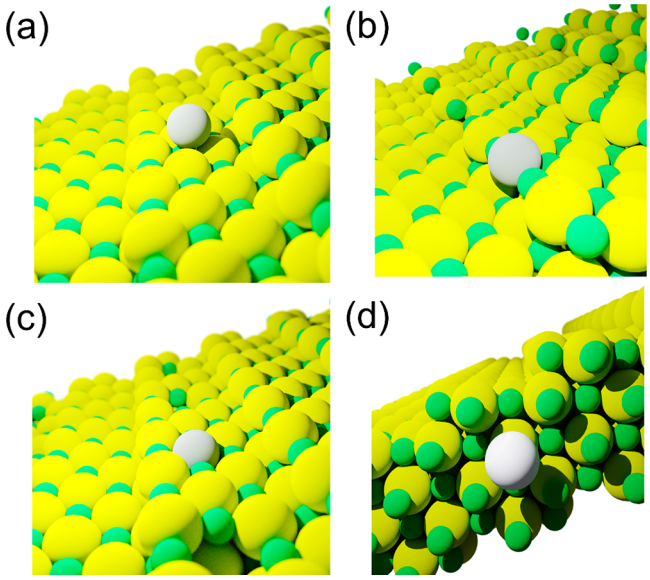

Figure 2. Representation of a single atom in different coordinating environments supported on a metal oxide framework with 1st shell M-O coordination number (CN) (a) 1, (b) 3, (c) 4, and (d) 6. (d) Simplified side view of a single atom located at subsurface position.

1.2. Dynamic Behavior of Solid Catalysts

Solid catalysts, especially SACs, can be quite dynamic under different reaction environments (such as temperature, pressure,

https://doi.org/10.1021/acs.chemrev.2c00495
Chem. Rev. 2023, 123, 379−444

Table 1. Advantages and Disadvantages of SACs

advantages	disadvantages
▶ Highly tunable binding energies to reacting species allowing to adjust catalytic activity to the maximum of the Brønsted−Evans−Polanyi relation.[33,34]	▶ Often high surface free energy
▶ Maximum dispersion, theoretically high catalytic efficiency (unless catalysts with small clusters and monolayers, which also offer 100% dispersion, are considered).	▶ High risk of agglomeration under harsh reaction conditions or pretreatments.
▶ Emerging applications in wide range of materials such as thermal, electro, photocatalysts, where knowledge driven approach between molecular and solid catalysts is key for the findings.	▶ Synthesis often results in nonuniform mixture of different species, challenging to adequately identify active species and characterize with readily available spectroscopic techniques.
▶ Potential for selective reaction pathway, minimization of side reactions.	▶ Limited to low metal concentration, high mass of catalyst, higher risk of mass-transfer limitations in comparison to clusters and nanoparticle catalysts.

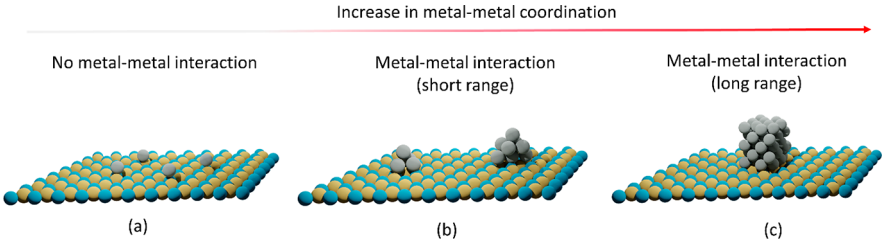

Figure 3. Schematic representation of transformation from supported single atom to nano- particle that can be tracked by XAS (from 1 to5 Å).

presence of gas mixture).[44,45] Some of the occurring processes are described in the following:

(a) Leaching/colloid formation. Solid catalysts can form molecular complexes or colloids in solution during reactions in the liquid phase. For example, during a Pd/Al_2O_3-catalyzed Heck reaction, molecular Pd complexes that leached to the solution were found to be the catalytically active centers.[46] In another study, Perez-Ramírez and co-workers showed that Pd single atoms incorporated in graphitic carbon nitride are highly active for the Suzuki coupling reaction.[47]

(b) Change in morphology. Methanol synthesis catalysts (Cu/ZnO) under syngas atmosphere were found to change from round-shaped Cu nanoparticles to more disc-like shapes under reducing environment.[48,49] Upon applying a more reducing atmosphere, the Zn atoms migrate from the support and form brass alloy. Thomas, Greaves, and co-workers combined *in situ* XAS and XRD to study both the short and long-range structural and chemical changes of the layered mineral aurichalchite (Cu_{5-x} $Zn_x(OH)_6(CO_3)_2$), precursor for the most commonly used methanol synthesis catalysts, and found that despite of significant change in crystallinity, the local environment and electronic structure of Cu^{2+} remains unchanged when heated to 450 °C.[50] In another study, Andreasen, Chorkendorff, and co-workers reported that, in a $Ru/MgAl_2O_4$ catalyst, Ru particles change their size and morphology during dry reforming of methane.[51]

(c) Redispersion/single atom formation. In the Pt/CeO_2 catalyst, it is shown that the noble metal reversibly disperses into small clusters and even single atoms under oxidizing condition or transforms into nanoparticles under reducing environment.[36,52,53] The dynamic behavior of automotive catalysts Pt/CeO_2-ZrO_2 is a well-established phenomenon, where $Pt-O-Ce^{4+}$ bond formation was observed on aging at 1073 K in air. However, under reductive atmosphere, when Ce^{4+} is reduced to Ce^{3+}, the Pt−O−Ce bond collapses.[54] Gänzler et al.[53] exploited this concept of redispersion in air and particle formation under reducing conditions for producing small Pt clusters using pulses of reducing agent. Christopher and co-workers showed Rh nanoparticle supported over TiO_2 disintegrate into Rh single atom under CO_2 reduction condition and observed change in the activity of the catalyst.[55] Wang et al. reported formation and migration of Au-CO complexes upon exposure of CO on Au surface which potentially alters the electronic structure of Au sites.[56] Grunwaldt et al. further showed in a Rh/Al_2O_3 catalyst under catalytic partial oxidation of methane (CPO) the Rh particles strongly changed their structure.[39] They disaggregate upon heating with CH_4/O_2 reaction mixture and form $Rh^I(CO)_2$ species whereas under H_2 atmosphere, Rh agglomerates.

(d) Oxide layer formation. Martin et al.[57] found that a bimetallic Pd−Pt catalyst supported over Al_2O_3 was formed only at a calcination temperature of 1073 K. The Pd−Pt nanoparticles undergo reversible changes in the composition of surface structure and chemical state under oxidizing or reducing atmosphere. When the catalyst was treated under oxidizing conditions, Pd segregates to the shell and oxidizes to form PdO. In contrast, under reducing conditions metallic Pd and Pd−Pt alloys were formed on the surface.

(e) Single site/dimer transformation. The Cu sites in Cu-SSZ-13 showed various dynamic transformations under selective catalytic reduction (SCR) reaction, as Grunwaldt and co-workers showed.[58] in this case, isolated Cu sites interconvert between Cu^{2+} and Cu^+ as ammonia complexes such as $Cu(NH_3)_2^+$ form dimeric bis (μ-oxo) Cu species in oxidizing gas mixtures.

(f) Strong metal support interaction (SMSI). $Co-Ru/TiO_2$ catalyst used for the Fischer−Tropsch process was partially covered by the support TiO_2 under the reduction condition.[59] This effect was found more prominent for anatase-supported catalysts than rutile, which has consequences for the catalytic activity. There are other factors contributing to metal support interactions such as alloying, charge transfer, and composite formation that strongly influence the catalytic behavior.[44]

(g) Alloying/dealloying. Alloying/dealloying can take place upon change of the gas atmosphere. An attractive concept has recently been reported by Wasserscheid and co-workers. They conclude that single atoms of Pt form under reaction conditions in a Pt−Ga metal solution and act as active center during propane dehydrogenation (supported catalytically active liquid metal solutions, SCALMS).[60] The Pt single atoms move from the bulk of Ga metal to the surface under reaction conditions. A similar behavior was observed for Rh−Ga, where Rh single

https://doi.org/10.1021/acs.chemrev.2c00495
Chem. Rev. 2023, 123, 379−444

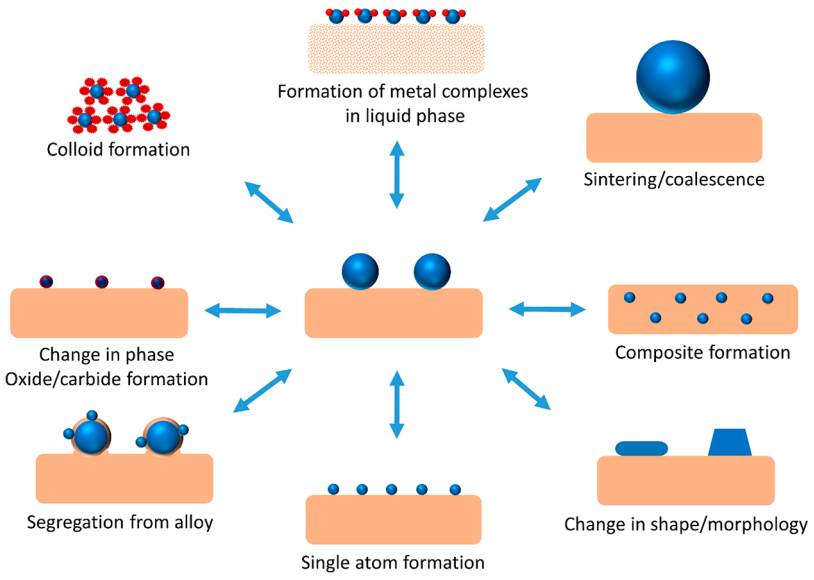

Figure 4. Schematics of major structural changes of a solid catalyst especially focused on single atom catalysts under reaction conditions.

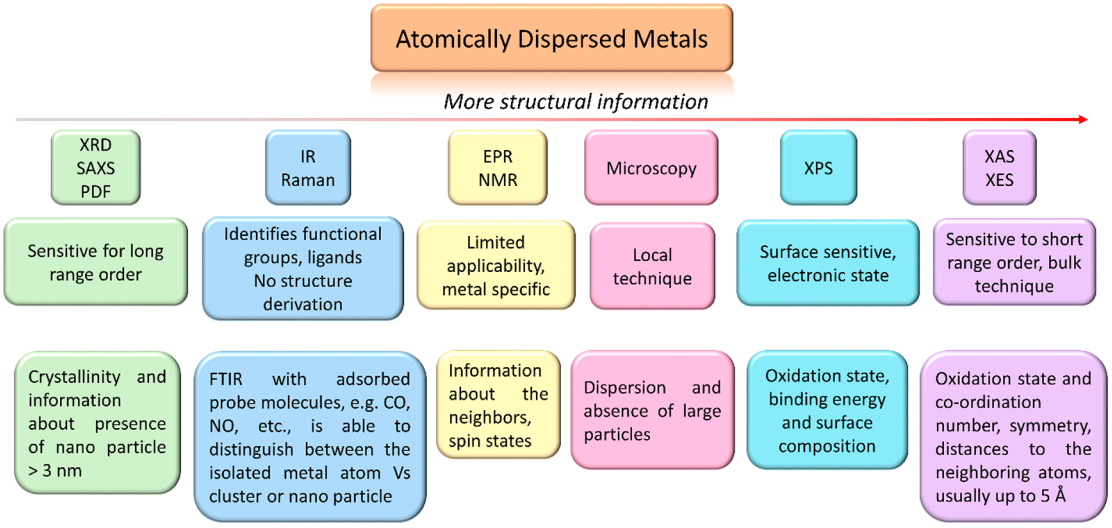

Figure 5. Overview of available techniques. The advantages/limitations and the amount of structural information of atomically dispersed catalysts that can be derived are shown.

atoms appear at the interface of the solution under constant presence of propane in the gas feed.[61]

(h) Composite formation. Parkinson and co-workers reported that the incorporation of Ir single atoms into a Fe_3O_4 (001) support can already occur at 450 K, rendering the noble metal inactive for adsorption of gas adsorbates.[62] Control of structural changes was already exploited to create an "intelligent" catalyst for emission control purposes. In a study by Mizuki et al., the reversible incorporation and particle formation[63] of platinum group metals supported on a perovskite support were used to suppress the growth of Pd particles during the entire lifetime of a vehicle. The Pd atoms move in and out of the perovskite host structure during the reaction. This is similar to the concept using Pt/CeO_2 reported by Gänzler et al.[53] where however, the single site Pt atoms stayed on the surface.

(i) Single atom alloy. Sykes, Flytzani-Stephanopolous, and others reported a concept using the formation of diluted alloy where single atoms are principally present within the host matrix of other metals.[64] Friend, Frenkel and their co-workers showed with the help of *in situ* characterization techniques how Pd single atom incorporated in Au matrix showed dynamic changes in structures upon treatment with oxygen, hydrogen and carbon monoxide at various temperatures.[65] Using $Pd_{0.04}Au_{0.96}$ nanoparticles supported on silica, the authors found that CO and O_2 induces sufficient thermodynamic driving force for segregation of Pd to the surface, whereas H_2 does not provide such driving force. At higher temperatures, a rapid rearrangement of the alloy was observed.

A summary of major structural changes of a solid catalyst under reaction conditions is presented in Figure 4. In many cases, these structural changes are found to be reversible. For example, Corma and co-workers concluded on the reversible transformations between Pt nanoparticles and Pt atoms inside Si-rich chabazite under oxidizing and reducing conditions.[66] Formation and breakup of Ir clusters in highly dealuminated zeolite Y was observed by Gates and co-workers.[67] To understand the dynamics of solid catalysts, *in situ*/*operando* studies can be valuable tool to track the structure and correlate it

https://doi.org/10.1021/acs.chemrev.2c00495
Chem. Rev. 2023, 123, 379−444

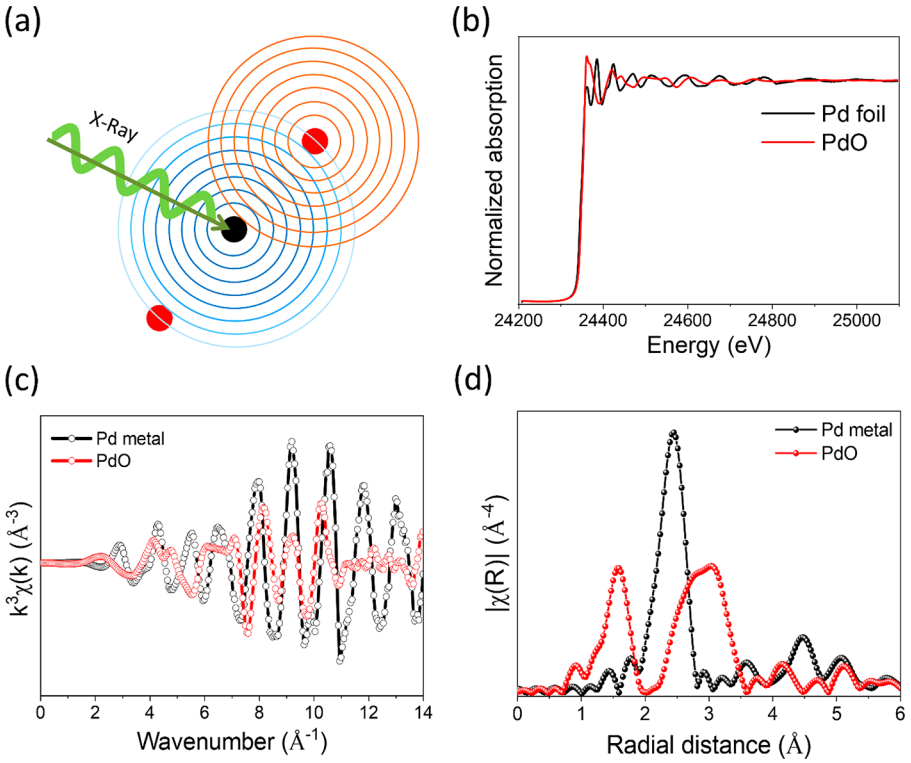

Figure 6. Overall information derived from XAS taking Pd metal and PdO as an example. (a) Schematic diagram of the X-ray absorption process, (b) normalized spectrum in energy space, (c) EXAFS spectrum in k-space (k^3-weighted) derived from normalized absorption, and (d) Fourier transformed (FT) EXAFS spectrum (R-space). The concentric circles in (a) represents wave behavior of the electron.

to the catalytic activity.[45,68−70] The term *operando*, which stands for studies truly under operating conditions, is frequently used in this field as featured by Weckhuysen,[71] Banares,[38,72] Topsøe,[73] Brückner,[74] and Wachs.[75] Preferentially, reaction rates and selectivities are measured at the same time and compared to studies in the lab reactors.

1.3. X-ray Absorption Spectroscopy (XAS) for Characterizing SACs

Knowing the structural details of active sites in heterogeneous catalysts is one of the major challenges since most of the available techniques can only give a certain piece of information. In homogeneous catalysis, the structure of the metal complex can be studied by nuclear magnetic resonance (NMR), single crystal X-ray diffraction (XRD), infrared (IR) spectroscopy, etc. In contrast, in heterogeneous catalysts, these techniques can only be applied to a certain extent due to the complexity and heterogeneity of the materials. With the rapid developments in surface and bulk analytical methods, many characterization tools are now frequently used to derive structural information at the atomic level. A schematic diagram showing some of these techniques for characterization of atomically dispersed solids and the respective information that can be obtained are shown in Figure 5. Readily accessible techniques like X-ray diffraction (XRD) and small-angle X-ray scattering (SAXS) are useful but have their limitations in deriving structural information of only up to small clusters/nanoparticles (<3 nm). Infrared (IR) spectroscopy, which is frequently used in characterizing solids, has limited use in terms of deriving geometric structures. However, with probe molecule such as CO and NO one can distinguish between single atoms and cluster very nicely if one can prevent structural changes during exposure and this technique is frequently used.[76,77] Electron paramagnetic resonance (EPR) or nuclear magnetic resonance are metal- (and even oxidation state) specific and fail to cover the broader range in the periodic table. Electron microscopy is a local technique and gives detailed insight but the information we obtain must be extrapolated over the entire range of material which is not possible without complementary other information. X-ray photoelectron spectroscopy (XPS) is practical but only limited to the surface species and concentration.

On the other hand, X-ray absorption spectroscopy (XAS) is very handy in deriving average structural information in short-range (up to 5 Å), and it is sensitive to both surface and bulk, covering a broad cross-section of the material. It is also an element specific method that rules out overlapping contributions from other elements. In fact, if all the atoms are present on the surface, XAS is a more sensitive technique that can be applicable to low concentrations of catalysts across the periodic table to derive the local structural environment, irrespective of metal loading. Moreover, XAS can also be applied to follow changes in both spatially and time-resolved manner during operation and can probe material in amorphous, crystalline and in homogeneous liquid phase. Hence, XAS is in heterogeneous catalysis and in particular in single atom catalysts more advantageous than other techniques when it comes to deriving the actual structure of an unknown material.

1.4. Hard X-ray Probes as Emerging Technique: Advanced Photon in/out Techniques and New Analysis Tools

1.4.1. Basics of X-ray Absorption Spectroscopy. In a typical X-ray absorption experiment, the sample is exposed to X-rays with the energy scanned over the absorption edge of the corresponding target element, which causes the core electron to be excited to a higher energy level or to the continuum.[78−80] The ejected electron has both particle as well as wave character and

https://doi.org/10.1021/acs.chemrev.2c00495
Chem. Rev. 2023, 123, 379−444

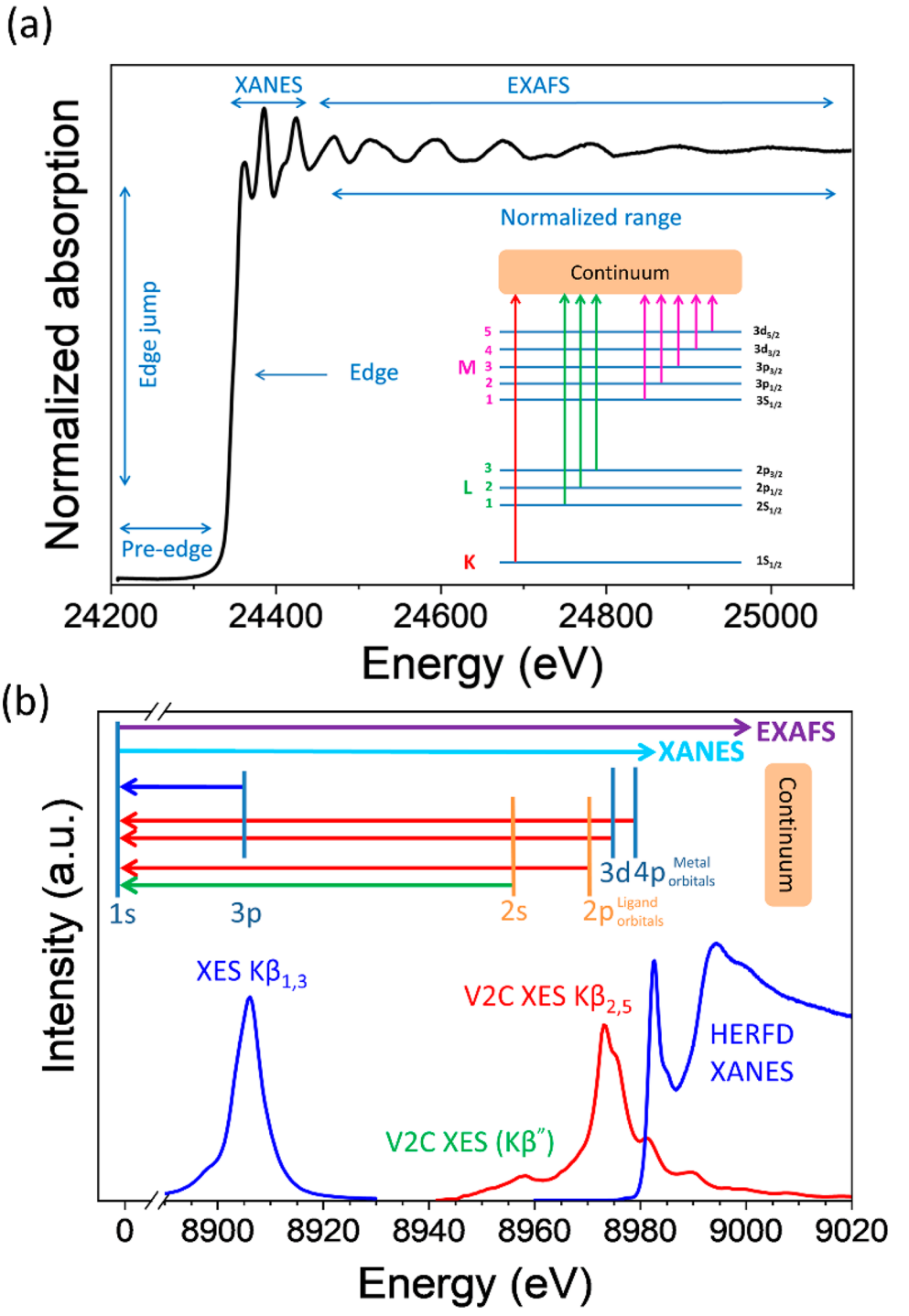

Figure 7. Schematic representation of (a) XAS spectra of Pd foil at Pd K-edge with various features and electronic transitions giving rise to different absorption edges, (b) XES spectra at Cu K-edge with different electronic transitions and the corresponding features obtained from it (represented with the same color).

the outgoing wave can be partially backscattered from its neighboring atoms. This results in a change in the wave function of the final state as the superposition of the forward and backscattered waves leads to positive and destructive interference depending on the energy. This leads to a modulation of the absorption probability. This modulated X-ray absorption above the absorption edge is called the extended X-ray absorption fine structure (EXAFS). From the shape of the X-ray absorption near-edge structure (XANES) and the EXAFS regime, we can derive information such as oxidation state of the target element, type, number, and distance of the neighbors.[81,82] The overall process and the various spectra derived from it are schematically represented in Figure 6. In a transmission experiment the absorption, μ in Figure 6b, is governed by Beer–Lambert's law as shown in eq 1:

$$\mu d = \log \frac{I_0}{I_t} \tag{1}$$

https://doi.org/10.1021/acs.chemrev.2c00495
Chem. Rev. 2023, 123, 379–444

where μ is the linear absorption coefficient measured as a function of energy, d is the sample thickness, I_0 is the intensity of the incident photons, and I_t is intensity of the transmitted photons.

Figure 6 represents an overall X-ray absorption phenomenon on Pd metal and the corresponding sets of data derived as part of the data extraction process. What kind of information do we essentially get out of these data? When an electron from 1s orbital of Pd K-shell is excited, it requires approximately 24350 eV, and the corresponding edge is called the K-edge. We can study different edges for a particular atom depending on the potential overlapping of different elements in the sample, the required energy resolution, the electronic transitions of interest, the capabilities of the beamline/instrument, the type of *in situ* cell and the X-ray window material, etc.

On the other hand, we can also study the X-ray emission lines caused by electrons from different orbitals of metal and ligands filling the core hole on the probed metal. A schematic diagram of a normalized XAS spectrum of Pd foil with all the crucial features and different edges that arise from corresponding electronic transitions is shown in Figure 7a. An X-ray emission spectrum (XES) measured near the Cu K-edge with the corresponding electronic transitions is shown in Figure 7b.[83] There are various electronic transitions possible from metal or ligand orbitals. For example, the blue curve featuring XES K$\beta_{1,3}$ arises from electronic transitions from metal 3p to 1s orbital. By scanning the energy of incident X-rays and selectively probing one emission line (e.g., K$\beta_{1,3}$) high energy resolution fluorescence detected (HERFD) X-ray near edge spectra (XANES) can be obtained. Similarly, the valence to core (vtc) XES Kβ" line arises from the 2s (lone pair on the ligand) to 1s (core hole of the probed metal) electronic transition. Another vtc XES K$\beta_{2,5}$ line is due to the X-ray emission from electronic transitions from molecular orbitals of the transition metal complex (mixed orbitals built from metal 3d and 4p and ligand 2p) to the core hole. For more detail we refer to the review by Glatzel and Bergmann on XES of 3d transition metal complexes (HERFD and RIXS) where they discuss in detail the corresponding electronic and structural information that can be obtained from the spectra.[84]

The important features from Figure 7 are explained in the following:

(a) Edge and pre-edge. The sharp rise in Figure 7a is commonly known as an X-ray absorption edge. As already mentioned, it arises due to the ejection of an electron from the core (1s orbital) with specific binding energy (approximately 24350 eV for palladium). This sharp rise is also called the K-edge, related to the excitation of orbitals from n = 1 state to unoccupied orbitals and continuum. The electronic transition is governed by the Fermi's golden rule, which tells that the probability to excite an electron is dependent on the wave functions of both the ground state and the excited state.[35,85] The kinetic energy of the photoelectron at this sharp edge is referred to as E_0 or the zero point energy. Energies below the excitation are termed as a pre-edge as shown in Figure 8. The pre-edge features are generally weak but, due to the selection rules, carry important information regarding symmetry and oxidation state. For example, in Figure 8, the pre-edge peak is due to the dipole-forbidden (quadrupole-allowed) 1s to 4d electronic transition of a Ru atom absorber in noncentrosymmetric geometry. With a centro-symmetric environment (e.g., octahedral coordination sphere of the Ru ion), this transition is very weak and hence the peak is of low intensity and in some cases not visible at all.

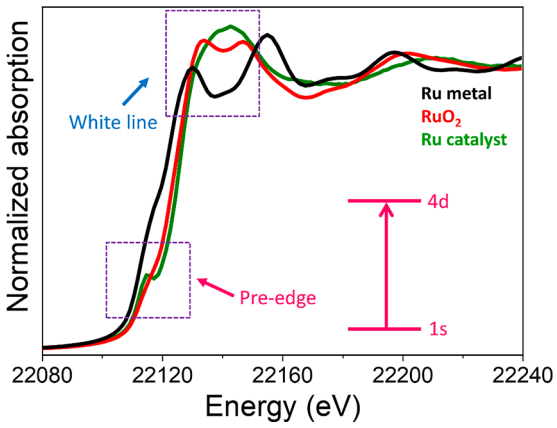

Figure 8. Comparisons of XANES spectra of Ru metal foil, RuO_2 and a Ru catalyst supported on CeO_2. The absorption features are different from each other as shown inside the dotted box; hence, it serves as a fingerprint to determine the oxidation state of a metal.

However, upon breaking the symmetry (for example, from octahedral to tetrahedral) the 4d-5p mixing results in weakly allowed electronic transition. Similarly, in the case of Cu, when the centro-symmetry is perturbed, the 1s to 3d electronic transition is possible through mixing of 4p and 3d orbitals. Hence, it shows strong pre-edge features.[86] For 3d and 4d metals, pre-edge features allow to assess the oxidation state and symmetry in both a qualitative and quantitative manner.[87]

(b) X-ray Absorption Near Edge Structure (XANES). The region of the sharp peak and the fine structure around it is known as XANES. This region can be a fingerprint of a material and give information regarding the oxidation state, neighbors, and coordination geometry (e.g., octahedral or tetrahedral) of an atom. As an example, if we compare the X-ray absorption spectra of Ru and RuO_2, we can clearly distinguish the oxidation states based on the features at the peak, which is defined by a term called "white line"[88] as shown in Figure 8. The term "white line" was introduced by Coster[89] because of saturated photographic negatives due to strong absorption in the measurements.

The XANES region is much quicker to measure than EXAFS and has many characteristic features. Therefore, it is helpful for transient *in situ*/*operando* studies. The corresponding information is usually derived through Linear Combination Fitting (LCF) and Principal Component Analysis (PCA), but also advanced machine learning algorithms have gained broader attention. A recent work by Frenkel and his co-workers developed a method based on an artificial neural network that enables the precise reconstruction of structural descriptors from the experimental XANES spectra.[90] Further examples are discussed in the chapters 4 and 5 of this review.

(c) Extended X-ray absorption fine structure (EXAFS) analysis. The oscillatory region above XANES (typically from 50 to 100 eV above the edge) is known as the EXAFS region, which gives information about coordination (atomic number (Z) of neighbors, their quantity and interatomic distance).[91−93] Close to the edge, the energy of the photoelectron is very low, resulting in long mean free path and, hence, multiple scattering events dominate at these low kinetic energies of the electron. The higher limit is defined by dampening of the EXAFS oscillations. At higher energies the EXAFS region consists of mainly single scattering events. The EXAFS spectrum can thus be often simplified as a sum of individual scattering events according to eq 2 (the EXAFS equation):

https://doi.org/10.1021/acs.chemrev.2c00495
Chem. Rev. 2023, 123, 379−444

$$\chi(k) = {S_o}^2 \sum_i N_i \frac{f_i(k)}{k{D_i}^2} e^{-2D_i/\lambda(k)} e^{-2k^2\sigma_i^2} \sin(2kD_i + \delta_i(k)) \quad (2)$$

where ${S_0}^2$ is the amplitude reduction factor, N is the degeneracy of the scattering path, $f(k)$ is the scattering function, k is the wave vector of the photoelectron, λ is the mean free path of the photoelectron, σ^2 is the mean square radial displacement, also known as Debye−Waller factor, δ is the phase shift of the couple absorber/scatterer, and i represents a particular shell of neighbors. The amplitude reduction factor or passive electron reduction factor represents many body effects during the photo absorption process including often some experimental parameters and typically values in the range of 0.7 to 1. The degeneracy of the scattering paths, N, is equivalent to the coordination number if only one shell with a single scattering event is considered. The distance, D, represents the effective half path length, which for single scattering paths is equal to the interatomic distance. The scattering probability decreases as the square of the interatomic distance, D between the absorber and the scattering neighboring atom. The Debye−Waller factor, σ^2 takes into account static (${\sigma_D}^2$) and thermal disorder(${\sigma_T}^2$) in interatomic distances and is represented by the equation

$$\sigma^2 = {\sigma_T}^2 + {\sigma_D}^2 \quad (3)$$

Frenkel et al. evaluated the disorder parameters from the temperature-dependent EXAFS data by taking into account nanoscale metal clusters.[94] Clausen and Nørskov discussed the influence of temperature in deriving structural parameters from EXAFS.[95]

1.4.2. EXAFS Fitting. Starting with an initial model structure, EXAFS fitting allows the refinement of structural parameters like coordination number (N), energy shift (E_o), bond distance (D) and Debye−Waller factor (σ^2) by employing the least-square method in either k or R space.[81,96] Due to the damping factor $e^{-2k^2\sigma_i^2}$ in the EXAFS equation, χ(k) decreases with higher k and for this reason is often multiplied by different weights such as k, k^2 or k^3. The used weighting is selected depending on the data quality (signal-to-noise ratio) and also on the nature of the nearest neighbors, since scattering functions are peaking at different k values for low- and high-Z elements. Software for EXAFS data analysis and fitting (such as IFEFFIT/Demeter or Larch[97] by Ravel and Newville[98]) rely on ab initio codes such as FEFF[99,100] to calculate theoretical scattering amplitudes and phases. The GNXAS,[101,102] code is also frequently used for this purpose.

The EXAFS fitting should have a certain acceptable range of free parameters not exceeding the number of independent data points, and also provide statistical errors which should be reported together with the fits. Even though there is no hard and fast rule, according to a number of studies carried out at room temperature,[103,104] the typical range of free parameters and their errors are shown in Table 2. These values might vary for multiple shell analyses and experiments performed at different temperatures. Too large deviations from the typical parameters should be critically assessed and may indicate that the initial structural model needs to be reconsidered.

1.4.3. Wavelet Transform (WT) Analysis of EXAFS. Wavelet transform is an alternative to FT transform and has the ability to visualize in 2D map the backscattering amplitude as a function of both wave vector k and interatomic distance R. Due to this, one can qualitatively resolve neighbors at similar interatomic distances but different Z numbers.[105,106] WT analysis is very useful for visualizing the spectra; compared to FT, one may be able to receive the first qualitative conclusions about the local environment of the absorber atom without the need to fit the EXAFS data. This may be also useful for building the initial model for the EXAFS fit. However, because the way one transforms the spectra (FT or WT) does not affect the physics behind the EXAFS phenomenon the same limitations apply to the amount of information that can be derived (e.g., one cannot distinguish between backscatterers with similar Z-numbers, e.g., O, N, C simply because their scattering functions are almost similar and not influenced by the way the data is analyzed). In order to refine the structural model EXAFS fit is still indispensable. Timoshenko et al. explained the advantage of WT over FT EXAFS on cubic perovskite-type polycrystalline ReO_3 as an example by using the Morlet wavelet.[107] The EXAFS spectra, FT transform EXAFS spectra, and wavelet transformation at Re L_3-edge of polycrystalline ReO_3 are shown in Figure 9. From the WT, one can clearly visualize the Re−O as well as the Re−Re scattering at 1.8 Å (4−6 $Å^{-1}$) and 3.7 Å (14−16 $Å^{-1}$). In a recent example, Pankin et al. showed a DFT-based study in which simulated and experimental WT EXAFS functions were compared to reveal the nuclearity of Cu species in zeolites.[108]

Hard X-rays compared to soft X-rays: XAS can be conducted using soft (low energy) or hard (high energy) X-rays. Usually, the border between the two regimes is drawn at about 2−5 keV with the range in between often called tender X-rays. While the physical principle behind the measurements is the same regardless of the X-ray energy, there are differences with respect to structural information obtained and experimental conditions applicable. Soft X-rays are often used to probe K-edges of light elements like C (283 eV), N (402 eV), or O (532 eV). For single atom catalysts, this offers the possibility to get complementary information on the surrounding ligands that basically comes from the support.[109,110] Also, L- and M-edges of many elements are accessible only with tender X-rays, such as the L_3-edges of Rh (3004 eV), Pd (3173 eV) or Ag (3351 eV). Such near-edge X-ray absorption fine structure (NEXAFS) spectra often yield more structural information as the excited electrons are stronger influenced by valence electrons than the energetically deeper lying K-shell electrons. Furthermore, due to less core-hole broadening soft and tender X-ray absorption spectra may be more feature-rich. On the other hand, the low energy of the

Table 2. EXAFS Fitting Parameters and Their Physical Interpretation with Typical Ranges and Errors (Spectra Measured at Room Temperature)[a]

free parameters	physical meaning	typical range	statistical error (maximum acceptable range)
Amplitude ${S_0}^2$	Data distortion, proper model (correlates with coordination number)	0.7−1.05	10%
Change in interatomic distance, del R	Deviation from the distance in the initial model	N/A	1% of R
Energy shift E_0	Edge energy of the ejected electron	±10 eV	0.1 ± 5%
Debye−Waller factor, σ^2	Thermal or static disorder in the bond	0.002−0.03 $Å^2$, always positive	5%

[a]The statistical errors shown in the table are mainly for 1st shell fitting. For details, please see, e.g., handbook by Calvin.[104].

https://doi.org/10.1021/acs.chemrev.2c00495
Chem. Rev. 2023, 123, 379−444

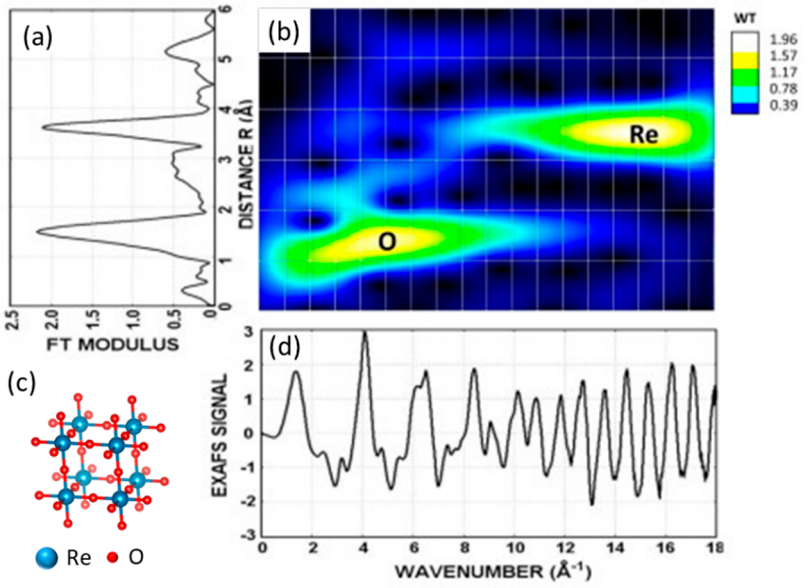

Figure 9. (a) FT EXAFS spectra at Re L_3-edge of ReO_3, (b) Morlet wavelet transformation, (c) model structure of ReO_3, and (d) EXAFS signal at Re L_3-edge. Adapted with permission from ref 107 Copyright 2008 Elsevier.

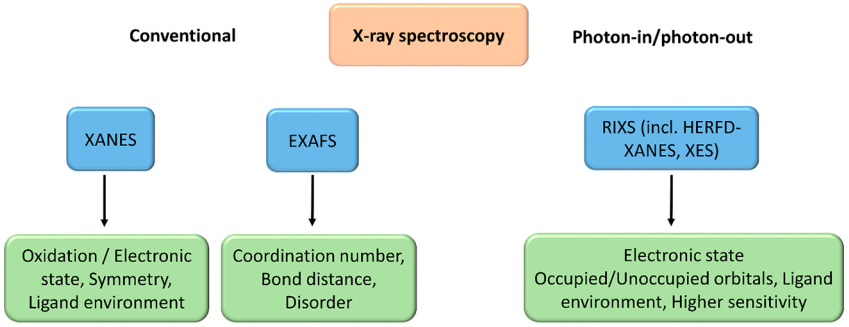

Figure 10. Information obtained from conventional X-ray spectroscopy vs photon-in/photon-out technique.

radiation leads to strong absorption of gases or light elements in the beam, which therefore demands vacuum conditions and complex sample manipulation/dilution. Furthermore, measurements are often possible only in fluorescence or electron yield modes. Complementarily, hard X-rays have the advantage of a high penetration depth allowing to measure under elevated pressures and through thicker samples and windows. Both aspects are critical to mimic real-life catalytic reaction conditions and are therefore mandatory for *operando* investigations. In several studies both hard and soft X-rays have been used.[111]

1.4.4. Application of XAS on Solids. XAS has been applied to characterize solids for a long time. Almost half a century ago, Stern, Sayers, and Lytle recognized the use of XAS for investigating nano crystalline solids[112] and only a few years later used it for catalysis. They reported that, with the help of Fourier transform analysis of X-ray absorption spectra, they could derive structural information such as coordination numbers and interatomic distances of the nearest neighbors. Lytle and co-workers in the late 80s investigated highly dispersed clusters of osmium, platinum and iridium (1 wt %) over silica or alumina support with the help of EXAFS.[113] According to their findings, small clusters dispersed on supports show lower average coordination numbers compared to bulk metal due to lower coordination on the surface of the higher metal atomic fraction on the cluster surface. Clausen, Topsøe, and co-workers investigated Co−Mo hydrodesulfurization catalysts with the help of XAS and found that Mo is present in a highly disordered manner in the calcined catalyst compared to the sulfide catalysts.[114] Iwasawa and Kuroda identified a highly active supported Mo_2 catalyst for metathesis reaction with the help of EXAFS spectroscopy.[115] EXAFS confirmed the paired nature of Mo to be the main reason for such a high activity of such catalysts. Asakura et al. studied the hydroformylation reaction on Rh dimers attached to SiO_2 and found dynamic behavior of Rh centers via *in situ* EXAFS and FTIR study.[116] Changes in Rh center bonding and coordination behavior were observed when the catalysts were exposed to reaction conditions. XAS has the potential to determine the size of clusters or nanoparticles via multiple scattering EXAFS analysis.[94,117−119]

There are various books and reviews on the applications of XAS and XES on a wide range of heterogeneous catalysts[35,120−125] and are highly recommended to expand the horizon, not only regarding the application in heterogeneous catalysis, but also on how X-rays are generated and measurements are performed at synchrotron light sources. More recently, Timoshenko and Roldan Cuenya reviewed the application of XAS for characterizing electrocatalysts under operating conditions.[126] Frenkel, Nuzzo, and their co-workers

https://doi.org/10.1021/acs.chemrev.2c00495
Chem. Rev. 2023, 123, 379−444

reviewed various characterization methods applicable to SACs.[127,128]

In SACs, XAS plays a vital role in identifying the environment of the isolated metal and provides very important information such as oxidation state and the coordination number of nearest neighbors of a particular atom of interest. As discussed earlier, Figure 5 shows the advantages of XAS over the other techniques in characterizing SACs. Conventional XAS has certain limitations such as distinguishing atoms with close atomic numbers, light scatterers, and detecting short-living chemical intermediate during catalysis due to their low concentrations. To tackle these limitations, emerging techniques such as high energy resolution fluorescence detected (HERFD) XANES and X-ray emission spectroscopy (XES) can be applied.[129−132] Pre-edge features at the K-edge arising from the 1s to 3d transition often gives valuable information, such as oxidation state and coordination geometry. However, conventional XAS spectroscopy is limited in deriving such information and therefore resonant inelastic X-ray scattering (RIXS) is more informative, where XAS and XES are combined.[84] Modulation excitation spectroscopy (MES) in combination with XAS has the advantage of elucidating catalyst dynamics under transient conditions and can be further applied for understanding the dynamic behavior of SACs.[133−137] Figure 10 shows the information that can be derived from X-ray spectroscopy and is useful in the field of single-atom catalysis.

The data reduction and fitting are the most tedious part of the whole process. A few conventional methods used for data analysis and some advanced techniques are shown in Figure 11.

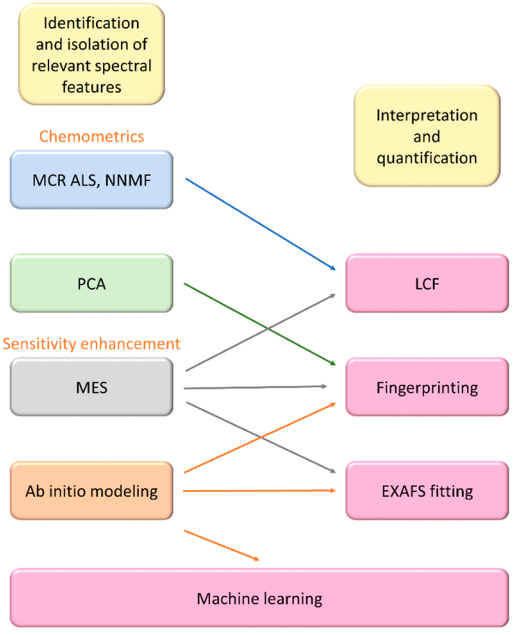

Figure 11. Different techniques involved in the data analysis of the X-ray spectroscopy is shown. Arrows show the data flow at various levels.

Advanced techniques such as machine learning, chemometrics,[138] multivariate curve resolution[139] alternating least-squares (MCR ALS), and non-negative matrix factorization (NNMF) algorithm have been very useful for rapid analysis of large data sets.[140] One should also keep in mind that the data derived from EXAFS fitting has certain errors as shown in Table 2 and discrepancies between experimental and predicted spectra from the first principle.[141]

There are different categories of SACs that have been discovered in the past few years supported on different surfaces. In the following part of the review, we will classify them based on the nature of the support and discuss the most relevant examples within the defined category.

2. SINGLE-ATOM CATALYSTS (SACS): STRATEGIES TOWARD SYNTHESIS AND THEIR REACTIVITY OVER DIFFERENT SUPPORTS

Many synthetic strategies have been developed to achieve high stability and resistance toward sintering/agglomeration of SACs over the past few years.[142−144] The rationale behind new synthetic routes also depends on the application of the SACs. Thermal trapping[145] or oxidative redispersion at high temperature (>873 K) is found to be effective for the application of SACs as three-way catalysts because catalytic converters can easily reach such high temperature. SACs over 2D support materials are ideal for electrochemical applications since these materials are conductive. Likewise, the ion-exchange method is effective for preparing SACs under confinement because it allows ions to diffuse through the pores. Mechanochemical or ball-milling[146,147] synthetic routes are emerging as greener methods. Some of the synthetic categories starting from industrially practiced routes such as impregnation,[148−152] coprecipitation,[20,153−156] to the advanced methods such as atomic layer deposition (ALD),[157−161] photochemical,[162−164] or electrochemical.[165−168] The major design strategies of SACs and the common treatment methods to achieve them are summarized in the Figure 12.

In the following, we will discuss the examples of SACs supported over various material and discuss the most promising examples within each category.

2.1. SACs Incorporated over Oxide Supports

2.1.1. SACs Dispersed on Metal Oxides Surfaces. Metal oxides, hydroxides, sulfides, and carbides are prominent classes of materials where single atoms of transition metals can be stabilized within their framework or on the surface at a defect site[169,170] which can arise from a cation, anion, or pair vacancy at different positions of the lattice as shown in Figure 13. These defect sites often provide binding possibilities for the extraneous atom, which occupies these vacancies and optimizes the energy of the system. There are many ways to create a defect site e.g., temperature-induced,[171] light-induced,[172] via chemical methods,[173,174] introducing dopants,[175] etc.

SACs are often stabilized at the defect sites on the surface of a metal oxide. In some of the first examples of SACs, Qiao et al.[20] prepared Pt single atoms over FeO_x via coprecipitation with two different loadings of 0.17 wt % Pt (sample A) and 2.5 wt % Pt (sample B). The Pt SAC was characterized by STEM, XAS, and CO-FTIR, which point toward the presence of isolated Pt atoms all over FeO_x. An XAS investigation at the Pt L_3-edge demonstrated that the Pt is positively charged, as indicated by the features of white line intensity in Figure 14b. The absence of the second shell Pt−Pt coordination as shown in Figure 14c at a distance of 2.81 Å and the presence of Pt−Fe at 2.88 Å is a direct evidence of the isolated nature of the Pt atoms in sample A. The first shell Pt−O coordination number at 1.9 Å suggests that the platinum atom is probably stabilized on the FeO_x surface through a Pt−O−Fe bond. However, one must keep in mind that EXAFS is an averaging technique and these results only refer to the as-prepared state of the catalysts and not its working state. The parameters derived from fitting are the average of all

https://doi.org/10.1021/acs.chemrev.2c00495
Chem. Rev. 2023, 123, 379−444

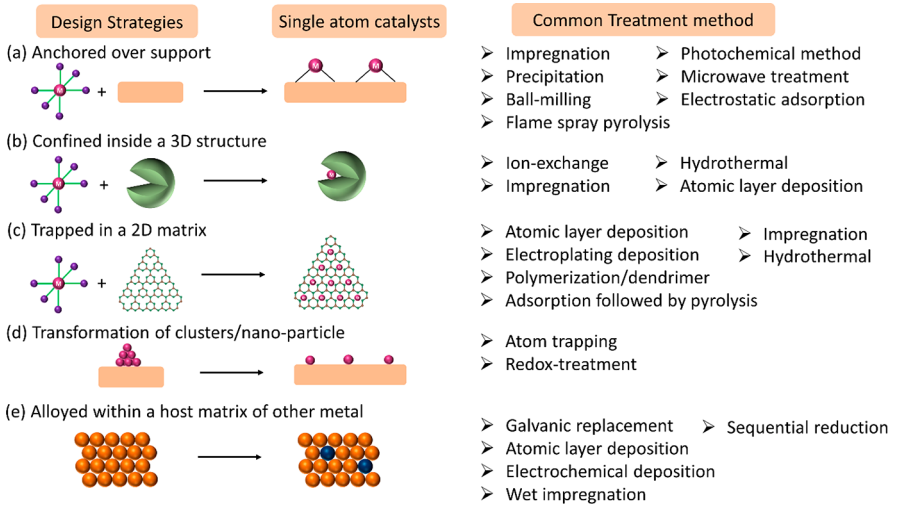

Figure 12. Various design strategies to obtain single-atom catalysts (SACs) and their common treatment method for preparation.

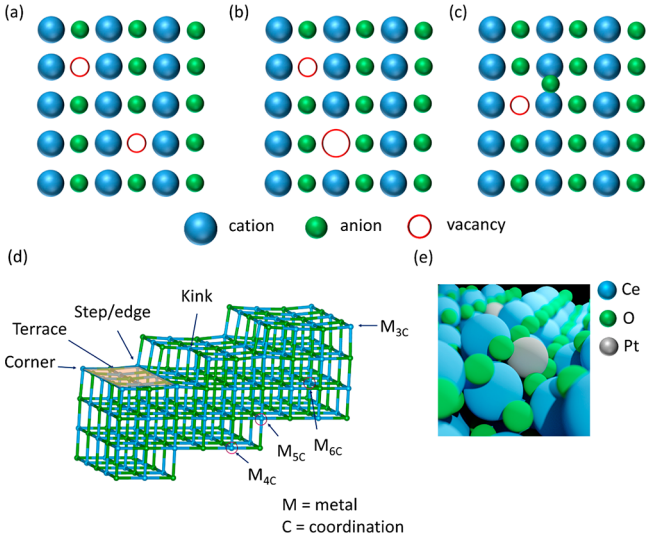

Figure 13. (a) Divacancy, (b) ion-pair vacancy (Schottky defect), (c) dislocation of ion (Frenkel defect), and (d) a typical defect surface with various defect sites with coordinatively saturated/unsaturated atoms where single atom can bind, (e) example of a 4-fold Pt single site in CeO_2.

the different types of isolated platinum atoms present in the solid catalyst. DFT calculations suggested that the Pt atoms are located on 3-fold hollow sites on the O_3-terminated (001) surface of Fe_2O_3. Boubnov et al. have shown detailed comparisons of EXAFS spectra of Fe/Al_2O_3 with the help of DFT optimized model structures to accurately predict the contributions beyond the Fe−O first shell.[176]

In sample A with a low percentage of Pt on FeO_x, the Pt−O bond distance is 2.02 Å (after phase correction) which is close to the value determined for PtO_2, suggesting a covalent metal−support interaction through Pt−Fe bond. For sample B, a much lower Pt−Pt bonding distance than the bulk platinum was assigned to the presence of small Pt clusters, as reported elsewhere.[177]

The Pt SAC was used for the oxidation of CO, which is a very important reaction in the context of emission control.[178,179] The atomically dispersed catalyst was claimed to exhibit twice the specific rate ($mol_{CO}\ h^{-1}\ g_{metal}^{-1}$) than corresponding cluster or nanoparticles. DFT calculations also predicted that SACs on FeO_x support exhibits high stability with strong binding energies.[180] Similar examples of SACs on metal oxides were reported by others for the Water Gas Shift (WGS) reaction,[181−184] CO oxidation,[145,185−191] C−H bond activation,[192−194] CO_2 reduction,[195−197] alcohol oxidation,[156] hydrogenation,[198−202] reforming reaction,[203−206] NO oxidation,[207] hydroformylation reactions,[208−211] hydrosilylation reaction,[212,213] photocatalysis,[214] etc. Liu and co-workers investigated dynamic behavior and kinetic aspects of SACs on oxide supports with the help of *ab initio* electronic structure and molecular dynamics simulations.[215] They found that Au SACs at steps of ceria are more stable and reactive than the SACs located at terrace sites. Datye and Wang reported that Pt SACs supported on ceria shows a different behavior toward CO oxidation in the presence of steam[216] compared to their former research in the absence of steam. The presence of water vapor activates the lattice oxygen of ceria which subsequently participates in CO oxidation at low temperature. A water-mediated Mars−van Krevelen (MvK) type mechanism with the improved reactivity was proposed by Wang et al.[217] Pt SACs over ceria are active for propane dehydrogenation when Sn is added to the catalysts, as shown by Datye and Weckhuysen.[218] However, the Pt−Sn nanocluster is supposed to be the active site during catalysis. Guo et al. reported a low-temperature CO_2 methanation reaction over Ru/CeO_2 catalysts where Ru clusters (1.2 nm) showed superior catalytic activity over the Ru single atoms while Ru nanoparticles (4.0 nm) exhibited the lowest activity.[219] In this study, the researchers explained that both Strong Metal Support Interaction (SMSI) and H-spillover play an important role in determining the higher activity toward the methanation reaction. Single atoms and nanoparticles encounter SMSI that leads to activation of metal carbonyls and suppression of support dehydration, whereas in clusters, these two effects balance well resulting in better catalytic performance. Lou et al. studied the CO oxidation behavior of Pt SACs over different types of reducible and irreducible oxide supports.[220] According to their study, the presence of surface hydroxyl group and water significantly modifies the catalytic path of SACs for CO oxidation. Ammal et al.[183] carried out DFT calculations combined with a microkinetic modeling study to explain the superior activity of positively charged Pt single atoms supported on TiO_2 for the low temperature WGS reaction. According to

https://doi.org/10.1021/acs.chemrev.2c00495
Chem. Rev. 2023, 123, 379−444

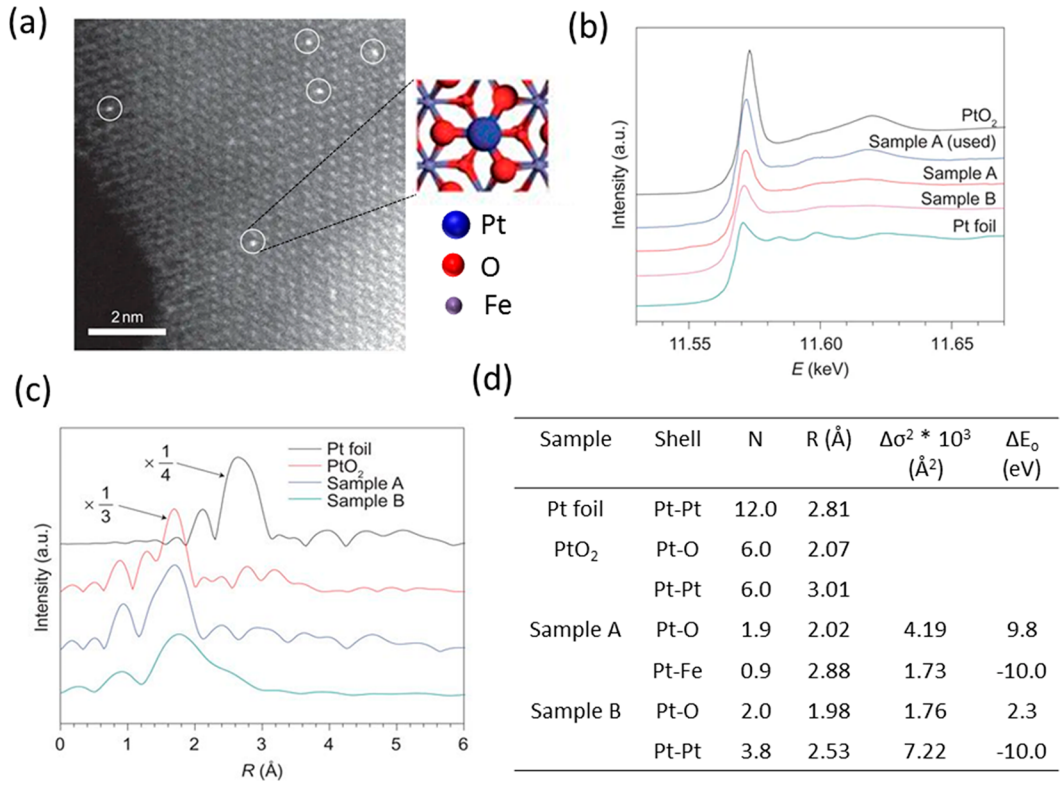

Sample	Shell	N	R (Å)	$\Delta\sigma^2 * 10^3$ (Å^2)	ΔE_0 (eV)
Pt foil	Pt-Pt	12.0	2.81		
PtO_2	Pt-O	6.0	2.07		
	Pt-Pt	6.0	3.01		
Sample A	Pt-O	1.9	2.02	4.19	9.8
	Pt-Fe	0.9	2.88	1.73	-10.0
Sample B	Pt-O	2.0	1.98	1.76	2.3
	Pt-Pt	3.8	2.53	7.22	-10.0

Figure 14. (a) HAADF-STEM image of Pt_1/FeO_x, (b) XANES spectra of the catalyst at Pt L_3-edge, (c) k^3-weighted Fourier transformed EXAFS spectra of Pt_1/FeO_x, and (d) the EXAFS parameters derived from the fit. Sample A and B correspond to 0.17 and 2.5 wt % of Pt, respectively. The k-space considered was between 2.8 and 10.0 Å^{-1} for the samples and between 2.8 and 13.8 Å^{-1} for the reference Pt foil and oxide. The spectra were represented without phase correction. Adapted with permission from ref 20. Copyright 2011 Nature Publishing Group.

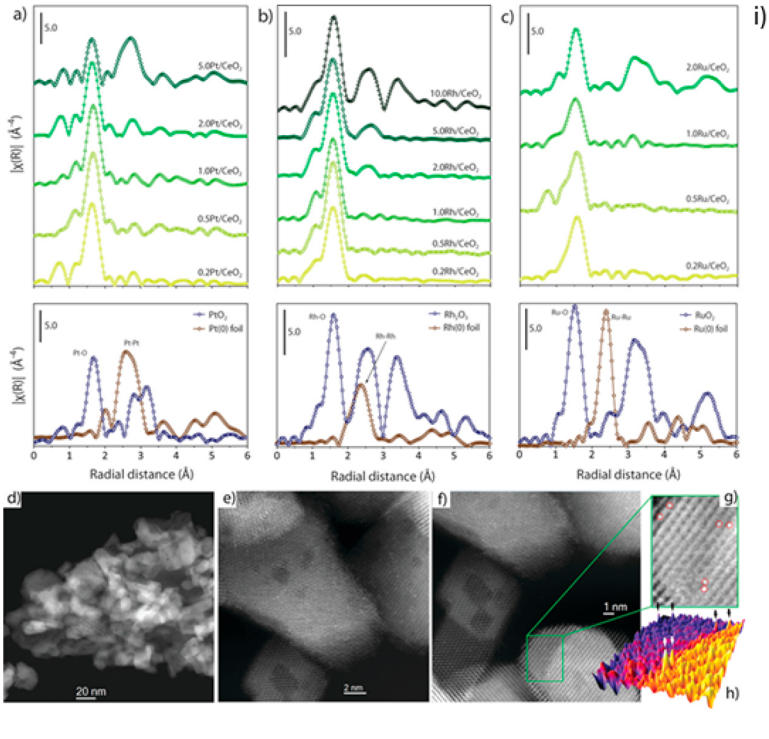

i)

M (at nm^{-2})	Coordination Number Pt-O	Rh-O	Ru-O
0.2	5.6 (0.7)	5.5 (0.7)	5.6 (0.4)
0.5	5.2 (0.6)	4.9 (0.4)	5.3 (0.4)
1	4.8 (0.4)	4.4 (0.4)	4.3 (0.3)
2	4.7 (0.4)	5.4 (0.4)	5.2 (0.4)
R (Å)	1.996 (0.005)	2.031 (0.002)	1.981 (0.005)
σ^2 (Å^2)	0.0018 (0.0006)	0.0028 (0.0004)	0.0071 (0.0001)
E_0 (eV)	10.5 (0.6)	-3.3 (0.5)	10.3 (0.6)
r-factor	0.0035	0.0145	0.0085

Figure 15. FT k^3-weighted EXAFS spectra of (a) Pt/CeO_2, (b) Rh/CeO_2, and (c) Ru/CeO_2 together with the corresponding reference oxide and foil (without phase correction), (d–g) C_s HAADF-STEM micrograph of Pt/CeO_2, (h) 3D map of the z-contrast of close-up view of (g) and (i) EXAFS free parameters obtained from fitting. The values in parentheses are errors from fitting. R, σ^2, E_0 and r represent the radial distance, Debye–Waller factor, energy shift and goodness of fit, respectively. Adapted with permission from reference 213 under creative Commons CC BY license.

https://doi.org/10.1021/acs.chemrev.2c00495
Chem. Rev. 2023, 123, 379–444

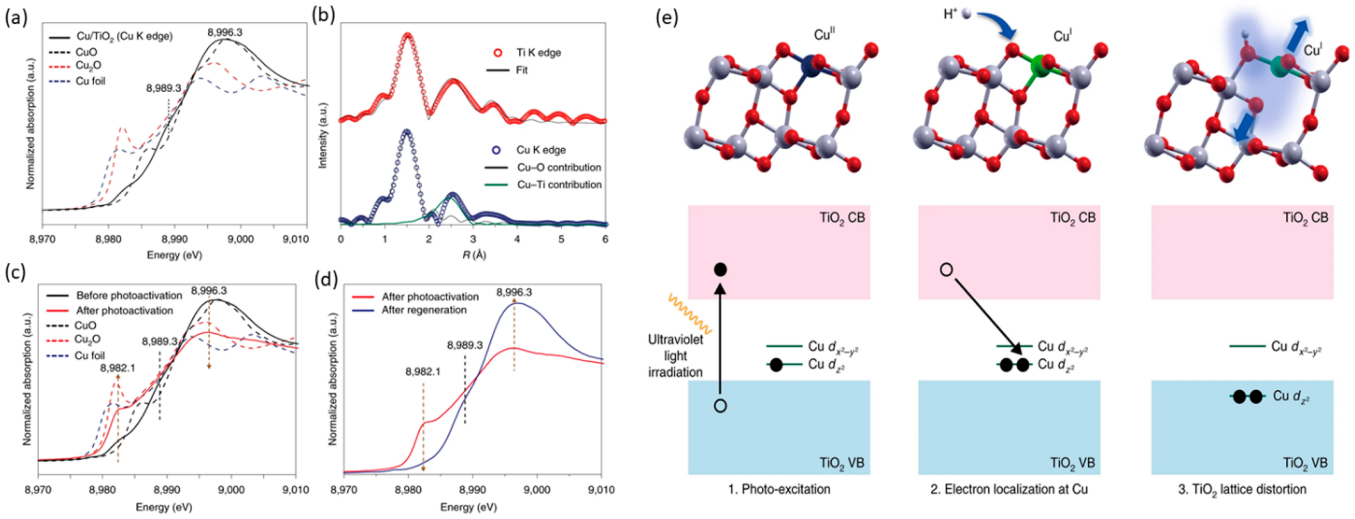

Figure 16. (a) Normalized XANES spectra at the Cu K-edge of Cu_1/TiO_2, (b) radial distribution of Ti and Cu at their K-edges of Cu_1/TiO_2, (c) comparison of normalized XANES spectra at Cu K-edge before and after photoactivation, (d) comparison of normalized XANES spectra at Cu K-edge after photoactivation and regeneration, and (e) DFT-optimized structures of Cu_1/TiO_2 during photoactivation. Adapted with permission from ref 222. Copyright 2019 Nature Publishing Group.

their study, the interface edge Pt and single Pt^{2+} sites on TiO_2 exhibit high activity below 573 K, whereas corner Pt interface sites becomes active at high temperatures. Wang et al. reported a transformation of Fe−Ru clusters supported on ceria to single atoms of Fe after being utilized for Fischer−Tropsch reaction.[221] The XAS study showed that the Fe−O−Fe scattering path disappeared in the sample after catalysis, pointing toward the presence of single atoms of Fe on CeO_2, whereas Ru is reduced under these conditions as confirmed by the formation of Ru−Ru bonds.

As catalysts are typically dynamic in their structure (Figure 4), the results reported above need to be taken with care. Preferentially in the next stage the catalysts need to be examined by *operando* techniques to unravel the local environment during the catalysis to make it clear whether they remain single sites. Iwasawa and his co-workers showed, with the help of *in situ* XAS measurements, reversible transformation of Pt nanoparticles to atomically dispersed species over MgO support at high temperature under oxidizing and reducing environments.[17] Atomically dispersed Pt over MgO was reduced with propane at 623 K to form Pt_6 clusters, which reverted to atoms upon exposure to oxygen at the same temperature. The Pt_1/MgO catalyst was found to be active for propane combustion whereas Pt_6/MgO was active for propane dehydrogenation.

In a study by Sarma et al.,[213] single-atom catalysts of Rh, Pt, and Ru stabilized on ceria via thermal trapping[145] were found to have a different coordination environment depending on the coverage, as shown in Figure 15. The coordination number derived from EXAFS fitting showed that for a metal coverage of 0.2 atom nm^{-2}, the atoms possess a high coordination number (similar to bulk metal oxide) for the first shell M-O bond as shown in Figure 15i.

The coordination number gradually decreased with an increase in coverage because there were more metal atoms available on the surface, and it reached a plateau before it started increasing again due to the formation of clusters and bulk metal oxide. This correlates with the behavior toward catalysis, where the authors performed hydrosilylation of a terminal olefin to produce linear alkylsilane. The Rh_1/CeO_2 catalyst with a higher coordination number and the lowest coverage did not show any catalytic activity. Moreover, the authors demonstrated that SACs of different metals exhibit different behavior; Rh_1/CeO_2 is highly selective for hydrosilylation, whereas Ru_1/CeO_2 is selective only for isomerization. Pt_1/CeO_2 was active for both reactions. Kim, Nam, Hyeon, and their co-workers showed an excellent example of reversible and co-operative photoactivation of Cu SACs supported on TiO_2.[222] The TiO_2 support adjacent to Cu single atom played a major role during the reversible electron transfer process. The XAS study showed that Cu is bonded to TiO_2 via a Cu−O bond with a coordination number of 6 at a distance of 1.95 Å and Cu−Ti bond with a coordination number of 4 at a distance of 2.98 Å, as shown in Figure 16b. The Cu_1/TiO_2 showed a remarkable activity for photocatalytic hydrogen generation. The XANES spectra represented in Figure 16a showed features that resembled Cu^{2+} species in the as-synthesized catalyst. During photoactivation, new features developed in the pre-edge region and the intensity of the white line dramatically decreased at 8996.3 eV meaning that Cu was in the reduced state, which quickly goes back to the original state when exposed to light. Supported by DFT calculations, they claimed a charge transfer when the electron from the valence band of TiO_2 is photo excited, that results in electron localization along the d_Z^2 of the Cu antibonding orbital and in local structural distortion of the TiO_2 lattice as shown in Figure 16e.

2.1.2. SACs Incorporated on Polyoxometalates (POMs) Framework. Polyoxometalates (POMs) are assemblies of metal oxide clusters in their anionic form that give rise to a rigid, symmetrical 3D structure.[223−225] There are various types of POMs synthesized in the last century. The atoms on the vertices can be replaced with transition metals that can act as a single site within the POM framework. For example, a Keggin type POM can be converted to a lacunary type under basic conditions and the vacant site can accommodate another metal as shown in Figure 17a. This is also applicable to other types of POMs such as the Wells Dawson as shown in Figure 17b.

Within the POM framework it is feasible to incorporate heteroatom with strong covalent interactions. For example, the Keggin type POMs can strongly hold other metals, whereas in lacunary POMs the vacant sites can be filled by any other

https://doi.org/10.1021/acs.chemrev.2c00495
Chem. Rev. 2023, 123, 379−444

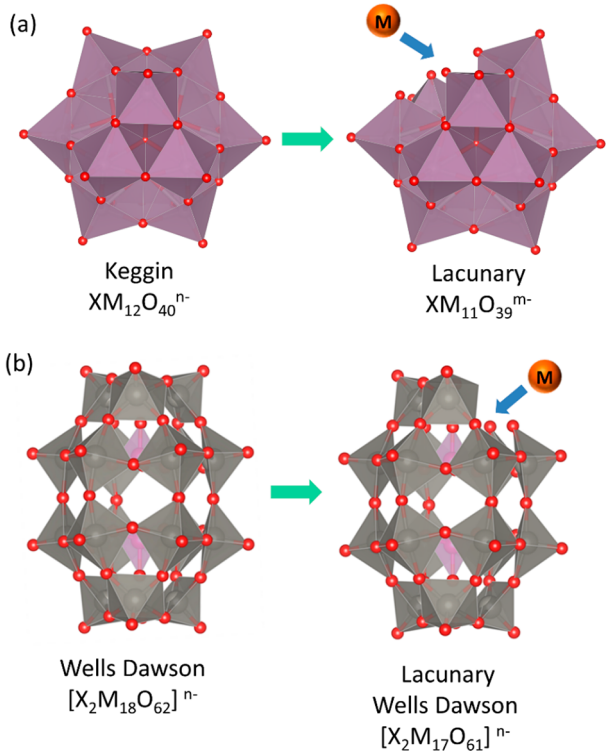

Figure 17. Polyhedral representation of (a) Keggin and lacunary type POM and (b) Wells Dawson and it is lacunary form. Also the binding site for the single atom is shown.

transition metal with appropriate size and charge.[226,227] The POM wheel or ball can accommodate certain transition metals inside the pocket that can act as a single site.[228−230] Zhang et al. showed that a Pt single atom could be stabilized in the polyoxometalate framework where Pt is coordinated to the oxygen of the phosphomolybdic acid ($H_3PMo_{12}O_{40}$).[231] The DFT optimized structure also revealed that Pt atoms indeed prefer to absorb on the PMA at the 4-fold hollow site with absorption energy of −5.72 eV. The Pt_1−PMA/AC catalyst is active for the hydrogenation of $-NO_2$, −C=O, −C=C, and −C≡C bonds.

Yan and co-workers showed atomically dispersed Rh over self-assembled phosphotungstic acid (PTA) where the Rh is located in a 4-fold hollow site with an absorbed O_2 molecule.[232] The FT EXAFS spectra did not show any Rh−Rh contribution at low coverage (0.2 wt %) as shown in Figure 18 and the Rh atoms were found to be highly oxidized (+3 oxidation state) in the PTA framework. The Rh SACs were studied for the oxidation of CO and the light-off curve of the catalysts 0.9 Rh/PTA is different from 0.2 Rh/PTA as shown in Figure 18c and d, the former being highly active compared to the latter. The shift in the light-off curve might be due to the presence of a small number of clusters in sample 0.9 Rh/PTA. The CO DRIFT study revealed, that on exposure to CO, there were $Rh(CO)_n^{x+}$ species which formed in the region of 2030−2110 cm^{-1} (fingerprint of CO vibrational frequency) as shown in Figure 18b, which lead to a partial reduction of Rh and subsequently the reaction proceeds. As shown in structure 3 of Figure 18e, CO interacts with the oxygen from the POM framework and forms CO_2, leaving a vacant O-site.

Liu and Su[233] studied computationally the metal−support interactions of a series of single atoms supported over Keggin type POM, $[PW_{12}O_{40}]^{3-}$. According to their study, the most preferred location for the single atoms are the 4-fold hollow sites on the POM and the bonding interaction occurs due to mixing of d-orbital of the isolated metal and the 2p orbital of the surface oxygen. Due to a significant contribution from the metal orbital toward bonding, a possible charge transfer from metal to POM is likely to happen based on their calculations. Lin and co-workers[234] also found with the help of DFT calculations that the

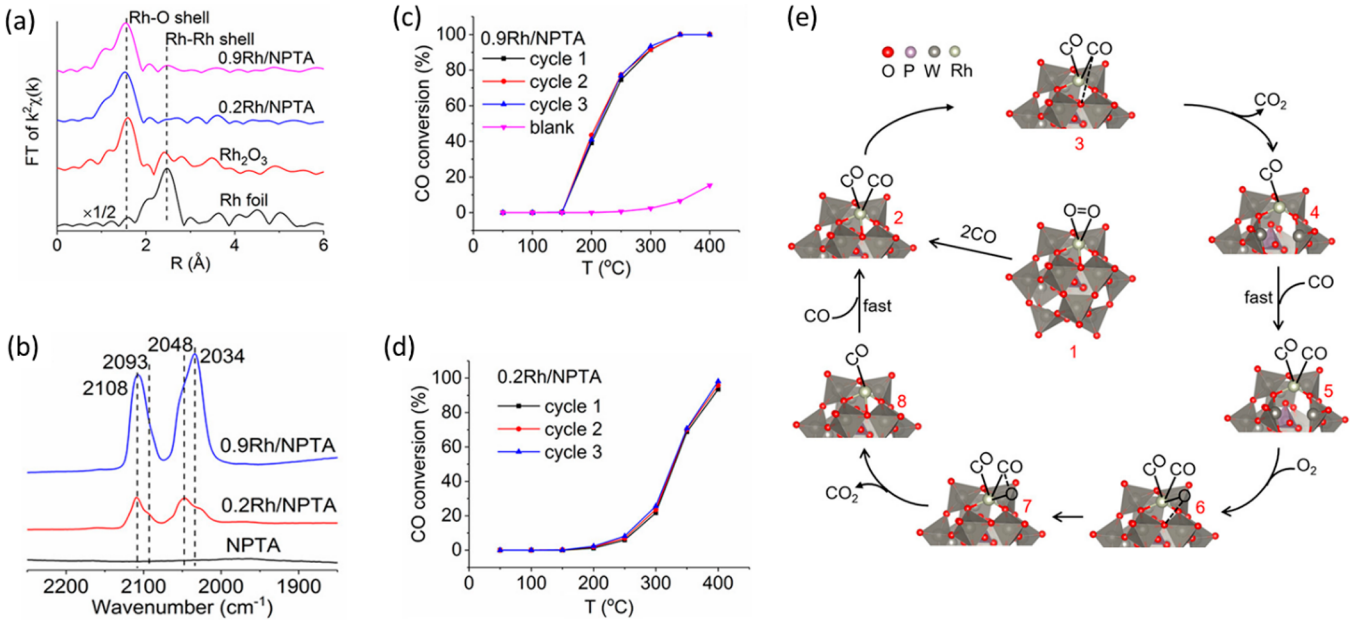

Figure 18. (a) FT k^2-weighted EXAFS spectra of Rh/PTA with the corresponding Rh foil and Rh_2O_3 reference, (b) DRIFT spectra of CO adsorption at room temperature, (c, d) light of curve (three consecutive cycles) for CO oxidation (gas mixtures: 2.5% CO, 2.5% O_2, and 95% Ar. GHSV = 24 000 h^{-1}), and (e) proposed mechanism of CO oxidation over Rh_1/PTA. Adapted with permission from ref 232. Copyright 2017 American Chemical Society.

https://doi.org/10.1021/acs.chemrev.2c00495
Chem. Rev. 2023, 123, 379−444

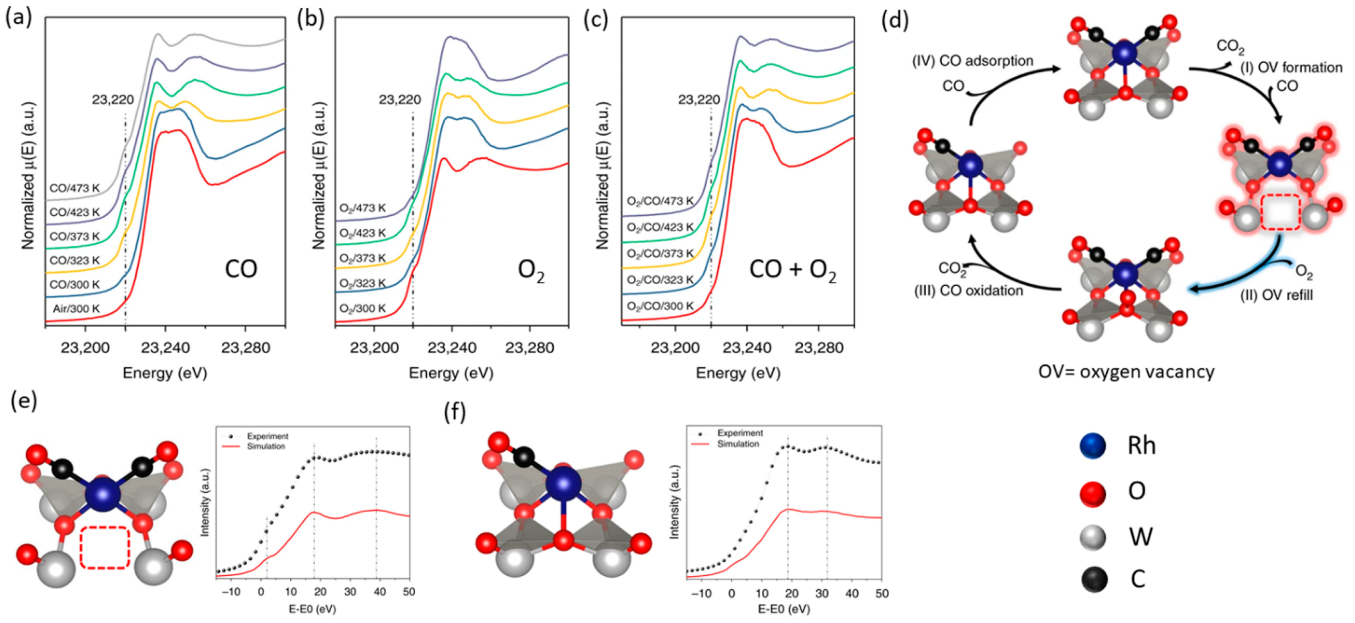

Figure 19. (a–c) Temperature resolved *in situ*/*operando* XANES spectra at the Rh K-edge under CO, O_2, and CO+O_2 gas mixture respectively, (d) proposed catalytic cycle for CO oxidation, (e, f) model structure of the reaction intermediate together with simulated XANES spectra. Adapted with permission from ref 235 under creative Commons CC BY license. Copyright 2019 The Author(s).

(a)

POM	Adsorption site	CN of Pt	E_{ad} (ev)	Pt-O (Å)	Bader charge
PMA	4-H	4	-5.72	2.00, 2.01, 2.01, 2.02	1.02
	O_{br}-O_{br}	4	-3.94	1.95, 1.95	
	O_C-O_{br}	2	-3.56	1.94, 1.95	
PTA	4-H	4	-4.96	2.02, 2.02, 2.03, 2.03	
	O_{br}-O_{br}	4	-3.12	2.00, 2.00	1.04
	O_C-O_{br}	2	-3.24	2.00, 1.97	
STA	4-H	4	-6.17	1.98, 1.98, 2.04, 2.04	
	O_{br}-O_{br}	4	-4.47	1.96, 1.96	1.28
	O_C-O_{br}	2	-4.32	1.95, 1.92	
SMA	4-H	4	-6.91	1.95, 1.96, 2.03, 2.03	
	O_{br}-O_{br}	4	-4.96	1.95, 1.95	1.27
	O_C-O_{br}	2	-4.62	1.90, 1.93	

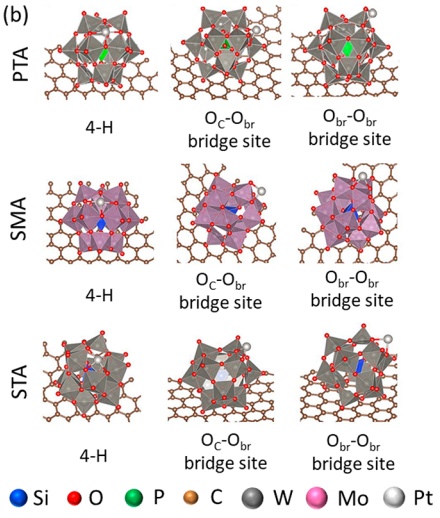

Figure 20. (a) List of important geometrical parameters and (b) the optimized DFT structures of Pt_1–POM/graphene. PMA = phosphomolybdic acid, PTA = phosphotungstic acid, STA= silicotungstic acid and SMA= silicomolybdic acid. H, O_c, and O_{br} represent hollow site, oxygen at corner, and oxygen at bridge position of the POM, respectively. Adapted with permission from ref 236. Copyright 2019 American Chemical Society.

single atoms of transition metals favor to occupying the 4-fold hollow coordination site on phosphomolybdic acid $[PMo_{12}O_{40}]^{3-}$.

However, another work by Yan and co-workers concluded that Rh SAC over phosphotungstic acid follows similar to the MvK type mechanism for the CO oxidation reaction, activation of O_2 being the rate-limiting step.[235] To reveal the structural change on the Rh center, the author collected the temperature resolved *in situ*/*operando* XANES spectra (Rh K-edge) at various temperatures under different gas environments as shown in Figure 19a–c. Under the CO environment, there are changes (intensity of white line) at the Rh K-edge around 23237 and 23255 eV at a temperature of 323 K. Also, these changes can be observed over a less prominent pre-edge peak at 23220 eV. These changes could mean distortion of the octahedral symmetry around the Rh center due to the creation of an oxygen vacancy as shown in the model Figure 19e. Simulated XANES spectra resemble the experimental in the presence of the O-vacancy and when the vacancy is refilled with the release of CO_2 as shown in Figure 19f. The authors reported that a simulation for the hexa-coordinated structure without O-vacancy and two CO molecules did not obtain a reasonable fit. Additional evidence of the creation of this vacancy is that the Rh center already oxidizes upon exposure to O_2 at a very low temperature ~323 K as shown in Figure 19b. A similar study at the W L_3-edge was carried out, which did not show significant changes in the XANES region. Together with the *in situ* DRIFTS and XPS study, the researchers claimed that the Rh single atom catalyzed CO oxidation indeed follows the unconventional MvK type mechanism. The study shows the relevance of *in situ*/

https://doi.org/10.1021/acs.chemrev.2c00495
Chem. Rev. 2023, 123, 379–444

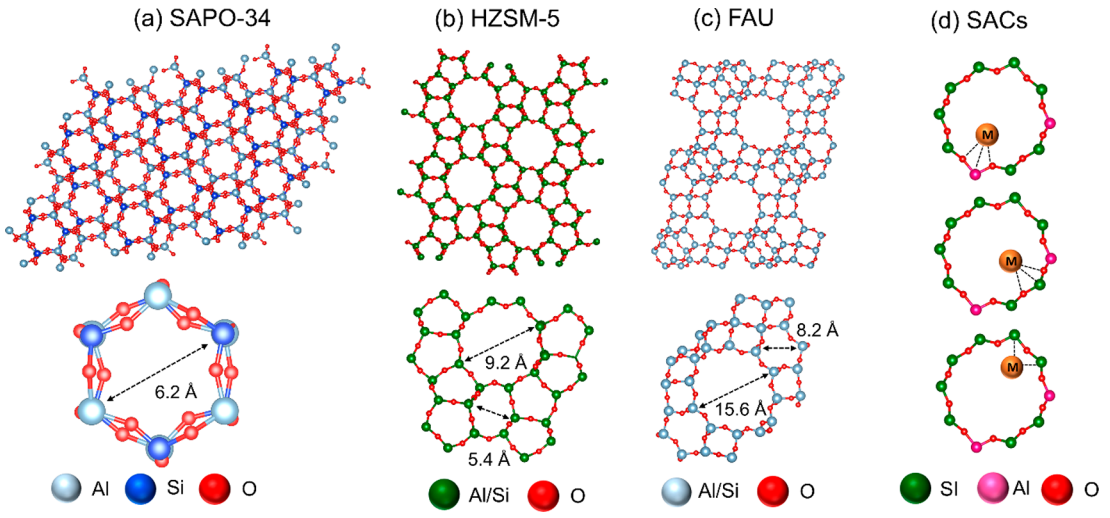

Figure 21. Representative examples of zeolite and its smaller unit with pore size (a) SAPO-34, (b) HZSM-5, (c) Faujasite (FAU), and (d) binding possibilities of a single atom inside the zeolite framework.

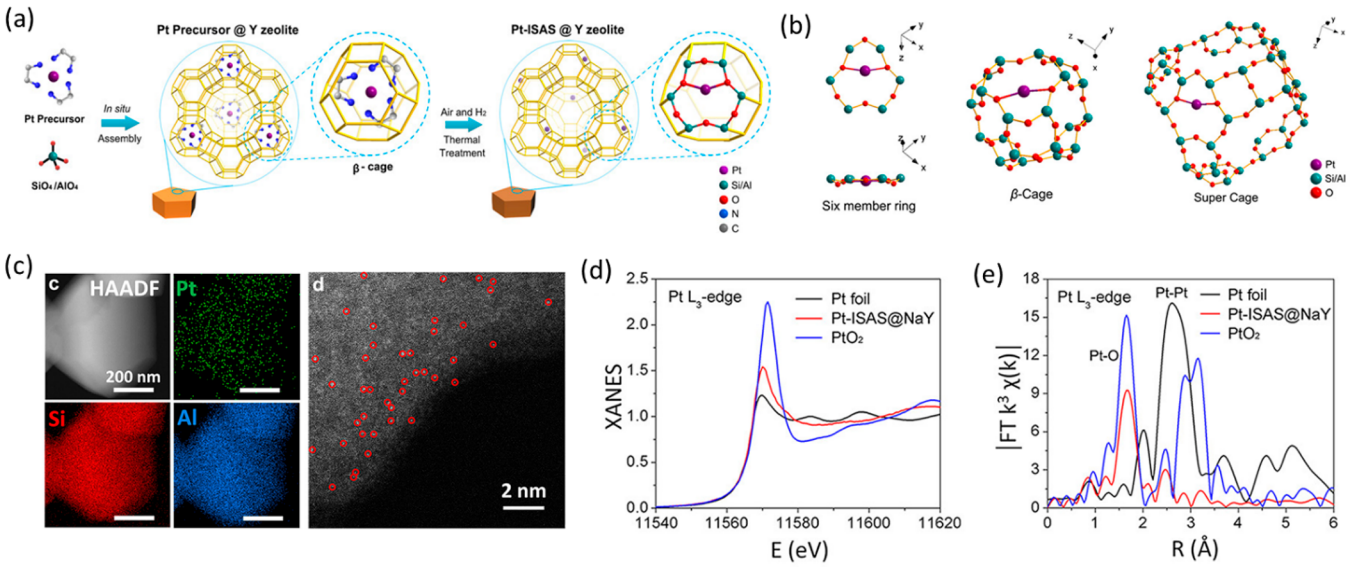

Figure 22. (a) Synthetic route of Pt single atom inside the zeolite Y, (b) calculated stable sites of the Pt atom, (c) C_s corrected HAADF-STEM image and the corresponding elemental mapping of Pt_1/zeolite Y (red circles shows the individual Pt atoms), (d) XANES spectra at the Pt L_3-edge of the Pt_1/zeolite Y (Pt-ISAS@NaY), and (e) FT k^3-weighted EXAFS spectra of Pt_1/zeolite Y (Pt-ISAS@NaY). Pt foil and PtO_2 are shown as references. ISAS stands for isolated single atomic site. Adapted with permission from ref 244. Copyright 2019 American Chemical Society.

operando spectroscopy in effectively tracking the O-vacancy formation and subsequently to understand the fundamentals of such a well-established reaction.

Sautet, Yan and their co-workers showed how the metal–support interaction affects the stability and hydrogenation activity for Pt single atom supported on different Keggin type POMs with different addenda and heteroatoms.[236] Both experimentally and with the help of DFT calculations, they showed that, despite the different Pt_1–POM interactions, the reaction pathways for the hydrogenation of propene are very similar. These results indicate the possibility of synthesizing different SACs with higher stability incorporated in POM with different addenda and heteroatoms. A list of critical geometrical parameters and their adsorption energies together with the optimized structures obtained from DFT calculations are shown in Figure 20. The parameters clearly indicate that with different adsorption sites of Pt over different POMs, the adsorption energy, bond distance and the charge on Pt varies. Moreover, the H_2 adsorption energy is weaker for Pt SACs compared to Pt clusters or nanoparticles. It is unclear whether Pt single sites remains unchanged during the reaction.

2.1.3. SACs Confined in Zeolites. Zeolites are 3D porous structures with cavities which are ideal to stabilize isolated transition metals within the zeolite framework.[237] Transition metals or their ions stabilized inside the pockets via covalent, electrostatic interactions. Some of the simplified versions of the representative examples of zeolites and binding of a single atoms inside the zeolite framework are shown in Figure 21.

Single-atoms stabilized inside zeolite framework have been observed by various researchers long before they were classified under SACs.[238−240] Due to the high surface area and the pore structure, they always have been found very attractive for catalytic applications. In the past decade, this field has been further expanded by enormous efforts to synthesize various

https://doi.org/10.1021/acs.chemrev.2c00495
Chem. Rev. 2023, 123, 379−444

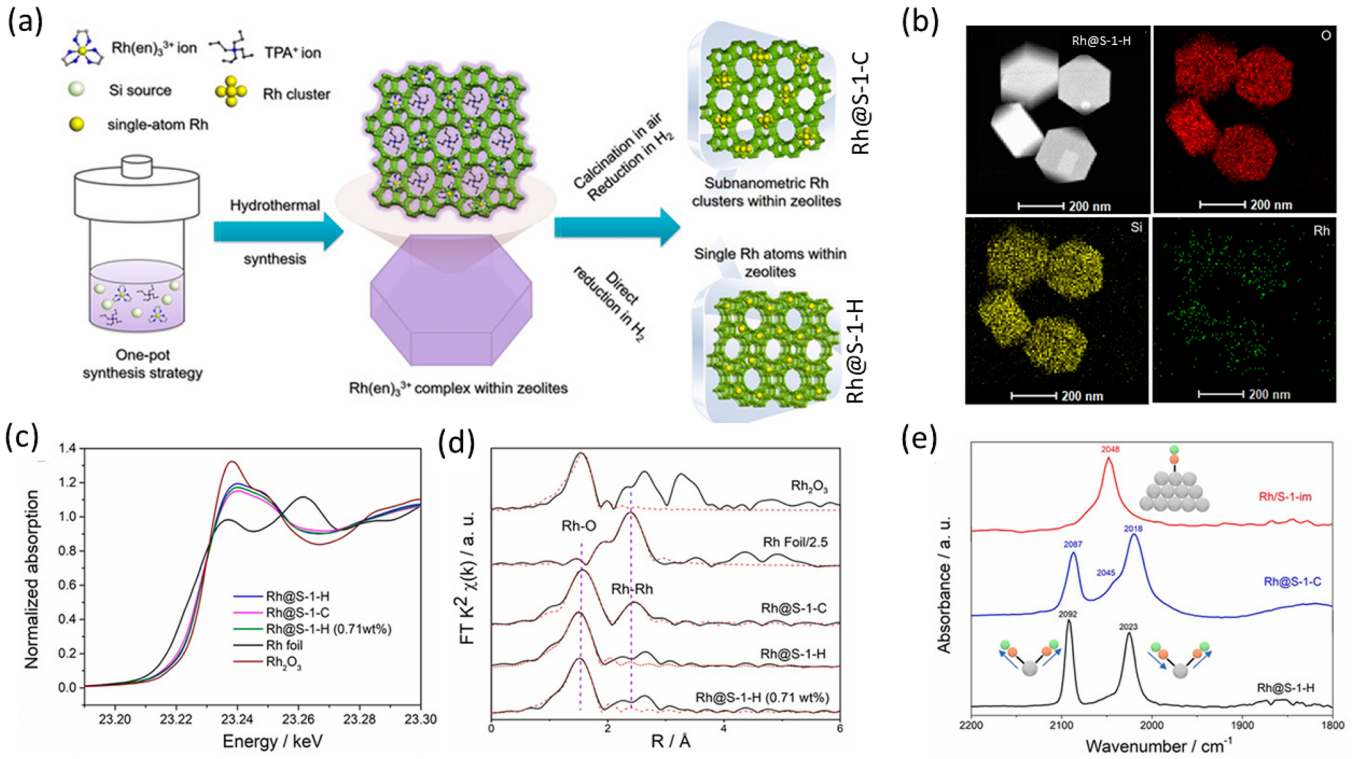

Figure 23. (a) Synthetic strategy of Rh_1@MFI zeolite followed by direct reduction (Rh@S-1-H) or calcination followed by reduction (Rh@S-1-C), (b) C_s-corrected HAADF-STEM image of Rh@S-1-H and the corresponding elemental mapping, (c) normalized XANES spectra at the Rh K-edge together with Rh foil and Rh_2O_3 as references, (d) FT k^2-weighted EXAFS spectra, and (e) *in situ* CO DRIFT spectra. Adapted with permission from ref 245. Copyright 2019 Wiley-VCH Verlag GmbH and Co. KGaA, Weinheim.

types of SACs inside the zeolite cavity. While Fe and Cu zeolites are prominent, having been utilized for selective catalytic reduction of NO_x,[132,241] methanol to olefin,[242] or methane to methanol process,[243] we focus here on the more demanding field of noble metals incorporated in zeolite. Chen, Li and their co-workers showed that single atom of various transition metals can be stabilized in the zeolite Y.[244] In their work, they have introduced metal-ethanediamine complex *in situ* into the β-cages during the crystallization process followed by thermal reduction treatment. The single atoms bound to the oxygen from the skeletal structure of the zeolite that gave the overall stability, as shown in Figure 22a and b. Upon introduction of the metal precursor to the zeolite Y, the crystallinity, porosity, and surface area remained the same and Pt atoms were found to be homogeneously distributed all over the zeolite as confirmed from the elemental mapping in Figure 22c. On further investigation of the Pt center via XAS at the Pt L_3-edge, the intensity of the white line matches with positively charged Pt. The FT EXAFS spectra indicates Pt−O scattering as shown in Figure 22e. However, there is weak scattering observed around 2.5 Å, which might be associated with the presence of a small amount of PtO_2 clusters or second shell scattering from the Si or Al atom. On CO pulse chemisorption, only a weak band at 2116 cm^{-1} was observed, which corresponds to vibrational frequency of linearly absorbed CO to the $Pt^{\delta+}$ center. The Pt_1/zeoliteY showed superior activity over the Pt nanoparticle for the dehydrogenation of ethane and isomerization of *n*-hexane, which is along the line with their DFT study. The DFT calculations also showed that there are stable locations of the Pt atom either in the six-member ring, β-cage, or in the super cages as shown in the Figure 22b and the interaction between Pt and oxygen from Al−O−Si bridges is much stronger than from Si−O−Si bridges. The recovered catalyst after the catalytic test showed cluster formation as confirmed by electron microscopy. This combination of techniques can be helpful in designing zeolite-supported SACs for other catalytic processes and to know the active state of the single site during operation.

Yu and co-workers studied the synthesis of Rh single atoms embedded in MFI type zeolite under *in situ* hydrothermal conditions.[245] For the synthesis, they have incorporated Rh-ethylenediamine complex in the synthetic route which was incorporated in the pores of the MFI zeolite. Upon direct reduction in pure H_2 at 500 °C, it results in the formation of single-atoms stabilized by the oxygen atoms within the zeolite framework and homogeneously distributed as shown in Figure 23a and b. An additional calcination step before the reduction results in the formation of clusters instead of single atoms. The catalysts were further characterized by XAS and *in situ* CO DRIFTS experiments as shown in Figure 23c−e. The normalized XANES spectra at the Rh K-edge indicate that Rh atoms are positively charged, and the FT EXAFS spectra suggest that Rh−O scattering is dominant in all the samples. However, there is a significant amount of Rh−Rh scattering observed in the sample Rh@S-1-C, indicating the presence of Rh clusters or nanoparticles. The EXAFS fitting results in a coordination number of 4.6 ± 0.1 of the sample Rh@S-1-H, which is slightly higher than the oxygen atoms in the zeolite framework. However, with the − OH group makes it possible. Additionally, the authors claimed that they did not observe any Rh−O−Rh scattering in this sample even though there was presence of an additional scattering path between 2 and 3 Å. The *in situ* CO DRIFT spectra showed two distinct peaks at 2092 and 2023 cm^{-1} that can be attributed to the symmetrical and asymmetrical stretching mode of $Rh^I(CO)_2$ species. The band around 2045

https://doi.org/10.1021/acs.chemrev.2c00495
Chem. Rev. 2023, 123, 379−444

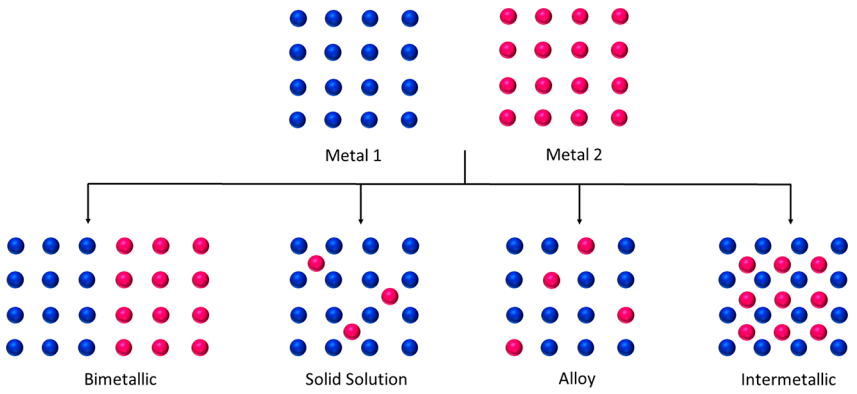

Figure 24. Structural representation of bimetallic, solid solution, alloy and intermetallic compounds formed from two different metals (metal 1 and metal 2).

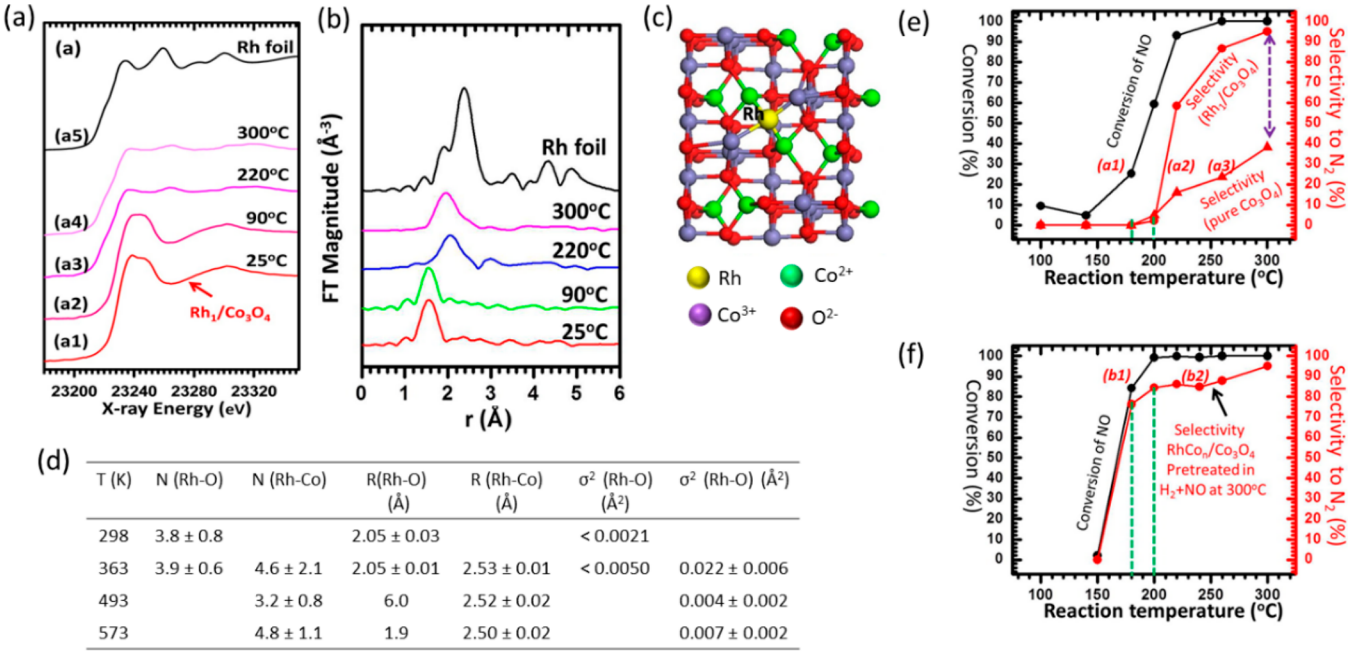

(d)

T (K)	N (Rh-O)	N (Rh-Co)	R(Rh-O) (Å)	R (Rh-Co) (Å)	σ² (Rh-O) (Å²)	σ² (Rh-O) (Å²)
298	3.8 ± 0.8		2.05 ± 0.03		< 0.0021	
363	3.9 ± 0.6	4.6 ± 2.1	2.05 ± 0.01	2.53 ± 0.01	< 0.0050	0.022 ± 0.006
493		3.2 ± 0.8	6.0	2.52 ± 0.02		0.004 ± 0.002
573		4.8 ± 1.1	1.9	2.50 ± 0.02		0.007 ± 0.002

Figure 25. (a) XANES spectra and (b) FT k^2-weighted EXAFS spectra (without phase correction) at Rh K-edge at different temperature of Rh single atom supported on Co_3O_4, (c) the model structure of Rh_1/Co_3O_4, (d) free parameters derived from EXAFS fit, (e) NO reduction profile with temperature without pretreatment, and (f) NO reduction profile with pretreatment at 573 K with 1:1 gas mixture of NO and H_2. Adapted with permission from ref 259. Copyright 2013 American Chemical Society.

cm^{-1} corresponds to CO absorbed on the Rh nanoparticles, which are mainly observed in the sample prepared by incipient impregnation Rh@S-1-im and in Rh@S-1-C, indicating the presence of small clusters of Rh in these samples. The catalysts were used for the hydrolysis of aminoborane to generate hydrogen and for the tandem hydrogen generation and reduction of nitroarenes. The catalyst with the higher number of atomically dispersed Rh (Rh@S-1-H) showed higher activity in both cases, signifying that atomic dispersion is the key toward higher activity.

This kind of study paves the way for generating single atoms inside the zeolite framework that was previously reported to generate only mixture of species or to stabilize with additional ligands.[246−249]

2.2. SACs as Composite Materials

2.2.1. SACs as Single Atom Alloy (SAA) and Intermetallic Structure (IMS). Alloys and intermetallic structures are an interesting class of materials that has been used for several applications in catalysis.[250−253] In alloys, the atoms are randomly distributed, whereas in intermetallic structures, each metal has defined crystallographic positions to their neighbor in the unit cell.[254−257] Marakatti et al.[251] addressed the distinction between intermetallic structure from bimetallic, solid solution, and alloy that can be formed from two different metals 1 and 2 as shown in Figure 24. From this figure it is evident that in solid solution, diluted alloy and intermetallic compounds, isolated metal can be incorporated in the host structures where there is interaction of the guest atom with the host. The blue sphere represents the host and the pink sphere represent the isolated metal. Hence it is clear that solid solution, diluted alloy, and intermetallic compounds can fall under the category of SACs where one of the metals is isolated in the matrix of the other metal. Even they can be interconverted as shown by Pan et al. in the case of Ag−Pt intermetallic compound made from the corresponding alloy.[258] Flytzani-Stephanopoulos and Sykes explained the importance of SAA for a rational design of heterogeneous catalysts that opens up possibilities to

https://doi.org/10.1021/acs.chemrev.2c00495
Chem. Rev. 2023, 123, 379−444

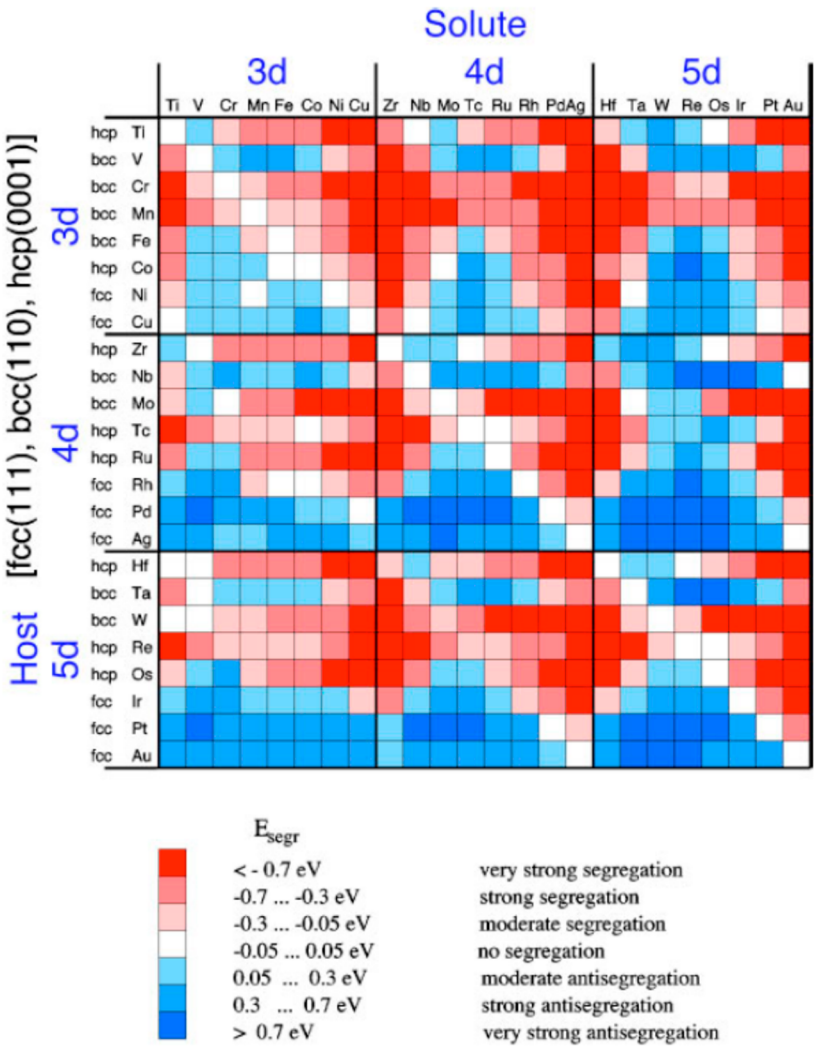

Figure 26. Calculated Surface segregation energies of metal impurities (solute) inside metal hosts for transition metals for the closed-packed surfaces. Adapted with permission from ref 269. Copyright 1999 American Physical Society.

synthesize various combinations of SAA for different catalytic activities.[5] Moreover, they raised concerns over catalysts poison that can be prevented over SAA as well as the behavior of various types of SAAs toward the activation of bonds such as H−H, C−H, N−H, O−H, and C=O.[5]

Wang et al.[259] have shown an example of rhodium intermetallic structure (IMS) as a catalytically active center for the reduction of nitric oxide, a widely studied reaction for the removal of NO_x from the atmosphere.[260−262] The XAS analysis shown in Figure 25 reveal that initially Rh atom is bonded to the Co_3O_4 surface through four oxygen atoms at a distance of 2.05 Å. However, when the catalyst is exposed to a gas mixture of NO and H_2 at a temperature of 363 K, additional bonds are formed at a distance of 2.53 Å which can be associated with the Rh−Co bond. The absence of Rh−Rh or Rh−O−Rh scattering shows that Rh centers are isolated in nature. At 573 K under the gas mixture ($NO+H_2$), the Rh−O shell completely vanishes and the first shell is dominated only by Rh−Co bonds. The XANES spectra measured at the Rh K-edge showed features associated with the Rh (III) oxidation state at room temperature as in Figure 25a. The intensity of the white line decreases significantly at 573 K, meaning that there is a structural change around the Rh atom. The EXAFS parameters derived from the fitting are shown in Figure 25d. It shows that there is already Rh−Co bond formation at 363 K along with the Rh−O bond. The resulting Rh_1Co_n/Co_3O_4 SACs are superior in catalytic behavior toward reduction of nitric oxide over Rh_1/Co_3O_4. In a similar example, Rh single atom on Co_3O_4 upon treatment with hydrogen at 573 K coordinates with Co atom forming an Rh_1/Co_n species, which was termed as isolated bimetallic sites as shown by the EXAFS study.[263] The NO reduction profile curve as shown in Figure 25e and f are clearly influenced by the pretreatment of the catalysts at 573 K with a gas mixture of NO and H_2 at a ratio of 1:1. In a different work, Feng et al. showed that palladium intermetallic structure with indium is highly selective for semihydrogenation of alkynes.[264] Other pioneering examples of singly dispersed surface bimetallic sites of Pt_1/Co_n, Pd_1/Co_m, Pd_1/Cu_n, and Pd_1/Au_n were shown by several other research groups with XAS as the main characterization technique.[265−268]

Nørskov and co-workers calculated surface segregation energies of single transition metal impurities in transition-metal hosts which can provide vital information about composition of an alloy at the surface and in the bulk.[269] A plot of the calculated surface segregation energies are represented in a 24 × 24 matrix as shown in Figure 26. The red colors corresponds to negative segregation energies which means the impurity (solute) atom favors surface alloying. On the contrary, the blue color corresponds to positive segregation

https://doi.org/10.1021/acs.chemrev.2c00495
Chem. Rev. 2023, 123, 379−444

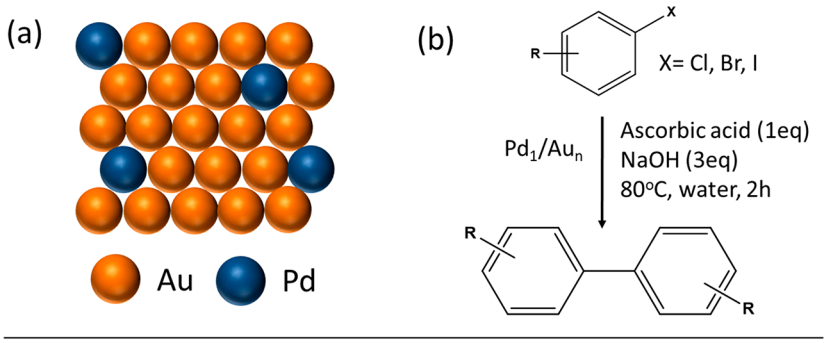

Samples	Scattering Path	Coordination number, N	Bond distance, R (Å)	Debye-Waller, σ^2 (Å^2)	Δ E (eV)
$Au_{10}Pd$	Pd-Au	9.2	2.80	0.020	-1.0
	Au-Au	8.0	2.79	0.0119	3.1
	Au-Pd	1.0	2.79	0.0144	3.1
Au_6Pd	Pd-Pd	1.0	2.82	0.0111	-7.3
	Pd-Au	7.7	2.79	0.0111	-7.3
	Au-Au	7.6	2.80	0.0101	3.0
	Au-Pd	1.2	2.79	0.0119	4.5

Figure 27. (a) Schematic representation of Pd SACs alloyed with Au, (b) Ullman coupling reaction of arylhalide over Pd_1/Au_n single atom alloy catalyst, (c) free parameters of different scattering paths derived from EXAFS at both Au L_3-edge and Pd K-edge.

energy which means that the impurity atom prefers to stay as bulk alloy. It is also worth mentioning here that the calculated segregation energies for the impurity atoms are for the close-packed surfaces which can vary for other surfaces and also in small particles. Recently Rao et al. investigated the stability of solute-host interaction with a machine learning approach.[270] In their work, they used DFT to calculate the stability of SAA relative to the subsurface, dimers, and adatoms and determined whether the solute diffused into the bulk, formed surface clusters, or avoided alloying with the host. It included 26 d-block elements to create 28 × 28 database and found that 250 combinations favored the SAA configuration and for the other 358 combinations, the SAA geometry was within 0.5 eV of the most stable configuration. Despite the fact that impurity or dopant atoms prefer to stay in the bulk, presence of adsorbate molecules and reaction temperature may enhance the stability of these atoms on the surface as recently discussed.[64]

From Figure 26, one can easily identify the best host−guest combination when designing such alloy combinations. Besenbacher et al. showed Au alloyed into the surface layer of Ni (111) increased the effectiveness of the catalyst for steam reforming of methane by increasing the barrier to C−H bond activation and decreasing the binding strength of carbon to the surface.[271] Ni alone as the catalyst leads to the formation of coke and ultimately catalyst deactivation whereas Au atoms that are alloyed into the surface layer facilitate in lowering the surface energy of Ni and hence more stability. The EXAFS spectra recorded *in situ* at the Au L_3-edge shows that only when there is a Ni neighbor at Ni interatomic distance, the experimental spectra fits well and hence confirms the surface alloying. In a different approach Marcinkowski et al. showed that by alloying Pt single atoms to Cu, C−H bond activation of methane is feasible in contrast to the Cu surface alone.[272] The catalyst is highly stable under operating conditions and resistant to coke formation.

In an example of SAA, Zhang et al.[273] reported that Pd in a Au host matrix can form single atom alloy which can promote Ullmann coupling of aryl chloride in water, a widely studied reaction in homogeneous catalysis. The EXAFS analysis showed that the isolated Pd sites are bonded to Au around it with a coordination number of 9.2 at a distance of 2.80 Å, as shown in Figure 27b. When the Au:Pd ratio is increased from 6:1 to 10:1, there is no longer any Pd−Pd backscattering path, indicating the isolated character of the Pd atoms in the alloy. Pd single atom alloy with Au supported on silica for the selective hydrogenation of acetylene showed similar EXAFS parameters.[274] This is a classic example of how homogeneous and heterogeneous catalysis bridges through SACs in order to achieve high selectivity for such an important coupling reaction, which is otherwise only possible with soluble molecular catalysts.

Sykes and his co-workers showed that such single atoms of Pd over Au (111) surface can catalyze the dissociative adsorption of H_2 at very low temperature (85 K) compared to pure Pd.[275] The facile dissociation of H_2 and weak adsorption of H atoms can assist selective hydrogenations reactions.[276,277] SAA of Pt in Cu (111) found to be highly tolerant toward CO poisoning due to weak binding of CO to single atoms of Pt compared to Pt cluster or nanoparticle supported over Cu.[278] k^3-weighted FT EXAFS data did not show any Pt−Pt scattering after $Pt_{0.008}/Cu$ SAA was exposed to gas mixtures of CO and $H_2/D_2/HD$. This result is valuable in designing catalysts for fuel cells, where CO tends to act as a poison for the traditional catalysts.

Zhang and co-workers showed that Pd SAA in Cu is highly active for the semihydrogenation of acetylene under simulated front end conditions to remove acetylene completely (i.e., higher concentration of H_2 and ethylene).[266] The weaker adsorption of ethylene over the Pd SAA compared to Pd cluster is the key for achieving the high selectivity toward semi-hydrogenation. The FT EXAFS spectra in Figure 28a confirm a

https://doi.org/10.1021/acs.chemrev.2c00495
Chem. Rev. 2023, 123, 379−444

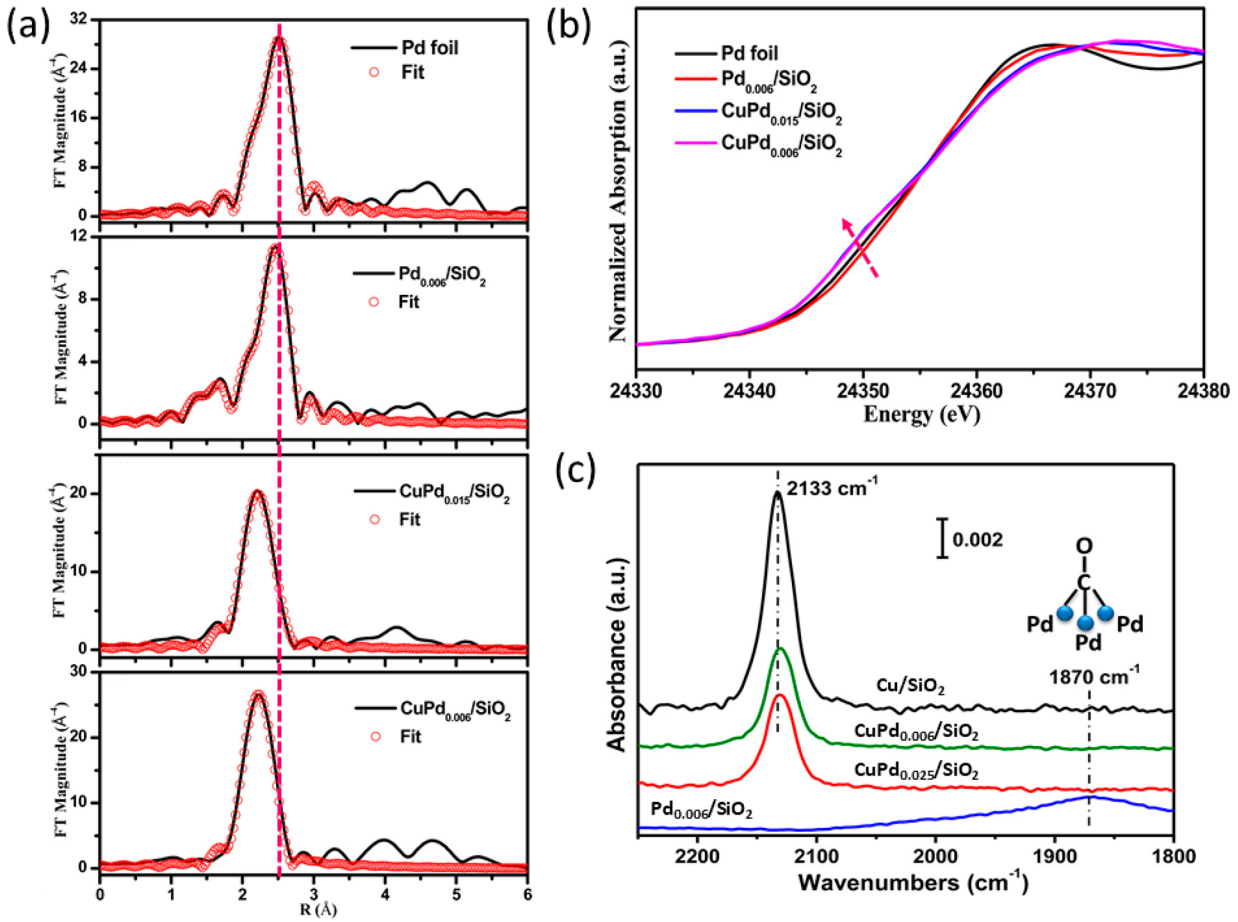

Figure 28. (a) FT k^3-weighted EXAFS spectra and (b) normalized XANES spectra at the Pd K-edge of $CuPd_{0.006}/SiO_2$, $CuPd_{0.015}/SiO_2$, $Pd_{0.006}/SiO_2$, and Pd foil are shown. (c) *In situ* FT-IR spectra of CO adsorption over Cu/SiO_2, $CuPd_{0.006}/SiO_2$, $CuPd_{0.025}/SiO_2$, and $Pd_{0.006}/SiO_2$ catalysts. Adapted with permission from ref 266. Copyright 2017 American Chemical Society.

gradual change in the first shell coordination around Pd when transforming from cluster to isolated form. The XANES spectra at the Pd K-edge in Figure 28b revealed that the adsorption edge of $CuPd_{0.015}/SiO_2$ and $CuPd_{0.006}/SiO_2$ are lower than Pd foil which is an indication that Pd bears higher electron density. The *in situ* FT-IR coupled with CO adsorption in Figure 28c shows a broad CO vibrational frequency at 1870 cm^{-1}, which is characteristic of CO adsorption on Pd small clusters and the peak at 2133 cm^{-1} is the peak of CO adsorption over Cu. However, on decreasing the Pd ratio, there is no peak observed corresponding to CO adsorption on Pd meaning that the Pd concentration on the surface is too low or fully coordinated, as revealed by the first shell Pd−Cu coordination number of around 12, obtained from the EXAFS fitting.

Pt−Fe IMS catalysts of Pt and Fe showed similar activity to SAA for the propane dehydrogenation reaction, as reported by Miller and Zhang.[254] Out of the three model compounds Pt_3Fe, PtFe, and $PtFe_3$ studied by resonant inelastic X-ray scattering (RIXS) and DFT, the authors found that the average energy of the filled 5d states of Pt decreases with an increase in Fe content i.e., $PtFe_3$ > PtFe > $FePt_3$. These results point toward the fact that by reducing the possibility of Pt agglomerations, which is primarily responsible for hydrogenolysis, the isolated form of Pt in the IMS ($PtFe_3$) promotes effective dehydrogenation of propane.

The *in situ* XAS spectra and the 2D RIXS planes are shown in Figure 29. The EXAFS spectra of $PtFe_3$ show presence of only one shell around 2.66 Å (phase corrected) which corresponds to Pt−Fe scattering path with a coordination number of 8.6. In order to determine the fraction of Pt exposed, instead of CO chemisorption, the authors used the difference of XANES spectra (ΔXANES) of the oxidized and reduced catalysts which was reported by the same group in their previous study.[279] The difference in intensity gives the information on the oxidized Pt on the surface. The RIXS plane gives the information on atomic ordering on the valence state of Pt. Along the *X*-axis in Figure 29c, the incident photon energy gives the information about the valence state of Pt and, along the *Y*-axis, the energy difference between the unfilled and filled valence state. For the catalysts Pt_3Fe, PtFe, and $PtFe_3$ the RIXS intensity shifts toward higher incident photon energy with values 11564.4, 11564.5, and 11564.6 eV, respectively with the corresponding energy loss of 3.1, 3.4, and 3.6 eV. In summary, when the Fe to Pt ratio increases, there is an upward shift of the Pt unfilled 5d states, which is accompanied by increase in energy loss because of the decrease in the energy of the filled states. All the catalysts showed similar activity toward propane dehydrogenation.

Bell and Gordon performed quantum mechanical screening of SAA for electrochemical reduction of CO_2 to hydrocarbons and found that single atoms of Cu, Ni, Pd, Pt, Co, Rh, and Ir over Au (100) and Ag (100) surface are highly active.[280] Au and Ag surface are also shown to be very stable against segregation with most of the solute metal impurities as shown in Figure 30. According to their findings, the initial reduction of CO_2 to CO

https://doi.org/10.1021/acs.chemrev.2c00495
Chem. Rev. 2023, 123, 379−444

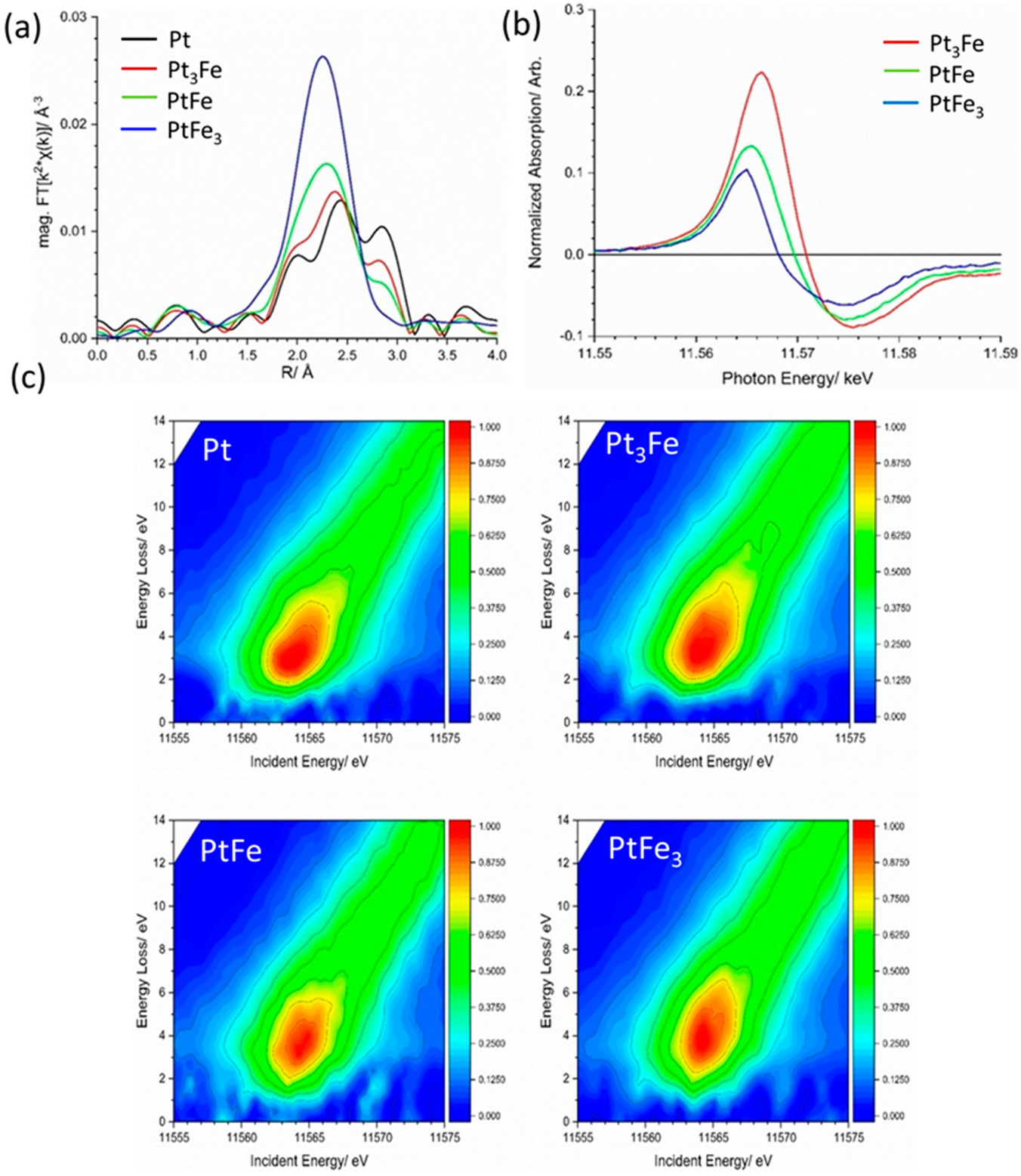

Figure 29. (a) FT k^2-weighted EXAFS spectra at Pt L_3-edge, (b) differences in XANES spectra (ΔXANES) at Pt L_3-edge, (c) RIXS spectra at Pt L_3-edge. Adapted with permission from ref 254. Copyright 2019 The Authors. Published by Wiley-VCH Verlag GmbH and Co. KGaA.

occurs on the Au and Ag matrix and then CO preferentially binds to the isolated atom and favors the formation of *CHO or *COH species over *H, which leads to CO reduction over proton reduction. The authors studied 28 combinations of SAA and found that more than 50% of them preferred CO_2 RR over HER. This kind of study can certainly help in finding the active sites in combination with XAS experiments.

Yang et al. studied the stability of Cu-based SAA for acetylene hydrogenation using DFT calculations and found that PdCu and PtCu SAA favors selective hydrogenation, whereas RhCu and NiCu are unstable and show surface restructuring through

https://doi.org/10.1021/acs.chemrev.2c00495
Chem. Rev. 2023, 123, 379−444

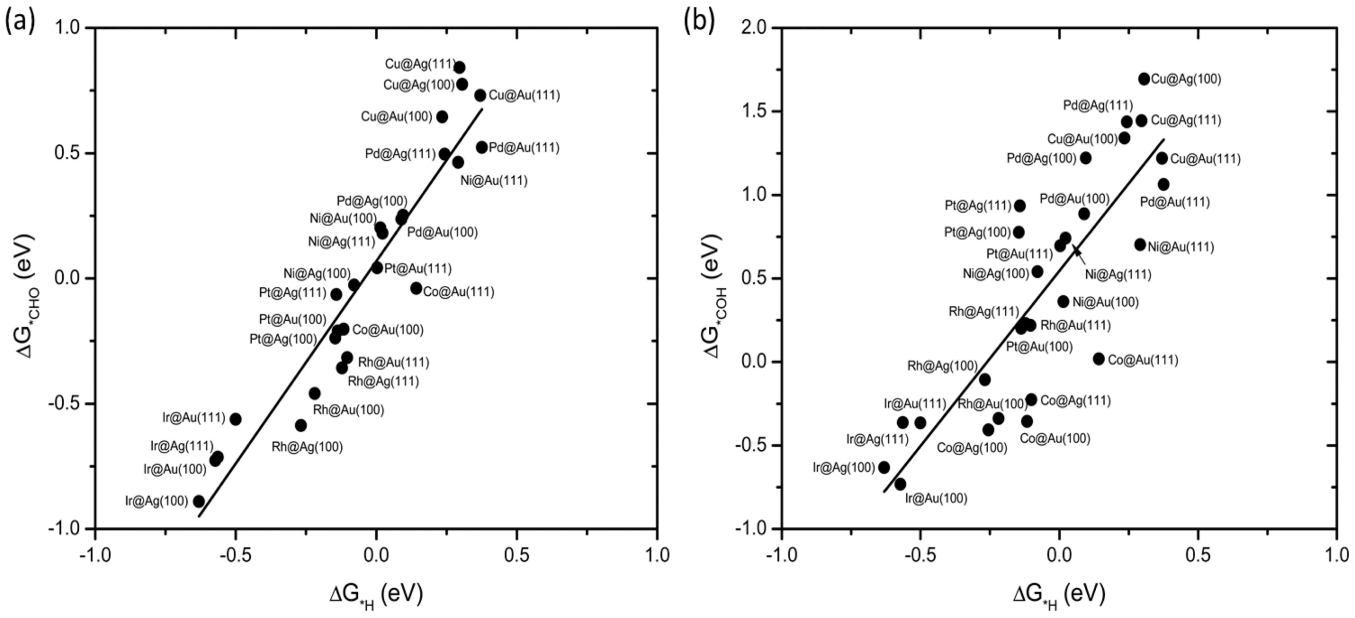

Figure 30. Gibbs free binding energy of *CHO and *COH versus *H on various single atoms in corresponding single crystal surface is represented in (a) and (b), respectively. Adapted with permission from ref 280. Copyright 2016 American Chemical Society.

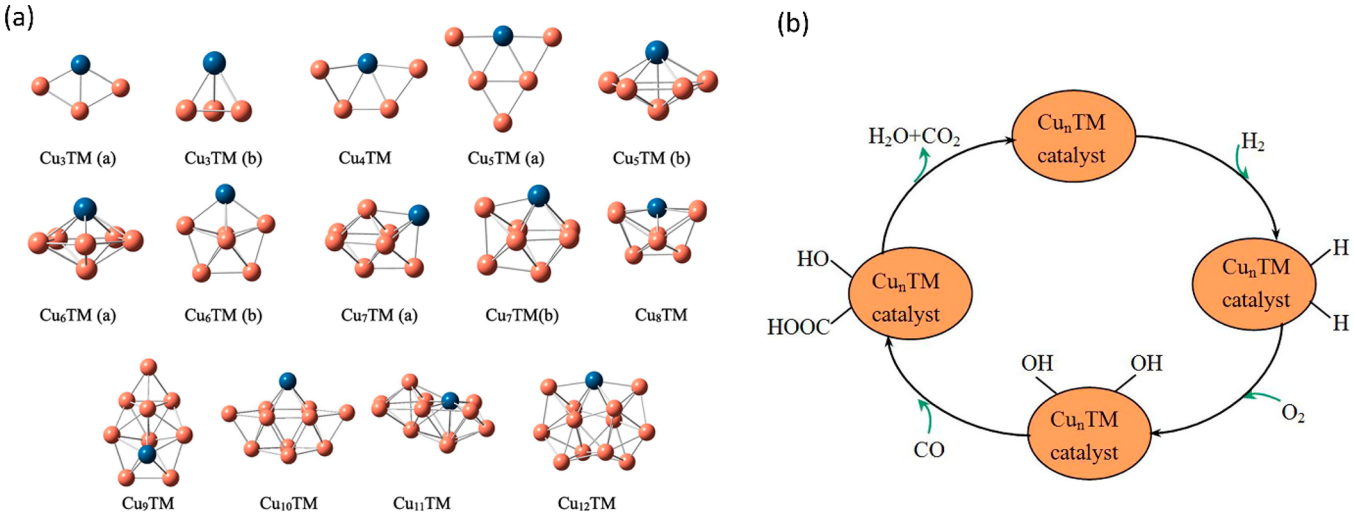

Figure 31. (a) DFT optimized geometry of SAA of different transition metals (TMs) (Ni, Pd, Pt) alloyed with Cu ($n = 3-12$) and (b) catalytic cycle of PROX with Langmuir−Hinshelwood type adsorption. Adapted with permission from ref 282. Copyright 2017 Elsevier B.V. All rights reserved.

aggregation of Rh and Ni atoms.[281] All the SAA catalysts are stable in vacuum. However, due to the adsorption of acetylene on the single site, surface restructuring happens over RhCu and NiCu. Guo et al. investigated SAA of various transition metals (TMs) alloyed with Cu and found that $PtCu_6$ exhibits significantly higher activity for H_2 dissociation and preferential oxidation (PROX) of CO over H_2.[282] The superior activity was ascribed to (a) lower activation energies and the negative adsorption energies and (b) weaker CO adsorption on the TM sites which provide good sites for O_2 adsorption activation. In their DFT calculations, the authors have studied multiple systems of SAA starting from Cu_3 to Cu_{12} (as shown in Figure 31) and showed the structural changes (bond length, symmetry) around the single atom when it absorbs H_2 or CO which is helpful tool for finding the active site.

Sun et al. showed that SAA of Pt in the Cu(111) surface supported on γ-alumina drastically enhanced the desorption of propylene relative to Pt_3Cu and many other SAA, which accelerate the dehydrogenation of propane to propylene drastically.[283] The authors synthesized Pt/Cu SAA over γ-alumina by incipient wetness impregnation and found that the catalyst was stable for 120 h in reaction stream at 793 K. DFT investigation suggested that the Pt/Cu SAA breaks the PtM alloy scaling relationship during the dehydrogenation of propane and favors the propylene formation without leading to any coking over the time. In an earlier work, Marcinkowski et al. further observed similar coke-resistant Pt/Cu SAA catalyst for efficient C−H bond activation.[272]

2.3. SACs Supported in Soft Matrices

2.3.1. SACs Incorporated on 2D Boron, Carbon Host. Soft 2D materials made of boron, carbon, and/or nitrogen are promising carriers as they are abundant and can be even derived from sources like biomass,[252] waste materials[284] and many others. This material class has very defined surfaces and often

https://doi.org/10.1021/acs.chemrev.2c00495
Chem. Rev. 2023, 123, 379−444

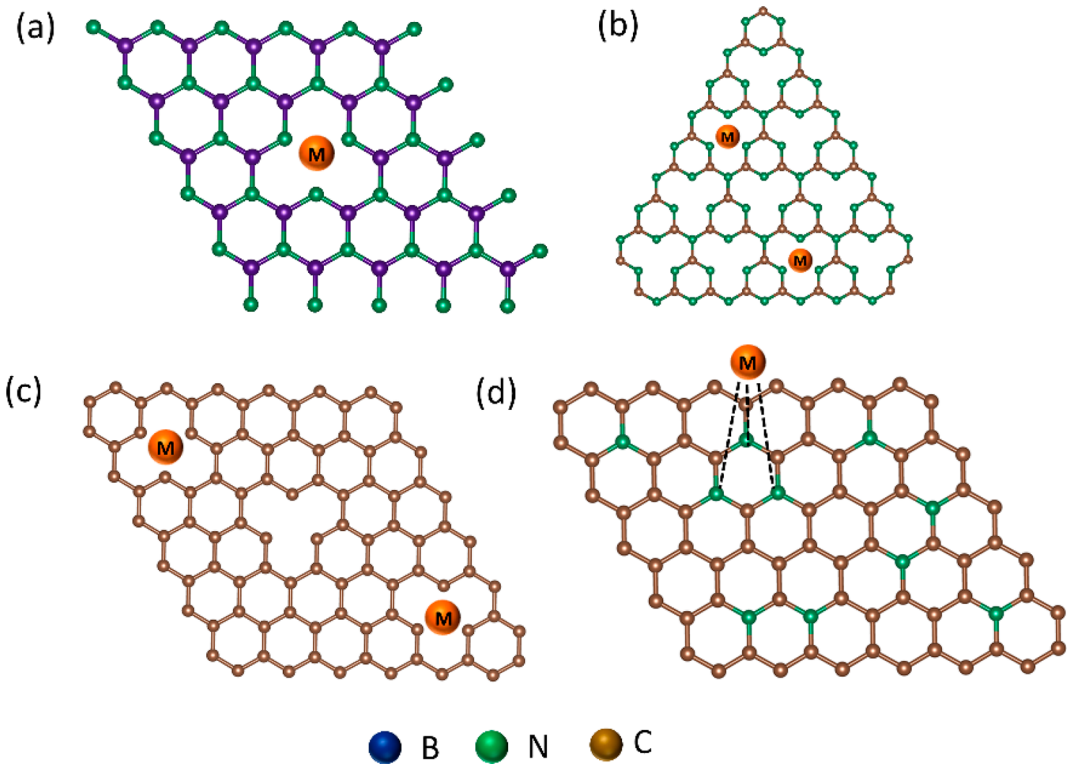

Figure 32. Examples of 2D carbon-like support (a) hexagonal boronitride (h-BN), (b) graphitic carbon nitride (g-C_3N_4), (d) defect carbon, and (e) N-doped carbon. Single atoms (M) can be incorporated in the pockets of these materials or stabilized through covalent interactions with the heteroatoms.

exhibit properties like electron conduction or light absorbing in the visible range which make them attractive for catalysis. The common synthesis strategy for these type of support materials involve pyrolysis,[285] solvothermal,[286] and arc discharge[287] which often create defect sites or vacancies where the isolated metal can be incorporated. When anchored over these materials, single atoms can bond strongly with heteroatoms like N, C, O, etc. via covalent interactions.[4,288−290] Few examples of 2D carbon like materials and their pockets where single atoms can be incorporated are shown in Figure 32 that has been reported as promising candidates for supports for SACs.[291−295]

Yang and co-workers describe in their theoretical work that Pt atoms can be stabilized in a defective graphene with a single vacancy where platinum is positively charged.[291] The Pt adatom in this case is more positively charged, which weakens the CO adsorption and facilitates the O_2 adsorption, hence enhancing the activity for CO oxidation. These findings inspired many others in designing effective single-atom catalysts over carbon-like 2D materials. However, one has to keep in mind that the interaction between Pt atoms and the supported graphene is not as strong as the Pt−Pt interaction in a cluster, which might lead to aggregation of Pt during the operating conditions. To prevent this, increasing the interaction between the adsorbed atom and support via introducing stronger coordinating atoms such as N, O, S, etc. or starting from well-defined molecules such as porphyrin, phenanthroline, even metal−organic framework (MOFs) structures can pave the way for future designing of these kinds of catalysts.

Zhang, Liu, and co-workers showed that Co single atoms over N-doped carbon prepared from Co-phenanthroline complex can promote aerobic oxidative cross-coupling of primary and secondary alcohols to produce α,β unsaturated ketones.[296] The same researchers also claimed Co single atoms dispersed as Co−N−C catalyst for excellent activity toward chemoselective hydrogenation of nitroarenes to produce azo compounds.[297] In a combined EXAFS and DFT study, the structure of Co was found to be $CoN_4C_8O_4$, where Co atom is coordinated to four N atoms in a porphyrin- like planar structure and two O_2 molecules above and below the plane.

Li and co-workers showed a different synthetic pathway for Co single atom supported on N-doped carbon material derived from metal−organic framework (MOF).[298] The synthesis is based on a pyrolysis process where a Zn/Co containing MOF was pyrolyzed at 1073 K. With the help of XAS results as shown in Figure 33, they confirmed the isolated nature of Co atoms as there is only first Co−N shell present. However, there are some features after the first shell and fitting the EXAFS between 2 and 4 Å would have been helpful in gaining further insight into the coordinating environment of Co. Upon increasing the pyrolysis temperature from 1073 to 1173 K there is a decrease in Co−N coordination from 4 to 2 as shown in Figure 33c and d. At even higher pyrolysis temperatures, Co−Co bonds formed due to sintering. The researchers speculate that Co atoms are present as a porphyrinic structure where Co is in square planar form and is highly active for ORR reaction. The MOF based synthetic strategy has also been applied to prepare single atom of Fe, Cu, W, etc. in N-doped carbon.[299−301]

Li and co-workers used graphitic carbon nitride (g-C_3N_4)[302] to stabilize Pt single atoms and characterize the local structure with XAS. FT EXAFS at the Pt L_3-edge shows one dominant peak around 2.0 Å (with phase correction), showing that the majority of Pt atoms are in an isolated environment as shown in Figure 34. If the Pt atoms are embedded in the structure of C_3N_4, then the theoretical Pt−N bond distance should be around 2.38

https://doi.org/10.1021/acs.chemrev.2c00495
Chem. Rev. 2023, 123, 379−444

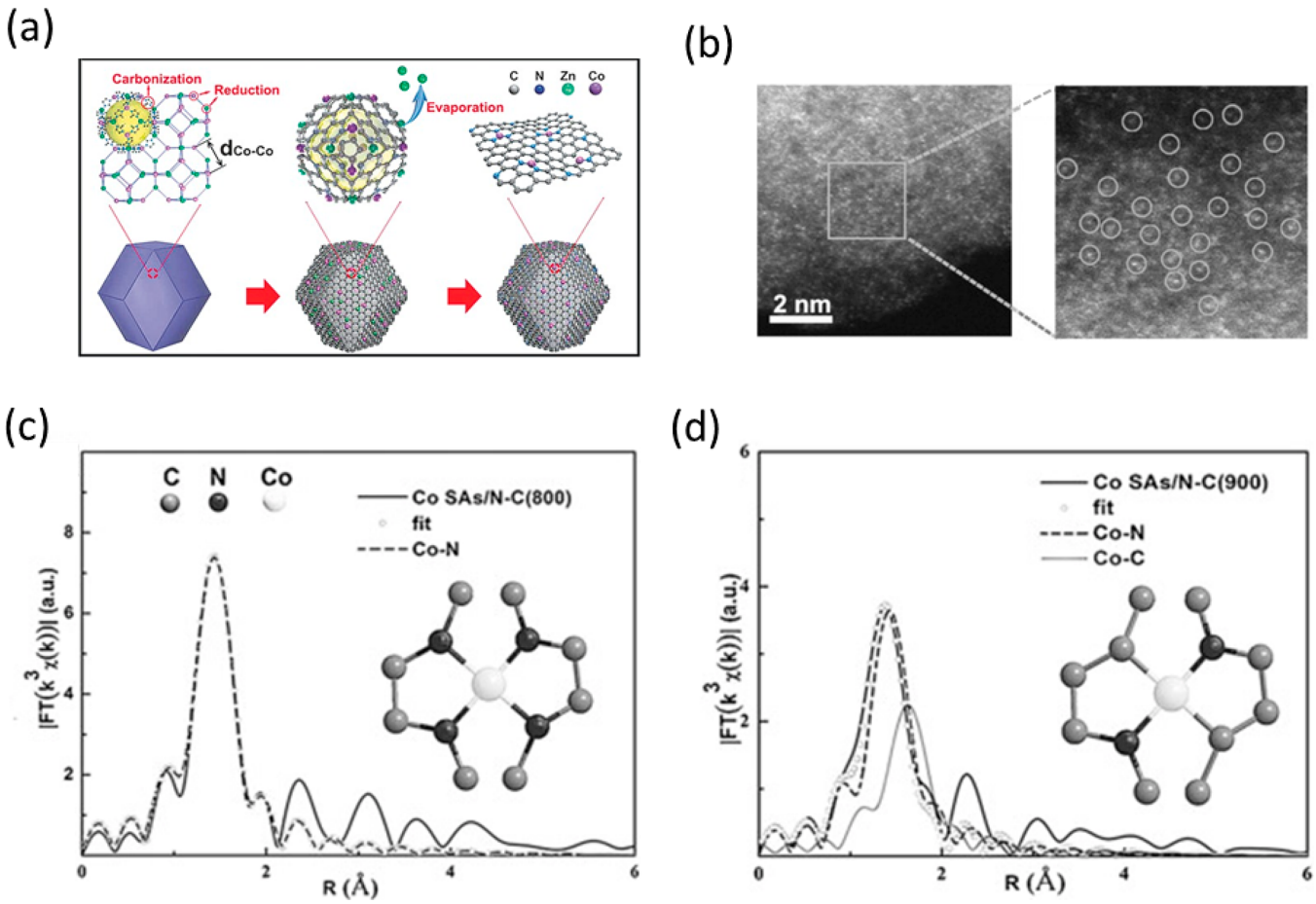

Figure 33. (a) Synthesis strategy of Co SACs over N-containing carbon, (b) HAADF-STEM image of Co SACs pyrolyzed at 1073 K, (c, d) FT k^3-weighted EXAFS spectra of Co SACs pyrolyzed at 1073 and 1173 K, respectively. Adapted with permission from ref 298. Copyright 2016 WILEY-VCH Verlag GmbH and Co. KGaA, Weinheim.

Å, which is much larger than the experimental value. Simulated spectra performed with FEFF code[303] show that the Pt atoms have a coordination number of 5 at a distance of 2.03 Å with a Debye−Waller factor of 0.0031 $Å^2$. According to the authors, the only possible way to incorporate a Pt atom in the C_3N_4 structure is stabilizing it on the top of the five-membered rings connecting to N and C of C_3N_4 structure, as shown in Figure 34d. A simple way to prove this would be to show the XANES spectra at the Pt L_3-edge and whether Pt is connected to oxygen (high white line intensity) or to either N or C (low white line intensity). The authors also studied ultrafast transient absorption spectroscopy and arrived at the conclusion that the Pt atoms make an intrinsic change of the surface trap states of g-C_3N_4, which is responsible for improved photocatalytic H_2 evolution from water. In comparison to the nano- particle, the Pt SACs exhibit eight times higher activity toward H_2 evolution.

A further approach to stabilize single atoms is incorporation in porphyrin-like structures.[304] Zitolo et al. used this strategy for Fe-porphyrin and showed the successful approach by EXAFS in unravelling the local structure of Fe which is found to be surrounded by four nitrogen atoms.[305] The EXAFS simulation was carried out with GNXAS code[101,102] and the XANES with MXAN code.[306,307] The study showed reasonably good agreement between the experimental and theoretical models where FeN_4 porphyrinic structure with different O_2 adsorption modes were fitting well. The catalytic investigations for the electrochemical reduction of dioxygen to water is greatly enhanced when the catalyst contains nitrogen. This can be associated with the basic character of nitrogen that favors the four-electron reduction pathway. The XANES spectra together with the model structures and structural parameters from the fit are shown in Figure 35. Other isolated form of Ni as Ni−N_4 and Ru as Ru−N_4 site are also found with the help of XAS.[308,309]

Chen et al. prepared molybdenum single atoms anchored on N-doped carbon via the combination of template and pyrolysis methods, using sodium molybdate as the precursor.[310] The characterization with XAS unraveled that the Mo is coordinated with one nitrogen and two carbon atoms. With the help of Fourier transformation (FT) and wavelet transformation (WT), they have shown the isolated nature of the molybdenum atoms as shown in Figure 36. The wavelet transformed contour plot in Figure 36c displays intensity maxima at 7.2 $Å^{-1}$ corresponding to Mo coordinated with N and C. The Mo−Mo contribution in Mo foil, Mo_2C, and MoN is clearly distinguishable in the WT contour plot. The Mo SACs anchored with one N atom and two C atoms showed exceptional activity toward HER compared to MoN and Mo_2C catalysts, which is along the line of the DFT calculations. A Mo−O path is also found in the EXAFS fit as shown in Figure 36f, which is due to the coordination of O_2 molecule to the Mo center.

2.3.2. SACs Incorporated in Metal−Organic Frameworks (MOFs)/Covalent Organic Frameworks (COFs). Alternative supporting materials are highly ordered porous 3D structures, especially MOFs[311,312] and COFs.[313] As they are

https://doi.org/10.1021/acs.chemrev.2c00495
Chem. Rev. 2023, 123, 379−444

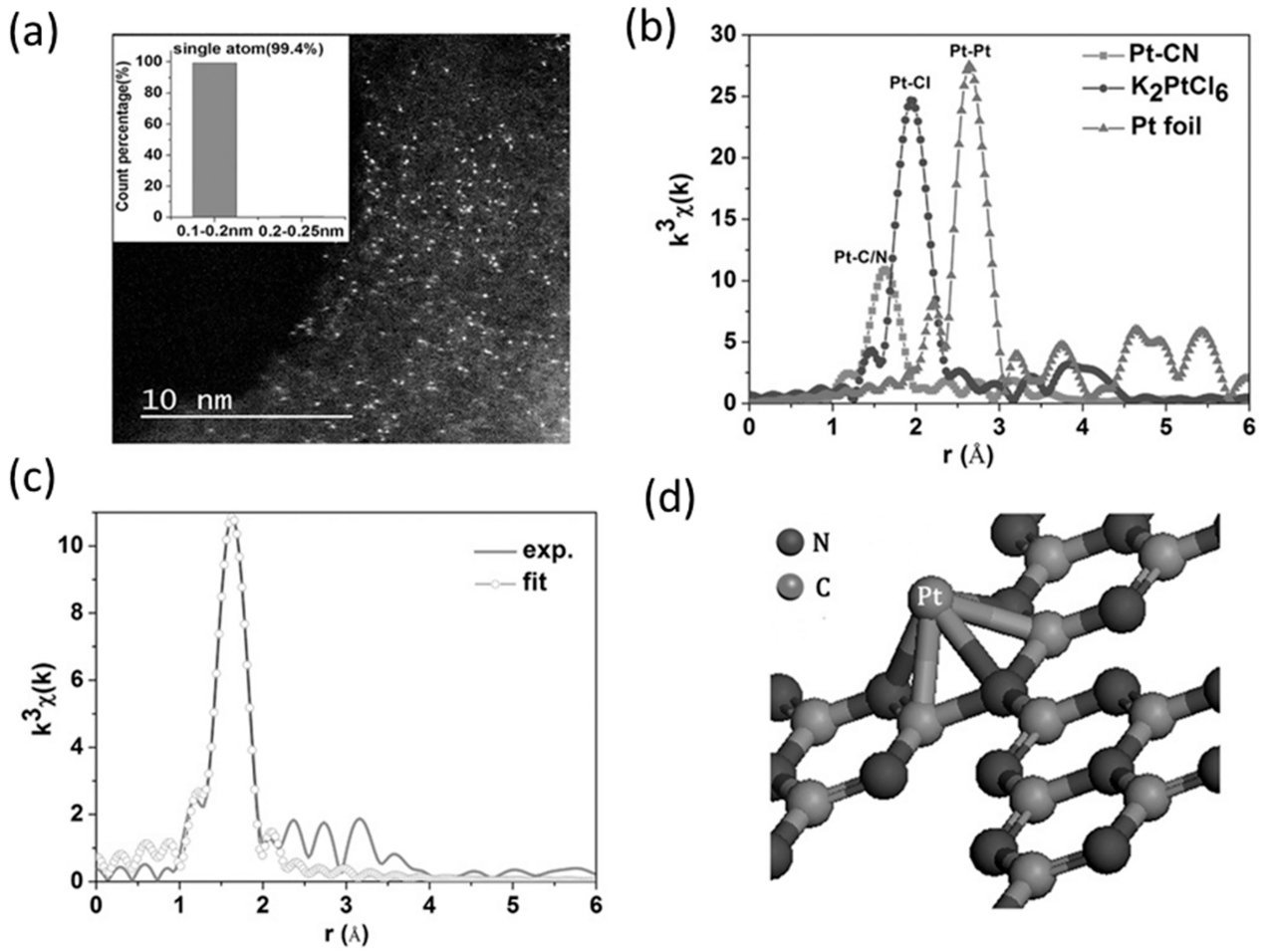

Figure 34. (a) C_s HAADF-STEM image of Pt single atom on g-C_3N_4, (b) FT k^3-weighted $\chi(k)$ function of Pt/g-C_3N_4 and reference Pt foil and K_2PtCl_6, (c) experimental versus fitting of the FT R-space (phase uncorrected), and (d) model of Pt single atoms on C_3N_4 network. Copyright with permission from ref 302. Copyright 2016 WILEY-VCH Verlag GmbH and Co. KGaA, Weinheim.

either made of organic and/or inorganic linkers, single atoms can be incorporated within these structures via different strategies as shown in Figure 37. Different synthetic strategies and structural arrangements of MOFs have been discussed by Bitzer et al.[314] The catalytically active ions can be incorporated directly into the structure as shown in Figure 37a or can be coordinated to a modified linker.

An example for the first case has been reported by Li et al. where the nickel ions were uniformly incorporated on the node of a Zr-based MOF, NU-1000 via atomic layer deposition (ALD).[315] NU-1000 consists of $Zr6(\mu_3\text{-}O)_4(\mu_3\text{-}OH)_4(H_2O)_4(OH)_4$ nodes and tetratopic 1,3,6,8-(p-benzoate)-pyrene ($TBAPy^{4-}$) linkers which can be used to bind ions with the −OH or -H_2O groups on the Zr_6 nodes as shown in Figure 38. Upon incorporation of nickel, they used XAS to elucidate the local environment of Ni atoms. FT k^3-weighted EXAFS spectra showed that the nickel atoms are isolated as presented in Figure 38a. Normalized XANES spectra at the Ni K-edge showed that the as-synthesized catalyst has Ni in +2 oxidation state. Upon activation under H_2 at 473 K, there are changes in the EXAFS and XANES spectra. The average Ni first shell coordination number decreased from 5.4 ± 0.6 to 5.0 ± 0.5 and also the Ni−O first shell bond distance from 2.056 and 2.033 Å. Considering the error in the measurements, these changes are not so significant. However, the author claimed that these structural changes might be due to the formation of small Ni−H species under the treatment of H_2. The formation of the Ni−H species is important as it was found to promote the hydrogenation of ethylene as well as oligomerization. Moreover, the authors claimed that the organic linkers present in the framework contribute to the overall stability of the Ni ions.

Ye and co-workers showed that single atoms of cobalt embedded in porphyrin like MOF where the light absorbing capacity of porphyrin and the CO_2 binding ability of Co was utilized for the photochemical reduction of CO_2.[316] XAS experiments performed at the Co K-edge suggests that the Co centers are isolated and the square planar configuration of the Co is confirmed from the strong pre-edge peak at 7715 eV. For understanding the CO_2 photoreduction mechanism, they showed that on irradiation of light to the Co-containing catalyst, the Co^{II} high spin state transforms to a low spin Co^{I} species. Thereafter on introducing CO_2, it oxidize back to Co^{II} confirming the involvement of Co in the catalytic cycle. Gotthardt et al. reported synthesis of a Pd containing MOF via postsynthetic modification of mixed-linker.[317] The catalyst was shown to be very active for liquid phase Heck reaction.

As discussed in the previous section of SACs supported on carbon, MOFs can also be used as precursors to synthesize SACs.[301,318−322] Since MOFs are high surface area materials with high porosity, the incorporated metal atoms can be accurately tunable to generate tailorable structures.

https://doi.org/10.1021/acs.chemrev.2c00495
Chem. Rev. 2023, 123, 379−444

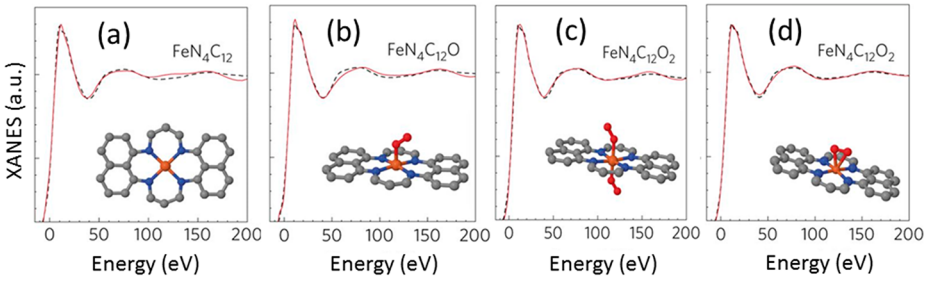

(e)

Model structure	Geometry	Fe-N (Å)	Fe-O (Å)	Bending (°)	R_{sq}
FeN_4C_{12}	4-fold	1.98 (3)			2.37
	5-fold	1.97 (3)	1.86 (4)	51 (5)	1.68
	6-fold end-on	2.00 (3)	1.87 (4)	33 (7)	1.17
	6-fold side-on	1.93 (3)	2.00 (4)	90 (0)	1.09
FeN_4C_{12}	6-fold end-on	2.01 (2)	1.88 (4)	55 (7)	1.05
	6-fold side-on	1.92 (2)	2.02 (3)	90 (0)	1.02

Figure 35. Experimental XANES spectra at the Fe K-edge (dashed black lines) and theoretically predicted (solid continuous red line) with different structures such as (a) FeN_4C_{12}, (b) FeN_4C_{12} with one O_2 molecule adsorbed in end-on mode, (c) FeN_4C_{12} with two O_2 molecules adsorbed in end-on mode, (d) FeN_4C_{12} with one O_2 molecule adsorbed in side-on mode, and (e) table of structural parameters obtained from XANES analysis. Color code: brown = Fe, blue = N, gray = carbon, and red = oxygen. Bending represents the angle between the two oxygens, R_{sq} is the residual function. Values in the parentheses are errors. Adapted with permission from ref 305. Copyright 2015, Nature Publishing Group.

2.3.2.1. SACs Incorporated in Covalent Organic Frameworks (COFs). In a recent example, Peng et al.[323] showed that single atoms of iron can be stabilized using a fully π conjugated iron phthalocyanine (FePc) rich covalent organic framework (COF) without any pyrolysis step involved. The FePc moieties are uniformly distributed in the COF which was further supported on graphene. This kind of synthesis route can be an alternative to the traditional pyrolysis method that generally ends up with a random distribution of single atoms. The intermolecular interaction between the iron phthalocyanine and the supported graphene made the SACs superior in performance for oxygen reduction reaction (ORR) and in Zn-air batteries. Among the other methods used to characterize the material, XAS was helpful to understand whether the Fe atoms were still intact within the framework or not. XAS performed at the Fe K-edge evidenced that the white line intensities of the Fe SACs and Fe-phthalocyanine complex are similar and quite different than the Fe foil shown in Figure 39. This suggests that Fe may be connected to an N atom of the phthalocyanine presented in the model structure of Figure 39f. The FT EXAFS spectra shown in Figure 39d discards the possibility of the presence of any Fe−Fe scattering path. However, there is an indication of presence of the second shell around the Fe atom at a distance between 2 and 3 Å. On further analysis, they found contribution of the Fe−N scattering path in both COF_{BTC} and pfSAC-Fe, whereas the Fe−C path is present only with the pfSAC-Fe. With the help of DFT calculations, they arrived at the conclusion that the electrons of graphene are attracted to the N-coordinated Fe sites that result in a Fe−C scattering path. Furthermore, the Fe center provide the bonding possibility of the oxygen to carry out the ORR reaction. This study shows that the SACs created in a more uniform way provides us the platform to understand the electronic environment better. Additionally, Zhong et al. synthesized covalent organic framework bearing single Ni sites (Ni-TpBpy) and utilized for the photocatalytic reduction of CO_2 to CO.[324]

2.3.3. SACs Inside Porous Organic Polymers (POPs) as Host. Porous organic polymers (POPs) are highly cross-linked amorphous polymers[325−327] that can act as supports for solid catalysts. Despite of the disadvantages in the catalytic application due to (a) diffusion limitations, and (b) polymer swelling, the functional groups present, such as carboxylic acid, sulfonic acid, or other coordinating groups that can strongly bind isolated metals and generate single atomic sites, can be highly active in catalysis. A study by Liu et al. showed that isolated palladium (>2 wt %) can be stabilized in +2 oxidation state coordinated to the oxygen atom of the polymer PDMS as verified by XAS.[328] The normalized XANES spectra and FT k^2-weighted EXAFS spectra are shown in Figures 40a and b.

From Figure 40a, the XANES spectra at the Pd K-edge shows features that resemble positively charged Pd; however the features are slightly different than the Pd^{II} complex e.g. Pd $(OAc)_2$. The k^2-weighted FT EXAFS spectra showed predominantly only first shell Pd−O at a distance of 1.6 Å (without phase correction). The solid-state ^{13}C NMR study did not show any change in the PDMS before and after incorporation of the Pd^{II} species indicating that the structural integrity of the polymer was not affected. The catalyst was investigated for the oxidative coupling of benzene to biphenyl in the presence of oxygen which showed superior activity than the homogeneous analog such as $Pd(OAc)_2$. Upon changing the polymer from PDMS to PDAS (polydiacetylenes), the catalytic activity significantly dropped due to the weaker interaction between the polymer and Pd^{2+}, which can be evident from the formation of Pd nanoparticles inside the polymer.

2.4. SACs over Other Supports

2.4.1. SACs Supported in Metal Carbides/Sulfides/Nitrides/Phosphides. Two-dimensional metal carbides, sul-

https://doi.org/10.1021/acs.chemrev.2c00495
Chem. Rev. 2023, 123, 379−444

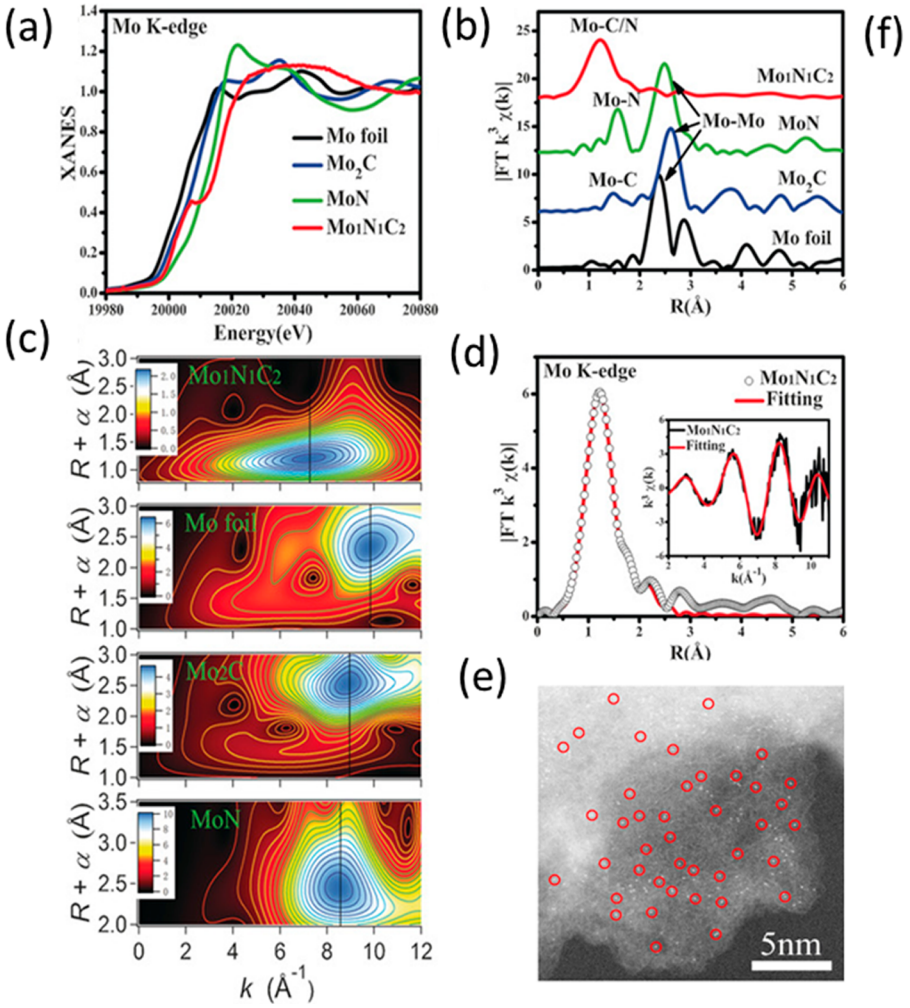

(f)

Free parameters	Path	Value
CN	Mo-C	2.3
	Mo-N	1.1
	Mo-O	0.9
R	Mo-C	1.87
	Mo-N	1.91
	Mo-O	1.78
σ^2	Mo-C	4.8
	Mo-N	7.1
	Mo-O	6.5
ΔE	Mo-C	4.6
	Mo-N	3.7
	Mo-O	5.8
r factor	0.0045	

Figure 36. (a) XANES and (b) FT k^3-weighted EXAFS and (c) WT-EXAFS spectra of $Mo_1N_1C_2$, MoN, Mo_2C, and Mo foil at Mo K-edge, (d) experimental (open circles) and fitted curve (continuous red line) of $Mo_1N_1C_2$, (e) HAADF-STEM image of $Mo_1N_1C_2$ catalyst after catalytic test, and (f) free parameters derived from EXAFS fitting. The value of S_0^2 was set as 0.85; k-range considered was between 2.0 and 10.5 $Å^{-1}$. Mo−O scattering path represents the coordination of molecular oxygen to Mo center. Adapted with permission from ref 310. Copyright 2017 Wiley-VCH Verlag GmbH and Co. KGaA, Weinheim.

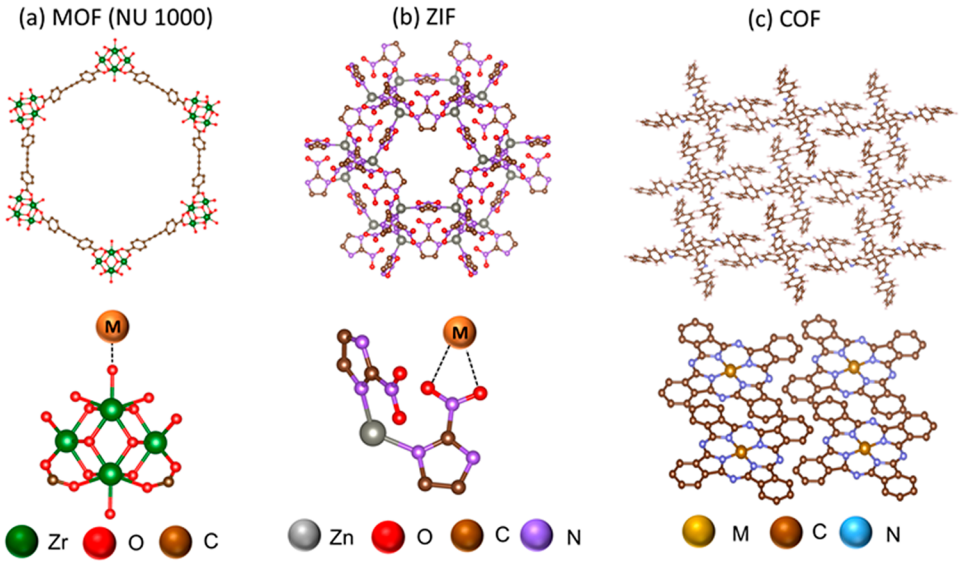

Figure 37. Representation of different types of MOF and COF and the binding sites of the single atom (a) metal−organic framework (NU-1000), (b) Zeolitic imidazolate framework (ZIF), (c) covalent organic framework (COF).

https://doi.org/10.1021/acs.chemrev.2c00495
Chem. Rev. 2023, 123, 379−444

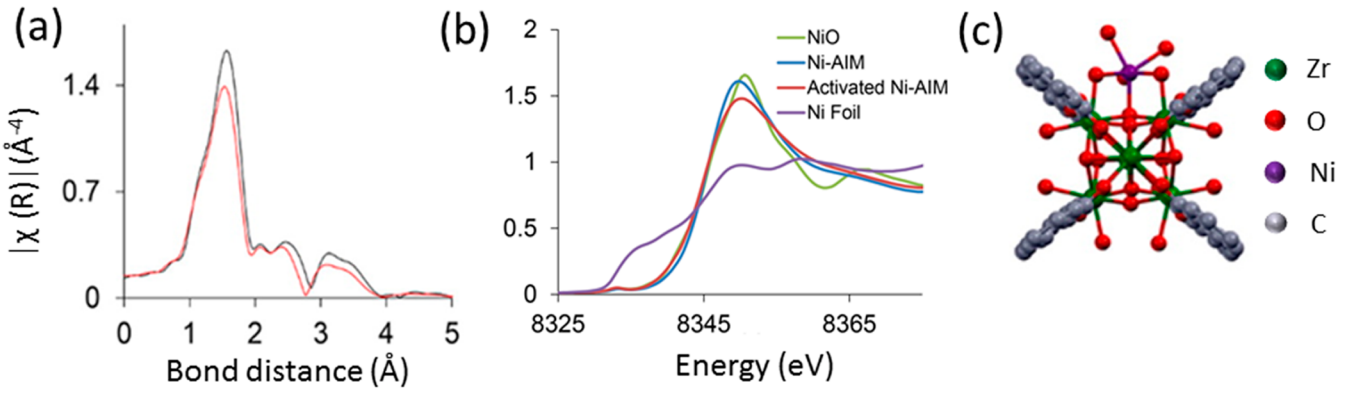

(d)

Sample	Path	Coordination number, N	Bond distance, R (Å)	Debye-Waller, σ^2 ($Å^2$)
Ni-MOF before activation	Ni-O	5.4 ± 0.6	2.056 ± 0.005	0.0060 ± 0.0012
Ni-MOF after activation	Ni-O	5.0 ± 0.5	2.033 ± 0.005	0.0071 ± 0.0012

Figure 38. (a) FT k^3-weighted EXFAS spectra of Ni-MOF catalyst before (black line) and after (red line) activation with 3% H_2/N_2 gas mixture at 573 K. (b) Ni K-edge XANES spectra of the catalyst together with NiO and Ni foil as reference, (c) Ni atom per six Zr node, and (d) table of free parameters derived from EXAFS fitting. Adapted with permission from ref 315. Copyright 2016 American Chemical Society.

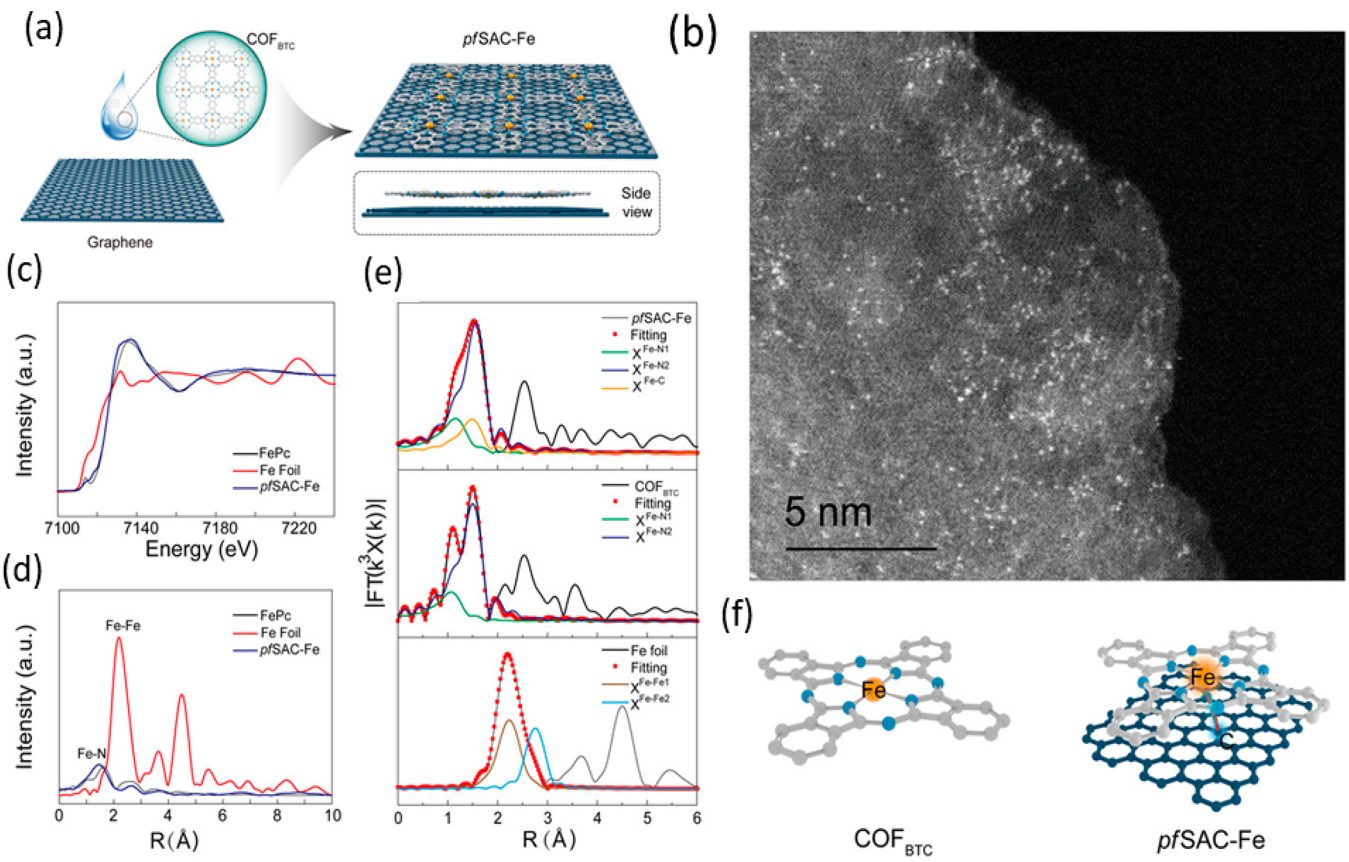

Figure 39. (a) Synthetic path of the Fe SAC, (b) HAADF-STEM image of Fe SAC, (c) XANES spectra of Fe SAC at the Fe K-edge with Fe foil and FePc as reference material, (d, e) FT k^3-weighted EXAFS spectra and the corresponding fit, and (f) simulated model structure from the EXAFS analysis of Fe SACs over graphene support. Adapted with permission from ref 323 under Creative Commons Attribution-NonCommercial license 4.0 (CC BY-NC).

https://doi.org/10.1021/acs.chemrev.2c00495
Chem. Rev. 2023, 123, 379−444

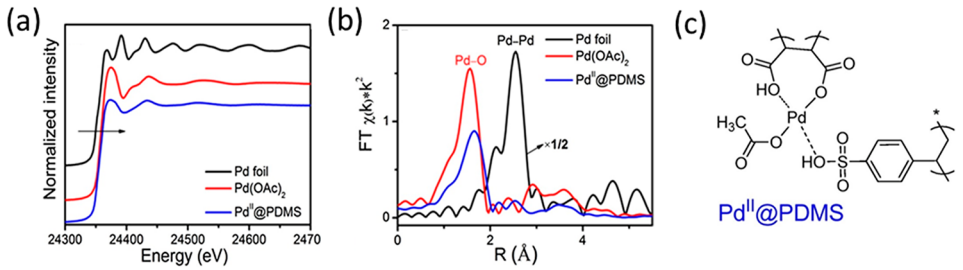

Figure 40. (a) Normalized XANES spectra at the Pd K-edge, (b) FT k^2-weighted EXAFS spectra of the Pd stabilized in porous organic polymer Pd@PDMS with reference Pd foil and Pd $(OAc)_2$ are shown, and (c) the model structure of Pd^{II} species stabilized in PDMS. Adapted with permission from ref 328. Copyright 2017 Elsevier B.V. All rights reserved.

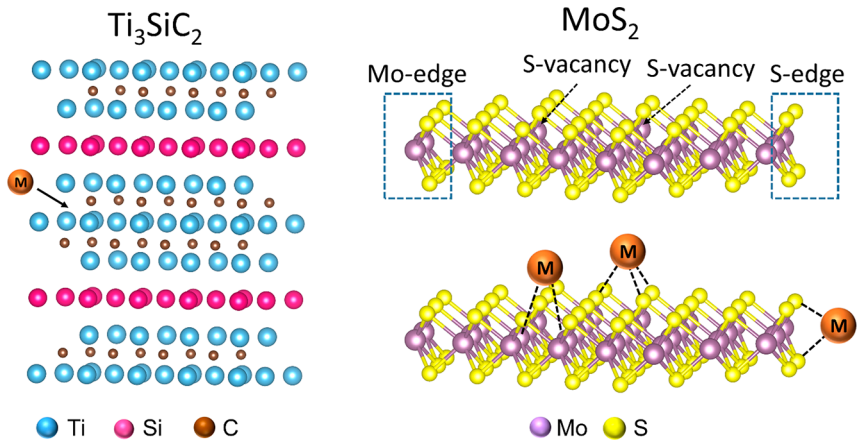

Figure 41. Incorporation of single atom in carbide (Ti_3SiC_2) and sulfide (MoS_2) structures to generate single-atom catalysts. The metals can also be stabilized to the sulfur on the edge.

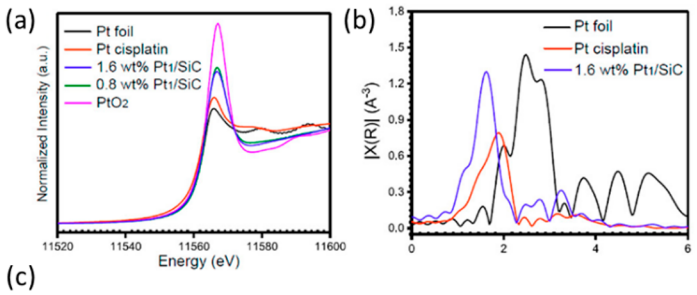

(c)

Sample	Shell	Coordination number, CN	Interatomic distance *R* (Å)	Debye–Waller factor, σ^2 (Å^2)
0.8 wt % Pt_1/SiC	Pt–O	3.0 ± 0.3	2.00 ± 0.01	0.003 ± 0.001
0.8 wt % Pt_1/SiC	Pt–Si	0.9 ± 0.6	3.09 ± 0.03	0.003 ± 0.008
1.6 wt % Pt_1/SiC	Pt–O	2.8 ± 0.3	2.02 ± 0.01	0.003 ± 0.001
1.6 wt % Pt_1/SiC	Pt–Si	0.8 ± 0.6	2.96 ± 0.03	0.003 ± 0.008

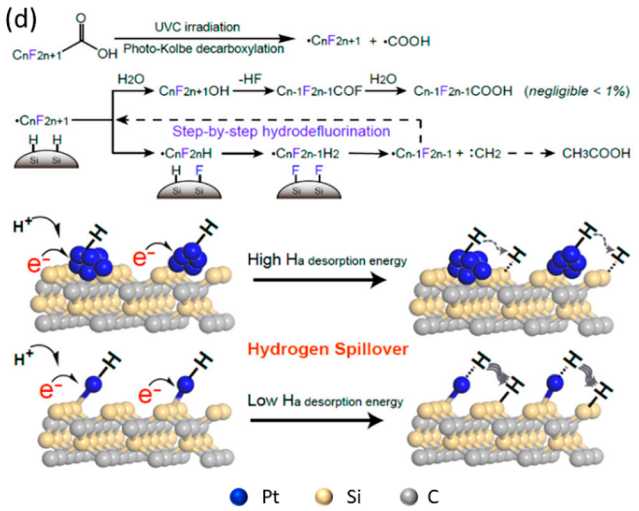

Figure 42. (a) Normalized XANES spectra and (b) FT k^3-weighted EXAFS spectra at the Pt L_3-edge, (c) table of free parameters derived from EXAFS equation, and (d) mechanism of photo-Kolbe decarboxylation and subsequent hydrodefluorination on Pt_1/SiC. Reproduced with permission from ref 331. Copyright 2018 American Chemical Society.

fides, and nitrides can host single atom in their structures covalently bonded through the support. These materials are highly stable and often exhibit defect sites or vacancies where metal ions can be incorporated.[149,329] 2D transition metal carbides are also known as MXenes with molecular formula $M_{n+1}X_nT_x$, where M is the transition metal, X is carbon or nitrogen, and T_x represents the functional group. These class of materials are shown for variety of applications due to their electronic, optical, chemical, and mechanical properties.[330] Typically it consists of two or more layers of transition metals packed into a honeycomb like 2D lattice, where X atoms are incorporated between the layers as shown in the left-hand side of Figure 41. MoS_2 exhibit interestingly a layered structure and is also semiconducting. Hence, it can be used for a wide variety of catalytic applications. Some of the sites where the transition metal can be incorporated in these structures are shown in Figure 41 (right).

https://doi.org/10.1021/acs.chemrev.2c00495
Chem. Rev. 2023, 123, 379−444

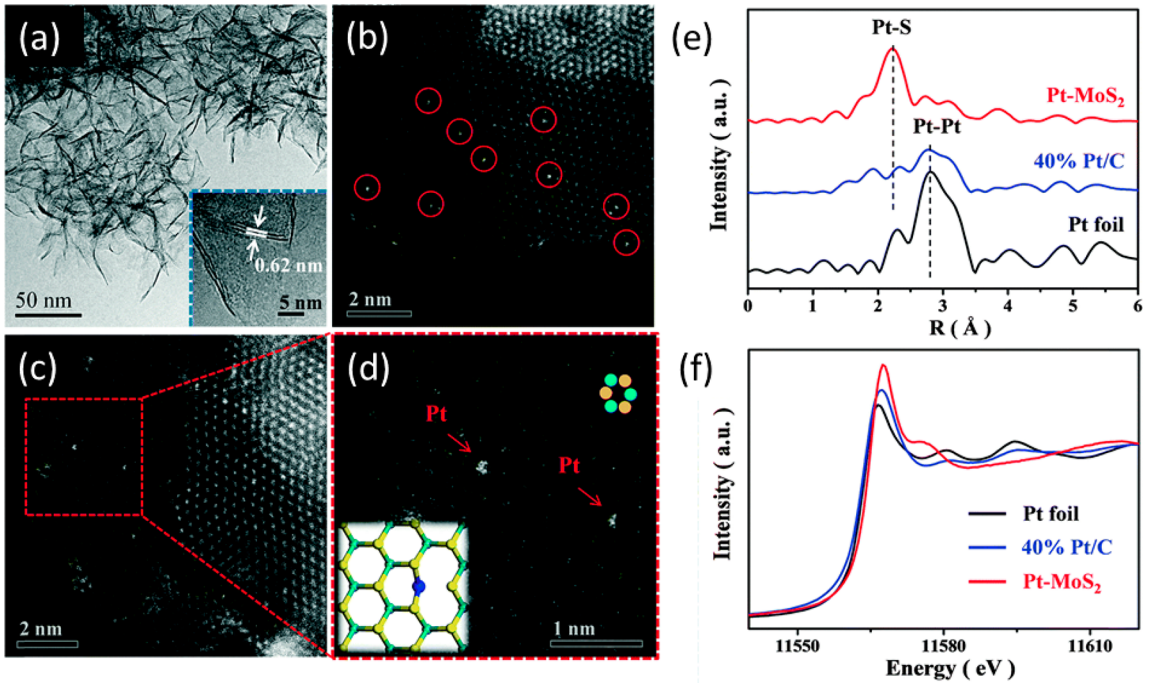

Figure 43. (a) TEM image and (b–d) HAADF-STEM images of Pt_1/MoS_2 (red circles are representing the single Pt atoms), (e) FT k^2-weighted EXAFS spectra of Pt_1/MoS_2, and (f) normalized XANES spectra of Pt_1/MoS_2 at the Pt L_3-edge. Pt foil and 40 wt % Pt/C are shown as references. Adapted with permission from ref 334. Copyright Royal Society of Chemistry.

Yang et al. carried out an XAS study on a catalyst containing 0.35 wt % Pt/TiN and showed presence of clusters whereas other spectroscopic studies evidenced the coexistence of single atoms as well. The catalysts were found to be active for various electro catalytic activities, however to distinguish the active species in these regards, *operando* spectroscopy will be more informative. On the other hand up to 1.6 wt % Pt can be dispersed as single atom over SiC as shown by Huang et al.[331] The EXAFS fitting showed that the Pt atoms are bonded to the SiC with approximately three carbon atoms in the first coordination sphere. The Pt_1/SiC is active for C–F bond activation. According to their research, the hydrogen spillover from Pt single atoms is quite effective onto the SiC support, which results in Si–H bonds that fulfill the further hydrodefluorination (cf. Figure 42). There is also possibility to have Pt–C bond in the first shell that cannot be distinguished by XAS.

Zhou, Ma, and their co-workers studied Pt SACs over α-MoC for chemoselective hydrogenation of nitrobenzene.[151] In this SAC, Pt was found to be CO-tolerant with Pt loading of 0.25 wt % and the XAS study revealed that the Pt atoms were isolated and carried positive charge. Zhang et al. called MXene as superexcellent support for confining single atom due to the formidable metal–support interactions.[332] The authors discussed the properties, synthesis and electrocatalytic applications of single atom incorporated in various MXenes structures. Ramalingam et al. showed Ru single atom over Ti_3C_2Tx MXene for hydrogen evolution reaction.[333]

SACs Supported on Metal Sulfides. Bao and his co-workers showed that Pt SACs on MoS_2 exhibit superior activity in electrocatalytic H_2 evolution reaction over MoS_2.[334] The single atoms of Pt are present as dopant in the MoS_2 lattice at a Pt–S bond distance of 2.2 Å bearing slightly positive charge on it as confirmed from the EXAFS and XANES spectra at Pt L_3-edge (see Figure 43). According to their study, Pt atoms were doped on a few layers of MoS_2, which drastically changed the adsorption behavior of H on the neighboring S atoms and hence the catalytic activity. However, the study did not show many details of the coordinating environment of Pt atoms from the EXAFS analysis, and a small Pt–Pt contribution could not be neglected as shown in Figure 43e.

Using computation, Nørskov and Cui[335] showed that transition metal (Fe, Co, Ni, or Cu) doped MoS_2 accounts for the enhanced hydrogen evolution during electro-catalysis. There are many other examples of SACs prepared on MoS_2, WS_2, NiS_2, etc., which are claimed to show superior catalytic performance compared to nanoparticles.[336−339] Li et al. reported the synergetic interaction of Pt single atoms supported on MoS_2 for CO_2 hydrogenation.[340] The presence of a significant number of neighboring Pt atoms promotes the hydrogenation of CO_2 to methanol and formic acid, whereas their absence produces only methanol. DFT calculations suggest that the presence of neighboring atoms favors an alternative reaction pathway where CO_2 is first hydrogenated to formic acid and subsequently to methanol.

Jiang et al. showed a dynamic Ir single site generated over metal phosphides ($(Ni_{0.74}Fe_{0.26})_3P$) during oxygen evolution reaction (OER).[341] Based on *operando* XAS experiments and DFT calculations, the authors concluded that during OER isolated Ir sites undergo a deprotonation step to form multiple active sites, which promote O–O coupling. In addition, after the subsequent electrochemical activation, the authors observed that the isolated Ir atoms turn into a stable state with higher valence and more oxygen ligands around it. However, metal phosphides are still used seldomly for stabilizing SACs.

2.4.2. SACs in Perovskites as Host Structure. Perovskite-type oxide structures with general formula ABO_3 (where cation A is larger than B) are already quite known in the field of heterogeneous catalysis for their unique properties.[342−344] For example, Nishihata and co-workers showed that Pd containing perovskite with formula $LaFe_{0.57}Co_{0.38}Pd_{0.05}O_3$ is highly active as

https://doi.org/10.1021/acs.chemrev.2c00495
Chem. Rev. 2023, 123, 379−444

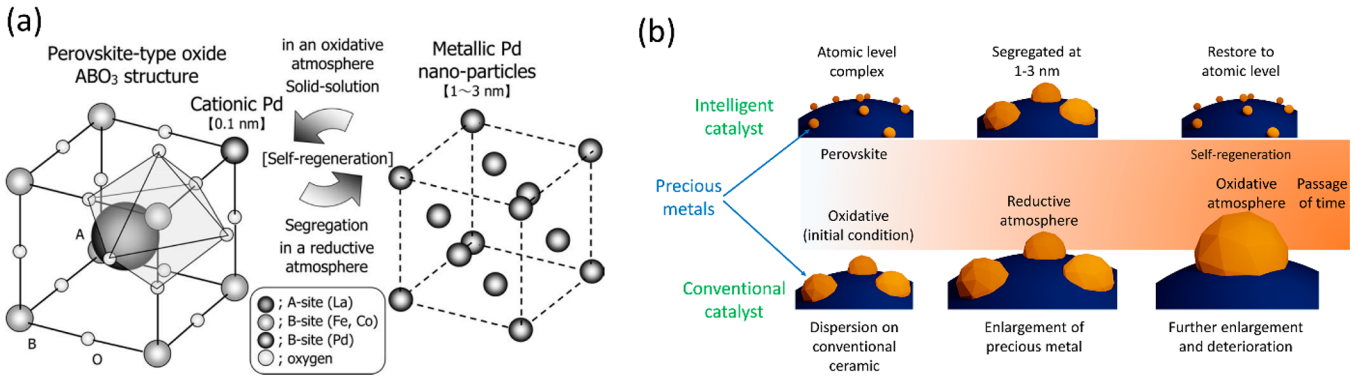

Figure 44. Schematics of dynamic behavior of (a) Pd incorporated on perovskite structure ("intelligent catalyst") and, (b) differences between conventional and intelligent catalyst under oxidative and reductive atmosphere. Adapted with permission from ref 345. Copyright 2005, Springer Science Business Media, Inc.

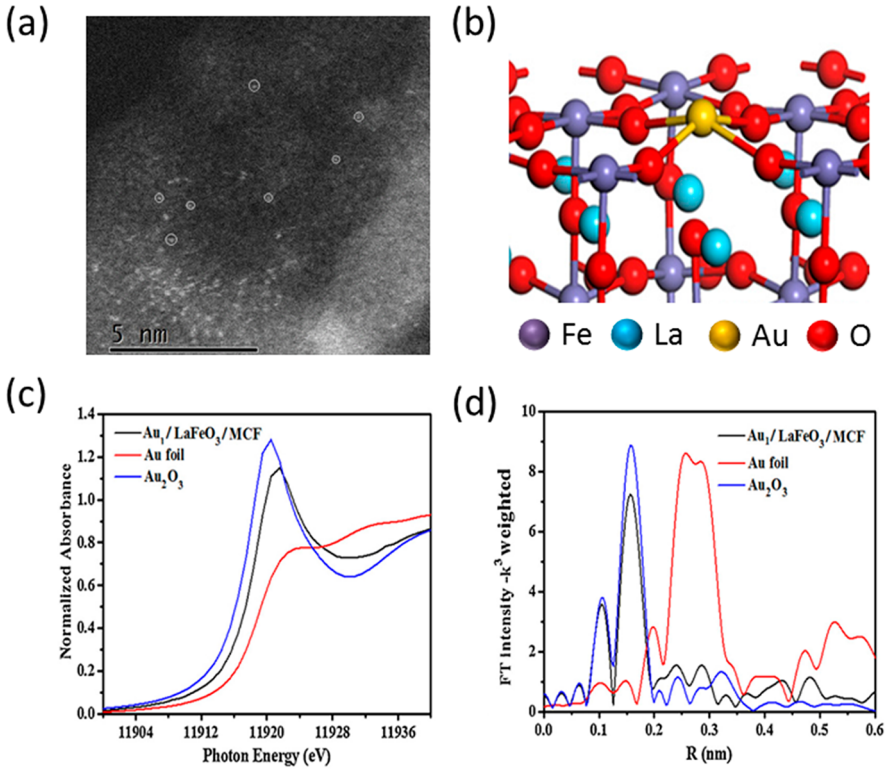

Figure 45. (a) HAADF-STEM image of $Au_1/LaFeO_3$/MCF, (b) DFT optimized model structure of the $Au_1/LaFeO_3$, (c) XANES, and (d) FT k^3-weighted EXAFS spectra of $Au_1/LaFeO_3$ together with the reference Au foil and Au_2O_3 are shown. Adapted with permission from ref 347. Copyright 2019 Elsevier B.V. All rights reserved.

an exhaust gas catalyst.[343] The catalysts are cycled under the oxidative and reductive environment and the palladium atoms reversibly move in and out of the perovskite structure, which was coined as "Intelligent catalyst".[345] A schematic diagram and comparison with the conventional catalyst is shown in Figure 44. The dynamic behavior of the Pd prohibits sintering and further agglomeration and was further confirmed by *in situ* energy-dispersive X-ray absorption fine structure (DXAFS) analysis with 10 ms resolution.[346] Since the atom has a defined position inside the lattice, metal substituted perovskite on a support can be a prospective material under the category of SACs.

Tian et al.[347] has recently shown that $LaFeO_3$ perovskite can stabilize single Au atoms up to a calcination temperature 973 K in air supported on mesocellular foam (MCF) silica. The Au SACs on $LaFeO_3$-MCF were introduced by a deposition-precipitation method. Among other characterization techniques, HAADF-STEM images and XAS spectra are shown in Figure 45. The XANES collected at the Au L_3-edge suggests that the Au atoms are oxidic and the oxidation state of Au is close to +3. The FT EXAFS spectra as shown in Figure 45d hint at the presence of first shell around Au at a distance of 2.2 Å (with phase correction), which is associated with Au−O coordination with coordination number 4 derived from EXAFS fitting. However, according to the authors, the possibility of having some contribution from the Au−Au scattering cannot be neglected. Upon introducing an Au−Au scattering path into the fit, did not improve the fitting results. According to the DFT calculations, adsorption of Au atom in the (001) O-hollow sites and in the Fe substituted vacancies match the geometry of the Au atom that fits to the EXAFS results. The SAC of Au was used for the CO

https://doi.org/10.1021/acs.chemrev.2c00495
Chem. Rev. 2023, 123, 379−444

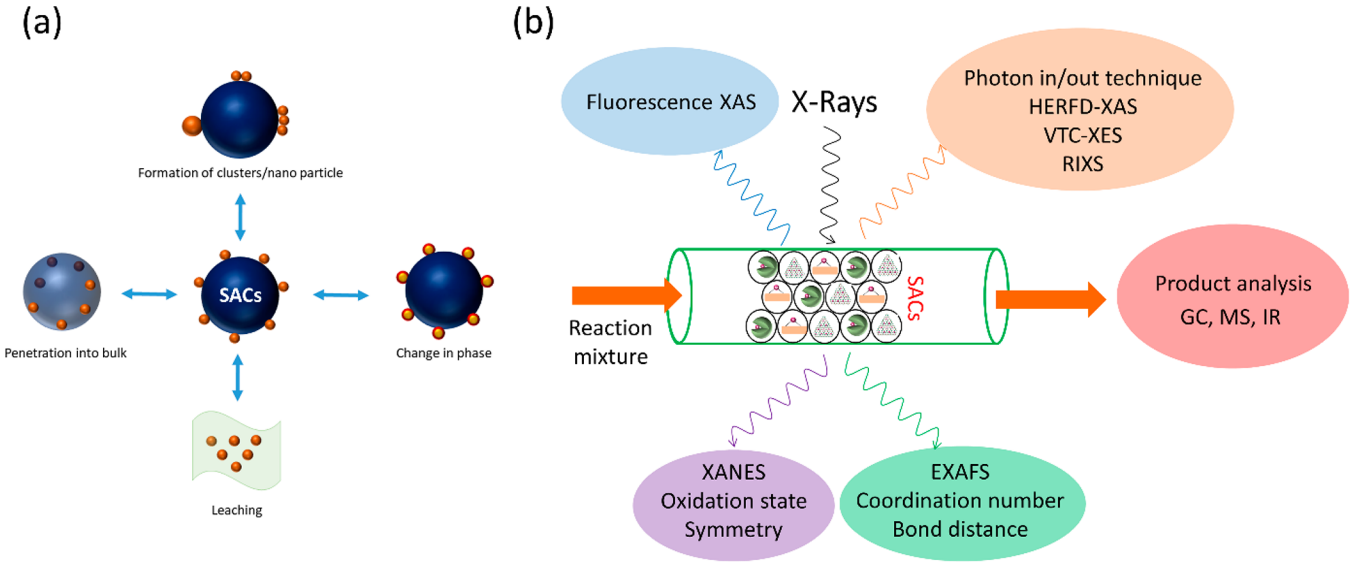

Figure 46. (a) Various possible structural changes in SACs under reaction conditions and (b) X-ray techniques that can be implemented on SACs under operating condition and the information gained from it are shown.

oxidation reaction after calcination at 700 °C. The light-off curve showed 20% conversion up to a temperature of 150 °C which reaches 100% conversion at 170 °C. This drastic change in the CO oxidation curve can be explained only when there is a dramatic structural change in the active center of the catalyst. Up to three consecutive runs, the CO light-off curve did not show any change, meaning that the possibility of the deactivation of the catalyst is highly unlikely, as also confirmed from electron microscopy study. The authors explained that at low temperature the single atoms of Au promote oxygen dissociation and form a surface oxide layer, as explained by Alves et al. and hence result in a decline in reactivity.[348] However, at high temperatures, this possibility is less and the CO oxidation is the dominant pathway. DFT calculations suggest that the CO oxidation reaction follows a Mars-van-Krevelen type of mechanism with a strong CO adsorption and low vacancy formation energy. This result implies that perovskite-type materials are promising for further applications as SACs. Additional investigations to find out the nature of the active sites during operating conditions are necessary to gain more insight into the reaction mechanism.

Wan et al., with the help of DFT calculations, showed that Pt single atom stabilized over (100) surfaces of $SrBO_3$ perovskite which is a promising material for methane dissociative adsorption and C−H bond activation.[349] The authors found that the Pt single atoms on the A-termination 100 surface are negatively charged compared to Pt single atoms on the B-termination surface, which are responsible for such strong adsorption of methane.

2.5. Summary of SACs over Various Supports

SACs are attractive materials for catalysis and can be obtained via different synthesis routes using various supports as outlined in this section and summarized in Figure 12. Most of the synthetic routes can easily be scaled up for large amounts. The applications in various catalytic systems such as thermal, photocatalysis, and electro-catalysis also make them perfect candidates for industrially relevant catalytic reactions.[350,351] Moreover, the tunable charge and coordination around single atoms make them an ideal candidate to bridge the gap between different fields of catalysis. From the point of view of characterization, there are still challenges with XAS being one of the reliable and universal tools that can be applicable across the periodic table irrespective of metal loadings. However, in many cases, the fate of single atoms remains open under operating conditions. The SAC are an excellent starting point to investigate whether and how the structure is preserved under operating conditions. Hence, the next step in single atom catalysis requires in-depth studies using *in situ/operando* spectroscopic tools to shed more light into these relationships. We discuss the potential of *operando* spectroscopy, the dynamics of such catalysts under reaction condition, and especially of X-ray absorption spectroscopy in this field in the following section.

3. *IN SITU/OPERANDO* XAS STUDIES ON SACS: TRACKING THE FATE OF SINGLE ATOM CATALYSTS

In situ/operando spectroscopic techniques are required to track the evolution of active centers during catalysis. As discussed earlier, SACs, like all other catalysts, may structurally transform. As SACs are designed with striking synthetic efforts, as shown in section 2, the validation of their structure under reaction conditions is key for the final interpretation of the results. SACs can undergo various transformations under reaction conditions depicted in Figure 46a. As already discussed in section 1, X-ray spectroscopic techniques are ideal for studying these transformations and various methods can be used (cf. Figure 46b). Also Li et al.[352] have recently emphasized in a perspective article that, among the emerging *in situ/operando* techniques for characterizing SACs, XAS is one of the most attractive ones. Conventional XAS can be extended in terms of time (fast scanning), space (microscopy/tomography), and concentration (determination of promotor and poisonous atoms).

3.1. *In Situ/Operando* Studies at Synchrotron Radiation Sources

In order to perform an *operando* XAS study, special care should be taken to design cells since, depending on the objective of the study, the requirements might vary significantly.[353] Like in the laboratory where a reactor is designed for a special aim, also for *operando* spectroscopy different cells have been designed, taking various boundary conditions from the reaction (gas/liquid

https://doi.org/10.1021/acs.chemrev.2c00495
Chem. Rev. 2023, 123, 379−444

Scheme 2. Schematic Representation of *In Situ/Operando* Set up Together with a Capillary Microreactor Cell in an X-ray Absorption Beamline. Adapted with permission from ref 358. Copyright 1998 Elsevier Science B.V. All Rights Reserved

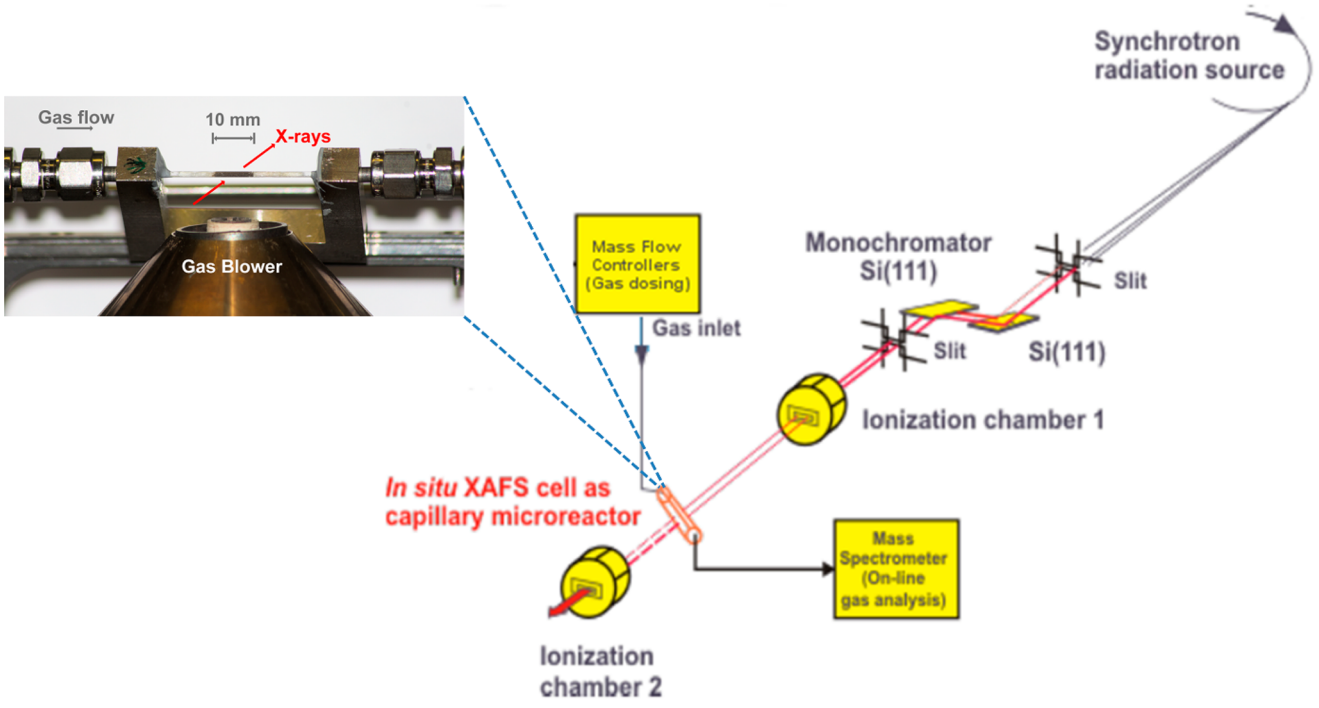

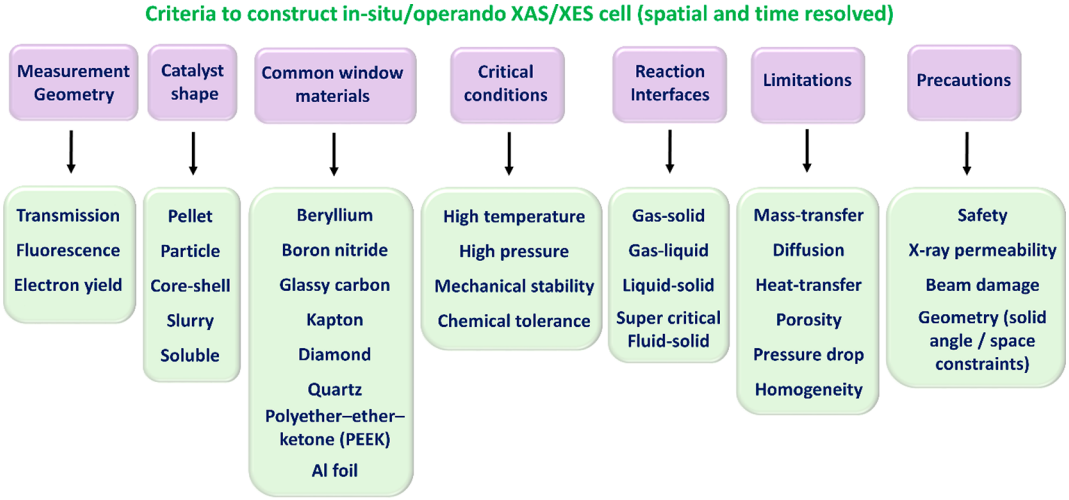

Figure 47. Various criteria to be considered while constructing a proper cell for *in situ/operando* XAS/XES experiments.

phase, fast/slow reaction rate, high/low external and internal mass transport, high/low temperature, high/low pressure) into account. The fluorescence X-ray detection requires different geometry than transmission. In addition, if XAS is used in combination with other spectroscopic techniques such as FT-IR, RAMAN, or with XRD, special design is necessary. Hence, the *in situ* and *operando* cells, which are nowadays used, go much beyond the early designs by Lytle et al.,[354] Koningsberger et al.,[355] or Dalla Betta et al.[356] in the 80s. Hence, we report here on different cell designs depending on the research area of SACs. A simple schematic of an *in situ/operando* set up at a XAS beamline is represented in Scheme 2.[48,357]

3.2. Concept of Designing Cells: Finding the Best Compromise

3.2.1. Cells for Gas-Phase Reactions. X-rays have the advantage that they can penetrate through matter, which makes it ideal for *in situ/operando* studies of solid catalysts. However, the materials used to construct a cell need to absorb as little of the incident or transmitted/emitted X-rays as possible. At the same time, the window materials should have sufficient structural strength at the required temperatures and pressures. For this purpose, the materials that are often used include quartz (in form of thin capillaries for high temperature experiments), Kapton, beryllium, glassy carbon, etc. For solid samples, homogeneous distribution of the metal within the sample and packing of the solid inside the reactor are also important. A list of

https://doi.org/10.1021/acs.chemrev.2c00495
Chem. Rev. 2023, 123, 379−444

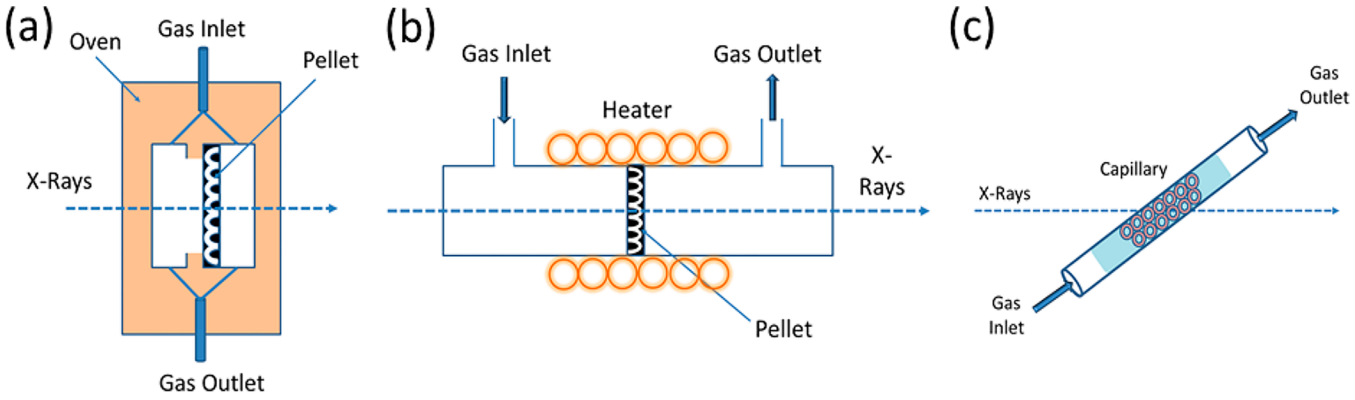

Figure 48. Cells for *in situ* XAS study (a) pellet cell with gas flowing around the pellet, (b) pellet cell with gas flowing directly through the pellet, and (c) capillary cell for plug flow reactor geometry. Reproduced with permission from ref 364. Copyright Royal Society of Chemistry.

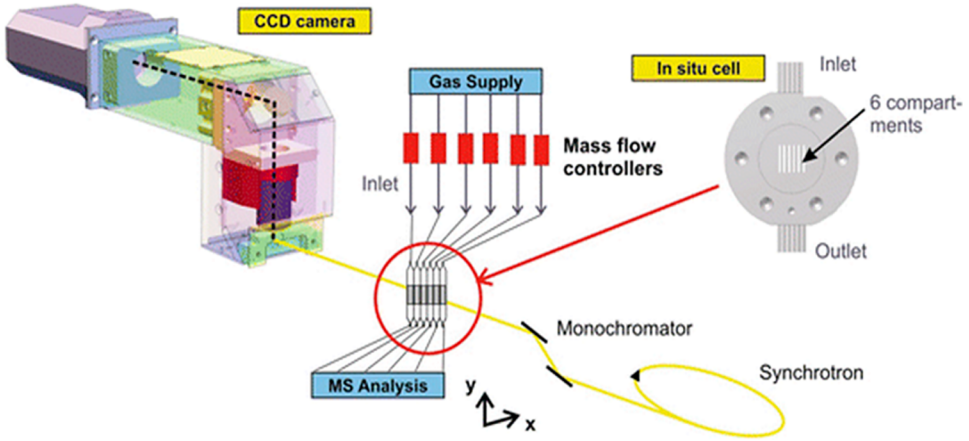

Figure 49. High throughput *in situ* XAS cell with microreactor and fast-moving CCD camera. Adapted with permission from ref 369. Copyright IOP Publishing Ltd.

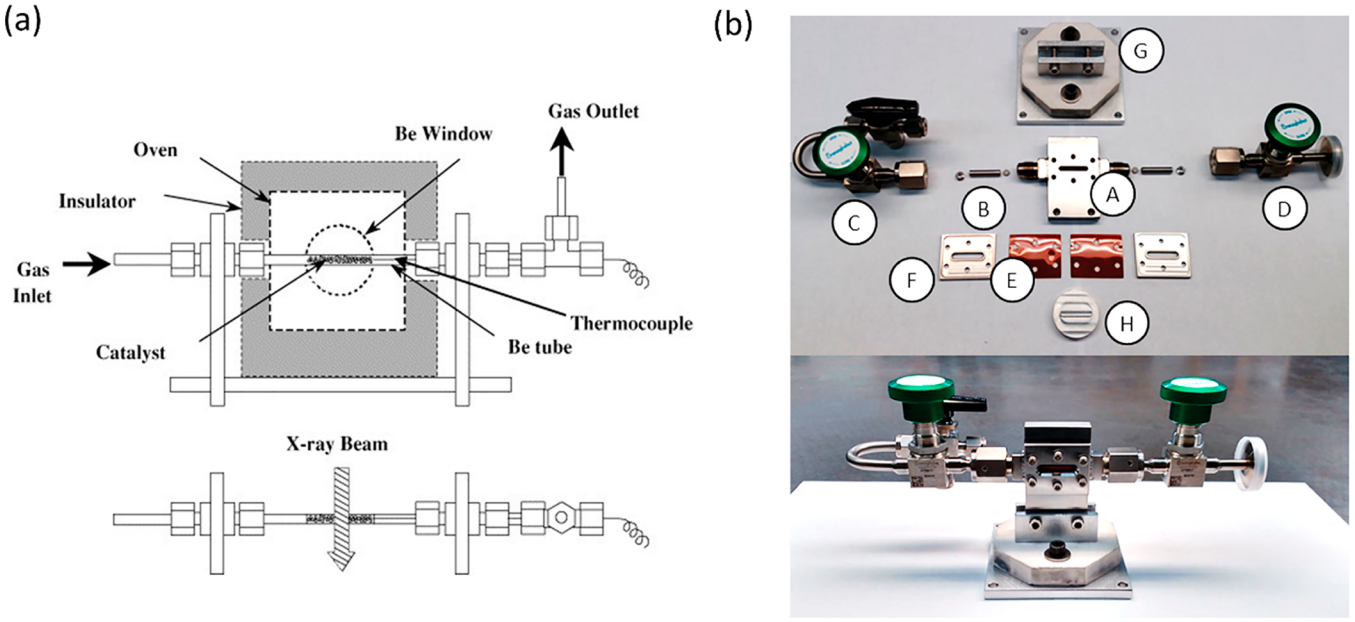

Figure 50. (a) High-pressure reaction cell and (b) a cell that can operate under vacuum or in reactive gas atmosphere. In (b), (A) cell body; (B) powder containment system, from left to right: hollow set screw, spacer, stainless steel fit; (C) inlet valve assembly; (D) outlet valve assembly; (E) polyimide windows; (F) window retainer plates; (G) mounting adapter; (H) sample press. Adapted with permission from refs 370 and 371. Copyright 2006 Elsevier B.V. All rights reserved. Rights managed by AIP Publishing.

https://doi.org/10.1021/acs.chemrev.2c00495
Chem. Rev. 2023, 123, 379−444

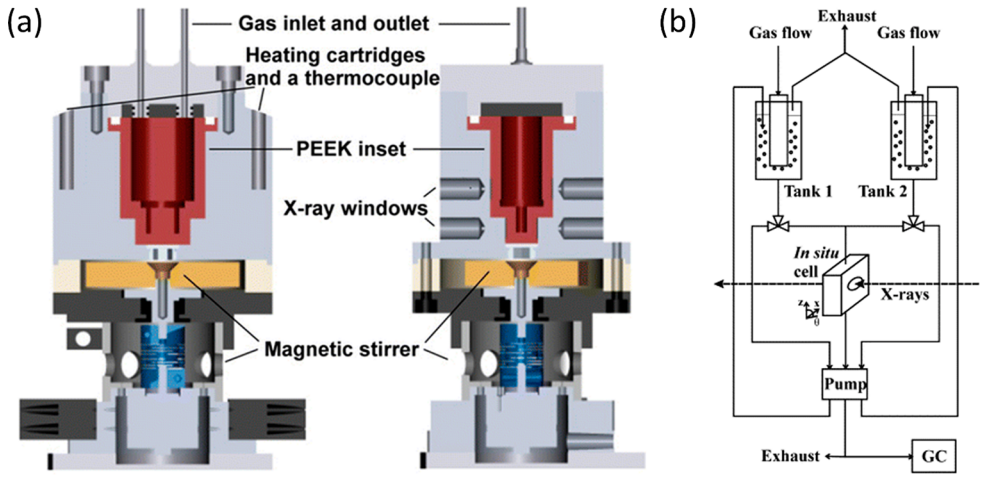

Figure 51. Schematic diagram of *in situ* cells for (a) batch reactions and (b) continuous flow fixed-bed reactions. The cell (a) can hold temperature and pressure up to 473 K and 150 bar. Adapted with permission from refs 363 and 373, respectively. Copyright 2017, Springer International Publishing Switzerland. Copyright 2002 Elsevier Science (USA). All rights reserved.

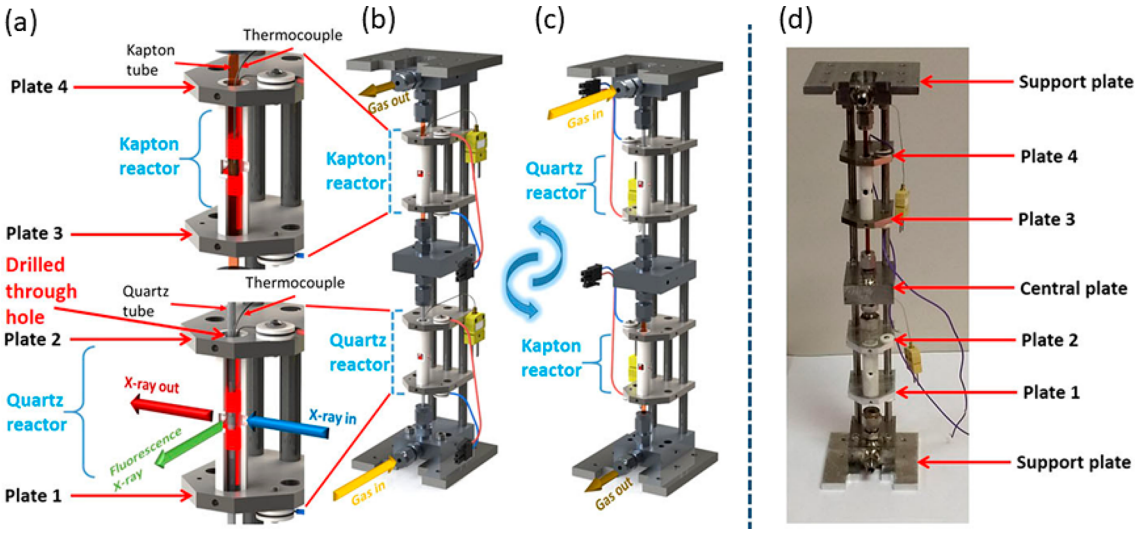

Figure 52. (a) Internal structure of the dual reactor with different components, (b) structure of the dual reactor at an orientation of the quartz reactor at the bottom, (c) structure of the dual reactor at an orientation of the kapton reactor at the bottom, and (d) an image of the reactor. Adapted with permission from ref 375. Rights managed by AIP Publishing.

criteria for designing a cell for *in situ*/*operando* XAS/XES studies is summarized in the Figure 47.

A number of synchrotrons offer a wide range of cells designed by research groups for different applications.[359−362] We have outlined the important criteria as a consequence of a compromise of chemical engineering and spectroscopy aspects to be considered while constructing an *in situ* cell.[363,364] The general concepts of a few *in situ* XAS cells for solid−gas and liquid−solid reactions have been summarized by Grunwaldt.[363] One of the most prominent is the capillary microreactor by Clausen et al.[365,366] and Thomas, Greaves et al.,[50] which has been commercialized by Claeys.[367] Some cells reported over the past years are shown in Figure 48.

A pellet cell as shown in Figure 48a and b allows for high-quality EXAFS data with a uniform sample thickness when there is sufficient porosity in the pellet to discard any diffusion limitation that might occur. A cell in the form of a micro reactor (ideal thickness d/length l and no dead volume), given e.g. in Figure 48c, needs catalysts pressed and sieved to approximately 80−120 μm particle size (generally 1/10 of the reactor diameter).[365] A modified version that allows low-temperature studies was achieved by Hannemann et al.[368] that can measure powders and wafers and is suitable for both gas and liquid phase reactions together with online product analysis. The calculation of Reynolds, Schmidt and Sherwood numbers for the assessment of the contribution of film and pore diffusion have been discussed thoroughly for pellet and capillary cell by taking examples of reduction of CuO/ZnO, reduction of PdO/ZrO_2 and methane oxidation over PdO_x/ZrO_2.[364]

Even a high throughput *in situ* XAS study is possible with a micro reactor, which allows up to ten samples to be measured simultaneously with an sensitive CCD detector as proposed by Grunwaldt et al.[369] A schematic diagram is shown in the Figure 49.

Bare, Gates, and co-workers designed two further highly interesting cells for *in situ* XAS studies that can operate (a) at high temperature (873 K) and pressure (14 bar)[370] and (b) under vacuum or in reactive atmospheres[371] as shown in Figure 50. The latter can also be used both in transmission as well as fluorescence mode up to a temperature of 573 K.

https://doi.org/10.1021/acs.chemrev.2c00495
Chem. Rev. 2023, 123, 379−444

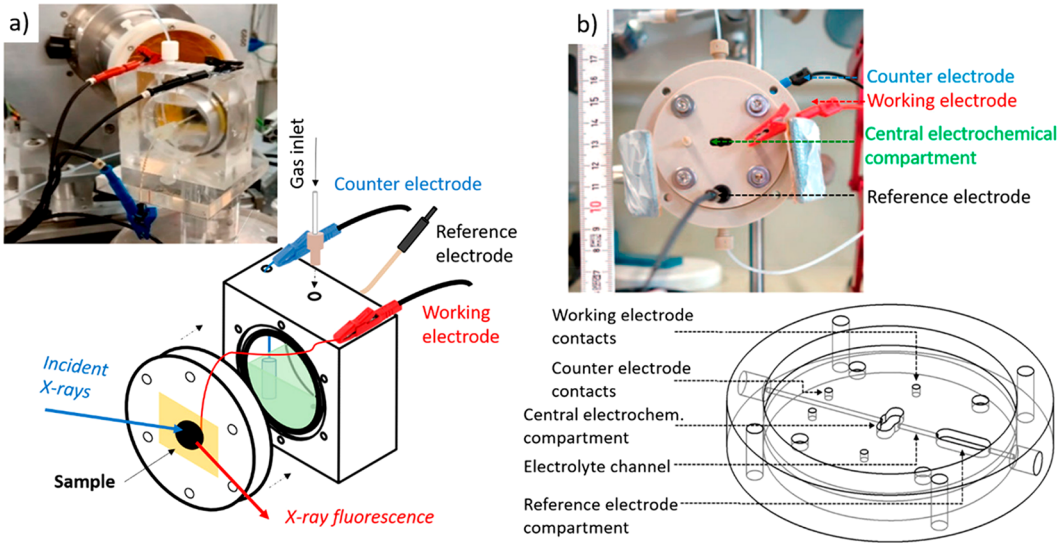

Figure 53. Schematic diagram of (a) a large volume electrochemical cell used for XAS measurements in fluorescence mode. (b) An electrochemical cell with continuous electrolyte flow through a syringe pump for XAS measurements in transmission and fluorescence modes. Adapted with permission from refs 126 and 378. Copyright 2020 American Chemical Society under Creative Commons CC-BY agreement. Creative Commons Attribution 4.0 License (CC BY, http://creativecommons.org/licenses/by/4.0/).

3.2.2. Cells for Liquid-Phase and Electrochemical Reactions. For liquid-phase reactions, time-resolved changes on the solid catalyst depend on liquid−solid mass transfer and diffusion of the reactants and products through the solid. Liquid phase reactions under pressure are usually carried out in an autoclave as the reactor. We have designed a continuous flow[372,373] and a batch autoclave reactor cell setup.[374] The cell has two different X-ray beam paths to probe both the liquid phase and the solid catalyst (see Figure 51).

Tao and his co-workers developed a dual reactor for *operando* XAS measurements of elements with low absorption edge energy in the fluorescence mode.[375] The dual reactor system contains a quartz reactor to perform high-temperature reactions up to 1223 K and a Kapton reactor that remains at a temperature up to 723 K for collecting data under the same gas flow through the reactor, as shown in the Figure 52. This cell has a very specific application for when two or more edges are studied at different energies.

There are many more cells designed by individual research groups and to discuss all of them is beyond the scope of this review. Our aim is to show various *in situ* cells that can fit in the field of SACs.

Also in electro-catalysis, several cells have been developed in the past decade for *in situ/operando* XAS measurements. There are certain limitations in finding the best compromise for electrochemical cells; for example, (a) bubble formation, (b) achieving a minimum mass transport limitations through electrolyte, (c) achieving high temperature, etc., that makes the cell design very challenging. Roldan Cuenya, Strasser, and their co-workers[376] designed a large volume single compartment cell with a three electrodes system where the sample acts as a working electrode (detais, cf. Figure 53a). The cell can be used for measurements in fluorescence mode. Our group[377] has recently showed with the help of *operando* XAS the structural changes of IrO_2 during OER reaction using similar cell designed by Binninger et al.[378] The combined approach of XAS together with MES showed that at a higher over potential (above 1.5 V) Ir−Ir interaction was observed during OER. In a different approach, a small compartment electrochemical cell with a layer of electrolyte was achieved by Schmidt and co-workers[378,379] as shown in Figure 53b. This cell can be used for measurements both in fluorescence and transmission modes.

3.3. Tracking the Active Sites of SACs for Gas−Solid Reactions

The interaction with gaseous species is often inducing changes for the catalytic active sites. As previously mentioned, possible scenarios for highly dispersed sites include electronic changes due to gas phase adsorbates, migration on the support material, agglomeration to clusters or nanoparticles, or even the redispersion into single atoms. Here we discuss different scenarios, what can happen to catalysts that are reported as single site catalysts in the literature.

3.3.1. Stable Single Atom Catalysts under Reaction Conditions. Datye and co-workers made a comparative study of Pd/Al_2O_3 and $Pd/La-Al_2O_3$ SACs taking CO oxidation as the model reaction and followed the change of local environment around the Pd atoms with the help of *operando* XAS (Figure 54). This study has inspired many others showing the need of *operando* investigation to understand the stability of SACs and reversibility under oxidizing and reducing atmosphere. Atomically dispersed Pd on La-doped alumina is a promising catalyst for CO oxidation, where *operando* XAS (taking quartz reactor) proved that the presence of intermingled atomically dispersed Pd and La ions on the γ-alumina supports plays a vital role during catalysis.[186] La-doped γ-alumina has been found to be a highly stable sinter-resistant material where the La^{3+} ions incorporate into a 4-fold hollow Al^{3+} vacant site as shown in Figure 54f−h.[380] In a different work, atomically dispersed Pd^{2+} over mesoporous Al_2O_3 was reported to be active and selective for the aerobic oxidation of allylic alcohols.[381] Datye and co-workers showed the temperature-dependent XAS study of the atomically dispersed Pd on La-doped alumina as more sinter-resistant than the Pd on alumina under CO oxidizing environment (mixture of 1% CO in He and 1% O_2 in He). Moreover, if sintered, the catalytic activity can be completely regenerated at 973 K on exposure to air.

https://doi.org/10.1021/acs.chemrev.2c00495
Chem. Rev. 2023, 123, 379−444

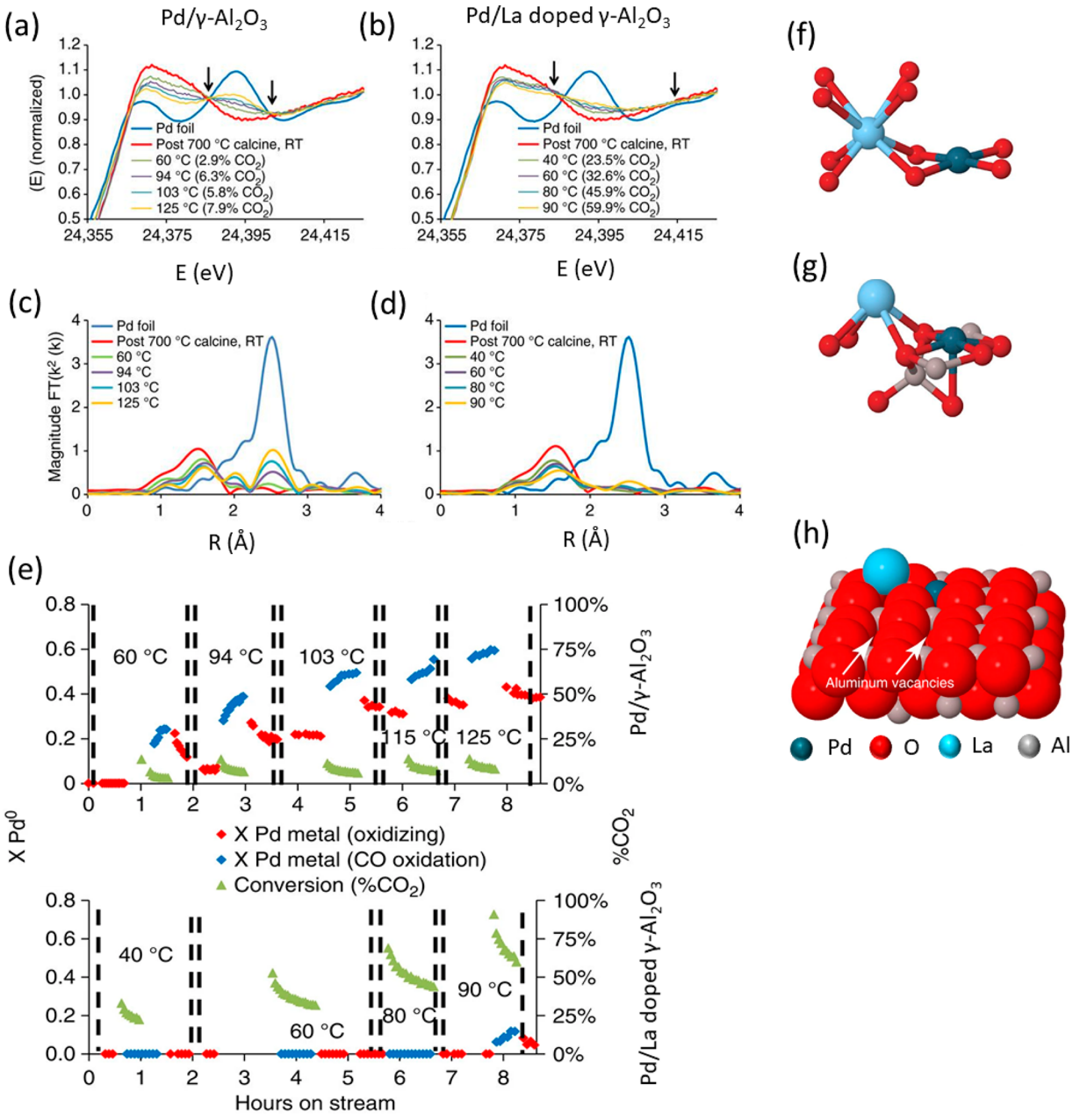

Figure 54. (a, b) Normalized XANES spectra at Pd K-edge and (c, d) k^2-weighted FT EXAFS spectra of Pd/γ-Al_2O_3 and Pd/La-doped γ-Al_2O_3. The spectra were collected at different temperatures under CO oxidizing conditions. (e) Fraction of Pd^0 formed under operating conditions of the catalysts Pd/γ-Al_2O_3 and Pd/La-doped γ-Al_2O_3. (f) Model of Pd over La-doped La_2PdO_4 structure, (g) model for EXAFS fit including the aluminum atom and, (h) space-filling model of γ-Al_2O_3 (100) surface. Adapted with permission from ref 186. Copyright 2014, Nature Publishing Group, a division of Macmillan Publishers Limited. All Rights Reserved.

According to the XANES spectra in Figure 54a, Pd^{2+} is rapidly reducing to Pd^0 under CO oxidation conditions for the Pd/γ-Al_2O_3 sample. In contrast, Pd was reported to stay in a positive oxidation state when supported on La doped γ-Al_2O_3 as shown in Figure 54b. Also, FT EXAFS data evidenced the formation of Pd−Pd bonds in Pd/γ-Al_2O_3 catalyst at 313 K. The Pd/La doped γ-Al_2O_3 was found to be active starting from 313 K. At this low temperature, no fraction of Pd^0 was observed. Based on these results, the authors claimed that Pd^+ is the active species during CO oxidation. The low-temperature CO oxidation activity and the sinter-resistant behavior of the Pd^{2+} SACs over La-doped alumina make this system highly attractive for the application as a catalyst in the exhaust-gas treatment. Despite both having single sites in the as-synthesized catalysts, Pd/Al_2O_3 and Pd/La−Al_2O_3 behave differently under the reaction conditions. The presence of La^{3+} ion is the key toward the higher stability of the Pd SACs. This kind of *operando* experiment is very helpful in understanding the change in local geometry of the catalytically active center.

Xin, Karim, and their co-workers performed *in situ* IR and *operando* XAS in combination with quantum chemical calculations to identify the active site of $Ir_1/MgAl_2O_4$ for CO oxidation reaction.[382] The authors found that the catalyst forms $Ir(CO)_2$ species under CO treatment, which transforms into a very stable Ir(CO)(O) complex upon introducing oxygen. The Ir(CO)(O) species was identified at reaction conditions with

https://doi.org/10.1021/acs.chemrev.2c00495
Chem. Rev. 2023, 123, 379−444

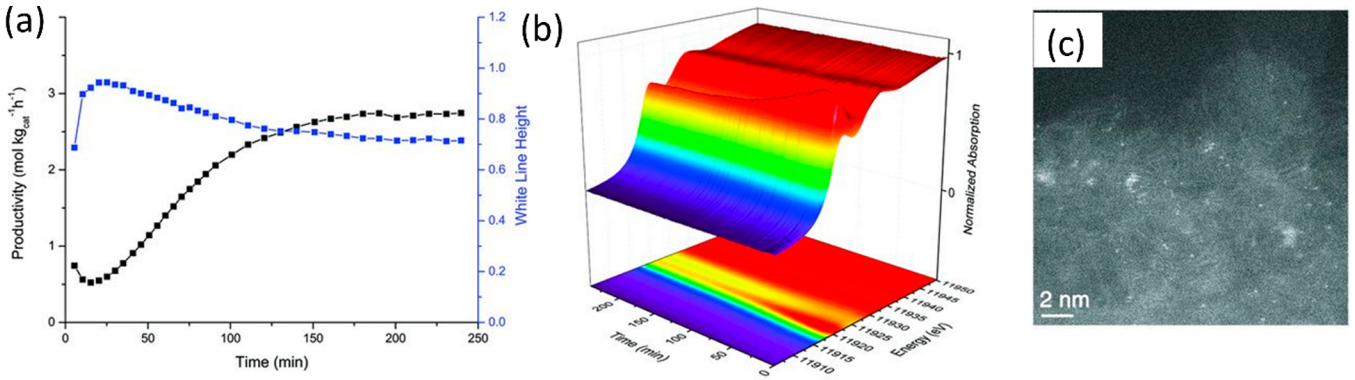

Figure 55. (a) Acetylene hydrochlorination productivity and white line intensity of a Au single atom catalyst supported on carbon as a function of time on stream with (b) corresponding XANES spectra at the Au L_3-edge. (c) Correlation of the catalyst productivity with the white line height indicates that under steady state conditions, both Au(I) and Au(III) species are present and participate in the reaction. Adapted with permission from ref 383. Copyright 2017, American Association for the Advancement of Science.

the help of DRIFTS studies and the HERFD-XANES spectra measured at the Ir L_3-edge. The CO band of Ir(CO)(O) species appeared at 2092 cm^{-1}, which is shifted from the Ir $(CO)_2$ species that appears around 2070 cm^{-1}. Also the HERFD-XANES spectra measured at the Ir L_3-edge shifted to higher energy due to partial oxidation of Ir even though no significant increase in the white line intensity was observed. The DFT calculations indicate that the O_2 activation step has a negligible barrier and the rate-determining step is the creation of a vacant coordination sphere at Ir single atom sites which plays important role during the reaction.

Hutchings and co-workers investigated the Au catalyzed acetylene hydrochlorination to identify the oxidation state and structure of the catalytically active Au sites.[383] The authors prepared highly dispersed Au supported on carbon catalysts via impregnation of a $HAuCl_4$-aqua regia solution (Au/C-AR), a $HAuCl_4$−HNO_3 solution (Au/C-HNO_3), and a $[Au(S_2O_3)_2]^{3-}$ solution (Au/C−S_2O_3), respectively. *In situ* XAS was performed using a fixed-bed polyimide (Kapton) microreactor inside a heater block. According to the XANES spectra using the normalized white-line intensity as fingerprint, Au/C-AR was claimed to mainly contain Au species in the oxidation state +1 and +3. The productivity of the as-prepared catalyst was reported to increase over the first hour on stream by a factor of 3, as shown in Figure 55a, suggesting strong structural transformations and the formation of the active sites under operating conditions. After the introduction of the reactants, a rapid white-line increase from 0.68 to 0.94 was observed indicating an oxidation to Au(III). Over time, the average oxidation state decreased (Figure 55b) suggesting the formation of more Au(I) sites correlating to an increase in catalytic activity. By recording XANES at the Cl K-edge, the same group investigated the ligand speciation during this induction period. The results indicated that surface chlorination is responsible for this behavior due to the formation of highly oxidizing Cl_2, which reoxidize Au(I).[384] EXAFS analysis was used to confirm the absence of Au−Au bonds and thus Au nanoparticles. By further evaluating the white-line intensity features of the of Au/C-HNO_3 and Au/C−S_2O_3 catalysts, the authors demonstrated that the presence of both, Au(I) and Au(III) ions are critical for high catalytic activity as shown in Figure 55c. Under steady state conditions, the ratio of Au(I) and Au(III) was found to be approximately 1.5 for all the catalysts. Based on these findings, a Au(I)−Au(III)-redox couple mechanism was proposed by the authors. DFT calculations supported this claim by proposing a catalytic cycle involving Au(I) and Au(III). The authors concluded that the heterogeneous Au catalysts active for acetylene hydrochlorination are analogs to soluble single site catalysts where the redox couple Au^I/Au^{III} is maintained by highly oxidizing Cl_2 and prevent agglomeration.

3.3.2. Agglomeration of Single Atoms to Clusters and Nanoparticles. In many of the conducted *in situ* studies, it was found that the stability of the SACs are highly dependent on the reaction conditions. As discussed in the previous example, the Pd single site can be regenerated under oxidizing environment at elevated temperature. Corma and co-workers investigated the stability of single atom Pt/zeolite catalysts using ETEM.[385] The noble metal single atoms seemed to reversibly form clusters under model CO oxidation conditions in the electron microscope. While a stoichiometric CO/O_2 mixture and temperatures up to 300 °C led to sintering, elevated temperatures, or the absence of CO favored redispersion of the Pt entities. Under water−gas-shift reaction conditions, the stability of the single atoms decreased further, and Pt clusters were observed for temperature over 100 °C.

Piccolo and co-workers reported a similar dynamic behavior of Pt single sites supported on γ-alumina for CO oxidation.[386] *Operando* XAS measurements of the powder catalyst at the Pt L_3-edge was used to monitor the Pt oxidation state and particle size under various reducing and oxidizing atmospheres. After incipient wetness impregnation and calcination at 300 °C, Pt^{m+} atoms ($m \geq 2$) were found in the sample. In this state, the Pt catalyst was poorly active. Under CO oxidation conditions, a gradual transformation to active $Pt^{\delta+}$ clusters was claimed based on EXAFS results, which showed an increase of the Pt−Pt scattering feature around 2.6 Å. This agglomeration process led to higher activity. As this was found to be irreversible, the sintering to even larger clusters cannot be circumvented.

The situation has been found different for the Pt/CeO_2 system where both redispersion to Pt single sites and cluster/particle formation could be achieved by applying different reaction conditions. In fact, due to the strong dependence on the reaction conditions, the reported catalytic activities e.g., for CO oxidation are fairly widespread as the catalyst pretreatment is one of the key aspects for this type of system. Matsumoto and co-workers reported the high dispersion of Pt over CeO_2 under oxidizing conditions and elevated temperatures.[387] By applying XAS and ETEM measurements, the authors observed Pt

https://doi.org/10.1021/acs.chemrev.2c00495
Chem. Rev. 2023, 123, 379−444

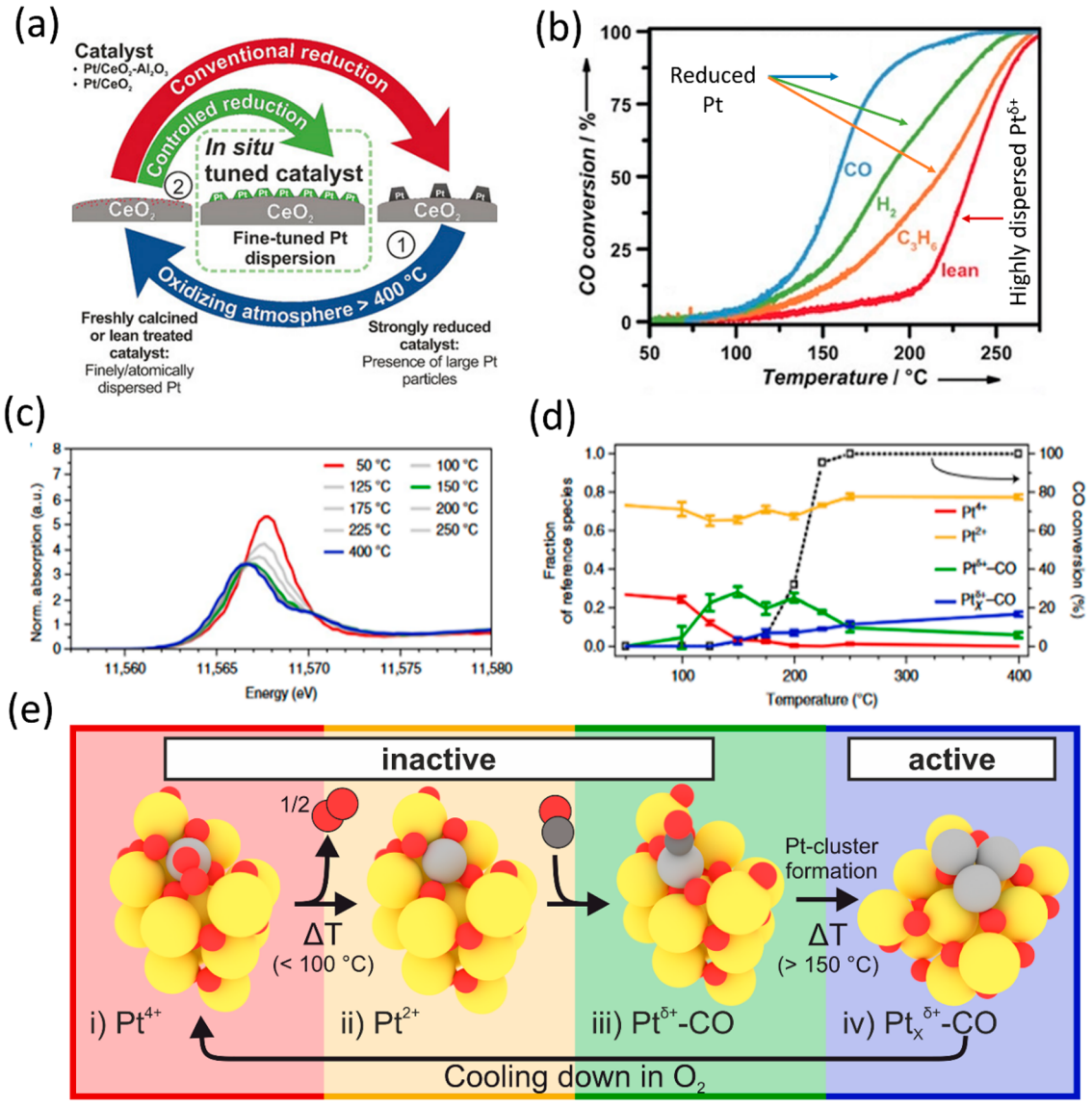

Figure 56. (a) Schematic representation of the Pt state in CeO_2 based catalysts depending on the pretreatment, (b) CO light-off curve after activation with different reductant (C_3H_8, H_2 and CO), (c) HERFD-XANES of a Pt/CeO_2 single catalyst at the Pt L_3-edge under CO oxidation conditions and (d) corresponding linear combination analysis using references extracted by MCR-ALS together with CO conversion. (e) Scheme showing structural changes and evolution of Pt single sites during CO oxidation. Adapted with permission from refs 53 and 390. Copyright 2017 Wiley-VCH Verlag GmbH and Co. KGaA, Weinheim. Copyright 2020 The Author(s), under exclusive license to Springer Nature Limited.

oxidation and redispersion of sintered 2 wt % Pt/CeZrY based car exhaust gas catalyst. Gänzler et al.[53] exploited this behavior to first redisperse Pt and then generate uniform Pt nanoparticles by short, reductive pulses (Figure 56a). The formation of these small nanoparticles enhanced the catalytic activity strongly—even compared to a conventional reduction—emphasizing the critical role of any pretreatments under different reductants (Figure 56b). Jones et al.[388] proved that also an atomic dispersion is possible at elevated temperatures such as 800 °C. As there is strong discussion on the reactivity of single Pt atoms, clusters and particles on ceria,[389] tracking the Pt state and fate in such prepared catalysts under reaction conditions is thus very important. This has also been the focus of work in our group in a recent study.[390]

For this purpose, an atomically dispersed Pt/CeO_2 catalyst was prepared by incipient wetness impregnation followed by a high-temperature calcination at 800 °C for 12 h under hydrothermal conditions. In agreement with previous studies,[391,392] EXAFS analysis showed the Pt ions to be preferably anchored at 4-fold hollow sites on the CeO_2 surface, which can be generated in the presence of Pt at elevated temperatures. For tracking the structure of Pt under reaction conditions, HERFD-XANES measurements at the Pt L_3-edge were performed (Figure 56c). Due to the higher energy resolution using fluorescence detection, more information on the catalyst structure and state can be derived from the white line slope, height, and Pt L_3-edge position than with conventional XANES. Analogously, HERFD-XANES was also used in combination with EXAFS to identify few-atom clusters and sintering of Pt depending on the exposed TiO_2 support facets.[393] For Pt single sites supported on CeO_2, it was observed that under CO oxidation conditions (1000 ppm of CO, 10% O_2), a distinct decrease of the white line is observed up to 150 °C with no significant CO conversion (Figure 56c). At higher temperatures, a shift of the white line toward lower energies was then accompanied by the onset of CO oxidation. To quantify the data

https://doi.org/10.1021/acs.chemrev.2c00495
Chem. Rev. 2023, 123, 379−444

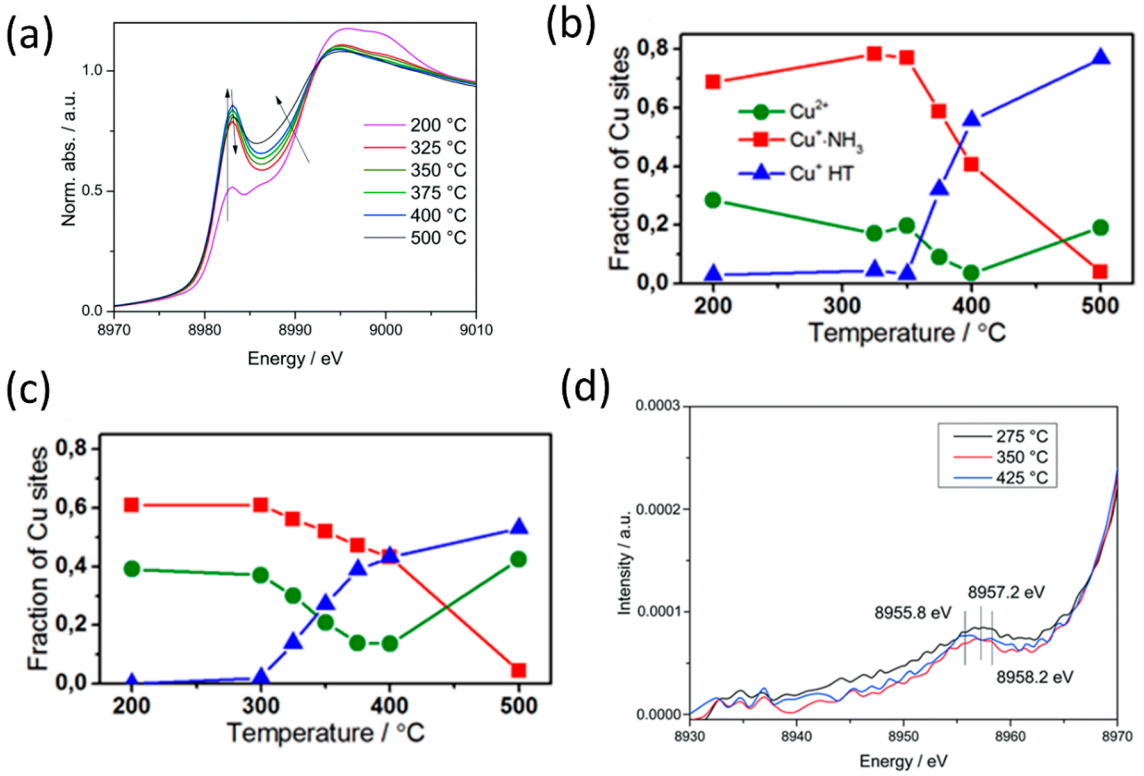

Figure 57. (a) *Operando* XANES spectra at Cu K-edge during NH_3 SCR reaction, (b, c) linear combination analysis of Cu species in a low and highly loaded Cu-SSZ-13 catalyst under NH_3 SCR conditions, respectively. For the fitting, Cu references were extracted by MCR-ALS, and (d) evolution of vtc XES spectra Kβ'' region at different temperatures for the higher loaded Cu catalyst. Adapted with permission from ref 58 under Creative Commons Attribution-NonCommercial 3.0 Unported License. Royal Society of Chemistry.

using a linear combination analysis (Figure 56d), four reference states were extracted using the multivariate curve resolution-alternating least-squares (MCR-ALS)[394] algorithm and assigned using experimental Pt reference spectra as well as calculated spectra based on models from DFT calculations. At low temperatures, Pt is anchored on the CeO_2 surface. Some oxygen can hereby reversibly adsorb/desorb with only minor changes to the local Pt geometry.[395] With increasing temperature, oxygen desorption seems to be favored and CO adsorption takes place. As Pt single atoms must restructure for adsorbing CO, the process occurs only at higher temperatures of around 100 °C. In this configuration the catalyst was still found to be inactive for CO oxidation. At 150 °C, a shift of the white line toward lower energies is observed and attributed to the formation of clusters. At the same time, CO oxidation set it. A schematic diagram of the species evolved during reaction and the species that were truly responsible for the catalytic activity and those that stayed as spectator are shown in Figure 56e. In contrast to the study of Piccolo and co-workers, for Pt single atoms on Al_2O_3, this agglomeration process is reversible. Pt clusters transformed back again to atomically dispersed species during cooling in oxidizing conditions. The single sites are an ideal starting point for tracking the changes. However, the catalytic activity occurred only upon Pt cluster formation. As they redisperse under certain conditions this underlines the need for more *operando* characterization in the future to unravel whether single atoms or clusters/particles are present under reaction conditions.

A prominent example for single site catalysis in emission control is Cu-SSZ-13, a Cu-Zeolite with chabazite structure that is very active in the selective catalytic reduction (SCR) of NO_x by NH_3 and has been studied by various groups.[58,396,397] We have used standard XAS in combination with valence-to-core XES to unravel the structure of the active Cu sites during SCR reaction. Interestingly, a dual-maxima of NO conversion profile with a dip activity around 275 °C was reported for the Cu-SSZ-13 catalysts, also known as a seagull profile. This indicates a transformation of the active species at 300 °C as shown in Figure 57a. As a starting point, two samples with 0.5 and 1.2 wt % were tested and characterized in the as-prepared state. Up to 300 °C, the SCR activity in terms of turnover frequency was 3 times larger for the higher loaded sample. At elevated temperatures the NO conversion aligns between the catalysts. In both low and high Cu containing samples, virtually identical $[Cu(H_2O)_x]^{2+}$ solvated species were found in the hydrated state. After dehydration, the 1.2 wt % sample was found to have more mono or bis(μ-oxo) dimeric Cu species. The isolated Cu species in the low loaded catalyst seemed to be inhibited by NH_3 at low temperatures. To unravel the role of these species in the reaction mechanism, a linear combination analysis was performed using references obtained by MCR-ALS. Using this approach, Cu^{2+}, $[Cu(NH_3)_x]^+$ and NH_3-free Cu^+ sites were shown to actively participating in the reaction. Compared to the low loaded sample, more Cu^{2+} was found for the 1.2 wt % catalyst, while $[Cu(NH_3)_x]^+$ was lower in the seagull-temperature region above 300 °C (Figure 57b,c). This was linked to a lower NH_3 inhibition and an easier reoxidation of reduced Cu sites during the reaction. Using *operando* vtc XES (Figure 57d), a temperature dependent change between two structures as a function of the NH_3 or NO presence could be identified for the highly loaded sample. Below the seagull region at 275 °C, a shift of the Kβ'' line to higher energies (8957.2 eV) was reported in the NH_3 oxidation mixture compared to a reference oxygen/

https://doi.org/10.1021/acs.chemrev.2c00495
Chem. Rev. 2023, 123, 379−444

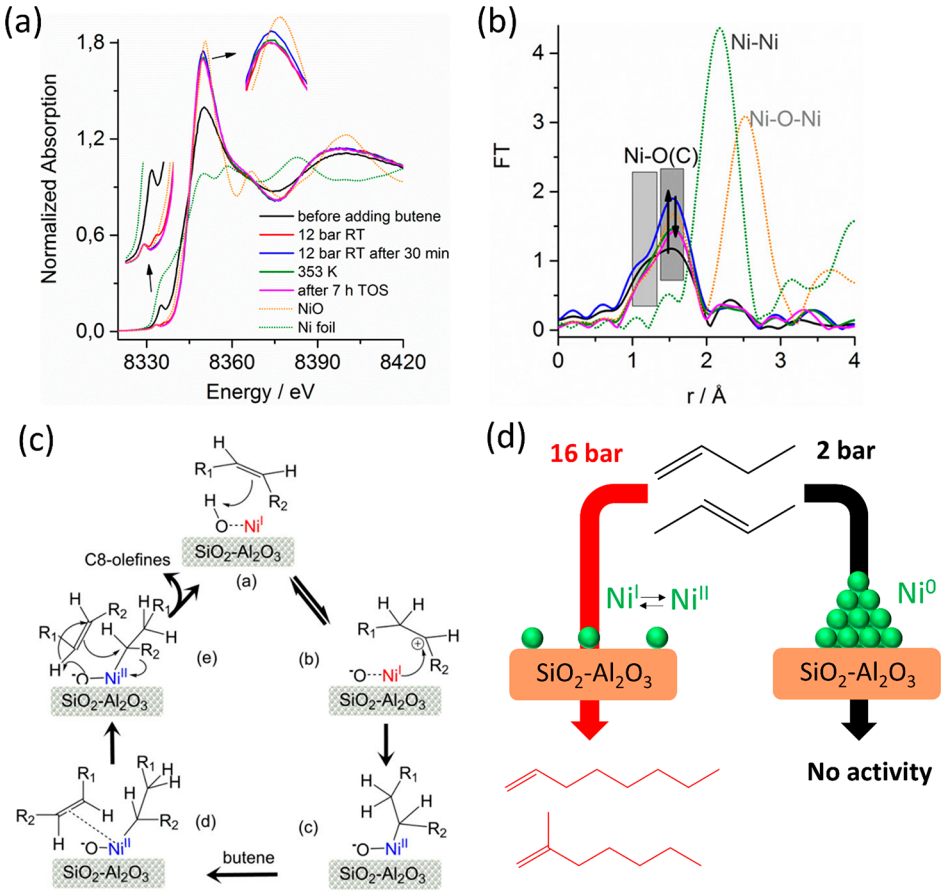

Figure 58. (a) *Operando* XANES and (b) FT-EXAFS of a Ni single atom catalyst for the butene oligomerization at the Ni K-edge. (c) Mechanism of butene isomerization and (d) schematics of the butene isomerization over Ni SACs and nanoparticle. Structural changes of the coordination geometry can be deducted by pronounced changes of the pre-edge peak of the XANES spectra. The exchange of ligands during the course of the reactions can also be seen in the FT-EXAFS spectra. Adapted with permission from ref 398. Copyright 2016 American Chemical Society.

water atmosphere (8956.9 eV). At higher temperatures of 350 and 425 °C, the oxidation and desorption of NH_3 led to a change in the intensity of the Kβ'' region yielding two maxima at 8955.8 eV and at 8958.2 eV.

Based on these results, we were able to identify the vicinity of Cu sites as the prerequisite for high SCR activity at low temperatures. The absence of dimeric Cu species in the low Cu containing sample made the sample prone to NH_3 inhibition and constrained the reoxidation step. At high temperatures, NH_3 desorption improves the mobility of Cu in the zeolite structure rendering them active for the SCR reaction. The formation of $[Cu(NH_3)]_x]^+$ that resembles molecular species and interconversion of Cu sites under the reaction conditions emphasizes the need for *operando* spectroscopic investigation to validate the structure−activity relationship.

3.4. Tracking the Active Sites of SACs for Liquid−Solid Reactions

The group of Brückner and co-workers[398] investigated the butene oligomerization by Ni single atoms (0.6 wt %) supported on Al_2O_3−SiO_2 using a combination of *operando* electron paramagnetic resonance and *in situ* X-ray absorption spectroscopy. Qualitative XANES characterization by comparison of the white-line intensity of the as-prepared catalyst with Ni^0 and NiO indicated the presence of monovalent Ni(I). Upon exposure to a raffinate containing various butane and butene isomers, an immediate increase in white-line intensity was observed at a temperature and pressure of 353 K and 12.4 bar, respectively. *In situ* XANES indicated a further, but slower oxidation to Ni(II) over the time. Simultaneously to the Ni oxidation, a transformation of the coordinating environment could be identified due to changes of the pre-edge feature. The authors speculate that in the first step, the split of the pre-edge peak at 8335 eV to one at 8336 and 8333.7 eV is induced by a ligand exchange of the 4-fold coordinated Ni species with butene molecules as shown in Figure 58a. This exchange of ligands was also observed by EXAFS analysis (Figure 58b). An introduction of butene led to decrease of a backscattering path at 1.93 Å, which the authors attributed to ligands from catalyst, while the coordination path of the species at 2.06 Å increased. After 30 min on stream, the pre-edge feature at 8333.7 eV vanishes, which was correlated to the formation of 6-fold coordinated Ni. EXAFS results furthermore confirmed the presence of single sites due to the absence of Ni−O−Ni or Ni−Ni interactions. Based on these observations, the authors proposed a reaction scheme with single Ni atoms being the active species as shown in Figure 58c and d. Finally, the authors conducted the same experiment at a lower pressure of 2 bar, which triggered the formation of Ni nanoparticles under reaction conditions and no catalytic activity has been observed over the Ni nanoparticles. The formation of Ni nanoparticles is highly suppressed at elevated pressure (∼12 bar), which confirms that the stability of SACs is highly dependent on the reaction conditions. This large difference in catalyst behavior underlines the use of operating conditions for deriving structure−activity correlations.

https://doi.org/10.1021/acs.chemrev.2c00495
Chem. Rev. 2023, 123, 379−444

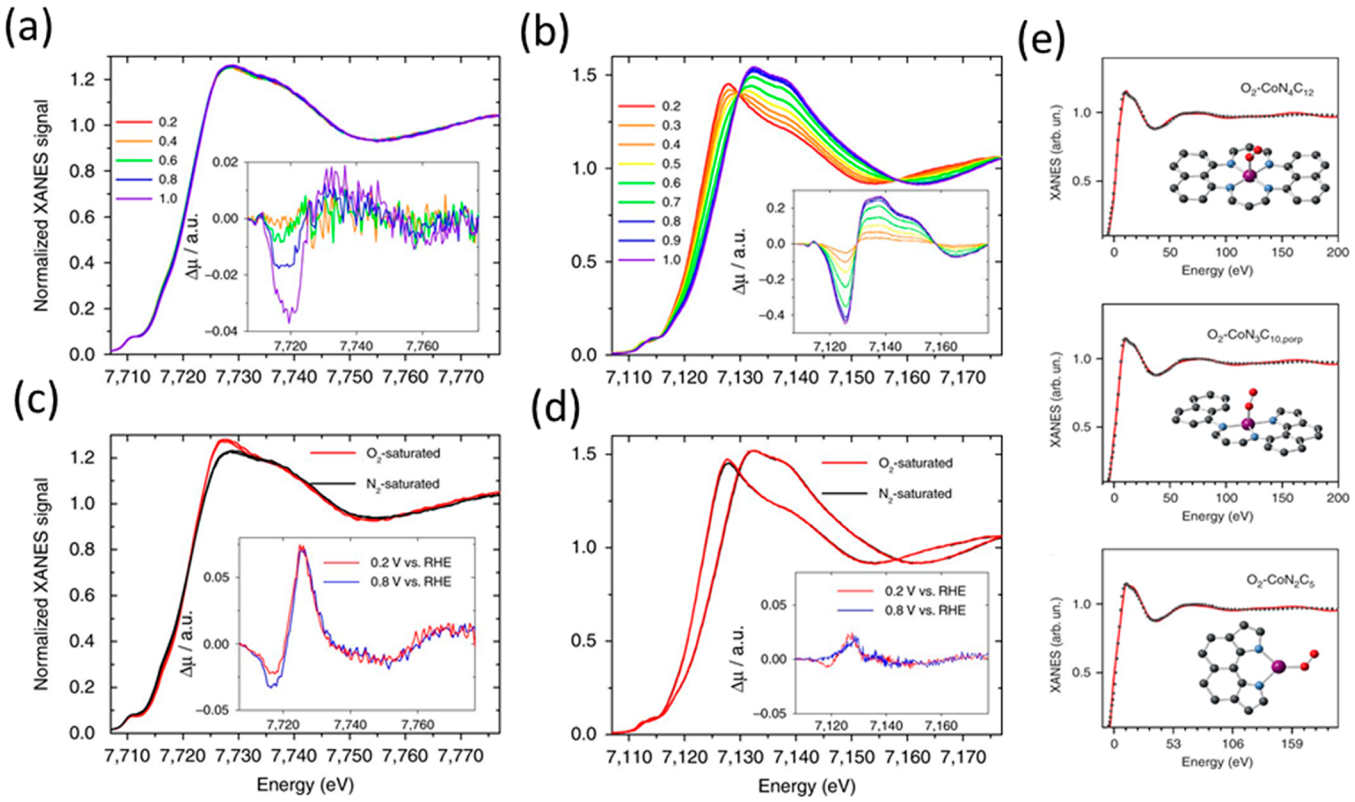

Figure 59. Normalized XANES spectra at different potential (a) at Co K-edge, (b) at Fe K-edge, (c) at Co K-edge in the presence of oxygen or nitrogen, (d) at Fe K-edge in the presence of oxygen or nitrogen, and (e) different model structures of Co−N−C material with O_2 bounded to Co center with the corresponding fitting. The spectra were measured in the presence of 0.5 M H_2SO_4. $\Delta\mu$ spectra in (a) and (b) are obtained by subtracting normalized XANES spectra at every potential to the spectrum measured at 0.2 V potential versus RHE. $\Delta\mu$ spectra in (c) and (d) are obtained by subtracting normalized XANES spectra recorded in the presence of O_2 to the one recorded in N_2. Color code in (e): purple (cobalt), red (oxygen), blue (nitrogen), and gray (carbon). Adapted with permission from ref 401 under Creative Commons CC BY license http://creativecommons.org/licenses/by/4.0/.

Catalytic carbon−carbon coupling via the Heck reaction was the focus of the study of Perrson, Martin-Matute, and Zou et al.[399] In their previous work,[400] the authors reported an unexplainable rapid catalytic deactivation for Pd single atoms supported in a metal organic framework. Therefore, *operando* XAS together with powder X-ray diffraction were employed to identify the structural changes during the reaction. XANES and EXAFS experiments conducted at the Pd K-edge indicated strong changes in the chemical environment already upon exposure to the reaction mixture exchanging Cl^- for N-based ligands. The formed short-lived Pd^0 species started to oxidize upon heating. Up to 80 °C, Pd was found to be still anchored by the MOF ligands as isolated Pd^{2+} species close to the state in the precatalyst as observed in the XANES spectra. As indicated by the formation of Pd−Pd (at 2.65−2.67 Å) and Pd−Cl bonds (2.35−2.42 Å), small (approximately 10−20 atoms) Pd nanoclusters partly covered with chloride ions were reported to form at 90 °C. This Cl^--poisoning was found to be responsible for the decreasing catalytic activity triggered by the consumption of available reagent. Based on these insights on the deactivation process gathered by *operando* XAS, the authors proposed adapted reaction conditions to prolong the lifetime of the noble metal catalyst. Our group in the past also investigated the Pd catalyzed Heck reaction with *in situ* QEXAFS studies in the subsecond time scale and found that supported Pd particles corrode and the formed molecular Pd species were the catalytically active center.[46]

Even though there has been quite some examples of SACs that are claimed to be highly active, many studies lack *in situ*/*operando* characterization. Leaching of atoms to the liquid phase forming homogeneous complexes can often lead to exceptional activities as outlined in the Figure 4. There are also challenges such as mass transfer limitations, diffusion limitations and one has to take it into account these parameters while conducting *in situ*/*operando* studies.

3.5. SACs for Electrochemical Reactions: A Liquid−Solid Interface

3.5.1. Oxygen Reduction Reaction (ORR). In a study on Fe (Fe−N−C) and Co (Co−N−C) SACs for oxygen reduction reaction (ORR), Zitolo et al. identified the active sites during catalysis with the help of *operando* XAS.[401] Co and Fe SACs were prepared over N-containing carbon material via pyrolysis. With the combined study of XAS, magnetic susceptibility measurements and DFT calculations, they showed the detailed structure and electronic state of the SACs. The *operando* XANES spectra measured at different potentials from 0.2 to 1.0 V did not show any significant changes at the Co K-edge, as shown in Figure 59a and c. However, there are changes (shift toward higher energy) at the Fe K-edge under similar reaction conditions, as shown in Figure 59b and d. According to their explanations, the changes toward higher energy in the Fe-edge of the Fe SACs are found to be associated with both oxidation state of iron as well as low to high spin crossover, as explained elsewhere.[402,403] The presence of O_2 clearly shows an influence on the Co SACs ($\Delta\mu$ spectra in

https://doi.org/10.1021/acs.chemrev.2c00495
Chem. Rev. 2023, 123, 379−444

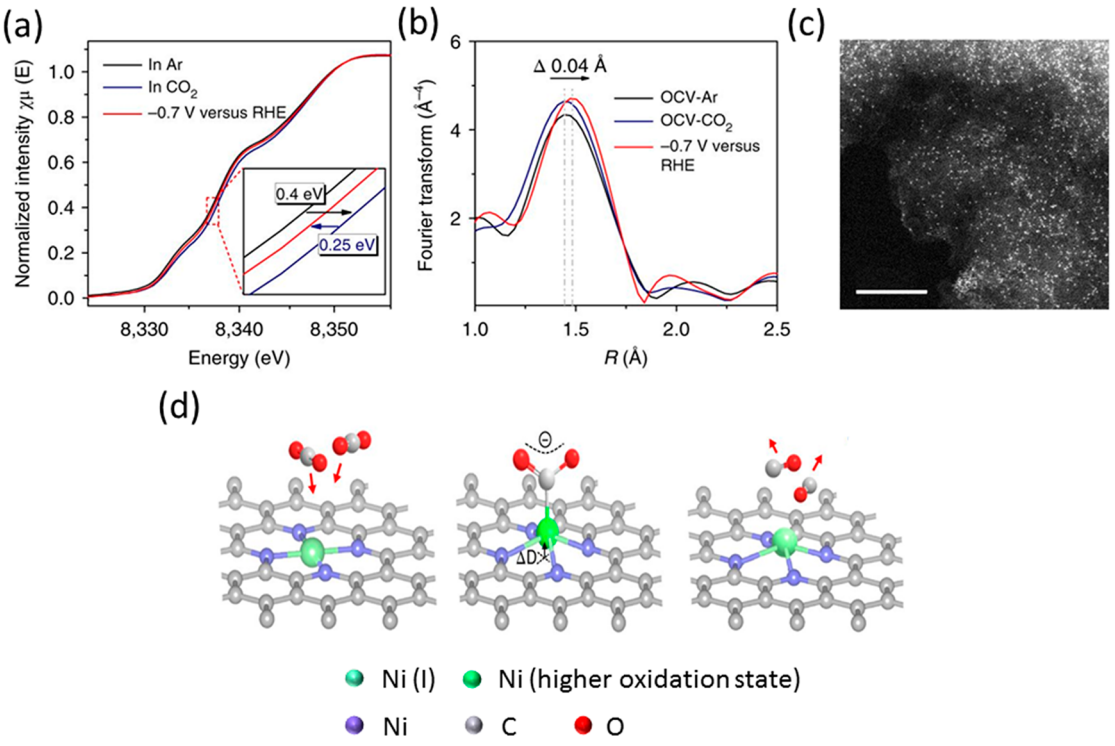

Figure 60. (a) Normalized XANES spectra at Ni K-edge at different biases in an aqueous solution of 0.5 $MKHCO_3$ at room temperature in the presence of 1 atm Argon or CO_2. The enlarged spectra are shown in inset, (b) FT k^3-weighted EXAFS spectra, (c) HAADF-STEM image of Ni_1 supported on N-doped graphene, and (d) structural changes in the Ni atom during the CO_2 reduction. ΔD is the displacement of Ni atom out of the plane when it binds to CO_2 and forms a higher oxidation state due to charge transfer. The applied potential was −0.7 V versus RHE. The scale bar in the micrograph is 5 nm. Adapted with permission from ref 406. Copyright 2018, Springer Nature.

Figure 59c) due to the weak interaction of oxygen with cobalt, whereas Fe was not affected at all. The XANES simulation performed at the Co K-edge fits well with the experiment when the Co atom is considered to bind with four nitrogen in a square planar CoN_4C_{12} structure at a distance of 1.96−1.97 Å with an additional O_2 molecule at a distance of 2.23 Å as shown in Figure 59e.

The XANES spectra of the Fe−N−C catalyst point toward the existence of a Fe−O bond, oxygen being sourced from either O_2 or H_2O whereas for the Co−N−C catalyst, the Co center being less oxophilic, the Co−O formed only in O_2 saturated electrolyte. DFT calculations revealed that the O_2 adsorption energy of the Co SACs (−0.8 to −1.2 eV) is significantly smaller than that of the Fe SACs (−1.8 eV). This is in line with the experimentally observed redox peak around 0.75 V (vs RHE) for Fe SACs and 1.25 V (vs RHE) for Co SACs for the ORR. The authors claim that this was the first direct *operando* evidence of adsorption of molecular oxygen on the Co−N−C catalyst, which was studied by other groups in a different system.[404,405] This kind of detailed study shows correlations for the ORR activity with those that has been previously studied on molecular M-N_4 macrocycles[405] and would certainly help in rational design of this type of catalyst and optimizing other electrocatalytic systems. The study here shows that the SACs are highly stable within the soft C and N containing matrix and even able to bind molecular oxygen during ORR and *operando* XAS has been a guiding tool to follow the structural changes around the Co atom.

3.5.2. CO_2 Reduction Reaction (CO_2 RR). Atomically dispersed Ni (I) with a d^9 electronic configuration has been identified for the electrochemical reduction of CO_2 to CO at a mild overpotential of 0.61 V as reported by Zhang, Liu, and co-workers.[406] The authors performed *operando* XPS and XAS measurements on atomically dispersed Ni stabilized in the N-containing (A-Ni-NG) and S-containing (A-Ni-NSG) graphene to understand the structural changes of the isolated Ni center during catalysis. The *operando* XAS study revealed that the atomically dispersed positively charged low-valent Ni is the catalytically active center for electrochemical CO_2 reduction. As shown in Figure 60a, the XANES spectra at Ni K-edge are shifted by 0.4 eV to higher energy under the applied potential (−0.7 V vs RHE) when the aqueous solution is saturated with CO_2 in the presence of $KHCO_3$ as an electrolyte. This means that the Ni is in a higher oxidation state due to the interaction of the Ni with the CO_2 molecule that could possibly lead to a charge transfer from Ni (i) to the carbon atom. The delocalization of the unpaired electron in the Ni $3d_{x^2-y^2}$ and the charge transfer to the C 2P orbital of CO_2 can give rise to $CO_2^{\delta-}$ species.[407] The FT EXAFS spectra in Figure 60b shows a shift of 0.04 Å and an increase in the intensity of the Ni−N first shell when the solution is saturated with CO_2 compared to that of Ar. According to the authors, the shift in bond distance is associated with displacement of the Ni atom above the plane and the intensity difference is related with the extra coordination to C atom of the CO_2 molecule. During the electro catalytic process, the Ni K-edge spectra are shifted back to the lower energy which indicates the recovery of low valent Ni after the redox cycle. The authors claimed that the Ni SACs retained their structure and do not agglomerate to form clusters or nanoparticles under the operating potential. The study here helps in understanding the structural change around the Ni center for a highly demanding electrochemical CO_2 reduction,

https://doi.org/10.1021/acs.chemrev.2c00495
Chem. Rev. 2023, 123, 379−444

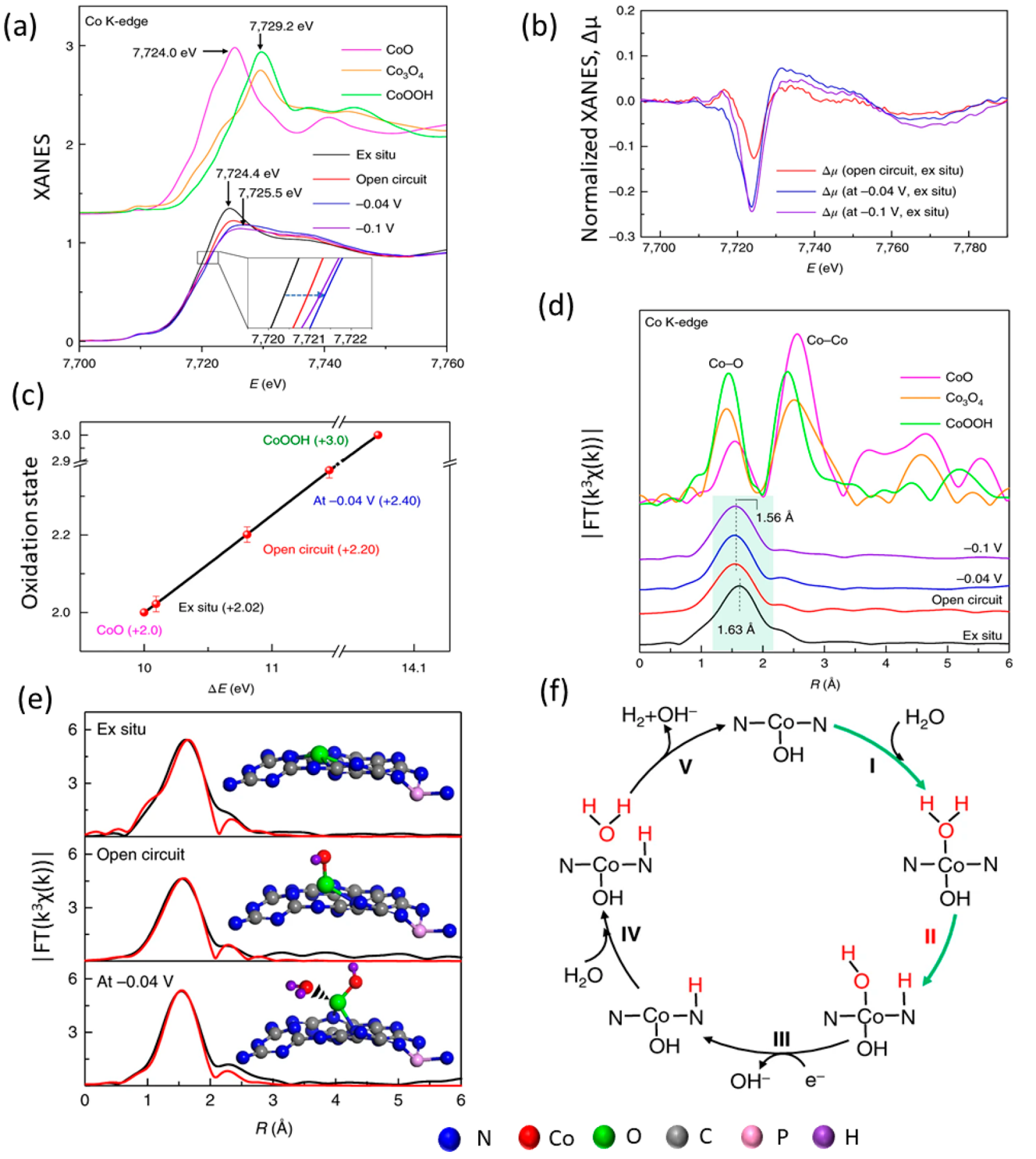

Figure 61. (a) *Operando* XANES spectra at the Co K-edge of Co_1/PCN at different applied voltages (−0.04 V, −0.1 V and *ex situ*) during electrocatalytic HER together with the references CoO, Co_3O_4 and CoOOH. Inset is the magnified pre-edge XANES region, (b) normalized difference in XANES spectra, (c) average oxidation states of Co from the XANES spectra with standard deviation from 3 independent measurements, (d) FT k^3-weighted EXAFS spectra (shaded region shows the variations in the peak and intensity), (e) 1st shell fitting of the EXAFS spectra with corresponding geometric configurations, and (f) proposed mechanism of HER. Adapted with permission from ref 414. Copyright 2018, Springer Nature.

which can be further extended to the other established system.[408−410]

Jiang et al. showed Ni single atoms in graphene nanosheets for CO_2 reduction where *in situ* XAS analysis confirmed that Ni atoms bearing positive charges are the active centers during catalysis.[411] Cobalt single atoms with $Co-N_5$ site anchored on hollow N-doped porous carbon sphere are shown to be highly active for CO_2 reduction reaction. The *in situ* XAS study at Co K-edge suggests an increase in the oxidation state of cobalt under reduction potential, proving that the CO_2 electrochemical reduction is dependent on the Co electronic state.[412] Another study led by Genovese et al.[413] showed that the single Fe (II) site

https://doi.org/10.1021/acs.chemrev.2c00495
Chem. Rev. 2023, 123, 379−444

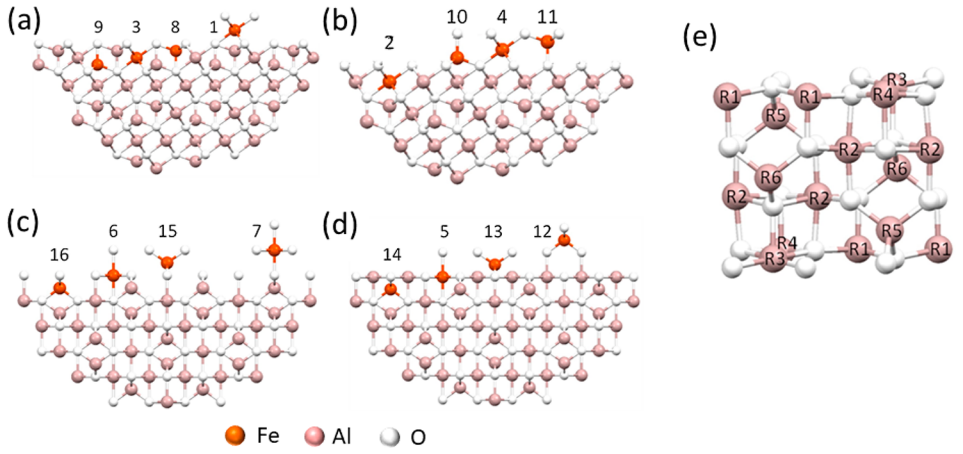

Figure 62. Location of Fe atoms replacing Al in different sites on (a) $(222)_1$ surface, (b) $(222)_2$ surface, (c) $(400)_1$ surface, (d) $(400)_2$ surface of the cleaved Al_3O_4 crystals, and (e) the Al sites (R1-R6) that can be replaced by Fe in the $Al_{16}O_{24}$ unit cell. Adapted with permission from ref 176. Copyright 2016 Elsevier B.V. All rights reserved.

coordinated by nitrogen is highly active for the electrochemical reduction of CO_2. The *operando* XAS study performed at Fe K-edge shows the reversible redox character of the *Fh*-FeOOH nanostructures on N-doped carbon and the structural changes under the applied potential.

3.5.3. Hydrogen Evolution Reaction (HER). Yao, Wei and co-workers identified the active sites of Co SACs over carbon-based material during the electro catalytic hydrogen evolution reaction (HER).[414] The single atoms of Co were immobilized by forming a structurally uniform Co_1-N_4 unit in the framework of phosphorized carbon nitride (PCN). *Operando* XAS experiments were conducted to understand the dynamic behavior of the Co atoms in an alkaline solution. The results revealed that there was a formation of high valent OH-Co_1-N_2 moiety when the Co_1-N_4 site interacts with the KOH electrolyte as shown in Figure 61. The formation of this Co moiety further allows a water molecule to adsorb and create an H_2O-(OH-Co_1-N_2) intermediate, which promotes the dissociation of water. *Operando* XAS spectroscopy was performed in an electrochemical cell where the working electrode was made of porous carbon cloths together with the catalyst incorporated in it. Compared to the *ex situ* sample, the catalysts under applied potential shows a shift of the absorption edge toward higher energy by 0.5 eV accompanied by the broadening of the peak. This means that there is an increase of the Co oxidation state (also observed when the applied voltage increase from −0.04 to −0.1 V) as shown in Figure 61a. The variation in the normalized XANES spectra is more visible in Figure 61b. From the fitted average oxidation states of Co from the XANES region in Figure 61c, it is clear that the *ex situ* sample has oxidation state close to +2, which is also consistent with the data obtained from the XPS results. However, under an open circuit and at an applied potential of −0.04 V, the oxidation state increases to +2.2 and +2.4, respectively.

The FT EXAFS spectra, as shown in Figure 61d indicate that the first shell Co−O/Co-N peak shifts from 1.63 to1.56 Å (assuming that the choice of E_0 values are consistent) on increase in applied reduction potential and also the features of the oscillations after the first shell are slightly different. For further quantitative analysis, the researchers performed EXAFS fitting for the first-shell and found that the *ex situ* sample is coordinated to four N atoms, which under open-circuit changes to two N and one O based on their best fit results. Upon an applied reduction potential of −0.04 V, there is an additional O coordination which remains in the same distance on further increase in reduction potential to −1 V. The fit and the proposed structure from DFT calculations are shown in Figure 61e. Based on these results and together with theoretical calculations, the researchers proposed a mechanistic pathway as depicted in Figure 61f. The high oxidation state of Co SACs facilitates a strong charge-transfer occurring on HO-Co_1-N_2 moiety, which boosts the water dissociation step and hence the alkaline HER activity. The authors did not observed any formation of agglomerates during the reaction. This study here provides insights into an electrocatalytic reaction where the reaction medium creates a new type of active species and its adsorption behavior which can be helpful to understand other electrochemical processes under the true reaction conditions.

SACs are proven to be stable for many electrochemical reactions under applied potential. However, in many cases dynamic behavior (restructuring of the active center) has been observed which indicates that *in situ*/*operando* spectroscopic investigation is required to claim their long-term stability

4. DFT-ASSISTED XAS STUDIES ON SACS

4.1. Supported over Bulk Metal Oxides

DFT calculations have proven to be a very powerful tool of solid catalysts in finding trends in reactivity, screening stability, catalytic activity, and identification of active sites.[415−417] Moreover, DFT-based models are becoming powerful in predicting and fitting unknown molecular structures, especially in the field of SACs, that can have multiple single atom host sites. The isolated active metal centers show a dynamic behavior generating new active centers during catalysis. Interpretation of XAS data is typically based on iterative refining of a structural model until a calculated spectrum matches the experimental one. The success of this iterative refinement process heavily depends on the initial structural model. Traditionally starting models are constructed as a combination of one or several coordination shells taken from the well characterized bulk structures of metals, alloys, simple and mixed metal oxides, etc., which are found in crystallographic databases. SAC structures, however, have often markedly different coordination environments compared to the bulk reference compounds which leads to difficulties in obtaining reasonable fits with models based on

https://doi.org/10.1021/acs.chemrev.2c00495
Chem. Rev. 2023, 123, 379−444

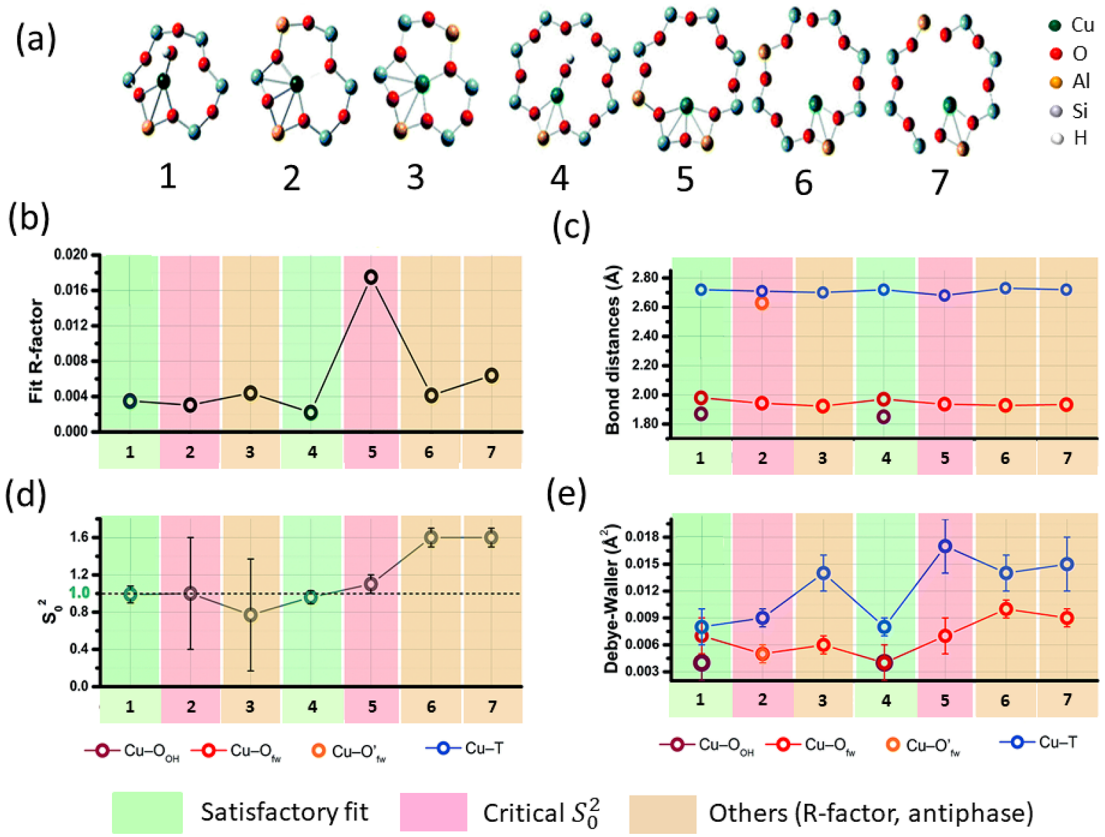

Figure 63. Summary of fitting parameters obtained from EXAFS equation for isolated Cu (II) site in Cu-SSZ-13 with the DFT optimized model structures representing (a) model structures (b) goodness of fit R factor values, (c) average bond distance, (d) amplitude reduction factor S_0^2, and (e) Debye−Waller factor. Different color code indicates the acceptability of the fit. The *X*-axis represents the number that corresponds to different model structures represented in (a). Adapted with permission from ref 421 under Creative Commons Attribution 3.0 Unported License.

bulk crystal structures. To overcome these challenges SAC structural models based on DFT-optimized structures were successfully used. Apart from allowing to obtain better fits, the DFT-assisted EXAFS analysis additionally enables more precise identification of the exact location of the single atoms among several potential hosting sites. Some of the examples have been discussed already in this review.[235,305,401] While DFT-optimized models are useful but not always strictly necessary in the case of EXAFS fitting, they are indispensable if XANES, XES, and RIXS data need to be analyzed and modeled.[122,418]

One prominent example in this direction has been the identification of the structure of Fe species on γ-alumina studied by Boubnov et al.[176] From an EXAFS fitting with 24 different DFT optimized models, it was found that the trivalent Fe atoms are coordinated to 4−5 oxygen atoms and located in the octahedral sites of γ-alumina both in monatomic and biatomic form. The model structures considered in the fitting process were anchored on the (222) and (400) surface in the Al_3O_4 crystal and the $Al_{16}O_{24}$ unit cell, as shown in Figure 62. Out of all the possible models, Fe at 1, 3, 6, 7, R2, R3, and R4 showed the best fit where Fe is in the octahedral position. Further analysis of the pre-edge XANES region suggests that model R4 is less likely, and the analysis of the higher shells shows a significant misfit for the model R3. Accordingly, the possibility of Fe being in the tetrahedral site is quite negligible. This kind of study demonstrates the potential in solving the identification of the structure of single sites based on a combination of EXAFS, XANES, XES and RIXS spectra with the help of DFT optimized model systems.

In a further work, Sarma et al. showed a systematic DFT-assisted XAS study on SACs of five different metals (Pt, Pd, Ir, Rh, and Ru) supported over MgO.[419] In this work, up to 14 DFT optimized model structures were selected based on the confinement of the single atom in the MgO lattice and it was found that the single atoms prefers to stabilize in the higher confinement regime. The single atoms preferred to be in highly coordinated step-edges or subsurface positions. Chen et al. identified catalytically active cationic Pt single site over MgO with DFT calculation combined with automated analysis of EXAFS spectra.[420]

4.2. Confined in Zeolite Framework

Lamberti and his co-workers[421] identified the nature and location of isolated Cu sites with the help of a DFT-assisted XAS study on activated Cu-SSZ-13 catalysts, which are highly active for selective catalytic reduction (SCR) reaction.[37] Different types of Cu species have been confirmed at different reaction conditions by *in situ* FTIR and XAS studies. XANES simulations and an EXAFS fitting were performed on a wide variety of optimized DFT structures to obtain a possible model with satisfactory free parameter values. A graphical presentation is shown in Figure 63. The fits were performed on the EXAFS spectra collected at Cu K-edge at a temperature of 673 K under O_2.

From Figure 63, Cu (II) single sites with three coordination numbers (model 1, 2, 4, 5) seem to result in acceptable fitting parameters. Among these models, 1 and 5 showed a very high value of Debye−Waller factor for the Cu-T path and hence the

https://doi.org/10.1021/acs.chemrev.2c00495
Chem. Rev. 2023, 123, 379−444

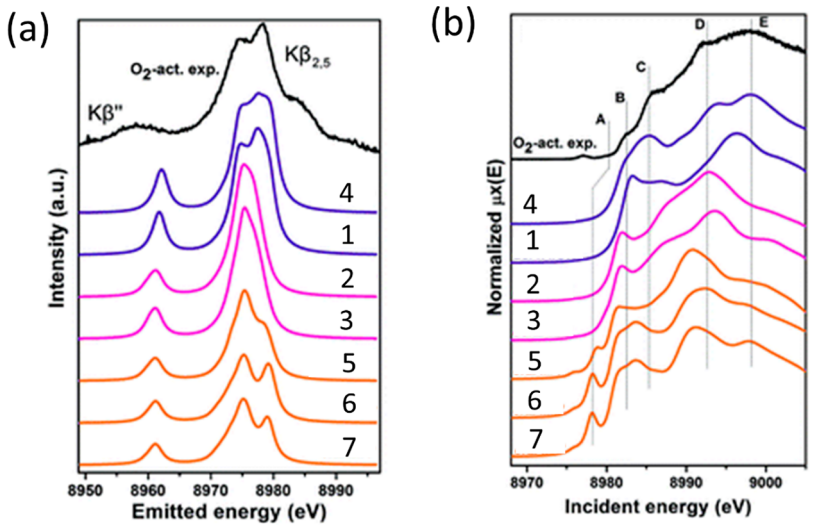

Figure 64. Experimental (black curve) and simulated (a) XES and (b) HERFD-XANES spectra of different DFT optimized model structures at the Cu K-edge. The name corresponds to the same models shown in Figure 63. A, B, C, D, and E represents different features present in the experimental XANES spectra. Adapted with permission from ref 421 under Creative Commons Attribution 3.0 Unported License.

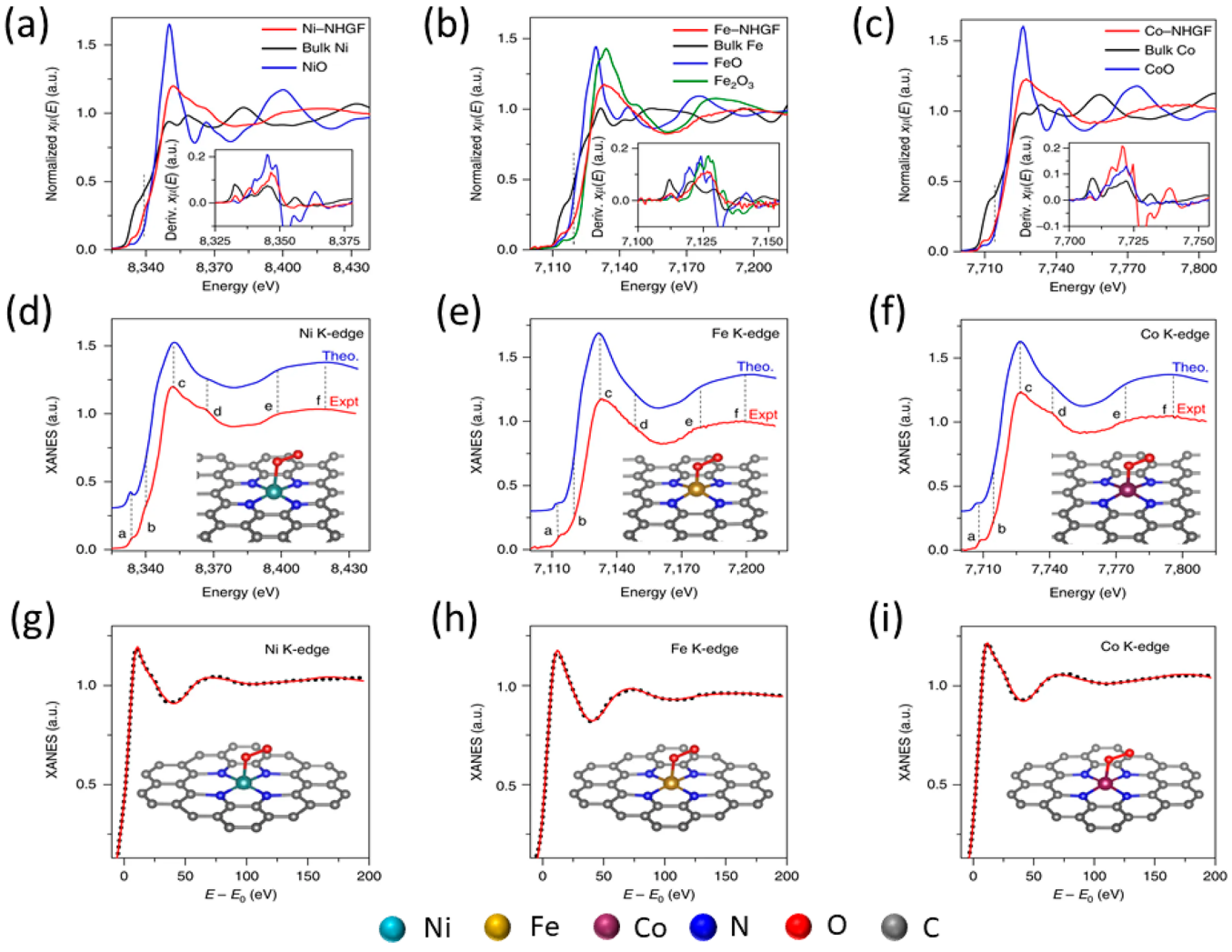

Figure 65. (a–c) Experimental XANES spectra at the K-edge of Ni, Fe, and Co in the N-doped graphene framework together with the pure metal and oxide as reference, (d–f) comparison between the experimental and simulated XANES spectra, and (g–i) comparison between the experimental curve and the best fitted curve. Adapted with permission from ref 425. Copyright 2018, The Author(s).

https://doi.org/10.1021/acs.chemrev.2c00495
Chem. Rev. 2023, 123, 379–444

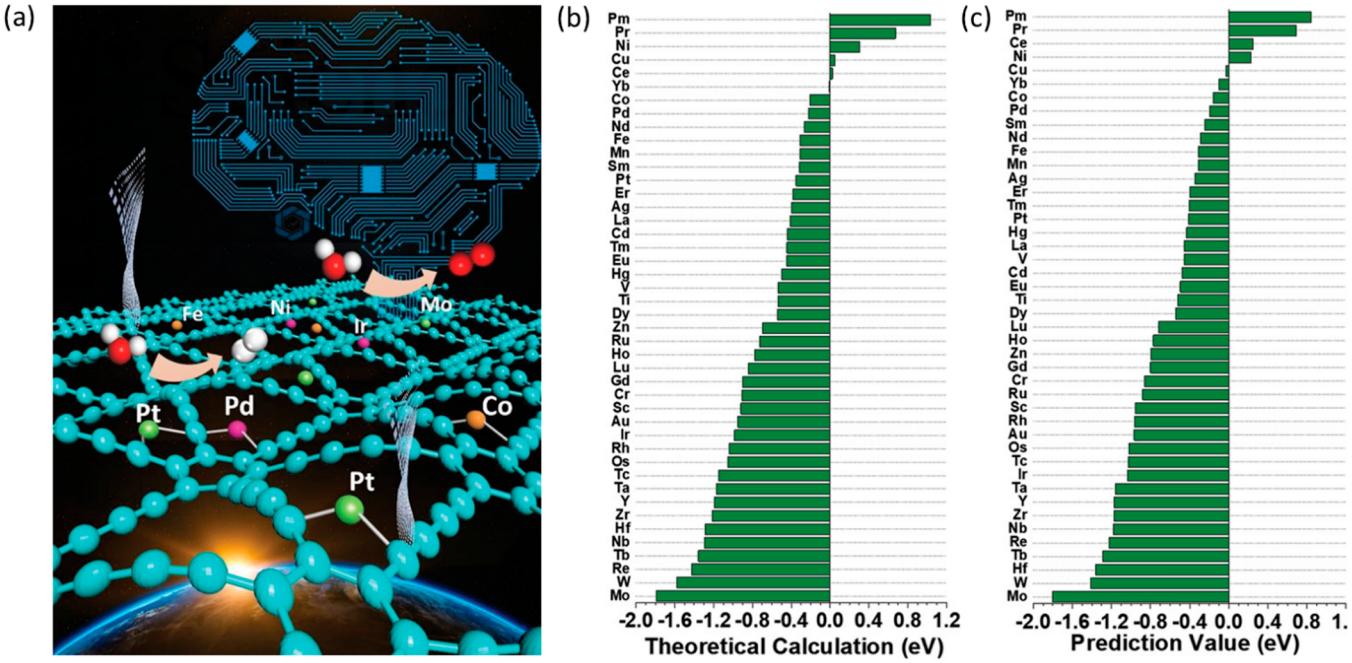

Figure 66. (a) Schematic diagram of introducing ML on single atoms over graphdiyne for HER, (b) theoretically calculated values of H-adsorption energies, and (c) predicted values of H-adsorption energies of different metals. Adapted with permission from ref 429. Copyright 2020 WILEY-VCH Verlag GmbH and Co. KGaA, Weinheim.

acceptable structures are 4 and 2. Furthermore, XANES simulations were carried out on high energy resolution fluorescence detected (HERFD) XANES spectra at the Cu K edge, which confirms that the majority of the Cu (II) species are in the form that represents the model structure 4, which was further confirmed by simulation of the XES spectra. The simulated XANES and XES spectra are shown in Figure 64. Both Giordanino et al.[422] and Zhang et al.[423] showed that DFT simulated XANES spectra are able to differentiate between the local environments of isolated Cu^{+} with a linear configuration and Cu^{2+} with a square planar configuration inside SSZ-13. Our group has studied the NH_3−SCR reaction over Cu-SSZ-13 with the help of *operando* HERFD-XAS and vtc XES at the Cu K-edge.[424] The structural evolution of Cu-SSZ-13 catalyst was studied under 12 different relevant SCR conditions. The experimental spectra were further simulated using reference compounds and DFT calculations. Strong adsorption of NH_3 on Cu^{2+} was observed which reacted with NO from the gas phase and finally Cu^{+} reoxidizes slowly in the presence of O_2. The reaction mechanism is found to be quite different than SCR reaction over Fe-ZSM-5.[132]

Recently, Pankin et al.[108] carried out DFT-assisted EXAFS simulations on the same system and performed a wavelet transformation (WT) analysis for the identification and visualization of atomic distributions, which are an advanced step for confirming the nuclearity of identical species as discussed earlier in the section 1.3. Only the XANES simulation shown in Figure 64 was not able to differentiate the Cu nuclearity.

For single atom catalysts confined in zeolite framework, the complementary interpretation of XANES and EXAFS data based on models from DFT calculations is highly desirable to substantiate mechanistic insights and follow the structural dynamics.

4.3. Inside Carbon-like Host Materials

As discussed previously, Zitolo et al.[305,401] showed, with the help of XANES and EXAFS simulations, how the Fe and Co single atoms in porphyrin-like structures (MN_4C_{12}) or pyridinic like structures (MN_4C_8) bind to oxygen. However, these moieties are challenging to incorporate in a graphene matrix. In an alternative approach, Fei et al.[425] synthesized single Fe, Ni, and Co atoms embedded in N-doped holey graphene frameworks via the hydrothermal treatment of graphene oxide with metal precursors and characterized them with various techniques. The DFT-assisted XANES simulation of the MN_4C_4 (M = Ni, Co, Fe) moieties incorporated in the graphene matrix showed very good agreement between the experimental and simulated spectra as shown in Figure 65. The XANES simulation at the K-edge of Fe, Ni, and Co were performed using the FDMNES code in the framework of real space full multiple scattering using Muffin-tin approximation for the potential.[100,426,427] The dioxygen molecule adsorbing on the metal center with end-on orientation was predicted to be the best model by DFT that fits with the experiment. These SACs are claimed to be highly active for many catalytic applications such as OER and ORR, CO_2 reduction, and even highly demanding N_2 reduction.

"SACs can exhibit various coordination environment when incorporated in a host support material. Hence in many cases it is noticed that DFT assisted XAS analysis has the advantage to identify the local structure. In the future, this will be more routine in the area of SACs"

5. MACHINE LEARNING APPROACH TOWARD SACS

The machine learning approach is a step further to build better models and predictions of reaction pathways.[428] Huang and his co-workers carried out work on the discovery of atomic catalysts by theoretical calculations with machine learning strategy.[429] In their work, they have investigated graphdiyne based SACs toward their performance on HER. Transition metals as well as

https://doi.org/10.1021/acs.chemrev.2c00495
Chem. Rev. 2023, 123, 379−444

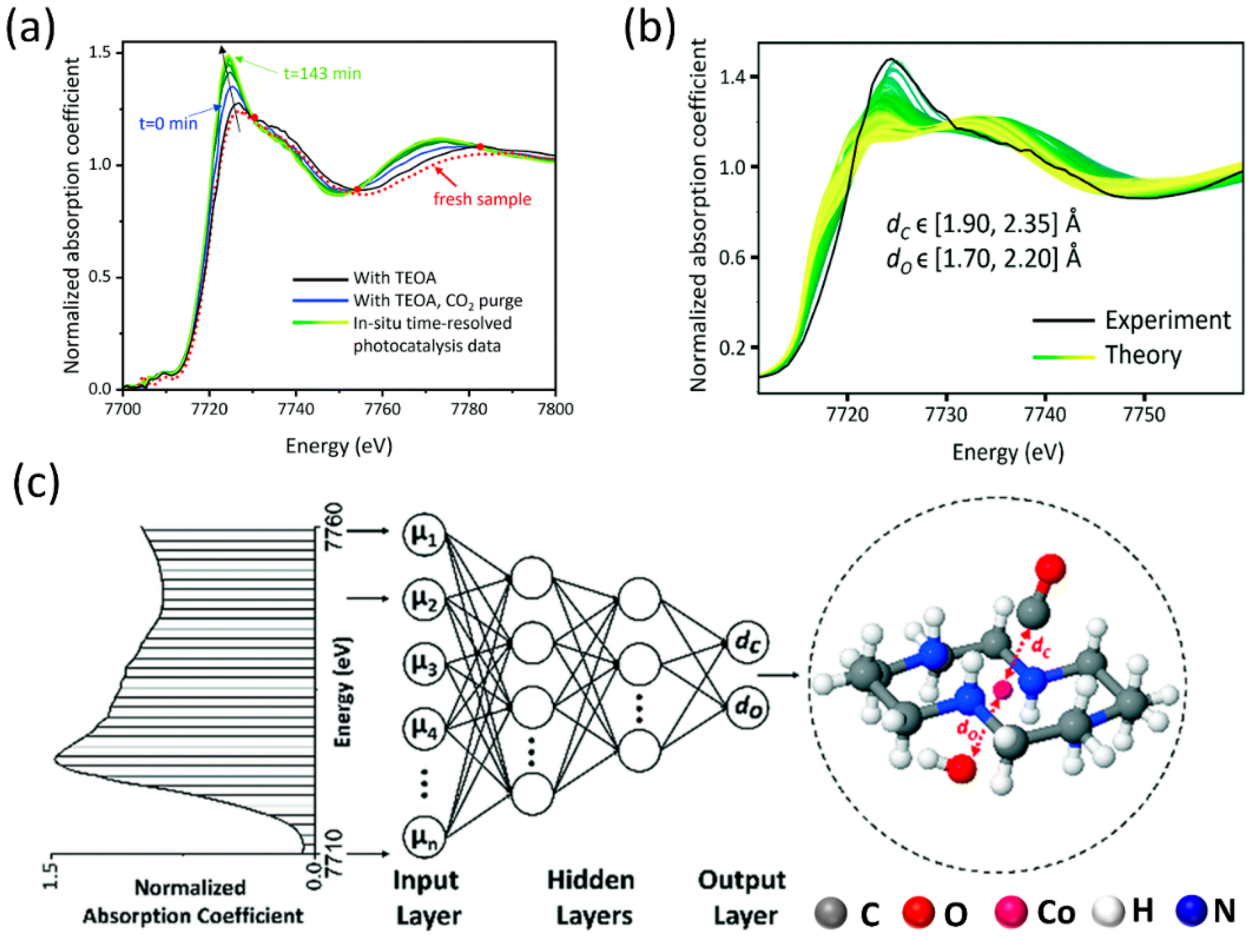

Figure 67. (a) XANES spectra at Cu K-edge during photocatalytic reduction of CO_2, (b) comparisons of experimental (black) and all theoretical XANES spectra with two descriptor changing (d_C and d_O), and (c) scheme of application of NN-XANES to SACs system of Co-cyclam-CO. Adapted with permission from ref 433. Copyright Royal Society of Chemistry.

lanthanides were considered in order to study the H adsorption energies, adsorption trends, electronic structures, and reaction pathway as well as to find the active sites supported on graphdiyne. Moreover, they applied the bagged-tree method as the machine learning (ML) algorithm for predicting the adsorption energies of the single atoms over graphdiyne with Fuzzy C-Means model.[430,431] To date, the DFT assisted study took into account the H-adsorption energy as a pivotal tool toward HER. Here, ML was used to accurately predict the H-adsorption energy by introducing multiple parameters such as electronegativity, electron affinity, ionization potential, d/f electrons, active sites, and mass numbers. The predicted values from DFT showed higher accuracy than the one obtained via ML. One reason might be the use of relatively small databases or the need for further improvements in the algorithm system. Nevertheless, they introduced a redox energy barrier to all the elements based on their previous study[432] to quantify the electron transfer study between the single atoms and graphdiyne. The value of H-adsorption energy obtained from the theoretical calculation and from ML is shown in Figure 66. This kind of study creates further opportunities in designing and predicting reaction pathways with the help of ML in the area of SACs.

Frenkel, Li, and co-workers demonstrated machine learning assisted modeling of XAS spectra of SACs that is able to be used for both qualitative and quantitative analyses of isolated metal structures.[433] In their work as shown in Figure 67, Co SACs were synthesized by grafting molecular Co complex over C_3N_4 semiconductor for the photocatalytic reduction of CO_2. The authors followed the XANES spectra at the Co K-edge under reaction conditions with different ML approaches, including principle component analysis (PCA), linear combination analysis (LCF), K-means clustering, and neural network (NN). The results obtained from the ML approach match closely with the experimental results for understanding the electron transfer pathway during CO_2 photoreduction. Both PCA and K-means clustering of XANES spectra suggested presence of two species during the reaction that is also confirmed in the Co catalyzed homogeneous photocatalytic reaction of CO_2. Using ML approach, key intermediates on the catalyst surface, similar to those produced using the homogeneous Co-cyclam were confirmed. A scheme of the approach is shown in Figure 67c. This sort of study certainly opens up new possibilities in the future for the structural elucidation of SACs with a ML approach during operation and bridging the knowledge between homogeneous and heterogeneous catalysis.

Until now, recording XAS spectra for SACs, data reduction and fitting, and afterward its interpretation is still time-consuming since the measurements take longer than usual due to the low concentration of the metal content. In *operando* spectroscopy, hundreds of spectra are recorded with different variables and to analyze each and every spectra effectively, tools

https://doi.org/10.1021/acs.chemrev.2c00495
Chem. Rev. 2023, 123, 379−444

like machine learning[434,435] might be very useful to obtain the first insights from the data already in the synchrotron. Timoshenko and Frenkel[434] showed an example of how the ML approach can be used to obtain structural information from XANES spectra—especially useful when full EXAFS cannot be obtained. Moreover, an artificial neural network approach has been shown for tracking the local structural as well as *in situ* changes in the coordination environment of iron atoms by XAS. In their work, they have developed a method for direct interpretation of EXAFS features in terms of radial distribution function with the help of machine learning.[436] The method was applied on bulk iron undergoing a temperature-induced phase transition from body-centered cubic (bcc) structure to face-centered cubic (fcc) structure at 1190 K as an example. Compared to conventional EXAFS analysis, this method allows the extraction of the radial distribution function in the longer range of interatomic distances at such a high temperature, which is otherwise difficult experimentally.

6. CONCLUSION AND OUTLOOK

Single-atom catalysts is a growing field in heterogeneous catalysis that gives a solid platform to understand the nature of active sites at the atomic level with the help of advanced spectroscopic technique like X-ray absorption/emission spectroscopy and related element-specific techniques. Unlike other techniques to characterize solids, XAS gives the possibility to study the local structure of the absorbing metal atom. This is ideal for single-atom catalysts where hardly any other technique is available to unravel the structure and oxidation state of the element of interest. As it is a bulk-averaging technique, XAS is highly sensitive for single site catalysts (both SACs and SSHCs), which are highly uniform and do not have atoms in the middle of a particle that would act as a spectator. In this way, XAS can result in element-specific information, in fact, for all the metals across the periodic table. The examples presented show that starting from conventional XAS, this can be extended to various X-ray techniques which can be applied to characterize SACs. Conventional techniques provide oxidation states and symmetry (from XANES) and coordination numbers and bond distance (from EXAFS) of the supported single atoms. In a similar manner, advanced photon-in/photon-out techniques can be applied to derive such information where the conventional technique fails. For example, to distinguish between atoms with very close Z number and atoms that poorly scatter and to detect short-lived species during catalysis. Techniques like HERFD-XANES, vtc XES, and RIXS are new alternatives in the area of SACs. For the data reduction and analysis, DFT assisted studies are attractive for accurate prediction of the active center (fitting and simulation). All X-ray based studies reported in this review can also be conducted under reaction conditions. In this respect methods like LCF, PCA, and MES are extremely helpful to analyze time-resolved data and to follow the kinetics of a reaction. With the help of wavelet transformation, distinct visualization of neighbors that are at least separated by one row in the periodic table is possible. However, over interpretation with this kind of technique is also frequently noticed in the area of SACs. e.g., WT cannot distinguish between N and O, in this case vtc XES is a viable approach. Furthermore, it is notable, that with the new generation of synchrotron light sources with high photon flux, sample damage is of great concern and, hence, data should be analyzed in a critical manner and with complementary techniques. While analyzing XAS data, quality control is also important, e.g. with respect to the following aspects: (a) minimum k-range range is required for EXAFS analysis, at least up to 11−12 $Å^{-1}$, (b) while comparing spectra of different samples, the k values should be consistent, (c) comparisons of white line intensities of reference samples should be performed with samples measured in the same beamline, and (d) values of the fit should be reported with errors.

Single atoms are ideal systems both with respect to atom efficiency and with respect to X-ray absorption techniques, as the number of spectator atoms are minimized. In addition, they are an ideal starting point for studying catalysts as the starting state is defined. Various strategies have been discussed throughout the review to synthesize SACs. The simplest ones are techniques like impregnation, coprecipitation, ion exchange, galvanic replacement, atom trapping, pyrolysis under inert atmosphere, ball-milling, and adsorption. More recently, photochemical/electrochemical deposition and flame spray pyrolysis have also been found attractive for the synthesis of SACs. Depending on the method of preparation and pretreatment procedure, the ligands attached in the metal center can play an important role during catalysis. In this review, we considered those examples where single atom active center is free from the ligand of the precursor material. The various classes of SACs are discussed based on the support that they are anchored on which includes the following classes: (a) fixation on metal oxides, incorporated on polyoxometalate framework, confined in zeolite, since this type of support often exhibits defect sites or vacancies that act as a binding site to the single atom, (b) as composite materials such as an alloy, intermetallic structure, and solid solution where the single atom can easily be accommodated into a matrix of other metal with uniform or random distribution, (c) on the soft matrices like carbon, MOFs/COFs, and POPs which can provide pockets, smaller confinement regime to stabilize the single atom, and (d) on metal carbides, sulfides, nitrides, and perovskite as host structure, which are emerging material classes in terms of their catalytic application.

Despite the various strategies established for designing SACs and the excellent catalytic activities in various highly important reactions, the fate of single atoms needs to be scrutinized under reaction conditions. SACs can undergo various structural changes under reaction conditions such as phase transformations, composite formation, reversible transformations between single site and clusters/particles, or even leaching into the solution. Up to now this has only been studied in selected cases. They show that care has to be taken if the catalyst structure was not studied under reaction conditions. The various examples in this review emphasize that SACs are prone to undergo such changes pronouncedly due to their high surface mobility. Some of the cases have shown that under operating conditions SACs transform to ultrasmall clusters or vice versa depending upon the reaction conditions. In the case of the Pt/CeO_2 system this has been exploited to rationally improve the catalytic activity. In particular, XAS gives the option to track these changes as a function of time and in a spatially resolved manner.

Apart from the single crystal structures, DFT-assisted models serve as ideal starting models for an active site and thus are very powerful in guiding the way to fit experimental XAS data and to simulate spectra. To predict the active sites as close to reality as possible for a large data set, tools like machine learning/artificial neural network will pave our way for successful interpretation of recorded spectra and possible reaction intermediate. Machine learning is emerging as a potential technique to understand the complex and dynamic behavior of catalyst under *operando*

https://doi.org/10.1021/acs.chemrev.2c00495
Chem. Rev. 2023, 123, 379−444

conditions, and it will have a promising influence in the future in designing new types of SACs. ML assisted modeling of the XAS spectra of SACs for qualitative and quantitative analyses of the local structures of metal has already been demonstrated.

To unravel the mechanistic details of SACs, *in situ/operando* techniques are mandatory to elucidate the dynamic character of the SACs. A future challenge in this area will be to combine multiple *in situ/operando* techniques (e.g., XAS with IR). While XAS can be used to gain information about local structures of metals, IR is an ideal tool for deriving information about surrounding ligands. In order to follow the changes which occur during a reaction, the major challenge is to design a proper cell that can overcome limitations such as mass-transfer, heat-transfer, and diffusions, which is also able to reach harsh reaction conditions. We have discussed various possibilities of cells that many research groups developed and some of them are available at synchrotron light sources for different types of catalytic studies such as gas−solid phase, liquid−solid phase, electrochemical, photochemical, or even at the mixed interfaces. Electro and photo catalysis are emerging as hot topic especially in the context of alternative energy resources. For example, production of green hydrogen, conversion of CO_2 to fuel via photo or electro catalysis is highly demanding. In this context an efficient, highly stable, and recyclable catalyst is important. We have reviewed potential application of SACs in these areas and their future applicability.

In summary, we have covered in this review starting from the fundamental of XAS to advanced X-ray spectroscopy and the applicability of XAS in the area of SACs. To understand the dynamic structural change with the help of XAS and other photon in/out tools are also thoroughly discussed for the interest of the broader scientific community. With the newly upgraded synchrotron light sources across the world, we hope there will be new techniques developed in the future to achieve higher quality data and relatively fast.

AUTHOR INFORMATION

Corresponding Authors

Bidyut Bikash Sarma − *Institute for Chemical Technology and Polymer Chemistry, Karlsruhe Institute of Technology, 76131 Karlsruhe, Germany; Institute of Catalysis Research and Technology, Karlsruhe Institute of Technology, 76344 Karlsruhe, Germany;* orcid.org/0000-0002-5292-7890; Email: bidyut.sarma@kit.edu

Jan-Dierk Grunwaldt − *Institute for Chemical Technology and Polymer Chemistry, Karlsruhe Institute of Technology, 76131 Karlsruhe, Germany; Institute of Catalysis Research and Technology, Karlsruhe Institute of Technology, 76344 Karlsruhe, Germany;* orcid.org/0000-0003-3606-0956; Email: grunwaldt@kit.edu

Authors

Florian Maurer − *Institute for Chemical Technology and Polymer Chemistry, Karlsruhe Institute of Technology, 76131 Karlsruhe, Germany;* orcid.org/0000-0002-3307-4132

Dmitry E. Doronkin − *Institute for Chemical Technology and Polymer Chemistry, Karlsruhe Institute of Technology, 76131 Karlsruhe, Germany; Institute of Catalysis Research and Technology, Karlsruhe Institute of Technology, 76344 Karlsruhe, Germany;* orcid.org/0000-0003-3930-3204

Complete contact information is available at: https://pubs.acs.org/10.1021/acs.chemrev.2c00495

Author Contributions

CRediT: **Bidyut Bikash Sarma** conceptualization, data curation, formal analysis, methodology, writing-original draft, writing-review & editing; **Florian Maurer** methodology, writing-original draft, writing-review & editing; **Dmitry E. Doronkin** data curation, methodology, project administration, writing-original draft, writing-review & editing; **Jan-Dierk Grunwaldt** conceptualization, funding acquisition, methodology, project administration, resources, supervision, writing-review & editing.

Notes

The authors declare no competing financial interest.

Biographies

Bidyut Bikash Sarma is currently working as postdoctoral fellow at the Institute of Catalysis Research and Technology (IKFT) at Karlsruhe Institute of Technology (KIT) since February 2020. He received his PhD in 2016 at the Weizmann Institute of Science, Israel under the supervision of Prof. Ronny Neumann where his work was involved in tracking the active site of polyoxometalate during electron transfer-oxygen transfer reactions in homogeneous liquid phase. Afterwards he started his work at the department of heterogeneous catalysis under director Prof. Ferdi Schüth at the Max-Planck-Institute für Kohlenforschung, Germany where he received Max-Planck-Society postdoctoral fellowship (2016) and Alexander von Humboldt postdoctoral fellowship (2017). During this time, he investigated single atom catalysts for various gas and liquid phase reactions. In 2020, he moved to the Grunwaldt group at KIT where he has been working in understanding the dynamic behavior of solid and molecular catalysts with *in situ/operando* spectroscopy. In March 2022, he has been awarded Marie Curie post-doctoral fellowship at the University of Cambridge, UK.

Florian Maurer received his B.Sc. in Chemistry in 2014 and M.Sc. in Chemistry in 2016 from the Karlsruhe Institute of Technology (KIT). In 2021, he finished his PhD in the Institute of Technical Chemistry and Polymer Chemistry (ITCP) at KIT under the supervision of Prof. Dr. Jan-Dierk Grunwaldt, in whose group he is currently working as postdoctoral fellow. His research focuses on *in situ* and *operando* spectroscopy of noble metal based environmental catalysts using hard X-rays with the goal to identify and track the active sites in heterogeneous catalysts. He is responsible for the coordination of the collaboration research center CRC1441 "TrackAct" (www.trackact.kit.edu).

Dmitry E. Doronkin is a senior scientist at the Institute of Chemical Technology and Polymer Chemistry (ITCP) and Institute of Catalysis Research and Technology (IKFT) at Karlsruhe Institute of Technology (KIT) working there since 2012. He received his PhD in 2010 at N.D. Zelinsky Institute of Organic Chemistry RAS, Russia under the supervision of Prof. Alexandr Yu. Stakneev where his work was focused on exhaust gas remediation over Fe-modified zeolites. Afterwards he started his work at the Center of Individual Nanoparticle Functionality (CINF), department of Physics, Technical University of Denmark with Prof. Søren Dahl. During this time, he investigated supported metal and zeolite catalysts for selective catalytic reduction of NOx. In 2012 he moved to the Grunwaldt group at KIT where he has been responsible for *operando* spectroscopy of energy-related and environmental catalysts.

Jan-Dierk Grunwaldt is full professor and director at the Institute for Chemical Technology and Polymer Chemistry and Institute of Catalysis Research and Technology, Karlsruhe Institute of Technology (KIT), Germany. He obtained his PhD at the department of Technical

https://doi.org/10.1021/acs.chemrev.2c00495
Chem. Rev. 2023, 123, 379−444

Chemistry at the ETH Zürich, Switzerland under the supervision of Prof. A. Baiker where he worked on Low-temperature CO-oxidation on gold/oxide interfaces. He then worked as project manager at Haldor Topsøe, Lyngby, Denmark. Afterwards he acted as lecturer and senior scientist between 2001 and 2007 at the Institute of Chemical and Bioengineering, Department of Chemistry and Applied Biosciences, ETH Zürich, Switzerland. In 2008, he started as full professor at the Department of Chemical and Biochemical Engineering, DTU, Kgs. Lyngby, Denmark. Since 2010, he has been full professor in chemical technology and catalysis at KIT where his group works on heterogeneous catalysis and *operando* spectroscopy, chemical energy storage, sustainable chemistry, power-to-X processes, selective oxidation reactions, emission control and *in situ* characterization of heterogeneous catalysts using especially synchrotron radiation sources. He is presently speaker of two big initiatives "TrackAct" (CRC1441, www.trackact.kit.edu) and "DynaKat" (SPP2080, www.spp2080.org). He is adj. professor at DTU and has been recently guest professor at the University of Padua.

ACKNOWLEDGMENTS

This work has been supported by KIT, the CRC1441 (Project-ID 426888090), and the SPP2080 (GR3987/13-2). The authors would like to thank Dr. Thomas Eldridge, Dr. Abhijeet Gaur, Dr. Paolo Dolcet, Dominik Neukum, and Daria Gashnikova from KIT as well as the many collaborators, also within the above-mentioned initiatives, for fruitful discussions throughout the review preparation. We would like to thank the KIT light source, PETRA III, SOLEIL, SLS, ALBA, BESSY, ESRF, and further synchrotron radiation facilities for providing beamtime for our measurements.

ABBREVIATIONS

AC	Activated Carbon
ALD	Atomic Layer Deposition
COF	Covalent Organic Framework
CPO	Catalytic Partial Oxidation
Cs	Spherical aberration
DFT	Density Functional Theory
DRIFTS	Diffuse Reflectance Fourier Transform Infrared Spectroscopy
DW	Debye−Waller
ETEM	Environmental Transmission Electron Microscopy
EXAFS	Extended X-ray Absorption Fine Structure
FEFF	Free Energy Force Field
FT	Fourier Transformation
HAADF	High Angle Annular Dark Field
HERFD	High Energy Resolution Fluorescence Detected
IMS	Intermetallic Structure
IMNC	Intermetallic Nano-Crystals
IR	Infrared
LCF	Linear Combination Fitting
LDH	Layered Double Hydroxide
LH	Langmuir−Hinshelwood
LUMO	Lowest Occupied Molecular Orbital
MCF	Meso Cellular Foam
MCR ALS	Multivariate Curve Resolution Alternating Least Square
MES	Modulation Excitation Spectroscopy
ML	Machine learning
MOF	Metal−Organic Framework
MvK	Mars-van Krevelen
NG	Nitrogen Doped Graphene
NMR	Nuclear Magnetic Resonance
NNMF	Non-Negative Matrix Factorization
ORR	Oxygen Reduction Reaction
PCA	Principal Component Analysis
PCN	Phophorized Carbon Nitride
PDAS	Poly(diacetylenes)
PDF	Pair Distribution Function
PDMS	Poly(dimethylsiloxane)
PMA	Phosphomolybdic Acid
POM	Polyoxometalate
POP	Porous Organic Polymers
PROX	Preferential Oxidation
PTA	Phosphotungstic Acid
SAC	Single-Atom Catalyst
SAA	Single Atom Alloy
SCR	Selective Catalytic Reduction
SAXS	Small Angle X-ray Scattering
SMSI	Strong Metal Support Interaction
SOMC	Surface Organometallic Chemistry
SSHC	Single Site Heterogeneous Catalysis
STEM	Scanning Transmission Electron Microscopy
vtc	Valence to Core
WT	Wavelet Transformation
XAS	X-ray Absorption Spectroscopy
XANES	X-ray Absorption Near Edge Structure
XES	X-ray Emission Spectroscopy
XRD	X-ray Diffraction
XPS	X-ray Photoelectron Spectroscopy
ZIF	Zeolite Imidazole Framework

REFERENCES

(1) Basset, J.-M. *Modern Surface Organometallic Chemistry*; Wiley-VCH-Verlag: Weinheim, 2009.
(2) Miessner, H. Surface Chemistry in a Zeolite Matrix. Well-Defined Dinitrogen Complexes of Rhodium Supported on Dealuminated Y Zeolite. *J. Am. Chem. Soc.* **1994**, *116*, 11522−11530.
(3) Kosinov, N.; Liu, C.; Hensen, E. J. M.; Pidko, E. A. Engineering of Transition Metal Catalysts Confined in Zeolites. *Chem. Mater.* **2018**, *30*, 3177−3198.
(4) Wang, Y.; Mao, J.; Meng, X.; Yu, L.; Deng, D.; Bao, X. Catalysis with Two-Dimensional Materials Confining Single Atoms: Concept, Design, and Applications. *Chem. Rev.* **2019**, *119*, 1806−1854.
(5) Giannakakis, G.; Flytzani-Stephanopoulos, M.; Sykes, E. C. H. Single-Atom Alloys as a Reductionist Approach to the Rational Design of Heterogeneous Catalysts. *Acc. Chem. Res.* **2019**, *52*, 237−247.
(6) Thomas, J. M. The Concept, Reality and Utility of Single-site Heterogeneous Catalysts (SSHCs). *Phys. Chem. Chem. Phys.* **2014**, *16*, 7647−7661.
(7) Wang, A.; Li, J.; Zhang, T. Heterogeneous Single-atom Catalysis. *Nat. Rev. Chem.* **2018**, *2*, 65−81.
(8) Psaro, R.; Ugo, R.; Zanderighi, G. M.; Besson, B.; Smith, A. K.; Basset, J. M. Surface-Supported Metal Cluster Carbonyls. Chemisorption, Decomposition and Reactivity of $Os_3(CO)_{12}$, $H_2Os_3(CO)_{10}$ and $Os_6(CO)_{18}$ Supported on Silica and Alumina and the Investigation of the Fischer−Tropsch Catalysis with These Systems. *J. Org. Chem.* **1981**, *213*, 215−247.
(9) Gates, B. C. Supported Metal Clusters: Synthesis, Structure, and Catalysis. *Chem. Rev.* **1995**, *95*, 511−522.
(10) Fierro-Gonzalez, J. C.; Kuba, S.; Hao, Y.; Gates, B. C. Oxide- and Zeolite-Supported Molecular Metal Complexes and Clusters: Physical Characterization and Determination of Structure, Bonding, and Metal Oxidation State. *J. Phys. Chem. B* **2006**, *110*, 13326−13351.
(11) Basset, J. M.; Choplin, A. Surface Organometallic Chemistry - a New Approach to Heterogeneous Catalysis. *J. Mol. Catal.* **1983**, *21*, 95−108.

https://doi.org/10.1021/acs.chemrev.2c00495
Chem. Rev. 2023, 123, 379−444

(12) Copéret, C. Single-Sites and Nanoparticles at Tailored Interfaces Prepared via Surface Organometallic Chemistry from Thermolytic Molecular Precursors. *Acc. Chem. Res.* **2019**, *52*, 1697−1708.
(13) Flytzani-Stephanopoulos, M.; Gates, B. C. Atomically Dispersed Supported Metal Catalysts. *Annu. Rev. Chem. Biomol. Eng.* **2012**, *3*, 545−74.
(14) Gates, B. C. Atomically Dispersed Supported Metal Catalysts: Seeing is Believing. *Trends Chem.* **2019**, *1*, 99−110.
(15) Flytzani-Stephanopoulos, M. Supported Metal Catalysts at the Single-atom Limit - A Viewpoint. *Chin. J. Catal.* **2017**, *38*, 1432−1442.
(16) Fu, Q.; Saltsburg, H.; Flytzani-Stephanopoulos, M. Active Nonmetallic Au and Pt Species on Ceria-Based Water-Gas Shift Catalysts. *Science* **2003**, *301*, 935−938.
(17) Asakura, K.; Nagahiro, H.; Ichikuni, N.; Iwasawa, Y. Structure and Catalytic Combustion Activity of Atomically Dispersed Pt Species at MgO Surface. *Appl. Catal. A: Gen.* **1999**, *188*, 313−324.
(18) Thomas, J. M.; Raja, R.; Lewis, D. W. Single-site Heterogeneous Catalysts. *Angew. Chem., Int. Ed.* **2005**, *44*, 6456−82.
(19) Liu, J. Catalysis by Supported Single Metal Atoms. *ACS Catal.* **2017**, *7*, 34−59.
(20) Qiao, B.; Wang, A.; Yang, X.; Allard, L. F.; Jiang, Z.; Cui, Y.; Liu, J.; Li, J.; Zhang, T. Single-Atom Catalysis of CO Oxidation Using Pt_1/FeO_x. *Nat. Chem.* **2011**, *3*, 634−41.
(21) Cui, X.; Li, W.; Ryabchuk, P.; Junge, K.; Beller, M. Bridging Homogeneous and Heterogeneous Catalysis by Heterogeneous Single-Metal-Site Catalysts. *Nat. Catal.*. **2018**, *1*, 385−397.
(22) Yang, X.-F.; Wang, A.; Qiao, B.; Li, J.; Liu, J.; Zhang, T. Single-Atom Catalysts: A New Frontier in Heterogeneous Catalysis. *Acc. Chem. Res.* **2013**, *46*, 1740−1748.
(23) Liu, J. Catalysis by Supported Single Metal Atoms. *ACS Catal.* **2017**, *7*, 34−59.
(24) Liu, L.; Corma, A. Metal Catalysts for Heterogeneous Catalysis: From Single Atoms to Nanoclusters and Nanoparticles. *Chem. Rev.* **2018**, *118*, 4981−5079.
(25) Mitchell, S.; Vorobyeva, E.; Pérez-Ramírez, J. The Multifaceted Reactivity of Single-Atom Heterogeneous Catalysts. *Angew. Chem., Int. Ed.* **2018**, *57*, 15316−15329.
(26) Chen, Z. W.; Chen, L. X.; Yang, C. C.; Jiang, Q. Atomic (Single, Double, and Triple atoms) Catalysis: Frontiers, Opportunities, and Challenges. *J. Mater. Chem. A* **2019**, *7*, 3492−3515.
(27) Jiao, L.; Yan, H.; Wu, Y.; Gu, W.; Zhu, C.; Du, D.; Lin, Y. When Nanozymes Meet Single-Atom Catalysis. *Angew. Chem., Int. Ed.* **2020**, *59*, 2565−2576.
(28) Li, X.; Surkus, A.-E.; Rabeah, J.; Anwar, M.; Dastigir, S.; Junge, H.; Brückner, A.; Beller, M. Cobalt Single-Atom Catalysts with High Stability for Selective Dehydrogenation of Formic Acid. *Angew. Chem., Int. Ed.* **2020**, *59*, 15849−15854.
(29) Vile, G.; Albani, D.; Nachtegaal, M.; Chen, Z.; Dontsova, D.; Antonietti, M.; Lopez, N.; Perez-Ramirez, J. A stable Single-Site Palladium Catalyst for Hydrogenations. *Angew. Chem., Int. Ed.* **2015**, *54*, 11265−11269.
(30) Ding, S.; Hülsey, M. J.; Pérez-Ramírez, J.; Yan, N. Transforming Energy with Single-Atom Catalysts. *Joule* **2019**, *3*, 2897−2929.
(31) Resasco, J.; Christopher, P. Atomically Dispersed Pt-Group Catalysts: Reactivity, Uniformity, Structural Evolution, and Paths to Increased Functionality. *J. Phys. Chem. Lett.* **2020**, *11*, 10114−10123.
(32) Resasco, J.; DeRita, L.; Dai, S.; Chada, J. P.; Xu, M.; Yan, X.; Finzel, J.; Hanukovich, S.; Hoffman, A. S.; Graham, G. W.; et al. Uniformity is Key in Defining Structure-Function Relationships for Atomically Dispersed Metal Catalysts: The Case of Pt/CeO_2. *J. Am. Chem. Soc.* **2020**, *142*, 169−184.
(33) Logadottir, A.; Rod, T. H.; Nørskov, J. K.; Hammer, B.; Dahl, S.; Jacobsen, C. J. H. The Brønsted-Evans-Polanyi Relation and the Volcano Plot for Ammonia Synthesis over Transition Metal Catalysts. *J. Catal.* **2001**, *197*, 229−231.
(34) Anand, M.; Rohr, B.; Statt, M. J.; Nørskov, J. K. Scaling Relationships and Volcano Plots in Homogeneous Catalysis. *J. Phys. Chem. Lett.* **2020**, *11*, 8518−8526.
(35) Iwasawa, Y.; Asakura, K.; Tada, M. *XAFS Techniques for Catalysts, Nanomaterials, and Surfaces*; Springer International Publishing, A. G., 2018.
(36) Gänzler, A. M.; Casapu, M.; Maurer, F.; Störmer, H.; Gerthsen, D.; Ferré, G.; Vernoux, P.; Bornmann, B.; Frahm, R.; Murzin, V.; et al. Tuning the Pt/CeO_2 Interface by in Situ Variation of the Pt Particle Size. *ACS Catal.* **2018**, *8*, 4800−4811.
(37) Deka, U.; Juhin, A.; Eilertsen, E. A.; Emerich, H.; Green, M. A.; Korhonen, S. T.; Weckhuysen, B. M.; Beale, A. M. Confirmation of Isolated Cu^{2+} Ions in SSZ-13 Zeolite as Active Sites in NH_3-Selective Catalytic Reduction. *J. Phys. Chem. C* **2012**, *116*, 4809−4818.
(38) Bañares, M. A. Operando Spectroscopy: the Knowledge Bridge to Assessing Structure-Performance Relationships in Catalyst Nanoparticles. *Adv. Mater.* **2011**, *23*, 5293−5301.
(39) Grunwaldt, J.-D.; Basini, L.; Clausen, B. S. In-Situ EXAFS Study of Rh/Al_2O_3 Catalysts for Catalytic Partial Oxidation of Methane. *J. Catal.* **2001**, *200*, 321−329.
(40) Boyes, E. D.; LaGrow, A. P.; Ward, M. R.; Mitchell, R. W.; Gai, P. L. Single Atom Dynamics in Chemical Reactions. *Acc. Chem. Res.* **2020**, *53*, 390−399.
(41) Grunwaldt, J.-D.; Kappen, P.; Basini, L.; Clausen, B. S. Iridium Clusters for Catalytic Partial Oxidation of Methane—An In-Situ Transmission and Fluorescence XAFS Study. *Catal. Lett.* **2002**, *78*, 13−21.
(42) Lang, R.; Xi, W.; Liu, J.-C.; Cui, Y.-T.; Li, T.; Lee, A. F.; Chen, F.; Chen, Y.; Li, L.; et al. Non Defect-Stabilized Thermally Stable Single-Atom Catalyst. *Nat. Commun.* **2019**, *10*, 234.
(43) Sarma, B. B.; Agostini, G.; Farpón, M. G.; Marini, C.; Pfänder, N.; Prieto, G. Bottom-up Assembly of Bimetallic Nanocluster Catalysts from Oxide-Supported Single-Atom Precursors. *J. Mater. Chem. A* **2021**, *9*, 8401−8415.
(44) Kalz, K. F.; Kraehnert, R.; Dvoyashkin, M.; Dittmeyer, R.; Gläser, R.; Krewer, U.; Reuter, K.; Grunwaldt, J.-D. Future Challenges in Heterogeneous Catalysis: Understanding Catalysts under Dynamic Reaction Conditions. *ChemCatChem.* **2017**, *9*, 17−29.
(45) Grunwaldt, J. D. In-situ Analysis of Heterogeneous Catalysts in Chemical Energy Conversion. *Chemical Energy Storage*; De Gruyter: Berlin, 2013; 311−328.
(46) Reimann, S.; Stötzel, J.; Frahm, R.; Kleist, W.; Grunwaldt, J.-D.; Baiker, A. Identification of the Active Species Generated from Supported Pd Catalysts in Heck Reactions: An In-situ Quick Scanning EXAFS Investigation. *J. Am. Chem. Soc.* **2011**, *133*, 3921−3930.
(47) Chen, Z.; Vorobyeva, E.; Mitchell, S.; Fako, E.; Ortuno, M. A.; Lopez, N.; Collins, S. M.; Midgley, P. A.; Richard, S.; Vile, G.; et al. A Heterogeneous Single-Atom Palladium Catalyst Surpassing Homogeneous Systems for Suzuki Coupling. *Nat. Nanotechnol.* **2018**, *13*, 702−707.
(48) Grunwaldt, J.-D.; Molenbroek, A. M.; Topsøe, N. Y.; Topsøe, H.; Clausen, B. S. In-Situ Investigations of Structural Changes in Cu/ZnO Catalysts. *J. Catal.* **2000**, *194*, 452−460.
(49) Hansen, P. L.; Wagner, J. B.; Helveg, S.; Rostrup-Nielsen, J. R.; Clausen, B. S.; Topsøe, H. Atom-Resolved Imaging of Dynamic Shape Changes in Supported Copper Nanocrystals. *Science* **2002**, *295*, 2053−2055.
(50) Couves, J. W.; Thomas, J. M.; Waller, D.; Jones, R. H.; Dent, A. J.; Derbyshire, G. E.; Greaves, G. N. Tracing the Conversion of Aurichalcite to a Copper Catalyst by Combined X-ray Absorption and Diffraction. *Nature* **1991**, *354*, 465−468.
(51) Kehres, J.; Jakobsen, J. G.; Andreasen, J. W.; Wagner, J. B.; Liu, H.; Molenbroek, A.; Sehested, J.; Chorkendorff, I.; Vegge, T. Dynamical Properties of a $Ru/MgAl_2O_4$ Catalyst during Reduction and Dry Methane Reforming. *J. Phys. Chem. C* **2012**, *116*, 21407−21415.
(52) Ferré, G.; Aouine, M.; Bosselet, F.; Burel, L.; Cadete Santos Aires, F. J.; Geantet, C.; Ntais, S.; Maurer, F.; Casapu, M.; Grunwaldt, J.-D.; et al. Exploiting the Dynamic Properties of Pt on Ceria for Low-Temperature CO Oxidation. *Catal. Sci. Technol.* **2020**, *10*, 3904−3917.
(53) Gänzler, A. M.; Casapu, M.; Vernoux, P.; Loridant, S.; Cadete Santos Aires, F. J.; Epicier, T.; Betz, B.; Hoyer, R.; Grunwaldt, J.-D.

https://doi.org/10.1021/acs.chemrev.2c00495
Chem. Rev. 2023, 123, 379−444

Tuning the Structure of Platinum Particles on Ceria In Situ for Enhancing the Catalytic Performance of Exhaust Gas Catalysts. *Angew. Chem., Int. Ed.* **2017**, *56*, 13078−13082.
(54) Nagai, Y.; Dohmae, K.; Teramura, K.; Tanaka, T.; Guilera, G.; Kato, K.; Nomura, M.; Shinjoh, H.; Matsumoto, S. Dynamic In-situ Observation of Automotive Catalysts for Emission Control Using X-ray Absorption Fine Structure. *Catal. Today* **2009**, *145*, 279−287.
(55) Matsubu, J. C.; Yang, V. N.; Christopher, P. Isolated Metal Active Site Concentration and Stability Control Catalytic CO_2 Reduction Selectivity. *J. Am. Chem. Soc.* **2015**, *137*, 3076−3084.
(56) Wang, J.; McEntee, M.; Tang, W.; Neurock, M.; Baddorf, A. P.; Maksymovych, P.; Yates, J. T. Formation, Migration, and Reactivity of Au-CO Complexes on Gold Surfaces. *J. Am. Chem. Soc.* **2016**, *138*, 1518−1526.
(57) Martin, N. M.; Nilsson, J.; Skoglundh, M.; Adams, E. C.; Wang, X.; Velin, P.; Smedler, G.; Raj, A.; Thompsett, D.; Brongersma, H. H.; et al. Characterization of Surface Structure and Oxidation/Reduction Behavior of Pd-Pt/Al_2O_3 Model Catalysts. *J. Phys. Chem. C* **2016**, *120*, 28009−28020.
(58) Fahami, A. R.; Günter, T.; Doronkin, D. E.; Casapu, M.; Zengel, D.; Vuong, T. H.; Simon, M.; Breher, F.; Kucherov, A. V.; Brückner, A.; et al. The Dynamic Nature of Cu Sites in Cu-SSZ-13 and the Origin of the Seagull NOx Conversion Profile During NH_3-SCR. *React. Chem. Engin.* **2019**, *4*, 1000−1018.
(59) Bertella, F.; Concepción, P.; Martínez, A. TiO_2 Polymorph Dependent SMSI Effect in Co-Ru/TiO_2 Catalysts and its Relevance to Fischer−Tropsch Synthesis. *Catal. Today* **2017**, *289*, 181−191.
(60) Raman, N.; Wolf, M.; Heller, M.; Heene-Würl, N.; Taccardi, N.; Haumann, M.; Felfer, P.; Wasserscheid, P. GaPt Supported Catalytically Active Liquid Metal Solution Catalysis for Propane Dehydrogenation-Support Influence and Coking Studies. *ACS Catal.* **2021**, *11*, 13423−13433.
(61) Raman, N.; Maisel, S.; Grabau, M.; Taccardi, N.; Debuschewitz, J.; Wolf, M.; Wittkämper, H.; Bauer, T.; Wu, M.; Haumann, M.; et al. Highly Effective Propane Dehydrogenation Using Ga-Rh Supported Catalytically Active Liquid Metal Solutions. *ACS Catal.* **2019**, *9*, 9499−9507.
(62) Jakub, Z.; Hulva, J.; Meier, M.; Bliem, R.; Kraushofer, F.; Setvin, M.; Schmid, M.; Diebold, U.; Franchini, C.; Parkinson, G. S. Local Structure and Coordination Define Adsorption in a Model Ir_1/Fe_3O_4 Single-Atom Catalyst. *Angew. Chem., Int. Ed.* **2019**, *58*, 13961−13968.
(63) Tanaka, H.; Uenishi, M.; Taniguchi, M.; Tan, I.; Narita, K.; Kimura, M.; Kaneko, K.; Nishihata, Y.; Mizuki, J. The Intelligent Catalyst Having the Self-Regenerative Function of Pd, Rh and Pt for Automotive Emissions Control. *Catal. Today* **2006**, *117*, 321−328.
(64) Hannagan, R. T.; Giannakakis, G.; Flytzani-Stephanopoulos, M.; Sykes, E. C. H. Single-Atom Alloy Catalysis. *Chem. Rev.* **2020**, *120*, 12044−12088.
(65) Luneau, M.; Guan, E.; Chen, W.; Foucher, A. C.; Marcella, N.; Shirman, T.; Verbart, D. M. A.; Aizenberg, J.; Aizenberg, M.; Stach, E. A.; et al. Enhancing Catalytic Performance of Dilute Metal Alloy Nanomaterials. *Commun. Chem.* **2020**, *3*, 46.
(66) Moliner, M.; Gabay, J. E.; Kliewer, C. E.; Carr, R. T.; Guzman, J.; Casty, G. L.; Serna, P.; Corma, A. Reversible Transformation of Pt Nanoparticles into Single Atoms inside High-Silica Chabazite Zeolite. *J. Am. Chem. Soc.* **2016**, *138*, 15743−15750.
(67) Uzun, A.; Gates, B. C. Real-Time Characterization of Formation and Breakup of Iridium Clusters in Highly Dealuminated Zeolite Y. *Angew. Chem., Int. Ed.* **2008**, *47*, 9245−9248.
(68) Foster, A. J.; Lobo, R. F. Identifying Reaction Intermediates and Catalytic Active Sites Through In-situ Characterization Techniques. *Chem. Soc. Rev.* **2010**, *39*, 4783−93.
(69) Alayon, E. M. C.; Singh, J.; Nachtegaal, M.; Harfouche, M.; van Bokhoven, J. A. On Highly Active Partially Oxidized Platinum in Carbon Monoxide Oxidation over Supported Platinum Catalysts. *J. Catal.* **2009**, *263*, 228−238.
(70) Bañares, M. A. In Situ to Operando Spectroscopy: From Proof of Concept to Industrial Application. *Top. Catal.* **2009**, *52*, 1301−1302.
(71) Weckhuysen, B. M. Snapshots of a Working Catalyst: Possibilities and Limitations of In-situ Spectroscopy in the Field of Heterogeneous Catalysis. *Chem. Commun.* **2002**, 97−110.
(72) Bañares, M. A. Operando Methodology: Combination of In-situ Spectroscopy and Simultaneous Activity Measurements under Catalytic Reaction Conditions. *Catal. Today* **2005**, *100*, 71−77.
(73) Topsøe, H. Developments in Operando Studies and In-situ Characterization of Heterogeneous Catalysts. *J. Catal.* **2003**, *216*, 155−164.
(74) Brückner, A.; Kondratenko, E. Simultaneous Operando EPR/UV-vis/laser-Raman Spectroscopy — A Powerful Tool for Monitoring Transition Metal Oxide Catalysts during Reaction. *Catal. Today* **2006**, *113*, 16−24.
(75) Chakrabarti, A.; Ford, M. E.; Gregory, D.; Hu, R.; Keturakis, C. J.; Lwin, S.; Tang, Y.; Yang, Z.; Zhu, M.; Bañares, M. A.; Wachs, I. E. A Decade+ of Operando Spectroscopy Studies. *Catal. Today* **2017**, *283*, 27−53.
(76) Berlier, G.; Ricchiardi, G.; Bordiga, S.; Zecchina, A. Catalytic Activity of Fe Ions in Iron-based Crystalline and Amorphous Systems: Role of Dispersion, Coordinative Unsaturation and Al Content. *J. Catal.* **2005**, *229*, 127−135.
(77) Meunier, F. C. Relevance of IR Spectroscopy of Adsorbed CO for the Characterization of Heterogeneous Catalysts Containing Isolated Atoms. *J. Phys. Chem. C* **2021**, *125*, 21810−21823.
(78) Koningsberger, D. C.; Prins, R. *X-ray Absorption: Principles, Applications, Techniques of EXAFS, SEXAFS, and XANES*; Wiley: New York, 1988.
(79) Singh, J.; Lamberti, C.; van Bokhoven, J. A. Advanced X-ray Absorption and Emission Spectroscopy: In-situ Catalytic Studies. *Chem. Soc. Rev.* **2010**, *39*, 4754−66.
(80) Russell, A. E.; Rose, A. X-ray Absorption Spectroscopy of Low Temperature Fuel Cell Catalysts. *Chem. Rev.* **2004**, *104*, 4613−4636.
(81) Koningsberger, D. C.; Ramaker, D. E. Applications of X-Ray Absorption Spectroscopy in Heterogeneous Catalysis: EXAFS, Atomic XAFS and Delta XANES. *Handbook of Heterogeneous Catalysis*; Wiley, 2008; pp 774−805.
(82) Newville, M. Fundamentals of XAFS. *Reviews in Mineralogy and Geochemistry* **2014**, *78*, 33−74.
(83) Günter, T.; Doronkin, D. E.; Boubnov, A.; Carvalho, H. W. P.; Casapu, M.; Grunwaldt, J.-D. The SCR of NO_x with NH_3 Examined by Novel X-ray Emission and X-ray Absorption Methods. *Top. Catal.* **2016**, *59*, 866−874.
(84) Glatzel, P.; Bergmann, U. High Resolution 1s Core Hole X-ray Spectroscopy in 3d Transition Metal Complexes—Electronic and Structural Information. *Coord. Chem. Rev.* **2005**, *249*, 65−95.
(85) Adrien, P.; Dirac, M. The Quantum Theory of the Emission and Absorption of Radiation. *Proc. R. Soc. London.* **1927**, *114*, 243−265.
(86) Sarangi, R.; Aboelella, N.; Fujisawa, K.; Tolman, W. B.; Hedman, B.; Hodgson, K. O.; Solomon, E. I. X-ray Absorption Edge Spectroscopy and Computational Studies on $LCuO_2$ Species: Superoxide-Cu^{II} versus Peroxide-Cu^{III} Bonding. *J. Am. Chem. Soc.* **2006**, *128*, 8286−8296.
(87) Boubnov, A.; Lichtenberg, H.; Mangold, S.; Grunwaldt, J.-D. Identification of the Iron Oxidation State and Coordination Geometry in Iron Oxide- and Zeolite-based Catalysts Using Pre-edge XAS Analysis. *J. Sync. Rad.* **2015**, *22*, 410−426.
(88) Brown, M.; Peierls, R. E.; Stern, E. A. White Lines in X-ray Absorption. *Phys. Rev. B* **1977**, *15*, 738−744.
(89) Coster, D. Über die Absorptionsspektren im Röntgengebiet. *Zeitschrift für Physik* **1924**, *25*, 83−98.
(90) Marcella, N.; Liu, Y.; Timoshenko, J.; Guan, E.; Luneau, M.; Shirman, T.; Plonka, A. M.; van der Hoeven, J. E. S.; Aizenberg, J.; Friend, C. M.; Frenkel, A. I. Neural Network Assisted Analysis of Bimetallic Nanocatalysts using X-ray Absorption Near Edge Structure Spectroscopy. *Phys. Chem. Chem. Phys.* **2020**, *22*, 18902−18910.
(91) Teo, B. K. Chemical Applications of Extended X-Ray Absorption Fine-Structure (Exafs) Spectroscopy. *Acc. Chem. Res.* **1980**, *13*, 412−419.

https://doi.org/10.1021/acs.chemrev.2c00495
Chem. Rev. 2023, 123, 379−444

(92) Stern, E. A. Theory of the Extended X-ray-Absorption Fine Structure. *Phys. Rev. B* **1974**, *10*, 3027−3037.
(93) Sandstrom, D. R.; Lytle, F. W. Developments in Extended X-Ray Absorption Fine-Structure Applied to Chemical-Systems. *Annu. Rev. Phys. Chem.* **1979**, *30*, 215−238.
(94) Frenkel, A. I.; Hills, C. W.; Nuzzo, R. G. A View from the Inside: Complexity in the Atomic Scale Ordering of Supported Metal Nanoparticles. *J. Phys. Chem. B* **2001**, *105*, 12689−12703.
(95) Clausen, B. S.; Nørskov, J. K. Asymmetric Pair Distribution Functions in Catalysts. *Top. Catal.* **2000**, *10*, 221−230.
(96) Hayes, T. M.; Boyce, J. B. Extended X-Ray Absorption Fine Structure Spectroscopy. *Sol. St. Phys.* **1983**, *37*, 173−351.
(97) Newville, M. Larch: An Analysis Package for XAFS and Related Spectroscopies. *J. Phys.: Conf. Ser.* **2013**, *430* (012007), 012007.
(98) Ravel, B.; Newville, M. ATHENA, ARTEMIS, HEPHAESTUS: Data Analysis for X-ray Absorption Spectroscopy Using IFEFFIT. *J. Synch. Rad.* **2005**, *12*, 537−541.
(99) Rehr, J. J.; Kas, J. J.; Prange, M. P.; Sorini, A. P.; Takimoto, Y.; Vila, F. Ab Initio Theory and Calculations of X-ray Spectra. *C R Phys.* **2009**, *10*, 548−559.
(100) Rehr, J. J.; Albers, R. C. Theoretical Approaches to X-ray Absorption Fine Structure. *Rev. Mod. Phys.* **2000**, *72*, 621−654.
(101) Filipponi, A.; Di Cicco, A.; Natoli, C. R. X-ray-Absorption Spectroscopy and n-body Distribution Functions in Condensed Matter. I. Theory. *Phys. Rev. B* **1995**, *52*, 15122−15134.
(102) Filipponi, A.; Di Cicco, A. X-ray-Absorption Spectroscopy and n-body Distribution Functions in Condensed Matter. II. Data analysis and Applications. *Phys. Rev. B* **1995**, *52*, 15135−15149.
(103) Li, G. G.; Bridges, F.; Booth, C. H. X-Ray-Absorption Fine-Structure Standards - a Comparison of Experiment and Theory. *Phys. Rev. B* **1995**, *52*, 6332−6348.
(104) Calvin, S. *XAFS for everyone*; CRC Press, 2013.
(105) Muñoz, M.; Argoul, P.; Farges, F. Continuous Cauchy Wavelet Transform Analyses of EXAFS spectra: A Qualitative Approach. *Am. Mineral.* **2003**, *88*, 694−700.
(106) Funke, H.; Scheinost, A. C.; Chukalina, M. Wavelet Analysis of Extended X-ray Absorption Fine Structure Data. *Phys. Rev. B* **2005**, *71*, 094110.
(107) Timoshenko, J.; Kuzmin, A. Wavelet Data Analysis of EXAFS Spectra. *Comput. Phys. Commun.* **2009**, *180*, 920−925.
(108) Pankin, I. A.; Martini, A.; Lomachenko, K. A.; Soldatov, A. V.; Bordiga, S.; Borfecchia, E. Identifying Cu-oxo Species in Cu-zeolites by XAS: A Theoretical Survey by DFT-Assisted XANES Simulation and EXAFS Wavelet Transform. *Catal. Today* **2020**, *345*, 125−135.
(109) Lien, H.-T.; Chang, S.-T.; Chen, P.-T.; Wong, D. P.; Chang, Y.-C.; Lu, Y.-R.; Dong, C.-L.; Wang, C.-H.; Chen, K.-H.; Chen, L.-C. Probing the Active Site in Single-atom Oxygen Reduction Catalysts via Operando X-ray and Electrochemical Spectroscopy. *Nat. Commun.* **2020**, *11*, 4233.
(110) Shi, J.; Wei, Y.; Zhou, D.; Zhang, L.; Yang, X.; Miao, Z.; Qi, H.; Zhang, S.; Li, A.; Liu, X.; et al. Introducing Co-O Moiety to Co-N-C Single-Atom Catalyst for Ethylbenzene Dehydrogenation. *ACS Catal.* **2022**, *12*, 7760−7772.
(111) Frei, E.; Gaur, A.; Lichtenberg, H.; Heine, C.; Friedrich, M.; Greiner, M.; Lunkenbein, T.; Grunwaldt, J.-D.; Schlögl, R. Activating a Cu/ZnO: Al Catalyst - Much More than Reduction: Decomposition, Self-Doping and Polymorphism. *ChemCatChem.* **2019**, *11*, 1587−1592.
(112) Sayers, D. E.; Stern, E. A.; Lytle, F. W. New Technique for Investigating Noncrystalline Structures: Fourier Analysis of the Extended X-Ray Absorption Fine Structure. *Phys. Rev. Lett.* **1971**, *27*, 1204−1207.
(113) Via, G. H.; Sinfelt, J. H.; Lytle, F. W. Extended X-ray Absorption Fine Structure (EXAFS) of Dispersed Metal Catalysts. *J. Chem. Phys.* **1979**, *71*, 690−699.
(114) Clausen, B. S.; Topsoe, H.; Candia, R.; Villadsen, J.; Lengeler, B.; Als-Nielsen, J.; Christensen, F. Extended X-ray Absorption Fine Structure Study of the Cobalt-Molybdenum Hydrodesulfurization Catalysts. *J. Phys. Chem.* **1981**, *85*, 3868−3872.
(115) Sato, Y.; Iwasawa, Y.; Kuroda, H. EXAFS Study of Highly Active Mo_2 Catalyst. *Chem. Lett.* **1982**, *11*, 1101−1104.
(116) Asakura, K.; Kitamura-Bando, K.; Iwasawa, Y.; Arakawa, H.; Isobe, K. Metal-assisted Hydroformylation on a SiO_2-Attached Rhodium Dimer. In-situ EXAFS and FT-IR Observations of the Dynamic Behaviors of the Dimer Site. *J. Am. Chem. Soc.* **1990**, *112*, 9096−9104.
(117) Frenkel, A. Solving the Structure of Nanoparticles by Multiple-Scattering EXAFS Analysis. *J. Syn. Rad.* **1999**, *6*, 293−295.
(118) Calvin, S.; Miller, M. M.; Goswami, R.; Cheng, S. F.; Mulvaney, S. P.; Whitman, L. J.; Harris, V. G. Determination of Crystallite Size in a Magnetic Nanocomposite Using Extended X-ray Absorption Fine Structure. *J. Appl. Phys.* **2003**, *94*, 778−783.
(119) Marinkovic, N. S.; Sasaki, K.; Adzic, R. R. Determination of Single- and Multi-Component Nanoparticle Sizes by X-ray Absorption Spectroscopy. *J. Electro. Soc.* **2018**, *165*, J3222−J3230.
(120) van Bokhoven, J. A.; Lambertti, C. *X-Ray Absorption and X-Ray Emission Spectroscopy Theory and Applications*; John Wiley & Sons, Inc.: Chichester, West Sussex, 2016.
(121) Zimmermann, P.; Peredkov, S.; Abdala, P. M.; DeBeer, S.; Tromp, M.; Müller, C.; van Bokhoven, J. A. Modern X-ray Spectroscopy: XAS and XES in the Laboratory. *Coord. Chem. Rev.* **2020**, *423*, 213466.
(122) Rehr, J. J.; Ankudinov, A. L. Progress in the Theory and Interpretation of XANES. *Coord. Chem. Rev.* **2005**, *249*, 131−140.
(123) Bordiga, S.; Groppo, E.; Agostini, G.; van Bokhoven, J. A.; Lamberti, C. Reactivity of Surface Species in Heterogeneous Catalysts Probed by In-situ X-ray Absorption Techniques. *Chem. Rev.* **2013**, *113*, 1736−850.
(124) van Bokhoven, J. A.; Lambertti, C. Structure of Aluminum, Iron, and Other Heteroatoms in Zeolites by X-ray Absorption Spectroscopy. *Coord. Chem. Rev.* **2014**, *277*−*278*, 275−290.
(125) Grunwaldt, J.-D.; Frenkel, A. I. Synchrotron Radiation and Neutrons for Catalysis, Materials Research and Development. *Syn. Rad. News* **2018**, *31*, 56−58.
(126) Timoshenko, J.; Roldan Cuenya, B. In-Situ/Operando Electrocatalyst Characterization by X-ray Absorption Spectroscopy. *Chem. Rev.* **2021**, *121*, 882−961.
(127) Li, Y.; Frenkel, A. I. Deciphering the Local Environment of Single-Atom Catalysts with X-ray Absorption Spectroscopy. *Acc. Chem. Res.* **2021**, *54*, 2660−2669.
(128) Kottwitz, M.; Li, Y.; Wang, H.; Frenkel, A. I.; Nuzzo, R. G. Single Atom Catalysts: A Review of Characterization Methods. *Chemistry-Methods* **2021**, *1*, 278−294.
(129) Glatzel, P.; Sikora, M.; Smolentsev, G.; Fernández-García, M. Hard X-ray Photon-in Photon-out Spectroscopy. *Catal. Today* **2009**, *145*, 294−299.
(130) Lancaster, K. M.; Roemelt, M.; Ettenhuber, P.; Hu, Y.; Ribbe, M. W.; Neese, F.; Bergmann, U.; DeBeer, S. X-ray Emission Spectroscopy Evidences a Central Carbon in the Nitrogenase Iron-Molybdenum Cofactor. *Science* **2011**, *334*, 974.
(131) Delgado-Jaime, M. U.; Dible, B. R.; Chiang, K. P.; Brennessel, W. W.; Bergmann, U.; Holland, P. L.; DeBeer, S. Identification of a Single Light Atom within a Multinuclear Metal Cluster Using Valence-to-Core X-ray Emission Spectroscopy. *Inorg. Chem.* **2011**, *50*, 10709−10717.
(132) Boubnov, A.; Carvalho, H. W. P.; Doronkin, D. E.; Günter, T.; Gallo, E.; Atkins, A. J.; Jacob, C. R.; Grunwaldt, J.-D. Selective Catalytic Reduction of NO Over Fe-ZSM-5: Mechanistic Insights by Operando HERFD-XANES and Valence-to-Core X-ray Emission Spectroscopy. *J. Am. Chem. Soc.* **2014**, *136*, 13006−13015.
(133) Ferri, D.; Newton, M. A.; Nachtegaal, M. Modulation Excitation X-Ray Absorption Spectroscopy to Probe Surface Species on Heterogeneous Catalysts. *Top. Catal.* **2011**, *54*, 1070.
(134) Stötzel, J.; Lützenkirchen-Hecht, D.; Frahm, R.; Kimmerle, B.; Baiker, A.; Nachtegaal, M.; Beier, M. J.; Grunwaldt, J.-D. Investigation of the Ignition Behaviour of the Noble Metal Catalyzed Catalytic Partial Oxidation of Methane. *J. Phys. Conf. Ser.* **2009**, *190*, 012162.

https://doi.org/10.1021/acs.chemrev.2c00495
Chem. Rev. 2023, 123, 379−444

(135) Eyssler, A.; Kleymenov, E.; Kupferschmid, A.; Nachtegaal, M.; Kumar, M. S.; Hug, P.; Weidenkaff, A.; Ferri, D. Improvement of Catalytic Activity of $LaFe_{0.95}Pd_{0.05}O_3$ for Methane Oxidation under Transient Conditions. *J. Phys. Chem. C* **2011**, *115*, 1231−1239.
(136) Gaur, A.; Hartmann Dabros, T. M.; Høj, M.; Boubnov, A.; Prüssmann, T.; Jelic, J.; Studt, F.; Jensen, A. D.; Grunwaldt, J.-D. Probing the Active Sites of MoS_2 Based Hydrotreating Catalysts Using Modulation Excitation Spectroscopy. *ACS Catal.* **2019**, *9*, 2568−2579.
(137) König, C. F. J.; van Bokhoven, J. A.; Schildhauer, T. J.; Nachtegaal, M. Quantitative Analysis of Modulated Excitation X-ray Absorption Spectra: Enhanced Precision of EXAFS Fitting. *Phys. Chem. C* **2012**, *116*, 19857−19866.
(138) Guda, A. A.; Guda, S. A.; Lomachenko, K. A.; Soldatov, M. A.; Pankin, I. A.; Soldatov, A. V.; Braglia, L.; Bugaev, A. L.; Martini, A.; Signorile, M.; et al. Quantitative Structural Determination of Active Sites from In-situ and Operando XANES Spectra: From Standard ab initio Simulations to Chemometric and Machine Learning Approaches. *Catal. Today* **2019**, *336*, 3−21.
(139) Voronov, A.; Urakawa, A.; van Beek, W.; Tsakoumis, N. E.; Emerich, H.; Rønning, M. Multivariate Curve Resolution Applied to In-situ X-ray Absorption Spectroscopy Data: An Efficient Tool for Data Processing and Analysis. *Anal. Chim. Acta* **2014**, *840*, 20−27.
(140) Liu, C.-H.; Wright, C. J.; Gu, R.; Bandi, S.; Wustrow, A.; Todd, P. K.; O'Nolan, D.; Beauvais, M. L.; Neilson, J. R.; Chupas, P. J.; et al. Validation of Non-negative Matrix Factorization for Rapid Assessment of Large Sets of Atomic Pair Distribution Function Data. *J. Appl. Cryst.* **2021**, *54*, 768−775.
(141) Beckwith, M. A.; Ames, W.; Vila, F. D.; Krewald, V.; Pantazis, D. A.; Mantel, C.; Pécaut, J.; Gennari, M.; Duboc, C.; Collomb, M.-N.; et al. How Accurately Can Extended X-ray Absorption Spectra Be Predicted from First Principles? Implications for Modeling the Oxygen-Evolving Complex in Photosystem II. *J. Am. Chem. Soc.* **2015**, *137*, 12815−12834.
(142) Ji, S.; Chen, Y.; Wang, X.; Zhang, Z.; Wang, D.; Li, Y. Chemical Synthesis of Single Atomic Site Catalysts. *Chem. Rev.* **2020**, *120*, 11900−11955.
(143) Chen, Y.; Ji, S.; Chen, C.; Peng, Q.; Wang, D.; Li, Y. Single-Atom Catalysts: Synthetic Strategies and Electrochemical Applications. *Joule* **2018**, *2*, 1242−1264.
(144) Cheng, N.; Zhang, L.; Doyle-Davis, K.; Sun, X. Single-Atom Catalysts: From Design to Application. *Electro. Ener. Rev.* **2019**, *2*, 539−573.
(145) Jones, J.; Xiong, H.; DeLaRiva, A. T.; Peterson, E. J.; Pham, H.; Challa, S. R.; Qi, G.; Oh, S.; Wiebenga, M. H.; Hernández, X. I. P.; Wang, Y.; et al. Thermally Stable Single-Atom Platinum-on-Ceria Catalysts via Atom Trapping. *Science* **2016**, *353*, 150−154.
(146) Amrute, P.; Łodziana, Z.; Schreyer, H.; Weidenthaler, C.; Schüth, F. High-Surface-Area Corundum by Mechanochemically Induced Phase Transformation of Boehmite. *Science* **2019**, *366*, 485−489.
(147) He, X.; Deng, Y.; Zhang, Y.; He, Q.; Xiao, D.; Peng, M.; Zhao, Y.; Zhang, H.; Luo, R.; Gan, T.; et al. Mechanochemical Kilogram-Scale Synthesis of Noble Metal Single-Atom Catalysts. *Cell Rep. Phys. Sci.* **2020**, *1*, 100004.
(148) Wang, X.; Chen, X.; Thomas, A.; Fu, X.; Antonietti, M. Metal-Containing Carbon Nitride Compounds: A New Functional Organic-Metal Hybrid Material. *Adv. Mater.* **2009**, *21*, 1609−1612.
(149) Yang, S.; Kim, J.; Tak, Y. J.; Soon, A.; Lee, H. Single-Atom Catalyst of Platinum Supported on Titanium Nitride for Selective Electrochemical Reactions. *Angew. Chem., Int. Ed.* **2016**, *55*, 2058−2062.
(150) Lin, L.; Zhou, W.; Gao, R.; Yao, S.; Zhang, X.; Xu, W.; Zheng, S.; Jiang, Z.; Yu, Q.; Li, Y.-W.; et al. Low-Temperature Hydrogen Production from Water and Methanol using Pt/α-MoC Catalysts. *Nature* **2017**, *544*, 80−83.
(151) Lin, L.; Yao, S.; Gao, R.; Liang, X.; Yu, Q.; Deng, Y.; Liu, J.; Peng, M.; Jiang, Z.; Li, S.; et al. A Highly CO-Tolerant Atomically Dispersed Pt Catalyst for Chemoselective Hydrogenation. *Nat. Nanotechnol.* **2019**, *14*, 354−361.
(152) DeRita, L.; Resasco, J.; Dai, S.; Boubnov, A.; Thang, H. V.; Hoffman, A. S.; Ro, I.; Graham, G. W.; Bare, S. R.; Pacchioni, G.; et al. Structural Evolution of Atomically Dispersed Pt Catalysts Dictates Reactivity. *Nat. Mater.* **2019**, *18*, 746−751.
(153) Lin, J.; Qiao, B.; Liu, J.; Huang, Y.; Wang, A.; Li, L.; Zhang, W.; Allard, L. F.; Wang, X.; Zhang, T. Design of a Highly Active Ir/$Fe(OH)_x$ Catalyst: Versatile Application of Pt-Group Metals for the Preferential Oxidation of Carbon Monoxide. *Angew. Chem., Int. Ed.* **2012**, *51*, 2920−2924.
(154) Han, A.; Zhang, J.; Sun, W.; Chen, W.; Zhang, S.; Han, Y.; Feng, Q.; Zheng, L.; Gu, L.; Chen, C.; et al. Isolating Contiguous Pt Atoms and Forming Pt-Zn Intermetallic Nanoparticles to Regulate Selectivity in 4-nitrophenylacetylene Hydrogenation. *Nat. Commun.* **2019**, *10*, 3787.
(155) Qiao, B.; Liang, J.-X.; Wang, A.; Xu, C.-Q.; Li, J.; Zhang, T.; Liu, J. J. Ultrastable Single-Atom Gold Catalysts with Strong Covalent Metal-Support Interaction (CMSI). *Nano Res.* **2015**, *8*, 2913−2924.
(156) Li, T.; Liu, F.; Tang, Y.; Li, L.; Miao, S.; Su, Y.; Zhang, J.; Huang, J.; Sun, H.; Haruta, M.; et al. Maximizing the Number of Interfacial Sites in Single-Atom Catalysts for the Highly Selective, Solvent-Free Oxidation of Primary Alcohols. *Angew. Chem., Int. Ed.* **2018**, *57*, 7795−7799.
(157) George, S. M. Atomic Layer Deposition: An Overview. *Chem. Rev.* **2010**, *110*, 111−131.
(158) Sun, S.; Zhang, G.; Gauquelin, N.; Chen, N.; Zhou, J.; Yang, S.; Chen, W.; Meng, X.; Geng, D.; Banis, M. N. Single-atom Catalysis Using Pt/Graphene Achieved through Atomic Layer Deposition. *Sci. Rep.* **2013**, *3*, 1775 DOI: 10.1038/srep01775.
(159) Zhang, L.; Banis, M. N.; Sun, X. Single-atom Catalysts by the Atomic Layer Deposition Technique. *Nat. Sci. Rev.* **2018**, *5*, 628−630.
(160) Yan, H.; Cheng, H.; Yi, H.; Lin, Y.; Yao, T.; Wang, C.; Li, J.; Wei, S.; Lu, J. Single-Atom Pd_1/Graphene Catalyst Achieved by Atomic Layer Deposition: Remarkable Performance in Selective Hydrogenation of 1,3-Butadiene. *J. Am. Chem. Soc.* **2015**, *137*, 10484−10487.
(161) Stambula, S.; Gauquelin, N.; Bugnet, M.; Gorantla, S.; Turner, S.; Sun, S.; Liu, J.; Zhang, G.; Sun, X.; Botton, G. A. Chemical Structure of Nitrogen-Doped Graphene with Single Platinum Atoms and Atomic Clusters as a Platform for the PEMFC Electrode. *J. Phys. Chem. C* **2014**, *118*, 3890−3900.
(162) Liu, P.; Zhao, Y.; Qin, R.; Mo, S.; Chen, G.; Gu, L.; Chevrier, D. M.; Zhang, P.; Guo, Q.; Zang, D.; et al. Photochemical Route for Synthesizing Atomically Dispersed Palladium Catalysts. *Science* **2016**, *352*, 797.
(163) Wei, H.; Huang, K.; Wang, D.; Zhang, R.; Ge, B.; Ma, J.; Wen, B.; Zhang, S.; Li, Q.; Lei, M.; et al. Iced Photochemical Reduction to Synthesize Atomically Dispersed Metals by Suppressing Nanocrystal Growth. *Nat. Commun.* **2017**, *8*, 1490.
(164) Ge, X.; Zhou, P.; Zhang, Q.; Xia, Z.; Chen, S.; Gao, P.; Zhang, Z.; Gu, L.; Guo, S. Palladium Single Atoms on TiO_2 as a Photocatalytic Sensing Platform for Analyzing the Organophosphorus Pesticide Chlorpyrifos. *Angew. Chem., Int. Ed.* **2020**, *59*, 232−236.
(165) Fan, L.; Liu, P. F.; Yan, X.; Gu, L.; Yang, Z. Z.; Yang, H. G.; Qiu, S.; Yao, X. Atomically Isolated Nickel Species Anchored on Graphitized Carbon for Efficient Hydrogen Evolution Electrocatalysis. *Nat. Commun.* **2016**, *7*, 10667.
(166) Tavakkoli, M.; Holmberg, N.; Kronberg, R.; Jiang, H.; Sainio, J.; Kauppinen, E. I.; Kallio, T.; Laasonen, K. Electrochemical Activation of Single-Walled Carbon Nanotubes with Pseudo-Atomic-Scale Platinum for the Hydrogen Evolution Reaction. *ACS Catal.* **2017**, *7*, 3121−3130.
(167) Zhang, L.; Han, L.; Liu, H.; Liu, X.; Luo, J. Potential-Cycling Synthesis of Single Platinum Atoms for Efficient Hydrogen Evolution in Neutral Media. *Angew. Chem., Int. Ed.* **2017**, *56*, 13694−13698.
(168) Zhang, L.; Jia, Y.; Liu, H.; Zhuang, L.; Yan, X.; Lang, C.; Wang, X.; Yang, D.; Huang, K.; Feng, S.; et al. Charge Polarization from Atomic Metals on Adjacent Graphitic Layers for Enhancing the Hydrogen Evolution Reaction. *Angew. Chem., Int. Ed.* **2019**, *58*, 9404−9408.
(169) Nilius, N.; Sterrer, M.; Heyde, M.; Freund, H.-J. Atomic Scale Characterization of Defects on Oxide Surfaces. In *Defects at Oxide*

Surfaces; Jupille, J., Thornton, G., Eds.; Springer International Publishing: Cham, 2015; pp 29−80.
(170) Tuller, H. L.; Bishop, S. R. Point Defects in Oxides: Tailoring Materials Through Defect Engineering. *Annu. Rev. Mater. Res.* **2011**, *41*, 369−398.
(171) Nörenberg, H.; Briggs, G. A. D. Defect Formation on CeO_2(111) Surfaces After Annealing Studied by STM. *Surf. Sci.* **1999**, *424*, 352−355.
(172) Ricci, D.; Di Valentin, C.; Pacchioni, G.; Sushko, P. V.; Shluger, A. L.; Giamello, E. Paramagnetic Defect Centers at the MgO Surface. An Alternative Model to Oxygen Vacancies. *J. Am. Chem. Soc.* **2003**, *125*, 738−747.
(173) Xie, J.; Zhang, H.; Li, S.; Wang, R.; Sun, X.; Zhou, M.; Zhou, J.; Lou, X. W.; Xie, Y. Defect-Rich MoS_2 Ultrathin Nanosheets with Additional Active Edge Sites for Enhanced Electrocatalytic Hydrogen Evolution. *Adv. Mater.* **2013**, *25*, 5807−5813.
(174) Sang, X.; Xie, Y.; Lin, M.-W.; Alhabeb, M.; Van Aken, K. L.; Gogotsi, Y.; Kent, P. R. C.; Xiao, K.; Unocic, R. R. Atomic Defects in Monolayer Titanium Carbide ($Ti_3C_2T_x$) MXene. *ACS Nano* **2016**, *10*, 9193−9200.
(175) Zhang, N.; Jalil, A.; Wu, D.; Chen, S.; Liu, Y.; Gao, C.; Ye, W.; Qi, Z.; Ju, H.; Wang, C.; et al. Refining Defect States in $W_{18}O_{49}$ by Mo Doping: A Strategy for Tuning N_2 Activation towards Solar-Driven Nitrogen Fixation. *J. Am. Chem. Soc.* **2018**, *140*, 9434−9443.
(176) Boubnov, A.; Roppertz, A.; Kundrat, M. D.; Mangold, S.; Reznik, B.; Jacob, C. R.; Kureti, S.; Grunwaldt, J.-D. Towards Advanced Structural Analysis of Iron Oxide Clusters on the Surface of γ-Al_2O_3 using EXAFS. *Appl. Surf. Sci.* **2016**, *386*, 234−246.
(177) Xiao, L.; Wang, L. Structures of Platinum Clusters: Planar or Spherical? *J. Phys. Chem. A* **2004**, *108*, 8605−8614.
(178) Taylor, K. *Automobile catalytic converters*; Springer: Berlin, 1984.
(179) Grunwaldt, J.-D.; Maciejewski, M.; Becker, O. S.; Fabrizioli, P.; Baiker, A. Comparative Study of Au/TiO_2 and Au/ZrO_2 Catalysts for Low-Temperature CO Oxidation. *J. Catal.* **1999**, *186*, 458−469.
(180) Li, F.; Li, Y.; Zeng, X. C.; Chen, Z. Exploration of High-Performance Single-Atom Catalysts on Support M_1/FeO_x for CO Oxidation via Computational Study. *ACS Catal.* **2015**, *5*, 544−552.
(181) Lin, J.; Wang, A.; Qiao, B.; Liu, X.; Yang, X.; Wang, X.; Liang, J.; Li, J.; Liu, J.; Zhang, T. Remarkable Performance of Ir_1/FeO_x Single-Atom Catalyst in Water Gas Shift Reaction. *J. Am. Chem. Soc.* **2013**, *135*, 15314−15317.
(182) Yang, M.; Allard, L. F.; Flytzani-Stephanopoulos, M. Atomically Dispersed Au-$(OH)_x$ Species Bound on Titania Catalyze the Low-Temperature Water-Gas Shift Reaction. *J. Am. Chem. Soc.* **2013**, *135*, 3768−3771.
(183) Ammal, S. C.; Heyden, A. Water-Gas Shift Activity of Atomically Dispersed Cationic Platinum versus Metallic Platinum Clusters on Titania Supports. *ACS Catal.* **2017**, *7*, 301−309.
(184) Gu, X.-K.; Huang, C.-Q.; Li, W.-X. First-Principles Study of Single Transition Metal Atoms on ZnO for the Water Gas Shift Reaction. *Catal. Sci.Technol.* **2017**, *7*, 4294−4301.
(185) Moses-DeBusk, M.; Yoon, M.; Allard, L. F.; Mullins, D. R.; Wu, Z.; Yang, X.; Veith, G.; Stocks, G. M.; Narula, C. K. CO Oxidation on Supported Single Pt Atoms: Experimental and ab Initio Density Functional Studies of CO Interaction with Pt Atom on θ-Al_2O_3(010) Surface. *J. Am. Chem. Soc.* **2013**, *135*, 12634−12645.
(186) Peterson, E. J.; DeLaRiva, A. T.; Lin, S.; Johnson, R. S.; Guo, H.; Miller, J. T.; Hun Kwak, J.; Peden, C. H.; Kiefer, B.; Allard, L. F.; et al. Low-temperature Carbon Monoxide Oxidation Catalysed by Regenerable Atomically Dispersed Palladium on Alumina. *Nat. Commun.* **2014**, *5*, 4885.
(187) Li, Z.-Y.; Yuan, Z.; Li, X.-N.; Zhao, Y.-X.; He, S.-G. CO Oxidation Catalyzed by Single Gold Atoms Supported on Aluminum Oxide Clusters. *J. Am. Chem. Soc.* **2014**, *136*, 14307−14313.
(188) Yuan, Z.; Li, X.-N.; He, S.-G. CO Oxidation Promoted by Gold Atoms Loosely Attached in $AuFeO_3$- Cluster Anions. *J. Phys. Chem. Lett.* **2014**, *5*, 1585−1590.
(189) Qiao, B.; Liu, J.; Wang, Y.-G.; Lin, Q.; Liu, X.; Wang, A.; Li, J.; Zhang, T.; Liu, J. Highly Efficient Catalysis of Preferential Oxidation of CO in H_2-Rich Stream by Gold Single-Atom Catalysts. *ACS Catal.* **2015**, *5*, 6249−6254.
(190) Qiao, B.; Lin, J.; Wang, A.; Chen, Y.; Zhang, T.; Liu, J. Highly Active Au_1/Co_3O_4 Single-atom Catalyst for CO Oxidation at Room Temperature. *Chin. J. Catal.* **2015**, *36*, 1505−1511.
(191) Beniya, A.; Higashi, S. Towards Dense Single-atom Catalysts for Future Automotive Applications. *Nat. Catal.* **2019**, *2*, 590−602.
(192) Guo, X.; Fang, G.; Li, G.; Ma, H.; Fan, H.; Yu, L.; Ma, C.; Wu, X.; Deng, D.; Wei, M.; et al. Direct, Nonoxidative Conversion of Methane to Ethylene, Aromatics, and Hydrogen. *Science* **2014**, *344*, 616−619.
(193) Kwon, Y.; Kim, T. Y.; Kwon, G.; Yi, J.; Lee, H. Selective Activation of Methane on Single-Atom Catalyst of Rhodium Dispersed on Zirconia for Direct Conversion. *J. Am. Chem. Soc.* **2017**, *139*, 17694−17699.
(194) Xie, P.; Pu, T.; Nie, A.; Hwang, S.; Purdy, S. C.; Yu, W.; Su, D.; Miller, J. T.; Wang, C. Nanoceria-Supported Single-Atom Platinum Catalysts for Direct Methane Conversion. *ACS Catal.* **2018**, *8*, 4044−4048.
(195) Millet, M.-M.; Algara-Siller, G.; Wrabetz, S.; Mazheika, A.; Girgsdies, F.; Teschner, D.; Seitz, F.; Tarasov, A.; Levchenko, S. V.; Schlögl, R.; et al. Ni Single Atom Catalysts for CO_2 Activation. *J. Am. Chem. Soc.* **2019**, *141*, 2451−2461.
(196) Li, Y.; Hao, J.; Song, H.; Zhang, F.; Bai, X.; Meng, X.; Zhang, H.; Wang, S.; Hu, Y.; Ye, J. Selective Light Absorber-Assisted Single Nickel Atom Catalysts for Ambient Sunlight-driven CO_2 Methanation. *Nat. Commun.* **2019**, *10*, 2359.
(197) Zhu, Y.; Yuk, S. F.; Zheng, J.; Nguyen, M.-T.; Lee, M.-S.; Szanyi, J.; Kovarik, L.; Zhu, Z.; Balasubramanian, M.; Glezakou, V.-A.; et al. Environment of Metal-O-Fe Bonds Enabling High Activity in CO_2 Reduction on Single Metal Atoms and on Supported Nanoparticles. *J. Am. Chem. Soc.* **2021**, *143*, 5540−5549.
(198) Wei, H.; Liu, X.; Wang, A.; Zhang, L.; Qiao, B.; Yang, X.; Huang, Y.; Miao, S.; Liu, J.; Zhang, T. FeO_x-Supported Platinum Single-Atom and Pseudo-Single-Atom Catalysts for Chemoselective Hydrogenation of Functionalized Nitroarenes. *Nat. Commun.* **2014**, *5*, 5634.
(199) Xu, G.; Wei, H.; Ren, Y.; Yin, J.; Wang, A.; Zhang, T. Chemoselective Hydrogenation of 3-Nitrostyrene over a Pt/FeO_x Pseudo-Single-Atom-Catalyst in CO_2-expanded Liquids. *Green Chem.* **2016**, *18*, 1332−1338.
(200) Zhang, Z.; Zhu, Y.; Asakura, H.; Zhang, B.; Zhang, J.; Zhou, M.; Han, Y.; Tanaka, T.; Wang, A.; Zhang, T.; Yan, N. Thermally Stable Single Atom Pt/m-Al_2O_3 for Selective Hydrogenation and CO Oxidation. *Nat. Commun.* **2017**, *8*, 16100.
(201) Kuo, C.-T.; Lu, Y.; Kovarik, L.; Engelhard, M.; Karim, A. M. Structure Sensitivity of Acetylene Semi-Hydrogenation on Pt Single Atoms and Subnanometer Clusters. *ACS Catal.* **2019**, *9*, 11030−11041.
(202) Ma, Y.; Chi, B.; Liu, W.; Cao, L.; Lin, Y.; Zhang, X.; Ye, X.; Wei, S.; Lu, J. Tailoring of the Proximity of Platinum Single Atoms on CeO_2 Using Phosphorus Boosts the Hydrogenation Activity. *ACS Catal.* **2019**, *9*, 8404−8412.
(203) Gu, X.-K.; Qiao, B.; Huang, C.-Q.; Ding, W.-C.; Sun, K.; Zhan, E.; Zhang, T.; Liu, J.; Li, W.-X. Supported Single Pt_1/Au_1 Atoms for Methanol Steam Reforming. *ACS Catal.* **2014**, *4*, 3886−3890.
(204) Duarte, R. B.; Krumeich, F.; van Bokhoven, J. A. Structure, Activity, and Stability of Atomically Dispersed Rh in Methane Steam Reforming. *ACS Catal.* **2014**, *4*, 1279−1286.
(205) Chen, L.; Qi, Z.; Peng, X.; Chen, J.-L.; Pao, C.-W.; Zhang, X.; Dun, C.; Young, M.; Prendergast, D.; Urban, J. J.; et al. Insights into the Mechanism of Methanol Steam Reforming Tandem Reaction over CeO_2 Supported Single-Site Catalysts. *J. Am. Chem. Soc.* **2021**, *143*, 12074−12081.
(206) Zhang, S.; Chen, L.; Qi, Z.; Zhuo, L.; Chen, J.-L.; Pao, C.-W.; Su, J.; Somorjai, G. A. Insights into the Mechanism of n-Hexane Reforming over a Single-Site Platinum Catalyst. *J. Am. Chem. Soc.* **2020**, *142*, 16533−16537.
(207) Narula, C. K.; Allard, L. F.; Stocks, G. M.; Moses-DeBusk, M. Remarkable NO Oxidation on Single Supported Platinum Atoms. *Sci. Rep.* **2015**, *4*, 7238.

https://doi.org/10.1021/acs.chemrev.2c00495
Chem. Rev. 2023, 123, 379−444

(208) Lang, R.; Li, T.; Matsumura, D.; Miao, S.; Ren, Y.; Cui, Y. T.; Tan, Y.; Qiao, B.; Li, L.; Wang, A.; et al. Hydroformylation of Olefins by a Rhodium Single-Atom Catalyst with Activity Comparable to $RhCl(PPh_3)_3$. *Angew. Chem., Int. Ed.* **2016**, *55*, 16054−16058.
(209) Wang, L.; Zhang, W.; Wang, S.; Gao, Z.; Luo, Z.; Wang, X.; Zeng, R.; Li, A.; Li, H.; Wang, M.; et al. Atomic-level Insights in Optimizing Reaction Paths for Hydroformylation Reaction over Rh/CoO Single-Atom Catalyst. *Nat. Commun.* **2016**, *7*, 14036.
(210) Amsler, J.; Sarma, B. B.; Agostini, G.; Prieto, G.; Plessow, P. N.; Studt, F. Prospects of Heterogeneous Hydroformylation with Supported Single Atom Catalysts. *J. Am. Chem. Soc.* **2020**, *142*, 5087−5096.
(211) Li, T.; Chen, F.; Lang, R.; Wang, H.; Su, Y.; Qiao, B.; Wang, A.; Zhang, T. Styrene Hydroformylation with In Situ Hydrogen: Regioselectivity Control by Coupling with the Low-Temperature Water-Gas Shift Reaction. *Angew. Chem., Int. Ed.* **2020**, *59*, 7430−7434.
(212) Cui, X.; Junge, K.; Dai, X.; Kreyenschulte, C.; Pohl, M. M.; Wohlrab, S.; Shi, F.; Brückner, A.; Beller, M. Synthesis of Single Atom Based Heterogeneous Platinum Catalysts: High Selectivity and Activity for Hydrosilylation Reactions. *ACS Cent. Sci.* **2017**, *3*, 580−585.
(213) Sarma, B. B.; Kim, J.; Amsler, J.; Agostini, G.; Weidenthaler, C.; Pfänder, N.; Arenal, R.; Concepción, P.; Plessow, P.; Studt, F.; et al. One-Pot Cooperation of Single-Atom Rh and Ru Solid Catalysts for a Selective Tandem Olefin Isomerization-Hydrosilylation Process. *Angew. Chem., Int. Ed.* **2020**, *59*, 5806−5815.
(214) Sui, Y.; Liu, S.; Li, T.; Liu, Q.; Jiang, T.; Guo, Y.; Luo, J.-L. Atomically Dispersed Pt on Specific TiO_2 Facets for Photocatalytic H_2 Evolution. *J. Catal.* **2017**, *353*, 250−255.
(215) Liu, J.-C.; Wang, Y.-G.; Li, J. Toward Rational Design of Oxide-Supported Single-Atom Catalysts: Atomic Dispersion of Gold on Ceria. *J. Am. Chem. Soc.* **2017**, *139*, 6190−6199.
(216) Nie, N.; Mei, D.; Xiong, H.; Peng, B.; Ren, Z.; Pereira Hernandez, X. I.; DeLaRiva, A.; Wang, M.; Engelhard, M. H.; Kovarik, L.; et al. Activation of Surface Lattice Oxygen in Single-Atom Pt/CeO_2 for Low-Temperature CO Oxidation. *Science* **2017**, *358*, 1419−1423.
(217) Wang, C.; Gu, X.-K.; Yan, H.; Lin, Y.; Li, J.; Liu, D.; Li, W.-X.; Lu, J. Water-Mediated Mars-Van Krevelen Mechanism for CO Oxidation on Ceria-Supported Single-Atom Pt_1 Catalyst. *ACS Catal.* **2017**, *7*, 887−891.
(218) Xiong, H.; Lin, S.; Goetze, J.; Pletcher, P.; Guo, H.; Kovarik, L.; Artyushkova, K.; Weckhuysen, B. M.; Datye, A. K. Thermally Stable and Regenerable Platinum-Tin Clusters for Propane Dehydrogenation Prepared by Atom Trapping on Ceria. *Angew. Chem., Int. Ed.* **2017**, *56*, 8986−8991.
(219) Guo, Y.; Mei, S.; Yuan, K.; Wang, D.-J.; Liu, H.-C.; Yan, C.-H.; Zhang, Y.-W. Low-Temperature CO_2 Methanation over CeO_2-Supported Ru Single Atoms, Nanoclusters, and Nanoparticles Competitively Tuned by Strong Metal-Support Interactions and H-Spillover Effect. *ACS Catal.* **2018**, *8*, 6203−6215.
(220) Lou, Y.; Liu, J. CO Oxidation on Metal Oxide Supported Single Pt Atoms: The Role of the Support. *Ind. Eng. Chem. Res.* **2017**, *56*, 6916−6925.
(221) Wang, X.; Fu, X.-P.; Yu, W.-Z.; Ma, C.; Jia, C.-J.; Si, R. Synthesis of a Ceria-supported Iron-Ruthenium Oxide Catalyst and its Structural Transformation from Subnanometer Clusters to Single Atoms During the Fischer−Tropsch Synthesis Reaction. *Inorg. Chem. Front.* **2017**, *4*, 2059−2067.
(222) Lee, B.-H.; Park, S.; Kim, M.; Sinha, A. K.; Lee, S. C.; Jung, E.; Chang, W. J.; Lee, K.-S.; Kim, J. H.; Cho, S.-P.; et al. Reversible and Cooperative Photoactivation of Single-Atom Cu/TiO_2 Photocatalysts. *Nat. Mater.* **2019**, *18*, 620−626.
(223) Gumerova, N. I.; Rompel, A. Synthesis, Structures and Applications of Electron-rich Polyoxometalates. *Nat. Rev. Chem.* **2018**, *2*, 0112.
(224) Pope, M. T.; Müller, A. Polyoxometalate Chemistry: An Old Field with New Dimensions in Several Disciplines. *Angew. Chem., Int. Ed.* **1991**, *30*, 34−48.
(225) Song, Y.-F.; Tsunashima, R. Recent Advances on Polyoxometalate-based Molecular and Composite Materials. *Chem. Soc.Rev.* **2012**, *41*, 7384−7402.
(226) Patel, A.; Narkhede, N.; Singh, S.; Pathan, S. Keggin-type Lacunary and Transition Metal Substituted Polyoxometalates as Heterogeneous Catalysts: A Recent Progress. *Catal. Rev.* **2016**, *58*, 337−370.
(227) Tian, Y.; Plonka, A. M.; Ebrahim, A. M.; Palomino, R. M.; Senanayake, S. D.; Balboa, A.; Gordon, W. O.; Troya, D.; Musaev, D. G.; Morris, J. R.; et al. Correlated Multimodal Approach Reveals Key Details of Nerve-Agent Decomposition by Single-Site Zr-Based Polyoxometalates. *J. Phys. Chem. Lett.* **2019**, *10*, 2295−2299.
(228) Sarma, B. B.; Avram, L.; Neumann, R. Encapsulation of Arenes within a Porous Molybdenum Oxide $\{Mo_{132}\}$ Nanocapsule. *Chem. Eur. J.* **2016**, *22*, 15231−15236.
(229) Haviv, E.; Chen, B.; Carmieli, R.; Houben, L.; Cohen, H.; Leitus, G.; Avram, L.; Neumann, R. Guest Transition Metals in Host Inorganic Nanocapsules: Single Sites, Discrete Electron Transfer, and Atomic Scale Structure. *J. Am. Chem. Soc.* **2020**, *142*, 14504−14512.
(230) Kopilevich, S.; Gottlieb, H.; Keinan-Adamsky, K.; Müller, A.; Weinstock, I. A. The Uptake and Assembly of Alkanes within a Porous Nanocapsule in Water: New Information about Hydrophobic Confinement. *Angew. Chem., Int. Ed.* **2016**, *55*, 4476−4481.
(231) Zhang, B.; Asakura, H.; Zhang, J.; Zhang, J.; De, S.; Yan, N. Stabilizing a $Platinum_1$ Single-Atom Catalyst on Supported Phosphomolybdic Acid without Compromising Hydrogenation Activity. *Angew. Chem., Int. Ed.* **2016**, *55*, 8319−23.
(232) Zhang, B.; Asakura, H.; Yan, N. Atomically Dispersed Rhodium on Self-Assembled Phosphotungstic Acid: Structural Features and Catalytic CO Oxidation Properties. *Ind. Eng. Chem. Res.* **2017**, *56*, 3578−3587.
(233) Liu, C.-G.; Jiang, M.-X.; Su, Z.-M. Computational Study on M_1/POM Single-Atom Catalysts (M = Cu, Zn, Ag, and Au; POM = $[PW_{12}O_{40}]^{3-}$): Metal-Support Interactions and Catalytic Cycle for Alkene Epoxidation. *Inorg. Chem.* **2017**, *56*, 10496−10504.
(234) Yu, M.-a.; Feng, Y.; Gao, L.; Lin, S. Phosphomolybdic Acid Supported Single-Metal-Atom Catalysis in CO Oxidation: First-Principles Calculations. *Phys. Chem. Chem. Phys.* **2018**, *20*, 20661−20668.
(235) Hülsey, M. J.; Zhang, B.; Ma, Z.; Asakura, H.; Do, D. A.; Chen, W.; Tanaka, T.; Zhang, P.; Wu, Z.; Yan, N. In-situ Spectroscopy-Guided Engineering of Rhodium Single-Atom Catalysts for CO Oxidation. *Nat. Commun.* **2019**, *10*, 1330.
(236) Zhang, B.; Sun, G.; Ding, S.; Asakura, H.; Zhang, J.; Sautet, P.; Yan, N. Atomically Dispersed Pt_1-Polyoxometalate Catalysts: How Does Metal-Support Interaction Affect Stability and Hydrogenation Activity? *J. Am. Chem. Soc.* **2019**, *141*, 8185−8197.
(237) Corma, A. State of the Art and Future Challenges of Zeolites as Catalysts. *J. Catal.* **2003**, *216*, 298−312.
(238) Ortalan, V.; Uzun, A.; Gates, B. C.; Browning, N. D. Direct Imaging of Single Metal Atoms and Clusters in the Pores of Dealuminated HY Zeolite. *Nat. Nanotechnol.* **2010**, *5*, 506−510.
(239) Ehresmann, J. O.; Kletnieks, P. W.; Liang, A.; Bhirud, V. A.; Bagatchenko, O. P.; Lee, E. J.; Klaric, M.; Gates, B. C.; Haw, J. F. Evidence from NMR and EXAFS Studies of a Dynamically Uniform Mononuclear Single-Site Zeolite-Supported Rhodium Catalyst. *Angew. Chem., Int. Ed.* **2006**, *45*, 574−576.
(240) Uzun, A.; Bhirud, V. A.; Kletnieks, P. W.; Haw, J. F.; Gates, B. C. A Site-Isolated Iridium Diethylene Complex Supported on Highly Dealuminated Y Zeolite: Synthesis and Characterization. *J. Phys. Chem. C* **2007**, *111*, 15064−15073.
(241) McEwen, J. S.; Anggara, T.; Schneider, W. F.; Kispersky, V. F.; Miller, J. T.; Delgass, W. N.; Ribeiro, F. H. Integrated Operando X-ray Absorption and DFT Characterization of Cu-SSZ-13 Exchange Sites During the Selective Catalytic Reduction of NO_x with NH_3. *Catal. Today* **2012**, *184*, 129−144.
(242) Li, C.; Paris, C.; Martínez-Triguero, J.; Boronat, M.; Moliner, M.; Corma, A. Synthesis of Reaction-Adapted Zeolites as Methanol-to-

https://doi.org/10.1021/acs.chemrev.2c00495
Chem. Rev. 2023, 123, 379−444

Olefins Catalysts with Mimics of Reaction Intermediates as Organic Structure-Directing Agents. *Nat. Catal.* **2018**, *1*, 547−554.
(243) Hammond, C.; Forde, M. M.; Ab Rahim, M. H.; Thetford, A.; He, Q.; Jenkins, R. L.; Dimitratos, N.; Lopez-Sanchez, J. A.; Dummer, N. F.; Murphy, D. M.; et al. Direct Catalytic Conversion of Methane to Methanol in an Aqueous Medium by using Copper-Promoted Fe-ZSM-5. *Angew. Chem., Int. Ed.* **2012**, *51*, 5129−5133.
(244) Liu, Y.; Li, Z.; Yu, Q.; Chen, Y.; Chai, Z.; Zhao, G.; Liu, S.; Cheong, W.-C.; Pan, Y.; Zhang, Q.; et al. A General Strategy for Fabricating Isolated Single Metal Atomic Site Catalysts in Y Zeolite. *J. Am. Chem. Soc.* **2019**, *141*, 9305−9311.
(245) Sun, Q.; Wang, N.; Zhang, T.; Bai, R.; Mayoral, A.; Zhang, P.; Zhang, Q.; Terasaki, O.; Yu, J. Zeolite-Encaged Single-Atom Rhodium Catalysts: Highly-Efficient Hydrogen Generation and Shape-Selective Tandem Hydrogenation of Nitroarenes. *Angew. Chem., Int. Ed.* **2019**, *58*, 18570−18576.
(246) Liu, L.; Díaz, U.; Arenal, R.; Agostini, G.; Concepción, P.; Corma, A. Generation of Subnanometric Platinum with High Stability During Transformation of a 2D Zeolite into 3D. *Nat. Mater.* **2017**, *16*, 132−138.
(247) Wang, N.; Sun, Q.; Bai, R.; Li, X.; Guo, G.; Yu, J. In-situ Confinement of Ultrasmall Pd Clusters within Nanosized Silicalite-1 Zeolite for Highly Efficient Catalysis of Hydrogen Generation. *J. Am. Chem. Soc.* **2016**, *138*, 7484−7487.
(248) Lu, J.; Aydin, C.; Browning, N. D.; Gates, B. C. Imaging Isolated Gold Atom Catalytic Sites in Zeolite NaY. *Angew. Chem., Int. Ed.* **2012**, *51*, 5842−5846.
(249) Kistler, J. D.; Chotigkrai, N.; Xu, P.; Enderle, B.; Praserthdam, P.; Chen, C.-Y.; Browning, N. D.; Gates, B. C. A Single-Site Platinum CO Oxidation Catalyst in Zeolite KLTL: Microscopic and Spectroscopic Determination of the Locations of the Platinum Atoms. *Angew. Chem., Int. Ed.* **2014**, *53*, 8904−8907.
(250) Ferrando, R.; Jellinek, J.; Johnston, R. L. Nanoalloys: From Theory to Applications of Alloy Clusters and Nanoparticles. *Chem. Rev.* **2008**, *108*, 845−910.
(251) Marakatti, V. S.; Peter, S. C. Synthetically Tuned Electronic and Geometrical Properties of Intermetallic Compounds as Effective Heterogeneous Catalysts. *Prog. Solid State Chem.* **2018**, *52*, 1−30.
(252) Sankar, M.; Dimitratos, N.; Miedziak, P. J.; Wells, P. P.; Kiely, C. J.; Hutchings, G. J. Designing Bimetallic Catalysts for a Green and Sustainable Future. *Chem. Soc. Rev.* **2012**, *41*, 8099−139.
(253) Armbrüster, M.; Kovnir, K.; Behrens, M.; Teschner, D.; Grin, Y.; Schlögl, R. Pd-Ga Intermetallic Compounds as Highly Selective Semihydrogenation Catalysts. *J. Am. Chem. Soc.* **2010**, *132*, 14745−14747.
(254) Wegener, E. C.; Bukowski, B. C.; Yang, D.; Wu, Z.; Kropf, A. J.; Delgass, W. N.; Greeley, J.; Zhang, G.; Miller, J. T. Intermetallic Compounds as an Alternative to Single-Atom Alloy Catalysts: Geometric and Electronic Structures from Advanced X-ray Spectroscopies and Computational Studies. *ChemCatChem.* **2020**, *12*, 1325−1333.
(255) Armbrüster, M.; Schlögl, R.; Grin, Y. Intermetallic Compounds in Heterogeneous Catalysis—a Quickly Developing Field. *Sci. Technol. Adv. Mater.* **2014**, *15*, 034803.
(256) Cahn, R. W. Intermetallics: New Physics. *Contemporary Physics* **2001**, *42*, 365−375.
(257) Grin, Y. Crystal Structure and Bonding in Intermetallic Compounds. In *Comprehensive Inorganic Chemistry II*, 2nd ed.; Reedijk, J., Poeppelmeier, K., Eds.; Elsevier: Amsterdam, 2013; pp 359−373.
(258) Pan, Y.-T.; Yan, Y.; Shao, Y.-T.; Zuo, J.-M.; Yang, H. Ag-Pt Compositional Intermetallics Made from Alloy Nanoparticles. *Nano Lett.* **2016**, *16*, 6599−6603.
(259) Wang, L.; Zhang, S.; Zhu, Y.; Patlolla, A.; Shan, J.; Yoshida, H.; Takeda, S.; Frenkel, A. I.; Tao, F. Catalysis and In-situ Studies of Rh_1/Co_3O_4 Nanorods in Reduction of NO with H_2. *ACS Catal.* **2013**, *3*, 1011−1019.
(260) Shelef, M. Selective Catalytic Reduction of NO_x with N-Free Reductants. *Chem. Rev.* **1995**, *95*, 209−225.
(261) Zhang, R.; Liu, N.; Lei, Z.; Chen, B. Selective Transformation of Various Nitrogen-Containing Exhaust Gases toward N_2 over Zeolite Catalysts. *Chem. Rev.* **2016**, *116*, 3658−3721.
(262) Günter, T.; Pesek, J.; Schäfer, K.; BertótinéAbai, A.; Casapu, M.; Deutschmann, O.; Grunwaldt, J.-D. Cu-SSZ-13 as Pre-turbine NO_x-removal-catalyst: Impact of Pressure and Catalyst Poisons. *Appl. Catal. B: Environ.* **2016**, *198*, 548−557.
(263) Zhang, S.; Nguyen, L.; Liang, J.-X.; Shan, J.; Liu, J.; Frenkel, A. I.; Patlolla, A.; Huang, W.; Li, J.; Tao, F. Catalysis on Singly Dispersed Bimetallic Sites. *Nat. Commun.* **2015**, *6*, 7938.
(264) Feng, Q.; Zhao, S.; Wang, Y.; Dong, J.; Chen, W.; He, D.; Wang, D.; Yang, J.; Zhu, Y.; Zhu, H.; et al. Isolated Single-Atom Pd Sites in Intermetallic Nanostructures: High Catalytic Selectivity for Semihydrogenation of Alkynes. *J. Am. Chem. Soc.* **2017**, *139*, 7294−7301.
(265) Nguyen, L.; Zhang, S.; Wang, L.; Li, Y.; Yoshida, H.; Patlolla, A.; Takeda, S.; Frenkel, A. I.; Tao, F. Reduction of Nitric Oxide with Hydrogen on Catalysts of Singly Dispersed Bimetallic Sites Pt_1Co_m and Pd_1Co_n. *ACS Catal.* **2016**, *6*, 840−850.
(266) Pei, G. X.; Liu, X. Y.; Yang, X.; Zhang, L.; Wang, A.; Li, L.; Wang, H.; Wang, X.; Zhang, T. Performance of Cu-Alloyed Pd Single-Atom Catalyst for Semihydrogenation of Acetylene under Simulated Front-End Conditions. *ACS Catal.* **2017**, *7*, 1491−1500.
(267) Liu, R.; Zhang, L. Q.; Yu, C.; Sun, M. T.; Liu, J. F.; Jiang, G. B. Atomic-Level-Designed Catalytically Active Palladium Atoms on Ultrathin Gold Nanowires. *Adv. Mater.* **2017**, *29*, 1604571.
(268) Marcella, N.; Lim, J. S.; Płonka, A. M.; Yan, G.; Owen, C. J.; van der Hoeven, J. E. S.; Foucher, A. C.; Ngan, H. T.; Torrisi, S. B.; Marinkovic, N. S.; et al. Decoding Reactive Structures in Dilute Alloy Catalysts. *Nat. Commun.* **2022**, *13*, 832.
(269) Ruban, A. V.; Skriver, H. L.; Nørskov, J. K. Surface Segregation Energies in Transition-metal Alloys. *Phys. Rev. B* **1999**, *59*, 15990−16000.
(270) Rao, K. K.; Do, Q. K.; Pham, K.; Maiti, D.; Grabow, L. C. Extendable Machine Learning Model for the Stability of Single Atom Alloys. *Top. Catal.* **2020**, *63*, 728−741.
(271) Besenbacher, F.; Chorkendorff, I.; Clausen, B. S.; Hammer, B.; Molenbroek, A. M.; Nørskov, J. K.; Stensgaard, I. Design of a Surface Alloy Catalyst for Steam Reforming. *Science* **1998**, *279*, 1913−1915.
(272) Marcinkowski, M. D.; Darby, M. T.; Liu, J.; Wimble, J. M.; Lucci, F. R.; Lee, S.; Michaelides, A.; Flytzani-Stephanopoulos, M.; Stamatakis, M.; Sykes, E. C. H. Pt/Cu Single-Atom Alloys as Coke-Resistant Catalysts for Efficient C-H Activation. *Nat. Chem.* **2018**, *10*, 325−332.
(273) Zhang, L.; Wang, A.; Miller, J. T.; Liu, X.; Yang, X.; Wang, W.; Li, L.; Huang, Y.; Mou, C.-Y.; Zhang, T. Efficient and Durable Au Alloyed Pd Single-Atom Catalyst for the Ullmann Reaction of Aryl Chlorides in Water. *ACS Catal.* **2014**, *4*, 1546−1553.
(274) Pei, G. X.; Liu, X. Y.; Wang, A.; Li, L.; Huang, Y.; Zhang, T.; Lee, J. W.; Jang, B. W. L.; Mou, C.-Y. Promotional Effect of Pd Single Atoms on Au Nanoparticles Supported on Silica for the Selective Hydrogenation of Acetylene in Excess Ethylene. *New J. Chem.* **2014**, *38*, 2043−2051.
(275) Lucci, F. R.; Darby, M. T.; Mattera, M. F. G.; Ivimey, C. J.; Therrien, A. J.; Michaelides, A.; Stamatakis, M.; Sykes, E. C. H. Controlling Hydrogen Activation, Spillover, and Desorption with Pd-Au Single-Atom Alloys. *J. Phys. Chem. Lett.* **2016**, *7*, 480−485.
(276) Kyriakou, G.; Boucher, M. B.; Jewell, A. D.; Lewis, E. A.; Lawton, T. J.; Baber, A. E.; Tierney, H. L.; Flytzani-Stephanopoulos, M.; Sykes, E. C. H. Isolated Metal Atom Geometries as a Strategy for Selective Heterogeneous Hydrogenations. *Science* **2012**, *335*, 1209−12.
(277) Lucci, F. R.; Liu, J.; Marcinkowski, M. D.; Yang, M.; Allard, L. F.; Flytzani-Stephanopoulos, M.; Sykes, E. C. H. Selective Hydrogenation of 1,3-Butadiene on Platinum-Copper Alloys at the Single-Atom Limit. *Nat. Commun.* **2015**, *6*, 8550.
(278) Liu, J.; Lucci, F. R.; Yang, M.; Lee, S.; Marcinkowski, M. D.; Therrien, A. J.; Williams, C. T.; Sykes, E. C. H.; Flytzani-Stephanopoulos, M. Tackling CO Poisoning with Single-Atom Alloy Catalysts. *J. Am. Chem. Soc.* **2016**, *138*, 6396−6399.

https://doi.org/10.1021/acs.chemrev.2c00495
Chem. Rev. 2023, 123, 379−444

(279) Guo, N.; Fingland, B. R.; Williams, W. D.; Kispersky, V. F.; Jelic, J.; Delgass, W. N.; Ribeiro, F. H.; Meyer, R. J.; Miller, J. T. Determination of CO, H_2O and H_2 Coverage by XANES and EXAFS on Pt and Au during Water Gas Shift Reaction. *Phys. Chem. Chem. Phys.* **2010**, *12*, 5678−5693.
(280) Cheng, M.-J.; Clark, E. L.; Pham, H. H.; Bell, A. T.; Head-Gordon, M. Quantum Mechanical Screening of Single-Atom Bimetallic Alloys for the Selective Reduction of CO_2 to C_1 Hydrocarbons. *ACS Catal.* **2016**, *6*, 7769−7777.
(281) Yang, K.; Yang, B. Surface Restructuring of Cu-based Single-atom Alloy Catalysts under Reaction Conditions: the Essential Role of Adsorbates. *Phys. Chem. Chem. Phys.* **2017**, *19*, 18010−18017.
(282) Zheng, X.; Guo, L.; Li, W.; Cao, Z.; Liu, N.; Shi, Y.; Guo, J. Cu_nTM: Promising Catalysts for Preferential Oxidation of CO in H_2-rich Gas. *Comp. Theor. Chem.* **2017**, *1105*, 1−13.
(283) Sun, G.; Zhao, Z.-J.; Mu, R.; Zha, S.; Li, L.; Chen, S.; Zang, K.; Luo, J.; Li, Z.; Purdy, S. C.; et al. Breaking the Scaling Relationship via Thermally Stable Pt/Cu Single Atom Alloys for Catalytic Dehydrogenation. *Nat. Commun.* **2018**, *9*, 4454.
(284) Luong, D. X.; Bets, K. V.; Algozeeb, W. A.; Stanford, M. G.; Kittrell, C.; Chen, W.; Salvatierra, R. V.; Ren, M.; McHugh, E. A.; Advincula, P. A.; et al. Gram-Scale Bottom-Up Flash Graphene Synthesis. *Nature* **2020**, *577*, 647−651.
(285) Wu, H.; Li, H.; Zhao, X.; Liu, Q.; Wang, J.; Xiao, J.; Xie, S.; Si, R.; Yang, F.; Miao, S.; et al. Highly Doped and Exposed Cu(i)-N Active Sites within Graphene Towards Efficient Oxygen Reduction for Zinc-Air Batteries. *Energy Environ. Sci.* **2016**, *9*, 3736−3745.
(286) Deng, D.; Pan, X.; Yu, L.; Cui, Y.; Jiang, Y.; Qi, J.; Li, W.-X.; Fu, Q.; Ma, X.; Xue, Q.; et al. Toward N-Doped Graphene via Solvothermal Synthesis. *Chem. Mater.* **2011**, *23*, 1188−1193.
(287) Panchakarla, L. S.; Subrahmanyam, K. S.; Saha, S. K.; Govindaraj, A.; Krishnamurthy, H. R.; Waghmare, U. V.; Rao, C. N. R. Synthesis, Structure, and Properties of Boron- and Nitrogen-Doped Graphene. *Adv. Mater.* **2009**, *21*, 4726−4730.
(288) Gawande, M. B.; Fornasiero, P.; Zbořil, R. Carbon-Based Single-Atom Catalysts for Advanced Applications. *ACS Catal.* **2020**, *10*, 2231−2259.
(289) Chen, Z.; Zhao, J.; Cabrera, C. R.; Chen, Z. Computational Screening of Efficient Single-Atom Catalysts Based on Graphitic Carbon Nitride (g-C_3N_4) for Nitrogen Electroreduction. *Small Methods* **2019**, *3*, 1800368.
(290) Bakandritsos, A.; Kadam, R. G.; Kumar, P.; Zoppellaro, G.; Medved, M.; Tuček, J.; Montini, T.; Tomanec, O.; Andrýsková, P.; Drahoš, B.; et al. Mixed-Valence Single-Atom Catalyst Derived from Functionalized Graphene. *Adv. Mater.* **2019**, *31*, 1900323.
(291) Tang, Y.; Yang, Z.; Dai, X. A Theoretical Simulation on the Catalytic Oxidation of CO on Pt/Graphene. *Phys. Chem. Chem. Phys.* **2012**, *14*, 16566−16572.
(292) Lin, S.; Ye, X.; Johnson, R. S.; Guo, H. First-Principles Investigations of Metal (Cu, Ag, Au, Pt, Rh, Pd, Fe, Co, and Ir) Doped Hexagonal Boron Nitride Nanosheets: Stability and Catalysis of CO Oxidation. *J. Phys. Chem. C* **2013**, *117*, 17319−17326.
(293) Ma, D. W.; Li, T.; Wang, Q.; Yang, G.; He, C.; Ma, B.; Lu, Z. Graphyne as a Promising Substrate for the Noble-metal Single-Atom Catalysts. *Carbon* **2015**, *95*, 756−765.
(294) Gao, G.; Jiao, Y.; Waclawik, E. R.; Du, A. Single Atom (Pd/Pt) Supported on Graphitic Carbon Nitride as an Efficient Photocatalyst for Visible-Light Reduction of Carbon Dioxide. *J. Am. Chem. Soc.* **2016**, *138*, 6292−6297.
(295) Xue, Y.; Huang, B.; Yi, Y.; Guo, Y.; Zuo, Z.; Li, Y.; Jia, Z.; Liu, H.; Li, Y. Anchoring Zero Valence Single Atoms of Nickel and Iron on Graphdiyne for Hydrogen Evolution. *Nat. Commun.* **2018**, *9*, 1460.
(296) Zhang, L.; Wang, A.; Wang, W.; Huang, Y.; Liu, X.; Miao, S.; Liu, J.; Zhang, T. Co-N-C Catalyst for C-C Coupling Reactions: On the Catalytic Performance and Active Sites. *ACS Catal.* **2015**, *5*, 6563−6572.
(297) Liu, W.; Zhang, L.; Yan, W.; Liu, X.; Yang, X.; Miao, S.; Wang, W.; Wang, A.; Zhang, T. Single-Atom Dispersed Co-N-C Catalyst: Structure Identification and Performance for Hydrogenative Coupling of Nitroarenes. *Chem. Sci.* **2016**, *7*, 5758−5764.
(298) Yin, P.; Yao, T.; Wu, Y.; Zheng, L.; Lin, Y.; Liu, W.; Ju, H.; Zhu, J.; Hong, X.; Deng, Z.; et al. Single Cobalt Atoms with Precise N-Coordination as Superior Oxygen Reduction Reaction Catalysts. *Angew. Chem., Int. Ed.* **2016**, *55*, 10800−10805.
(299) Jiao, L.; Wan, G.; Zhang, R.; Zhou, H.; Yu, S.-H.; Jiang, H.-L. From Metal-Organic Frameworks to Single-Atom Fe Implanted N-Doped Porous Carbons: Efficient Oxygen Reduction in Both Alkaline and Acidic Media. *Angew. Chem., Int. Ed.* **2018**, *57*, 8525−8529.
(300) Qu, Y.; Li, Z.; Chen, W.; Lin, Y.; Yuan, T.; Yang, Z.; Zhao, C.; Wang, J.; Zhao, C.; Wang, X.; et al. Direct Transformation of Bulk Copper into Copper Single Sites via Emitting and Trapping of Atoms. *Nat. Catal.* **2018**, *1*, 781−786.
(301) Chen, W.; Pei, J.; He, C.-T.; Wan, J.; Ren, H.; Wang, Y.; Dong, J.; Wu, K.; Cheong, W.-C.; Mao, J.; et al. Single Tungsten Atoms Supported on MOF-Derived N-Doped Carbon for Robust Electrochemical Hydrogen Evolution. *Adv. Mater.* **2018**, *30*, 1800396.
(302) Li, X.; Bi, W.; Zhang, L.; Tao, S.; Chu, W.; Zhang, Q.; Luo, Y.; Wu, C.; Xie, Y. Single-Atom Pt as Co-Catalyst for Enhanced Photocatalytic H_2 Evolution. *Adv. Mater.* **2016**, *28*, 2427−31.
(303) Ankudinov, A. L.; Ravel, B.; Rehr, J. J.; Conradson, S. D. Real-space Multiple-scattering Calculation and Interpretation of X-ray Absorption Near-edge Structure. *Phys. Rev. B* **1998**, *58*, 7565−7576.
(304) Collman, J. P.; Brauman, J. I.; Collins, T. J.; Iverson, B.; Sessler, J. L. The "Pocket" Porphyrin: a Hemoprotein Model with Lowered Carbon Monoxide Affinity. *J. Am. Chem. Soc.* **1981**, *103*, 2450−2452.
(305) Zitolo, A.; Goellner, V.; Armel, V.; Sougrati, M.-T.; Mineva, T.; Stievano, L.; Fonda, E.; Jaouen, F. Identification of Catalytic Sites for Oxygen Reduction in Iron- and Nitrogen-Doped Graphene Materials. *Nat. Mater.* **2015**, *14*, 937−942.
(306) Benfatto, M.; Della Longa, S. Geometrical Fitting of Experimental XANES Spectra by a Full Multiple-Scattering Procedure. *J. Syn. Rad.* **2001**, *8*, 1087−1094.
(307) Benfatto, M.; Congiu-Castellano, A.; Daniele, A.; Longa, S. D. MXAN: a New Software Procedure to Perform Geometrical Fitting of Experimental XANES Spectra. *J. Syn. Rad.* **2001**, *8*, 267−269.
(308) Li, X.; Bi, W.; Chen, M.; Sun, Y.; Ju, H.; Yan, W.; Zhu, J.; Wu, X.; Chu, W.; Wu, C.; et al. Exclusive Ni-N_4 Sites Realize Near-Unity CO Selectivity for Electrochemical CO_2 Reduction. *J. Am. Chem. Soc.* **2017**, *139*, 14889−14892.
(309) Zhang, C.; Sha, J.; Fei, H.; Liu, M.; Yazdi, S.; Zhang, J.; Zhong, Q.; Zou, X.; Zhao, N.; Yu, H.; et al. Single-Atomic Ruthenium Catalytic Sites on Nitrogen-Doped Graphene for Oxygen Reduction Reaction in Acidic Medium. *ACS Nano* **2017**, *11*, 6930−6941.
(310) Chen, W. X.; Pei, J. J.; He, C. T.; Wan, J. W.; Ren, H. L.; Zhu, Y. Q.; Wang, Y.; Dong, J. C.; Tian, S. B.; Cheong, W. C.; et al. Rational Design of Single Molybdenum Atoms Anchored on N-Doped Carbon for Effective Hydrogen Evolution Reaction. *Angew. Chem., Int. Ed.* **2017**, *56*, 16086−16090.
(311) Furukawa, H.; Cordova, K. E.; O'Keeffe, M.; Yaghi, O. M. The Chemistry and Applications of Metal-Organic Frameworks. *Science* **2013**, *341*, 1230444.
(312) Wang, Q.; Astruc, D. State of the Art and Prospects in Metal-Organic Framework (MOF)-Based and MOF-Derived Nanocatalysis. *Chem. Rev.* **2020**, *120*, 1438−1511.
(313) Côté, A. P.; Benin, A. I.; Ockwig, N. W.; Keeffe, M.; Matzger, A. J.; Yaghi, O. M. Porous, Crystalline, Covalent Organic Frameworks. *Science* **2005**, *310*, 1166.
(314) Bitzer, J.; Kleist, W. Synthetic Strategies and Structural Arrangements of Isoreticular Mixed-Component Metal-Organic Frameworks. *Chem. Eur. J.* **2019**, *25*, 1866−1882.
(315) Li, Z.; Schweitzer, N. M.; League, A. B.; Bernales, V.; Peters, A. W.; Getsoian, A. B.; Wang, T. C.; Miller, J. T.; Vjunov, A.; Fulton, J. L.; et al. Sintering-Resistant Single-Site Nickel Catalyst Supported by Metal-Organic Framework. *J. Am. Chem. Soc.* **2016**, *138*, 1977−1982.
(316) Zhang, H. B.; Wei, J.; Dong, J. C.; Liu, G. G.; Shi, L.; An, P. F.; Zhao, G. X.; Kong, J. T.; Wang, X. J.; Meng, X. G.; et al. Efficient Visible-Light-Driven Carbon Dioxide Reduction by a Single-Atom Implanted

https://doi.org/10.1021/acs.chemrev.2c00495
Chem. Rev. 2023, 123, 379−444

Metal-Organic Framework. *Angew. Chem., Int.Ed.* **2016**, *55*, 14308−14312.
(317) Gotthardt, M. A.; Schoch, R.; Brunner, T. S.; Bauer, M.; Kleist, W. Design of Highly Porous Single-Site Catalysts through Two-Step Postsynthetic Modification of Mixed-Linker MIL-53(Al). *ChemPlusChem.* **2015**, *80*, 188−195.
(318) Zhao, C.; Dai, X.; Yao, T.; Chen, W.; Wang, X.; Wang, J.; Yang, J.; Wei, S.; Wu, Y.; Li, Y. Ionic Exchange of Metal-Organic Frameworks to Access Single Nickel Sites for Efficient Electroreduction of CO_2. *J. Am. Chem. Soc.* **2017**, *139*, 8078−8081.
(319) Gong, Y.-N.; Jiao, L.; Qian, Y.; Pan, C.-Y.; Zheng, L.; Cai, X.; Liu, B.; Yu, S.-H.; Jiang, H.-L. Regulating the Coordination Environment of MOF-Templated Single-Atom Nickel Electrocatalysts for Boosting CO2 Reduction. *Angew. Chem., Int. Ed.* **2020**, *59* (7), 2705−2709.
(320) Gong, Y.-N.; Jiao, L.; Qian, Y.; Pan, C.-Y.; Zheng, L.; Cai, X.; Liu, B.; Yu, S.-H.; Jiang, H.-L. Regulating the Coordination Environment of MOF-Templated Single-Atom Nickel Electrocatalysts for Boosting CO_2 Reduction. *Angew. Chem., Int. Ed.* **2020**, *59*, 2705−2709.
(321) Dou, S.; Dong, C.-L.; Hu, Z.; Huang, Y.-C.; Chen, J.-l.; Tao, L.; Yan, D.; Chen, D.; Shen, S.; Chou, S.; et al. Atomic-Scale CoO_x Species in Metal-Organic Frameworks for Oxygen Evolution Reaction. *Adv. Funct. Mater.* **2017**, *27*, 1702546.
(322) Luo, E.; Zhang, H.; Wang, X.; Gao, L.; Gong, L.; Zhao, T.; Jin, Z.; Ge, J.; Jiang, Z.; Liu, C.; et al. Single-Atom Cr-N_4 Sites Designed for Durable Oxygen Reduction Catalysis in Acid Media. *Angew. Chem., Int. Ed.* **2019**, *58*, 12469−12475.
(323) Peng, P.; Shi, L.; Huo, F.; Mi, C.; Wu, X.; Zhang, S.; Xiang, Z. A Pyrolysis-free Path Toward Superiorly Catalytic Nitrogen-Coordinated Single Atom. *Sci. Adv.* **2019**, *5*, No. eaaw2322.
(324) Zhong, W.; Sa, R.; Li, L.; He, Y.; Li, L.; Bi, J.; Zhuang, Z.; Yu, Y.; Zou, Z. A Covalent Organic Framework Bearing Single Ni Sites as a Synergistic Photocatalyst for Selective Photoreduction of CO_2 to CO. *J. Am. Chem. Soc.* **2019**, *141*, 7615−7621.
(325) Haupt, K.; Mosbach, K. Molecularly Imprinted Polymers and Their Use in Biomimetic Sensors. *Chem. Rev.* **2000**, *100*, 2495−2504.
(326) Zhang, Y.; Riduan, S. N. Functional Porous Organic Polymers for Heterogeneous Catalysis. *Chem. Soc. Rev.* **2012**, *41*, 2083−2094.
(327) McKeown, N. B.; Budd, P. M. Polymers of Intrinsic Microporosity (PIMs): Organic Materials for Membrane Separations, Heterogeneous Catalysis and Hydrogen Storage. *Chem. Soc. Rev.* **2006**, *35*, 675−683.
(328) Liu, Y. Q.; Zhou, Y.; Li, J.; Wang, Q.; Qin, Q.; Zhang, W.; Asakura, H.; Yan, N.; Wang, J. Direct Aerobic Oxidative Homocoupling of Benzene to Biphenyl over Functional Porous Organic Polymer Supported Atomically Dispersed Palladium Catalyst. *Appl. Catal., B* **2017**, *209*, 679−688.
(329) Yang, S.; Tak, Y. J.; Kim, J.; Soon, A.; Lee, H. Support Effects in Single-Atom Platinum Catalysts for Electrochemical Oxygen Reduction. *ACS Catal.* **2017**, *7*, 1301−1307.
(330) VahidMohammadi, A.; Rosen, J.; Gogotsi, Y. The World of Two-Dimensional Carbides and Nitrides (MXenes). *Science* **2021**, *372*, No. eabf1581.
(331) Huang, D.; de Vera, G. A.; Chu, C.; Zhu, Q.; Stavitski, E.; Mao, J.; Xin, H.; Spies, J. A.; Schmuttenmaer, C. A.; Niu, J.; et al. Single-Atom Pt Catalyst for Effective C-F Bond Activation via Hydrodefluorination. *ACS Catal.* **2018**, *8*, 9353−9358.
(332) Zhang, M.; Lai, C.; Li, B.; Liu, S.; Huang, D.; Xu, F.; Liu, X.; Qin, L.; Fu, Y.; Li, L.; et al. MXenes as Superexcellent Support for Confining Single Atom: Properties, Synthesis, and Electrocatalytic Applications. *Small* **2021**, *17*, 2007113.
(333) Ramalingam, V.; Varadhan, P.; Fu, H.-C.; Kim, H.; Zhang, D.; Chen, S.; Song, L.; Ma, D.; Wang, Y.; Alshareef, H. N.; et al. Heteroatom-Mediated Interactions between Ruthenium Single Atoms and an MXene Support for Efficient Hydrogen Evolution. *Adv. Mater.* **2019**, *31*, 1903841.
(334) Deng, J.; Li, H.; Xiao, J.; Tu, Y.; Deng, D.; Yang, H.; Tian, H.; Li, J.; Ren, P.; Bao, X. Triggering the Electrocatalytic Hydrogen Evolution Activity of the Inert Two-dimensional MoS_2 Surface via Single-atom Metal Doping. *Energy Environ. Sci.* **2015**, *8*, 1594−1601.
(335) Wang, H.; Tsai, C.; Kong, D.; Chan, K.; Abild-Pedersen, F.; Nørskov, J. K.; Cui, Y. Transition-Metal Doped Edge Sites in Vertically Aligned MoS_2 Catalysts for Enhanced Hydrogen Evolution. *Nano Res.* **2015**, *8*, 566−575.
(336) Luo, Z.; Ouyang, Y.; Zhang, H.; Xiao, M.; Ge, J.; Jiang, Z.; Wang, J.; Tang, D.; Cao, X.; Liu, C.; et al. Chemically Activating MoS_2 via Spontaneous Atomic Palladium Interfacial Doping Towards Efficient Hydrogen Evolution. *Nat. Commun.* **2018**, *9*, 2120.
(337) Dai, X.; Du, K.; Li, Z.; Liu, M.; Ma, Y.; Sun, H.; Zhang, X.; Yang, Y. Co-Doped MoS_2 Nanosheets with the Dominant CoMoS Phase Coated on Carbon as an Excellent Electrocatalyst for Hydrogen Evolution. *ACS Appl. Mater. Int.* **2015**, *7*, 27242−27253.
(338) Guan, Y.; Feng, Y.; Wan, J.; Yang, X.; Fang, L.; Gu, X.; Liu, R.; Huang, Z.; Li, J.; Luo, J.; Li, C.; Wang, Y. Ganoderma-Like MoS_2/NiS_2 with Single Platinum Atoms Doping as an Efficient and Stable Hydrogen Evolution Reaction Catalyst. *Small* **2018**, *14*, 1800697.
(339) Lou, Y.; Zheng, Y.; Li, X.; Ta, N.; Xu, J.; Nie, Y.; Cho, K.; Liu, J. Pocketlike Active Site of Rh_1/MoS_2 Single-Atom Catalyst for Selective Crotonaldehyde Hydrogenation. *J. Am. Chem. Soc.* **2019**, *141*, 19289−19295.
(340) Li, H.; Wang, L.; Dai, Y.; Pu, Z.; Lao, Z.; Chen, Y.; Wang, M.; Zheng, X.; Zhu, J.; Zhang, W.; et al. Synergetic Interaction Between Neighbouring Platinum Monomers in CO_2 Hydrogenation. *Nat. Nanotechnol.* **2018**, *13*, 411−417.
(341) Jiang, K.; Luo, M.; Peng, M.; Yu, Y.; Lu, Y.-R.; Chan, T.-S.; Liu, P.; de Groot, F. M. F.; Tan, Y. Dynamic Active-Site Generation of Atomic Iridium Stabilized on Nanoporous Metal Phosphides for Water Oxidation. *Nat. Commun.* **2020**, *11*, 2701.
(342) Tejuca, L. G.; Fierro, J. L. G.; Tascón, J. M. D. Structure and Reactivity of Perovskite-Type Oxides. In *Adv. Catal.*; Eley, D. D., Pines, H., Weisz, P. B., Eds.; Academic Press, 1989; Vol. *36*, pp 237−328.
(343) Nishihata, Y.; Mizuki, J.; Akao, T.; Tanaka, H.; Uenishi, M.; Kimura, M.; Okamoto, T.; Hamada, N. Self-Regeneration of a Pd-Perovskite Catalyst for Automotive Emissions Control. *Nature* **2002**, *418*, 164−167.
(344) Tanaka, H.; Taniguchi, M.; Uenishi, M.; Kajita, N.; Tan, I.; Nishihata, Y.; Mizuki, J. i.; Narita, K.; Kimura, M.; Kaneko, K. Self-Regenerating Rh- and Pt-Based Perovskite Catalysts for Automotive-Emissions Control. *Angew. Chem., Int. Ed.* **2006**, *45*, 5998−6002.
(345) Tanaka, H. An Intelligent Catalyst: The Self-Regenerative Palladium-Perovskite Catalyst for Automotive Emissions Control. *Catal. Surv. Asia* **2005**, *9*, 63−74.
(346) Uenishi, M.; Tanaka, H.; Taniguchi, M.; Tan, I.; Nishihata, Y.; Mizuki, J. i.; Kobayashi, T. Time Evolution of Palladium Structure Change with Redox Fluctuations in a $LaFePdO_3$ Perovskite Automotive Catalyst by High-speed Analysis with In-situ DXAFS. *Catal. Commun.* **2008**, *9*, 311−314.
(347) Tian, C.; Zhang, H.; Zhu, X.; Lin, B.; Liu, X.; Chen, H.; Zhang, Y.; Mullins, D. R.; Abney, C. W.; Shakouri, M.; et al. A New Trick for an Old Support: Stabilizing Gold Single Atoms on $LaFeO_3$ Perovskite. *Appl. Catal. B: Environ.* **2020**, *261*, 118178.
(348) Alves, L.; Ballesteros, B.; Boronat, M.; Cabrero-Antonino, J. R.; Concepción, P.; Corma, A.; Correa-Duarte, M. A.; Mendoza, E. Synthesis and Stabilization of Subnanometric Gold Oxide Nanoparticles on Multiwalled Carbon Nanotubes and Their Catalytic Activity. *J. Am. Chem. Soc.* **2011**, *133*, 10251−10261.
(349) Wan, Q.; Fung, V.; Lin, S.; Wu, Z.; Jiang, D. Perovskite-Supported Pt Single Atoms for Methane Activation. *J. Mater. Chem. A* **2020**, *8*, 4362−4368.
(350) Mitchell, S.; Pérez-Ramírez, J. Single Atom Catalysis: a Decade of Stunning Progress and the Promise for a Bright Future. *Nat. Commun.* **2020**, *11*, 4302.
(351) Datye, A. K.; Guo, H. Single Atom Catalysis Poised to Transition from an Academic Curiosity to an Industrially Relevant Technology. *Nat. Commun.* **2021**, *12*, 895.

https://doi.org/10.1021/acs.chemrev.2c00495
Chem. Rev. 2023, 123, 379−444

(352) Li, X.; Yang, X.; Zhang, J.; Huang, Y.; Liu, B. In-situ/Operando Techniques for Characterization of Single-Atom Catalysts. *ACS Catal.* **2019**, *9*, 2521−2531.
(353) Grunwaldt, J.-D.; Baiker, A. In-Situ Spectroscopic Investigation of Heterogeneous Catalysts and Reaction Media at High Pressure. *Phys. Chem. Chem. Phys.* **2005**, *7*, 3526−3539.
(354) Lytle, F. W.; Wei, P. S. P.; Greegor, R. B.; Via, G. H.; Sinfelt, J. H. Effect of Chemical Environment on Magnitude of X-ray Absorption Resonance at L_{III} Edges. Studies on Metallic Elements, Compounds, and Catalysts. *J. Chem. Phys.* **1979**, *70*, 4849−4855.
(355) Kampers, F. W. H.; Maas, T. M. J.; van Grondelle, J.; Brinkgreve, P.; Koningsberger, D. C. An In-situ Cell for Transmission EXAFS Measurements on Catalytic Samples. *Rev. Sci. Instrum.* **1989**, *60*, 2635−2638.
(356) Dalla Betta, R. A.; Boudart, M.; Foger, K.; Löffler, D. G.; Sánchez-Arrieta, J. Cell Fitted with thin Beryllium Windows for X-ray Absorption Under Pressures up to 14 MPa and Temperatures up to 700 K. *Rev. Sci. Instrum.* **1984**, *55*, 1910−1913.
(357) Grunwaldt, J.-D.; Clausen, B. S. Combining XRD and EXAFS with On-line Catalytic Studies for In-situ Characterization of Catalysts. *Top. Catal.* **2002**, *18*, 37−43.
(358) Clausen, B. S. Combined (Q)EXAFS/XRD: Technique and Applications. *Catal. Today* **1998**, *39*, 293−300.
(359) Grunwaldt, J.-D.; Hannemann, S.; Gttlicher, J.; Mangold, S.; Denecke, M. A.; Baiker, A. X-ray Absorption Spectroscopy on Heterogeneous Catalysts at the new XAS Beamline at ANKA. *Phys. Scr.* **2005**, 769.
(360) van Beek, W.; Safonova, O. V.; Wiker, G.; Emerich, H. SNBL, a Dedicated Beamline for Combined In-situ X-ray Diffraction, X-ray Absorption and Raman Scattering Experiments. *Phase Transitions* **2011**, *84*, 726−732.
(361) Abdala, P. M.; Safonova, O. V.; Wiker, G.; van Beek, W.; Emerich, H.; van Bokhoven, J. A.; Sa, J.; Szlachetko, J.; Nachtegaal, M. Scientific Opportunities for Heterogeneous Catalysis Research at the SuperXAS and SNBL Beam Lines. *Chimia* **2012**, *66*, 699−705.
(362) La Fontaine, C.; Barthe, L.; Rochet, A.; Briois, V. X-ray Absorption Spectroscopy and Heterogeneous Catalysis: Performances at the SOLEIL's SAMBA Beamline. *Catal. Today* **2013**, *205*, 148−158.
(363) Doronkin, D. E.; Lichtenberg, H.; Grunwaldt, J.-D. Cell Designs for In-situ and Operando Studies. In *XAFS Techniques for Catalysts, Nanomaterials, and Surfaces*; Iwasawa, Y., Asakura, K., Tada, M., Eds.; Springer International Publishing: Cham, 2017; pp 75−89.
(364) Grunwaldt, J.-D.; Caravati, M.; Hannemann, S.; Baiker, A. X-ray Absorption Spectroscopy Under Reaction Conditions: Suitability of Different Reaction Cells for Combined Catalyst Characterization and Time-resolved Studies. *Phys. Chem. Chem. Phys.* **2004**, *6*, 3037−3047.
(365) Clausen, B. S.; Topsøe, H. In-situ High Pressure, High Temperature XAFS Studies of Cu-Based Catalysts During Methanol Synthesis. *Catal. Today* **1991**, *9*, 189−196.
(366) Clausen, B. S.; Steffensen, G.; Fabius, B.; Villadsen, J.; Feidenhans'l, R.; Topsøe, H. In-situ Cell for Combined XRD and On-line Catalysis Tests: Studies of Cu-based Water Gas Shift and Methanol Catalysts. *J. Catal.* **1991**, *132*, 524−535.
(367) Fischer, N.; Claeys, M. Phase Changes Studied Under In-situ Conditions—A Novel Cell. *Catal. Today* **2016**, *275*, 149−154.
(368) Hannemann, S.; Casapu, M.; Grunwaldt, J.-D.; Haider, P.; Trussel, P.; Baiker, A.; Welter, E. A Versatile In-situ Spectroscopic Cell for Fluorescence/Transmission EXAFS and X-ray Diffraction of Heterogeneous Catalysts in Gas and Liquid Phase. *J. Syn. Rad.* **2007**, *14*, 345−354.
(369) Grunwaldt, J.-D. Shining X-rays on Catalysts at Work. *J. Phys. Conf. Ser.* **2009**, *190*, 012151.
(370) Bare, S. R.; Yang, N.; Kelly, S. D.; Mickelson, G. E.; Modica, F. S. Design and Operation of a High Pressure Reaction Cell for In-situ X-ray Absorption Spectroscopy. *Catal. Today* **2007**, *126*, 18−26.
(371) Hoffman, A. S.; Debefve, L. M.; Bendjeriou-Sedjerari, A.; Ouldchikh, S.; Bare, S. R.; Basset, J. M.; Gates, B. C. Transmission and Fluorescence X-ray Absorption Spectroscopy Cell/Flow Reactor for Powder Samples Under Vacuum or in Reactive Atmospheres. *Rev. Sci. Ins.* **2016**, *87*, 073108.
(372) Keresszegi, C.; Grunwaldt, J.-D.; Mallat, T.; Baiker, A. In-situ EXAFS Study on the Oxidation State of Pd/Al_2O_3 and $Bi\text{-}Pd/Al_2O_3$ During the Liquid-Phase Oxidation of 1-Phenylethanol. *J. Catal.* **2004**, *222*, 268−280.
(373) Grunwaldt, J.-D.; Keresszegi, C.; Mallat, T.; Baiker, A. In-situ EXAFS Study of Pd/Al_2O_3 During Aerobic Oxidation of Cinnamyl Alcohol in an Organic Solvent. *J. Catal.* **2003**, *213*, 291−295.
(374) Grunwaldt, J.-D.; Ramin, M.; Rohr, M.; Michailovski, A.; Patzke, G. R.; Baiker, A. High Pressure In-situ X-ray Absorption Spectroscopy Cell for Studying Simultaneously the Liquid Phase and the Solid/liquid Interface. *Rev. Sci. Ins.* **2005**, *76*, 054104.
(375) Nguyen, L.; Tang, Y.; Li, Y.; Zhang, X.; Wang, D.; Tao, F. Dual Reactor for In-situ/Operando Fluorescent Mode XAS Studies of Sample Containing Low-concentration 3d or 5d Metal Elements. *Rev. Sci. Instrum.* **2018**, *89*, 054103.
(376) Leonard, N.; Ju, W.; Sinev, I.; Steinberg, J.; Luo, F.; Varela, A. S.; Roldan Cuenya, B.; Strasser, P. The Chemical Identity, State and Structure of Catalytically Active Centers During the Electrochemical CO_2 Reduction on Porous Fe-Nitrogen-Carbon (Fe-N-C) Materials. *Chem. Sci.* **2018**, *9*, 5064−5073.
(377) Czioska, S.; Boubnov, A.; Escalera-López, D.; Geppert, J.; Zagalskaya, A.; Röse, P.; Saraçi, E.; Alexandrov, V.; Krewer, U.; Cherevko, S.; et al. Increased Ir-Ir Interaction in Iridium Oxide During the Oxygen Evolution Reaction at High Potentials Probed by Operando Spectroscopy. *ACS Catal.* **2021**, *11*, 10043−10057.
(378) Binninger, T.; Fabbri, E.; Patru, A.; Garganourakis, M.; Han, J.; Abbott, D. F.; Sereda, O.; Kötz, R.; Menzel, A.; Nachtegaal, M.; et al. Electrochemical Flow-Cell Setup for In-situ X-ray Investigations. *J. Electro. Soc.* **2016**, *163*, H906−H912.
(379) Fabbri, E.; Abbott, D. F.; Nachtegaal, M.; Schmidt, T. J. Operando X-ray Absorption Spectroscopy: A Powerful Tool Toward Water Splitting Catalyst Development. *Curr. Opin. Electrochem.* **2017**, *5*, 20−26.
(380) Wang, S.; Borisevich, A. Y.; Rashkeev, S. N.; Glazoff, M. V.; Sohlberg, K.; Pennycook, S. J.; Pantelides, S. T. Dopants Adsorbed as Single Atoms Prevent Degradation of Catalysts. *Nat. Mater.* **2004**, *3*, 143−146.
(381) Hackett, S. F. J.; Brydson, R. M.; Gass, M. H.; Harvey, I.; Newman, A. D.; Wilson, K.; Lee, A. F. High-Activity, Single-Site Mesoporous Pd/Al_2O_3 Catalysts for Selective Aerobic Oxidation of Allylic Alcohols. *Angew. Chem., Int. Ed.* **2007**, *46*, 8593−8596.
(382) Lu, Y.; Wang, J.; Yu, L.; Kovarik, L.; Zhang, X.; Hoffman, A. S.; Gallo, A.; Bare, S. R.; Sokaras, D.; Kroll, T.; et al. Identification of the Active Complex for CO Oxidation over Single-Atom Ir-on-$MgAl_2O_4$ Catalysts. *Nat. Catal.* **2019**, *2*, 149−156.
(383) Malta, G.; Kondrat Simon, A.; Freakley Simon, J.; Davies Catherine, J.; Lu, L.; Dawson, S.; Thetford, A.; Gibson Emma, K.; Morgan David, J.; Jones, W.; et al. Identification of Single-site Gold Catalysis in Acetylene Hydrochlorination. *Science* **2017**, *355*, 1399−1403.
(384) Malta, G.; Kondrat, S. A.; Freakley, S. J.; Morgan, D. J.; Gibson, E. K.; Wells, P. P.; Aramini, M.; Gianolio, D.; Thompson, P. B. J.; Johnston, P.; et al. In-situ K-edge X-ray Absorption Spectroscopy of the Ligand Environment of Single-Site Au/C Catalysts During Acetylene Hydrochlorination. *Chem. Sci.* **2020**, *11*, 7040−7052.
(385) Liu, L.; Zakharov, D. N.; Arenal, R.; Concepcion, P.; Stach, E. A.; Corma, A. Evolution and Stabilization of Subnanometric Metal Species in Confined Space by In-situ TEM. *Nat. Commun.* **2018**, *9*, 574.
(386) Dessal, C.; Len, T.; Morfin, F.; Rousset, J.-L.; Aouine, M.; Afanasiev, P.; Piccolo, L. Dynamics of Single Pt Atoms on Alumina during CO Oxidation Monitored by Operando X-ray and Infrared Spectroscopies. *ACS Catal.* **2019**, *9*, 5752−5759.
(387) Nagai, Y.; Dohmae, K.; Ikeda, Y.; Takagi, N.; Tanabe, T.; Hara, N.; Guilera, G.; Pascarelli, S.; Newton, M. A.; Kuno, O.; et al. In-situ Redispersion of Platinum Autoexhaust Catalysts: An On-line Approach to Increasing Catalyst Lifetimes? *Angew. Chem., Int. Ed.* **2008**, *47*, 9303−6.

https://doi.org/10.1021/acs.chemrev.2c00495
Chem. Rev. 2023, 123, 379−444

(388) Jones, J.; Xiong, H.; DeLaRiva, A. T.; Peterson, E. J.; Pham, H.; Challa, S. R.; Qi, G.; Oh, S.; Wiebenga, M. H.; Pereira Hernández, X. I.; Wang, Y.; Datye, A. K. Thermally stable single-atom platinum-on-ceria catalysts via atom trapping. *Science* **2016**, *353* (6295), 150.
(389) Maurer, F.; Beck, A.; Jelic, J.; Wang, W.; Mangold, S.; Stehle, M.; Wang, D.; Dolcet, P.; Gänzler, A. M.; Kübel, C.; et al. Surface Noble Metal Concentration on Ceria as a Key Descriptor for Efficient Catalytic CO Oxidation. *ACS Catal.* **2022**, *12*, 2473−2486.
(390) Maurer, F.; Jelic, J.; Wang, J.; Gänzler, A.; Dolcet, P.; Wöll, C.; Wang, Y.; Studt, F.; Casapu, M.; Grunwaldt, J.-D. Tracking the Formation, Fate and Consequence for Catalytic Activity of Pt Single Sites on CeO_2. *Nat. Catal.* **2020**, *3*, 824−833.
(391) Bruix, A.; Lykhach, Y.; Matolínová, I.; Neitzel, A.; Skála, T.; Tsud, N.; Vorokhta, M.; Stetsovych, V.; Ševčíková, K.; Myslivečeka, J.; et al. Maximum Noble-Metal Efficiency in Catalytic Materials: Atomically Dispersed Surface Platinum. *Angew. Chem., Int. Ed.* **2014**, *53*, 10525−10530.
(392) Dvorak, F.; Farnesi Camellone, M.; Tovt, A.; Tran, N. D.; Negreiros, F. R.; Vorokhta, M.; Skala, T.; Matolinova, I.; Myslivecek, J.; Matolin, V.; et al. Creating Single-atom Pt-ceria Catalysts by Surface Step Decoration. *Nat. Commun.* **2016**, *7*, 10801.
(393) Zhou, Y.; Doronkin, D. E.; Chen, M.; Wei, S.; Grunwaldt, J.-D. Interplay of Pt and Crystal Facets of TiO_2: CO Oxidation Activity and Operando XAS/DRIFTS Studies. *ACS Catal.* **2016**, *6*, 7799−7809.
(394) Cassinelli, W. H.; Martins, L.; Passos, A. R.; Pulcinelli, S. H.; Santilli, C. V.; Rochet, A.; Briois, V. Multivariate Curve Resolution Analysis Applied to Time-resolved Synchrotron X-ray Absorption Spectroscopy Monitoring of the Activation of Copper Alumina Catalyst. *Catal. Today* **2014**, *229*, 114−122.
(395) Dolcet, P.; Maurer, F.; Casapu, M.; Grunwaldt, J.-D. Insights into the Structural Dynamics of Pt/CeO_2 Single-Site Catalysts during CO Oxidation. *Catalysts* **2021**, *11*, 1−13.
(396) Oord, R.; Schmidt, J. E.; Weckhuysen, B. M. Methane-to-Methanol Conversion over Zeolite Cu-SSZ-13, and its Comparison with the Selective Catalytic Reduction of NO_x with NH_3. *Catal. Sci. Technolog.* **2018**, *8*, 1028−1038.
(397) Fickel, D. W.; Lobo, R. F. Copper Coordination in Cu-SSZ-13 and Cu-SSZ-16 Investigated by Variable-Temperature XRD. *J. Phys. Chem. C* **2010**, *114*, 1633−1640.
(398) Rabeah, J.; Radnik, J.; Briois, V.; Maschmeyer, D.; Stochniol, G.; Peitz, S.; Reeker, H.; La Fontaine, C.; Brückner, A. Tracing Active Sites in Supported Ni Catalysts During Butene Oligomerization by Operando Spectroscopy Under Pressure. *ACS Catal.* **2016**, *6*, 8224−8228.
(399) Yuan, N.; Pascanu, V.; Huang, Z.; Valiente, A.; Heidenreich, N.; Leubner, S.; Inge, A. K.; Gaar, J.; Stock, N.; Persson, I.; et al. Probing the Evolution of Palladium Species in Pd@MOF Catalysts during the Heck Coupling Reaction: An Operando X-ray Absorption Spectroscopy Study. *J. Am. Chem. Soc.* **2018**, *140*, 8206−8217.
(400) Carson, F.; Pascanu, V.; Bermejo Gómez, A.; Zhang, Y.; Platero-Prats, A. E.; Zou, X.; Martín-Matute, B. Influence of the Base on Pd@MIL-101-NH_2(Cr) as Catalyst for the Suzuki-Miyaura Cross-Coupling Reaction. *Chem. Eur. J.* **2015**, *21*, 10896−10902.
(401) Zitolo, A.; Ranjbar-Sahraie, N.; Mineva, T.; Li, J.; Jia, Q.; Stamatin, S.; Harrington, G. F.; Lyth, S. M.; Krtil, P.; Mukerjee, S.; et al. Identification of Catalytic Sites in Cobalt-Nitrogen-Carbon Materials for the Oxygen Reduction Reaction. *Nat. Commun.* **2017**, *8*, 957.
(402) Briois, V.; Sainctavit, P.; Long, G. J.; Grandjean, F. Importance of Photoelectron Multiple Scattering in the Iron K-Edge X-ray Absorption Spectra of Spin-Crossover Complexes: Full Multiple Scattering Calculations for Several Iron(II) Trispyrazolylborate and Trispyrazolylmethane Complexes. *Inorg. Chem.* **2001**, *40*, 912−918.
(403) Jia, Q.; Ramaswamy, N.; Hafiz, H.; Tylus, U.; Strickland, K.; Wu, G.; Barbiellini, B.; Bansil, A.; Holby, E. F.; Zelenay, P.; et al. Experimental Observation of Redox-Induced Fe-N Switching Behavior as a Determinant Role for Oxygen Reduction Activity. *ACS Nano* **2015**, *9*, 12496−12505.
(404) He, H.; Lei, Y.; Xiao, C.; Chu, D.; Chen, R.; Wang, G. Molecular and Electronic Structures of Transition-Metal Macrocyclic Complexes as Related to Catalyzing Oxygen Reduction Reactions: A Density Functional Theory Study. *J. Phys. Chem. C* **2012**, *116*, 16038−16046.
(405) Zagal, J. H.; Koper, M. T. M. Reactivity Descriptors for the Activity of Molecular MN_4 Catalysts for the Oxygen Reduction Reaction. *Angew. Chem., Int. Ed.* **2016**, *55*, 14510−14521.
(406) Yang, H. B.; Hung, S.-F.; Liu, S.; Yuan, K.; Miao, S.; Zhang, L.; Huang, X.; Wang, H.-Y.; Cai, W.; Chen, R.; et al. Atomically Dispersed Ni(i) as the Active Site for Electrochemical CO_2 Reduction. *Nat. Energy* **2018**, *3*, 140−147.
(407) Freund, H. J.; Roberts, M. W. Surface Chemistry of Carbon Dioxide. *Sur. Sci. Rep.* **1996**, *25*, 225−273.
(408) Gao, S.; Lin, Y.; Jiao, X.; Sun, Y.; Luo, Q.; Zhang, W.; Li, D.; Yang, J.; Xie, Y. Partially Oxidized Atomic Cobalt Layers for Carbon Dioxide Electroreduction to Liquid Fuel. *Nature* **2016**, *529*, 68−71.
(409) Zhao, C.; Dai, X.; Yao, T.; Chen, W.; Wang, X.; Wang, J.; Yang, J.; Wei, S.; Wu, Y.; Li, Y. Ionic Exchange of Metal-Organic Frameworks to Access Single Nickel Sites for Efficient Electroreduction of CO_2. *J. Am. Chem. Soc.* **2017**, *139*, 8078−8081.
(410) Ebner, S.; Jaun, B.; Goenrich, M.; Thauer, R. K.; Harmer, J. Binding of Coenzyme B Induces a Major Conformational Change in the Active Site of Methyl-Coenzyme M Reductase. *J. Am. Chem. Soc.* **2010**, *132*, 567−575.
(411) Jiang, K.; Siahrostami, S.; Zheng, T.; Hu, Y.; Hwang, S.; Stavitski, E.; Peng, Y.; Dynes, J.; Gangisetty, M.; Su, D.; et al. Isolated Ni Single Atoms in Graphene Nanosheets for High-Performance CO_2 Reduction. *Enery Environ. Sci.* **2018**, *11*, 893−903.
(412) Pan, Y.; Lin, R.; Chen, Y.; Liu, S.; Zhu, W.; Cao, X.; Chen, W.; Wu, K.; Cheong, W.-C.; Wang, Y.; et al. Design of Single-Atom Co-N5 Catalytic Site: A Robust Electrocatalyst for CO_2 Reduction with Nearly 100% CO Selectivity and Remarkable Stability. *J. Am. Chem. Soc.* **2018**, *140*, 4218−4221.
(413) Genovese, C.; Schuster, M. E.; Gibson, E. K.; Gianolio, D.; Posligua, V.; Grau-Crespo, R.; Cibin, G.; Wells, P. P.; Garai, D.; Solokha, V.; et al. Operando Spectroscopy Study of the Carbon Dioxide Electro-reduction by Iron Species on Nitrogen-doped Carbon. *Nat. Commun.* **2018**, *9*, 935.
(414) Cao, L.; Luo, Q.; Liu, W.; Lin, Y.; Liu, X.; Cao, Y.; Zhang, W.; Wu, Y.; Yang, J.; Yao, T.; et al. Identification of Single-atom Active Sites in Carbon-Based Cobalt Catalysts During Electrocatalytic Hydrogen Evolution. *Nat. Catal.* **2019**, *2*, 134−141.
(415) Nørskov, J. K.; Abild-Pedersen, F.; Studt, F.; Bligaard, T. Density Functional Theory in Surface Chemistry and Catalysis. *Proc. Nat. Aca. Sci.* **2011**, *108*, 937.
(416) Nørskov, J. K.; Bligaard, T.; Rossmeisl, J.; Christensen, C. H. Towards the Computational Design of Solid Catalysts. *Nat. Chem.* **2009**, *1*, 37−46.
(417) Grajciar, L.; Heard, C. J.; Bondarenko, A. A.; Polynski, M. V.; Meeprasert, J.; Pidko, E. A.; Nachtigall, P. Towards Operando Computational Modeling in Heterogeneous Catalysis. *Chem. Soc. Rev.* **2018**, *47*, 8307−8348.
(418) Zhou, Y.; Doronkin, D. E.; Zhao, Z.; Plessow, P. N.; Jelic, J.; Detlefs, B.; Pruessmann, T.; Studt, F.; Grunwaldt, J.-D. Photothermal Catalysis over Nonplasmonic Pt/TiO_2 Studied by Operando HERFD-XANES, Resonant XES, and DRIFTS. *ACS Catal.* **2018**, *8*, 11398−11406.
(419) Sarma, B. B.; Plessow, P. N.; Agostini, G.; Concepción, P.; Pfänder, N.; Kang, L.; Wang, F. R.; Studt, F.; Prieto, G. Metal-Specific Reactivity in Single-Atom Catalysts: CO Oxidation on 4d and 5d Transition Metals Atomically Dispersed on MgO. *J. Am. Chem. Soc.* **2020**, *142*, 14890−14902.
(420) Chen, Y.; Rana, R.; Sours, T.; Vila, F. D.; Cao, S.; Blum, T.; Hong, J.; Hoffman, A. S.; Fang, C.-Y.; Huang, Z.; et al. A Theory-Guided X-ray Absorption Spectroscopy Approach for Identifying Active Sites in Atomically Dispersed Transition-Metal Catalysts. *J. Am. Chem. Soc.* **2021**, *143*, 20144−20156.
(421) Borfecchia, E.; Lomachenko, K. A.; Giordanino, F.; Falsig, H.; Beato, P.; Soldatov, A. V.; Bordiga, S.; Lamberti, C. Revisiting the Nature of Cu Sites in the Activated Cu-SSZ-13 Catalyst for SCR Reaction. *Chem. Sci.* **2015**, *6*, 548−563.

https://doi.org/10.1021/acs.chemrev.2c00495
Chem. Rev. 2023, 123, 379−444

(422) Giordanino, F.; Borfecchia, E.; Lomachenko, K. A.; Lazzarini, A.; Agostini, G.; Gallo, E.; Soldatov, A. V.; Beato, P.; Bordiga, S.; Lamberti, C. Interaction of NH_3 with Cu-SSZ-13 Catalyst: A Complementary FTIR, XANES, and XES Study. *J. Phys. Chem. Lett.* **2014**, *5*, 1552−1559.
(423) Zhang, R.; McEwen, J.-S. Local Environment Sensitivity of the Cu K-Edge XANES Features in Cu-SSZ-13: Analysis from First-Principles. *J. Phys. Chem. Lett.* **2018**, *9*, 3035−3042.
(424) Günter, T.; Carvalho, H. W. P.; Doronkin, D. E.; Sheppard, T.; Glatzel, P.; Atkins, A. J.; Rudolph, J.; Jacob, C. R.; Casapu, M.; Grunwaldt, J.-D. Structural Snapshots of the SCR Reaction Mechanism on Cu-SSZ-13. *Chem. Commun.* **2015**, *51*, 9227−9230.
(425) Fei, H.; Dong, J.; Feng, Y.; Allen, C. S.; Wan, C.; Volosskiy, B.; Li, M.; Zhao, Z.; Wang, Y.; Sun, H.; et al. General Synthesis and Definitive Structural Identification of MN_4C_4 Single-atom Catalysts with Tunable Electrocatalytic Activities. *Nat. Catal.* **2018**, *1*, 63−72.
(426) Joly, Y. X-ray Absorption Near-edge Structure Calculations Beyond the Muffin-tin Approximation. *Phys. Rev. B* **2001**, *63*, 125120.
(427) Bunau, O.; Joly, Y. Self-consistent Aspects of X-ray Absorption Calculations. *J.Phys: Cond. Matter* **2009**, *21*, 345501.
(428) Kitchin, J. R. Machine Learning in Catalysis. *Nat. Catal.* **2018**, *1*, 230−232.
(429) Sun, M.; Dougherty, A. W.; Huang, B.; Li, Y.; Yan, C.-H. Accelerating Atomic Catalyst Discovery by Theoretical Calculations-Machine Learning Strategy. *Adv. Energy. Mater.* **2020**, *10*, 1903949.
(430) Pal, N. R.; Bezdek, J. C. On Cluster Validity for the Fuzzy c-Means Model. *IEEE Transactions on Fuzzy Systems* **1995**, *3*, 370−379.
(431) Pal, N. R.; Pal, K.; Keller, J. M.; Bezdek, J. C. A Possibilistic Fuzzy c-Means Clustering Algorithm. *IEEE Transactions on Fuzzy Systems* **2005**, *13*, 517−530.
(432) Sun, M.; Wu, T.; Xue, Y.; Dougherty, A. W.; Huang, B.; Li, Y.; Yan, C.-H. Mapping of Atomic Catalyst on Graphdiyne. *Nano Energy* **2019**, *62*, 754−763.
(433) Xiang, S.; Huang, P.; Li, J.; Liu, Y.; Marcella, N.; Kumar Routh, P.; Li, G.; Frenkel, A. I. Solving the Structure of "Single-Atom" Catalysts using Machine Learning - Assisted XANES Analysis. *Phys. Chem. Chem. Phys.* **2022**, *24*, 5116−5124.
(434) Timoshenko, J.; Frenkel, A. I. Inverting" X-ray Absorption Spectra of Catalysts by Machine Learning in Search for Activity Descriptors. *ACS Catal.* **2019**, *9*, 10192−10211.
(435) Timoshenko, J.; Lu, D.; Lin, Y.; Frenkel, A. I. Supervised Machine-Learning-Based Determination of Three-Dimensional Structure of Metallic Nanoparticles. *J. Phys. Chem. Lett.* **2017**, *8*, 5091−5098.
(436) Timoshenko, J.; Anspoks, A.; Cintins, A.; Kuzmin, A.; Purans, J.; Frenkel, A. I. Neural Network Approach for Characterizing Structural Transformations by X-Ray Absorption Fine Structure Spectroscopy. *Phys. Rev. Lett.* **2018**, *120*, 225502.

https://doi.org/10.1021/acs.chemrev.2c00495
Chem. Rev. 2023, 123, 379−444